MICROSCALE FLUID–STRUCTURE INTERACTIONS BETWEEN VISCOUS

INTERNAL FLOWS AND ELASTIC STRUCTURES

A Dissertation

Submitted to the Faculty

of

Purdue University

by

Vishal Anand

In Partial Fulfillment of the

Requirements for the Degree

of

Doctor of Philosophy

August 2020

Purdue University

West Lafayette, Indiana

THE PURDUE UNIVERSITY GRADUATE SCHOOL
STATEMENT OF DISSERTATION APPROVAL

Dr. Ivan C. Christov, Chair

    School of Mechanical Engineering

Dr. Sadegh Dabiri

    Agricultural and Biological Engineering

Dr. Ganesh Subbarayan

    School of Mechanical Engineering

Dr. Steven T. Wereley

    School of Mechanical Engineering

Approved by:

    Dr. Nicole L. Key

        Head of the Graduate Program

To my parents.

And to Dr. Scott Peck, psychologist, humanist, author of "The Road Less Traveled".

ACKNOWLEDGMENTS

I would like to extend my gratitude to my adviser Dr. Ivan Christov for his intellectual leadership, his meticulous editing of my writings, and foremost the childlike enthusiasm with which he approached the problems of my PhD, making them his own. I met him at a time when my academic career was in doldrums. He was kind enough to take me under his wings and help emancipate me from a truly tight corner. For that alone, but not just that, I am truly indebted.

Beyond his decision to choose to mentor me, I am also indebted to him for trying to soften my PhD path as much as possible. He is a scientist who carries out research for the thrill and pleasure of scientific pursuit itself. He also helped enhance the productivity of my research, by allowing me to work with undergraduates from IIT Madras as co-authors. This truly enhanced both the pace and the output of my research.

Obviously, I am also thankful to the IIT Madras undergraduates themselves namely, Joshua David and Sanjan Manchandimath. I find both these young gentlemen are exceptionally gifted, hard working and motivated, much more than I was in their age. I am sure both will attain dizzying heights in their career. I am also thankful to my lab mates for being fantastic teammates and helpful colleagues. I wish them well in their future endeavors.

Lastly, I am indebted to my parents from being what they are: selfless, kind, farsighted, and devoted to their children. This PhD, which was my dream, became a shared dream among the three of us by the bond which keeps us together.

Finally, a big dose of gratitude is due to psychologist, philosopher, and writer (late) Dr. Scott Peck. It was his book, "The Road Less Traveled" which inspired me to face the challenges of life with honor and discipline. Without his gift to mankind, I would be truly lost.

PREFACE

"The task of the theorist is to bring order into the chaos of the phenomena of nature, to invent a language by which a class of these phenomena can be described efficiently and simply." – Clifford Truesdell (1965).

Theory is the language in which nature speaks to us. Theory provides the bridge of abstraction between nature and human perception. A surgeon wields his scalpel, and a butcher wields his knife. Likewise, scientists postulate theories to deconstruct nature, with all the vagaries of her mind and the fickleness of her mien. This makes the theoretical scientist a visionary and a prophet, who takes the first and the most significant step in the taming the force of nature and making it a tool for being harnessed by rest of the humanity.

In this thesis, under the mentorship of my adviser Dr. Ivan Christov, we present solutions to engineering problems involving the phenomena of fluid–structure interaction at the microscale. Specifically, we formulate pressure drop–flow rate relationship for conduits of different shapes, like rectangular and cylindrical, conveying fluids of different rheological models, Newtonian and generalized Newtonian, and composed of different constituent materials, linearly elastic, hyperelastic, viscoelastic.

The mechanics of solids, as well as that of fluids, at least at low Reynolds numbers, is very well known, having been subjected to more than a century of research and analysis. The governing equation of both subsets of continuum mechanics are well understood, and they can be solved with aid of sophisticated software in machines of even moderate computational powers. What then, one may ask, is so special about the interactions of fluids and solids, as to warrant devoting a PhD thesis towards their exploration?

There are two ways to answer this question. The first, more utilitarian answer is to realize that not all scientists working in continuum mechanics have access to or knowledge of computational methods and resources. This answer is more pertinent for experimen-

talists. In such scenarios, if a mathematical expression which consists of barely of a few terms and is accessible with a pen and paper, captures the essential physics of the system correctly, then the need of a high fidelity simulation, requiring special resources, is totally obviated. And therefore, the scientist is spared of many otherwise wasted resources, in terms of money, time and effort.

The second and the more idealistic answer, is that the goal of science is to simplify, not to obfuscate. It is to unite and to generalize, not to segregate and to specialize. The more generic and far reaching a theory is, the higher a pedestal it occupies in the hierarchy of theories. When viewed through this lens, carrying out a computer simulation for each and every problem seems to defeat the purpose of the scientific method. A succinct theory, which encompasses a class of problems, is truer to the spirit of science and is more useful, than a computer simulation which addresses just a single problem.

TABLE OF CONTENTS

LIST OF TABLES

LIST OF FIGURES

ABSTRACT

Anand, Vishal Ph.D., Purdue University, August 2020. Microscale Fluid–Structure Interactions between Viscous Internal Flows and Elastic Structures. Major Professor: Ivan C. Christov.

This thesis examines the problem of low Reynolds number viscous fluid–structure interactions (FSIs) at the microscale. A myriad of examples of such phenomena exist, both in nature (blood flow in arteries, air flow in lungs), as well as in the laboratory (microfluidics devices, soft robotics). For this thesis, we restrict to internal flows in conduits with deformable walls. Specifically, two types of conduits of different cross-sectional shapes are considered: microchannels and microtubes. Both of these geometries are slender and thin. Different types of material behavior are considered, via constitutive laws, in the solid domain, namely linearly elastic, hyperelastic and viscoelastic; and in the fluid domain, namely Newtonian and power-law fluids with shear-dependent viscosity. Similarly, the geometry and dimensions of the structures allow us to use shell and plate theories in the solid domain, and the lubrication approximation of low Reynolds number flow in the fluid domain.

First, we study a rectangular microchannel with a deformable top wall of moderate thickness, conveying a power-law fluid at steady conditions. We obtain a nonlinear differential equation for pressure as a function of imposed steady flow rate, consisting of infinite expansions of hypergeometric functions. We also conduct simulations of FSI using the commercial computer-aided engineering (CAE) software ANSYS, to both benchmark our perturbative theory and to establish the limits of its applicability.

Next, we study fluid–structure interactions in a thin microtube constituted of a linearly elastic material conveying a generalized Newtonian fluid. Here, we employ the Donnell shell theory to model the deformation field in the structure of the tube. As a novel contribution, we formulate an analytical expression for the (radial) deformation of the tube using

the method of matched asymptotic expansions, taking into account the bending boundary layers near the clamped ends. Using our perturbative theory, we also improve certain classical but partial results, like Fung's model and the law of Laplace, to match with direct numerical simulations in ANSYS.

Subsequently, we explore FSI in hyperelastic tubes via the Mooney–Rivlin model. In a thin-walled vessel, we formulate a novel nonlinear relationship between (local) deformation and (local) pressure A similar approach for the thick-walled tube, yields a nonlinear ODE to be solved numerically. Due to strain hardening, the hyperelastic tube appears stiffer and supports higher pressure drops than a linearly elastic tube.

Finally, we study transient compressible flow being conveyed in a linearly viscoelastic tube. By employing a double perturbation expansion (for weak compressibility and weak FSI), a predictive relationship between the deformed radius, the flow rate and the (local) pressure is obtained. We find that, due to FSI, the Stokes flow takes a finite time to adjust to any changes emanating from the boundary motion. In the case of oscillatory pressure imposed at the inlet, acoustic streaming is shown to arise due to FSI in this compressible flow.

Fundamentally, the goal of the research in this thesis is to generate a catalog of flow rate–pressure drop relationships for different types of fluid–structure interactions, depending on the combinations of fluid mechanics and structural mechanics models (behaviors). These relationships can then be used to solve practical problems. We formulate a theory of hydrodynamic bulge testing, through which the elastic modulus is estimated from the pressure drop and flow rate measurements in a microchannel with a (thick and pres-stressed) compliant top wall, without measuring the deformation. A sensitivity analysis, via Monte Carlo simulation, shows that the hydrodynamic bulge test is only a slightly less accurate than the traditional bulge test, but is less susceptible to uncertainty emanating from the noise in measurements.

1. INTRODUCTION

1.1 Background

Microfluidics is the study of the manipulation of microscopic volumes of fluids at small scales [1]. The subfield of fluid mechanics pertaining to flows at small scales, i.e., *low Reynolds number hydrodynamics* [2] is not a new field. Here, the Reynolds number is defined as $Re = \rho \mathcal{V}_c \ell_c / \mu$, where ρ, $\mathcal{V}_c$, ℓ_c, μ are the fluid density, the characteristic flow velocity, a characteristic length scale, and the fluid viscosity, respectively. On the other hand, the emergence of flow technologies at the microscale (and thus the emergence of the term "microfluidics") occurred only in the 1990s [3]. Technological advancements in microfabrication processes over the few past decades [4–6], also reviewed in [7], have made microscale fluid mechanics more accessible experimentally. The insights gained from latter studies have been harnessed for a variety of applications, which in turn sparked keener interest in using microfluidics to solve global, medial and social problems [8]. For example, technological applications of microfluidics include electronic chip cooling [9, 10], lab-on-a-chip devices [11] such as lab-on-a-CD diagnostics [12, 13], *in vitro* isolation of cancer cells [14] and clinical pathology [15], and various micro-total analysis (μTAS) systems [16,17], amongst others. Microfluidic devices afford many advantages over their traditional counterparts: portability, low reagent consumption and short analyses times, often at higher resolutions than macroscopic counterparts [7].

Fittingly, the enthusiasm in the scientific world over microfluidics then inspires the question: what really transpires at the microscale to set in motion such striking physical phenomena and the ensuing scientific interest therein? The answer is the mathematical result that when a system shrinks in size, the ratio of the surface area to the volume increases, and therefore effects that depend on the surface area are stronger than those that depend on the volume. Perhaps, an inquisitive mind has observed tiny insects walking on water, and

wondered how they are able to pull off a feat so impressive. Of course, this is explained considering that the weight of the insect, which is related to its volume, is negligible in comparison to the surface tension between the tiny, hydrophobic legs of the insect and water [18]. Indeed, most of the phenomena observed at microscale can be explained using this result [7]. Surface tension and capillary phenomena become important [19]. And, the question of appropriate boundary condition, slip or no slip, becomes relevant once again at the microscale [20]. It is possible, indeed desirable, to actuate fluid flows at the microscale by using surface charge densities, leading to a complex interplay between electrostatics and fluid mechanics [21]. The limitations imposed by macroscale mechanical devices for fluid property measurements has fueled research into microfluidic rheometry [22, 23]. At the microscale, materials are soft and fluid–structure interaction abound [24]. It is this last aspect of microfludics that we focus on in this thesis.

1.2   Fluid–structure interactions: Definition and types

Definition *A fluid–structure interaction (FSI) is the coupling between stress and deformation fields of a fluid and a solid continuum, due to the exchange of information between them across their common interface.*

The "information" that is exchanged at the interface may pertain to the stress field of the flow (viscous stress and/or pressure) and the deformation field of the structure.

As with most phenomena in fluid mechanics, fluid–structure interactions can be classified on the basis of the Reynolds number (*high* vs. *low*), which generally translates to the scale of the physical system (*macro* vs. *micro*). Another important aspect of FSIs relates to the rheology of the fluid and solid continua. Fluid rheology is classified as *Newtonian* vs. *non-Newtonian*; solids can be *linearly elastic*, *hyperelastic*, etc. Perhaps counter intuitively, flow at low *Re* can also be compressible, especially if it is a gas flow, as opposed to a liquid flow. This realization ushers in a yet another classification of flows of FSIs as *compressible* vs. *incompressible* FSI. The final category of classification of the FSIs, for our purposes, relates to the nature of the confinement of the fluid: *internal* vs. *external* flow.

The approach to modeling the structural mechanics problem introduces further need to classify the FSI regimes: i.e., between those pertaining to *small-strain* theory, with their linear strain–displacement relationships, and those pertaining to *large-strain* theory, with their corresponding nonlinear strain–displacement relationships. For internal flows, the geometry of the conduit (e.g., cylindrical, rectangular, elliptical cross-section, etc.) becomes another distinguishing characteristics of the problem. The constitutive laws governing material response of the structure (e.g., linearly elastic, hyperelastic, viscoelastic, poroelastic, etc.) introduces new possibilities for different types of FSI. Additionally, both the flow and deformation fields may be steady or transient. In the case of transient FSI, other phenomena like wave propagation and instabilities may also be relevant, which adds even more variety to FSIs.

In this thesis, however, we restrict ourselves to *internal* flows at the *microscale*. Non-Newtonian fluids with *shear-dependent viscosity* are considered. Both compressible and incompressible flow regimes are analyzed. The material of the structure is modeled as either (i) *linearly elastic*, (ii) *hyperelastic* or (iii) *linearly viscoelastic*, depending on the physical context. For the linearly viscoelastic material, the deformation field is necessarily *transient*, but for the other materials, only the static response will be analyzed.

1.3 Literature survey

1.3.1 Theoretical and experimental investigation

In confined flows at low *Re*, the flow conduit may be made of a deformable material [25], such as polydimethylsiloxane (PDMS) (a polymeric gel) [4] or elastin (a constituent of arteries) [26]. Such "creeping" flows can delaminate an elastic membrane from a solid boundary, forming blisters [27] that are prone to a wealth of mechanical instabilities [28] and whose inflation dynamics are sensitive to the contact line conditions [29]. The hydrodynamic pressure within such conduits is affected by the deformation of the conduit as a result of two-way FSI. Specifically, the pressure drop across a soft microchannel is significantly smaller compared to the rigid case [30]. Consequently, deviations are

expected from the classical *Hagen–Poiseuille law* [31], which relates the viscous pressure drop across a length of pipe to the volumetric flow rate, fluid properties and physical dimensions. The goal of our study of *microscale fluid–structure interactions* is to mathematically analyze and quantify such deviations.

Extensive experimental work over the past decade has sought to address FSI in microfluidics, specifically the effect of FSI on the flow rate–pressure drop relationship in a soft microchannel [30, 32–36]. In one of the earliest works, [30] employed a scaling analysis to determine the relation between the maximal channel deformation and the hydrodynamic pressure within a soft PDMS-based microchannel. The top wall of the microchannel was allowed to be compliant, while the remaining three walls were held rigid. By inserting the scaling relationship into the Hagen–Poiseuille law for a rectangular microchannel, Gervais et al. [30] captured the observed nonlinear (quartic) relationship between the flow rate and the pressure drop for a Newtonian fluid (water). However, the approach in [30] is not predictive because it contains a fitting parameter (the unknown proportionality constant in the scaling relationship), which has to be determined *a posteriori* by experiments.

Christov et al. [37] analyzed the problem of steady FSI in a microchannel via perturbation methods. Specifically, they determined the flow rate–pressure drop relation for a long, shallow microchannel with a compliant top wall by coupling a Kirchhoff–Love thin-plate theory to viscous flow under the lubrication approximation. Confirming the general observation in [30] and matching the experimental measurement in [34], it was shown in [37] that the flow rate–pressure drop relation is a quartic polynomial and the fitting parameter was thus eliminated through mathematical analysis. This approach was extended in [38] to capture thick top walls, via the first-order shear deformation plate theory of Mindlin [39], and extensively validated against fully-3D two-way coupled direct numerical simulations [38]. More recently, the flow-induced deformation measurements reported in [30] were fully rationalized by a theory [40] taking into account the "full" elasticity problem for the thick, deformable top wall (i.e., dropping the assumption of a plate-like top wall). Importantly, however, in [37, 38, 40] the cross-sectional deformation profile of the microchannel's compliant wall was determined. The perturbation approach's generality is appealing as, in

theory, higher-order corrections to the flow rate–pressure drop relation can be obtained following the calculation in [41], wherein an *extended* lubrication theory was developed. This approach is valid for channels with modest aspect ratios and with shape changes on the order of the channel height.

Recently, Raj and Sen [42] documented an initial foray into the experimental interrogation of non-Newtonian FSIs in a microchannel. A rectangular microchannel with three rigid walls and a compliant top wall was manufactured from polydimethylsiloxane (PDMS). A 0.1% polyoxyethylene (PEO) solution was used as a shear-thinning non-Newtonian fluid. The pressure drop across 12 mm increments of the 30 mm-long microchannel was measured by a series of differential pressure sensors. (The microchannel was long and thin, having a width between 0.5 and 2 mm and height of 83 μm in the cross-section.) The deflection of the compliant top wall was measured using fluorescence imaging. Raj and Sen [42] then proposed a modeling approach for capturing the pressure drop as a function of the flow rate (and other material and geometric parameters) based on a modification of the early work in [30]. As mentioned earlier, the original approach in [30] is based on scaling arguments and, thus, contains a fitting parameter that cannot be predicted *a priori*. Due to their use of narrowly-applicable correlation for stretching of thin shells [43, pp. 29–33], Raj and Sen [42] do not obtain a flow rate–pressure drop prediction of much generality. Moreover, since the theoretical predictions were for Newtonian fluids only, they could not be compared with the experiments reported for non-Newtonian fluids.

The study of moderate-*Re* instabilities due to FSIs in soft tubes is a time-honored subject [44–46] primarily due to their relevance in modeling biological flow in the arteries and the lungs. Consequently, microtubes traditionally reside on the opposite end of the FSI spectrum from microchannels, in terms of Reynolds number. Specifically, the study of *collapsible tubes* interrogates the case of microtubes whose radius *decreases* owing to negative transmural pressure difference and eventually can completely collapse [47, 48]. Here, the flow field is one-dimensional, averaged across the cross section, but not developed [47]. Viscous effects are modeled using a pipe flow friction factor. A *tube law* is obtained to relate the local transmural pressure difference to the change in area due to circumferential

and axial bending and tension, from postulated simple relations [47] to rigorous derivations from shell theory [49]. Even though the problem of collapsible tubes involves liquid flow, [47] elegantly explained the analogy to gas dynamics: a *speed index*, akin to the Mach number, divides the flow into subcritical and supercritical regimes. The relevance of this moderate-to-high-*Re* FSI is soft tubes is evident in biofluid mechanics [50,51], for example in the contraction of the trachea during bouts of coughs [44]. The mathematical analysis of stability of such flows in three-dimensions is an ongoing challenge [52]. Nevertheless, there is also a need to develop accurate models for low-*Re* FSI in soft tubes due to the relevance to blood flow through small arteries [53]. Meng et al. [54] studied such a problem of drainage of liquids from collapsible tubes of circular and elliptical cross-sections. The tubes had been stretched initially with a prescribed tension in the radial direction and then filled with a fluid. The pressure built up inside the fluid is then a function of the prescribed tension. Assuming plane-strain conditions inside the structure with zero net axial force and the Hagen–Poiseuille law for the Newtonian flow within, a set of differential equations governing the evolution of the tube axes was obtained in [54]. Neither the flow rate nor pressure drop across the tube were specified initially, but they could be computed by this approach.

For FSIs in soft tubes, most of the latter research has focused on Newtonian fluids. Most of the biofluids are, however, non-Newtonian [55, 56]. Blood is often modeled as a Casson fluid, which has both a yield stress and a shear-dependent viscosity [57, Ch. 3]. Research on microscale FSIs has only just begun to take into account the non-Newtonian nature of the working fluids [42, 58–60]. Raj M *et al.* [59] performed experiments on FSIs in a microchannel with *circular* cross-section, which is more akin to a blood vessel. This conduit was fabricated from PDMS using a pull-out soft lithography process from a large slab. Xanthan gum was used as a non-Newtonian blood-analog fluid. Measurements of the pressure drop at different inlet flow rates were shown to match a simple mathematical model of one-way FSI, meaning that the pressure was calculated using the Hagen–Poiseuille law for a rigid tube and then imposed as a load on the structure, without coupling the microchannel shape change back into the hydrodynamics. Microtubes and microchannels of circular

cross-section are now of significant scientific interest due to "a new, direct peeling-based technique for building long and thin, highly deformable microtubes" [61], which can be used in building bioinspired and biocompatible soft devices [62].

In a recent series of works [58, 63, 64], two-way FSI coupling was employed to analyze the transient pressure and deformation characteristics of a shallow, deformable microtube. Employing the Love–Kirchhoff hypothesis, a relation was obtained between the internal pressure load in a soft tube and its radial and axial deformations, up to the leading order in slenderness. Treating the structural problem as quasi-static, an unsteady diffusion-like equation for the fluid pressure was obtained and analyzed for both Newtonian [63, 64] and generalized Newtonian [58] fluids. However, the effect of non-trivial deformation on the resulting flow rate–pressure drop relation for the tube (transient or steady-state) was not considered or benchmarked against simulations and/or experiments. Meanwhile, Vedeneev *et al.* [65] obtained results on moderate-Re instabilities in collapsible tubes conveying generalized Newtonian fluids.

Hyperelastic materials have the "advantage" of being completely specified by a strain energy functional from which the constitutive equation between stress and strain follows. The structural response of complex soft solids, such as biological tissue and blood vessels, can be appropriately described by a hyperelastic solid with a *pseudo* strain energy function (see, e.g., [57, Ch. 8 and Ch. 9]). Similarly, due to its complex constituents, blood is a non-Newtonian fluid and an appropriate rheological model (beyond the simple Newtonian viscous fluid) should be used (see, e.g., [57, Ch. 3]).

While it is common to assume the flow at low Re to be incompressible, perhaps counter intuitively, compressible flow of gases, even for at low Mach number $Ma \to 0$, have been observed experimentally in the low Re regime. For example, gas flows at the microscale find applications in several micro-electro-mechanical systems (MEMS) for pneumatic flow control and electronic cooling [66–68]. In these systems, sufficiently large pressure drops across a channel may lead to compressibility effects in the flow. A hallmark of low Mach number compressibility is the nonlinear axial pressure profile, as reported in the experiments in [69, Fig. 10]. Compressible flow at the microscale has been studied experi-

mentally in a straight, uniform-width channel [70]; in a channel that is straight but has nonuniform cross-section, with contractions and expansions [71]; and in a channel that has uniform cross-section but is not straight (has bends and junctions) [72]. Arkilic et al. [73] performed experiments on helium flow in microchannels to demonstrate compressible flow at low Re. The results of the experiments were explained by a theoretical analysis of compressible flow. The lubrication theory formulation of the Navier–Stokes equations was employed with a first-order slip velocity boundary condition expressed in terms of the Knudsen number $Kn = \lambda/a$, which is the ratio of the molecular mean free path of the gas λ to a characteristic length a of the system at the macro scale. Various regimes of the flow were delineated on the basis of the relative magnitudes of Ma and Re. The theory presented therein was verified independently in [70, 74], amongst others. A more recent experimental study [75] accounted for both compressibility of the flow and the compliance (bulging) of the channel.

Experimental investigations of compressible flow in channels have proceeded in tandem with the theoretical studies [73, 76–82]. Prud'Homme et al. [76] analyzed the compressible flow of a monoatomic ideal gas (with zero bulk viscosity) in a capillary with pressure imposed at the inlet and the outlet. The results showed that due to compressibility, the mass flow rate increases (in comparison to incompressible flow) for a fixed pressure drop across the capillary. In [76, 78], the lubrication approximation was imposed explicitly, by assuming negligible radial velocity and negligible radial pressure gradient. However, [78] assumed an arbitrary equation of state and also accounted for non-zero bulk viscosity, venturing beyond the monoatomic ideal gas model of compressible flow analyzed by [76]. These results can be used to account for compressibility effects while estimating viscosity of gases using capillary viscometers [77]. However, as noted in [78, 79], in compressible flow the absence of radial velocity does not generally imply the absence of a radial pressure gradient. Therefore, instead of assuming zero radial velocity and zero radial pressure gradient *a priori*, [79] solved the full Navier–Stokes equation for compressible flow, employing a perturbation expansion with the compressibility number (defined later) as the perturbation parameter. The results showed the fluid's convective inertia leads to a radial velocity

in the flow while a radial pressure gradient arises from non-zero bulk viscosity. Similar analysis was also carried out by [80] for compressible flow in a channel and by [81] for both channels and tubes.

Recently, there has been a resurgence of interest in low R compressibility effects, including taking into account microscale fluid–structure interactions (FSIs) [83–85]. The availability of new polymer-based materials like, polydimethylsiloxane (PDMS), a silicon-based polymeric material that allows the rapid and precise manufacture of microdevices [86], coupled with emergence of new manufacturing methods such as soft lithography [4], have revolutionized the microfluidics industry [8]. PDMS is "soft," meaning it has an elastic modulus on the order of a few MPa, compared to a GPa or more for "hard" materials such as steel. Therefore, PDMS-based microchannels and microtubes deform significantly under the influence of hydrodynamic pressure forces induced by viscous stresses during flow. The deformation in turn alters the cross-sectional shape, which modifies the velocity profile and, thus, the viscous stress in the flow, which then induce the pressure load on the structure. This feedback loop is an example of the two-way coupled nature of fluid–structure interactions (FSIs) [87].

The current literature on FSIs involing compressible flows has only addressed the case of linearly elastic structures [83–85]. However, in transient conditions, PDMS is known to exhibit a viscoelastic response [88, 89]. In biomechanics, many soft tissues are viscoelastic [57, Ch. 7]. The mechanical properties of lung tissues can be modeled by a linear viscoelastic model in the breathing frequency range [90]. In particular, the simplest useful model is the Kelvin–Voigt (KV) element consisting of a linearly elastic spring in parallel with a linearly viscous element. Under this modeling approach, [91] derived weakly nonlinear governing equations for wave propagation due to pulsatile flows in linearly viscoelastic tubes. They emphasized that "viscoelastic effects are very important and should be included in future studies" [91, p. 147], further motivating our work. Specifically, the amplitude of the wave reduced by 17%, when the viscoelasticity of the wall was included, compared to the purely elastic case. However, since their study addressed hemodynamics, compressibility effects were not addressed by the model.

Viscous damping of elastic structures is also a key design feature of soft robotic actuators [92–94]. Damping in a robotic actuator hastens stabilization by promoting energy dissipation [92]. Specifically, excess energy introduced into the system during the impact of a rigid object on a robotic hand performing grasping must be dissipated to ensure the smooth functioning of actuators, and to prevent damage to attached sensors. This dissipation of energy can be accomplished by using materials (such as rubbers, gels, sponges etc.) that exhibit viscoelasticity [92, 93]. Furthermore, recently, attention has turned to bio-inspired soft robotics [94]. As noted above, most biological tissues (like skin, muscles, etc.) are viscoelastic [57, Ch. 7], thus biomimetic soft robots are also designed with a viscoelastic material response in mind [94]. Most soft robots are actuated pneumatically [95] Thus, understanding *compressible* flows interacting with compliant*viscoelastic* structures may provide insight into the design of pneumatically actuated biomimetic soft robots. So far, however, the FSI literature on viscoelastic [91] or elastic [58, 63, 84] tubes with transient (inertial) response has only considered incompressible flow, while the FSI literature on compressible flows has only dealt with linearly elastic structures [84, 96], except for some systems-level modeling of wave speeds for water hammer phenomena in viscoelastic tubes [97, 98] at large Re. The present work fills a knowledge gap on compressible flow in viscoelastic tubes with transient response.

Elastic deformation of structure need not always be a peripheral, unwanted effect in microscale flows. FSIs can also be employed for passive control of flows in microchannels [99–101]. For example, Holmes et al. [100] carried out an experimental investigation of mechanically-actuated flow control within a flexible microchannel through a series of arches placed in the microchannel that function as valves to regulate and direct the flow. Meanwhile, Gomez et al. [101] harnessed an elastic snap-through mechanism to design a microfluidic fuse. In a microchannel with a thin elastic strip as one wall, buckling of the arch by the viscous flow underneath allows passive rapid transition between a constricted and an unconstricted flow state (with concomitant rapid changes in the flow conductivity of the microchannel).

A major phenomena pertaining to unsteady FSI in internal flows is peristalsis, wherein wave propagation in the elastic structure actuates the internal fluid flow. Indeed, peristalsis is the primary mechanisms of swallowing of food and its movement through esophagus in vertebrates and can also be used to construct an elastohydrodynamic model of swallowing [102]. Both single wave propagation [103] or propagation of a train of infinitesimally-small-amplitude waves [104] can be considered. Reflux and trapping are two major mechanisms of wave propagation in peristalsis [104]. Frequently, to enhance the ability to actuate the flow, peristalsis is combined with other microscale phenomena, such as electo-osmosis [103, 105] and interfacial slip, among others.

1.3.2 Applications

The theory of low *Re* FSI in internal flows has applications beyond the modified pressure drop–flow rate relationship. For example, low *Re* FSI theory can be leveraged to estimate the material property of a linear elastic solid through the framework of a novel *hydrodynamic* bulge test. A (traditional) bulge test involves clamping a thin elastic sheet over an orifice (or a window) and, then, measuring its deformation under a known (usually uniform) pressure field [106–108]. The measured deformation as a function of the known pressure load can then be converted to strain as a function of stress, by employing a suitable structural mechanics model (e.g., the theory of linear elasticity). In turn, knowing the stress as a function of the imposed strain allows for straightforward estimation of the elastic modulus of the material (assuming that the Poisson's ratio is known) [106–108]. Knowledge of the stress distribution within the structure is also used to estimate fracture properties of the material [109–111]. Several techniques have been proposed to improve the accuracy of "traditional" bulge tests. These improvements include, but are not limited to, accounting for the film's bending stiffness [112], accounting for pre-stress in the film [106, 113], considering the possibility of buckling [114] and better prediction of the stress distribution near edges [115] by using elastically clamped (instead of the traditional rigidly clamped) boundary conditions [109, 110].

One of the main sources of uncertainty in bulge tests is the experimental measurement of the film's deformation [108]. Traditionally, deformation has been measured by interferometric techniques and, less frequently, by high-resolution microscopy. Both of these measurement techniques have certain limitations. On the one hand, interferometers are prone to errors induced from external sources of vibrations [108], which limits the spatial resolution of the measurements and makes it difficult to accurately resolve deformations in the small-strain regime relevant to bulge testing [106, 108]. On the other hand, microscopes are not well suited to analyze samples with high reflectance, such as PDMS [108]. Thus, there is motivation for developing bulge testing techniques that bypass the deformation measurement altogether.

Often, bulge testing techniques discussed in the literature have focused on circular membranes [106], with only a few studies addressing the case of rectangular membranes with pre-stress [109–111, 116] using energy minimization methods [113]. Residual pre-stress (pre-tension) is common in samples being tested because the thin film of material has to be stretched taut over an orifice (say, a rectangular microchannel) to ensure that it is flat before the commencement of the experiment [117, 118]. Furthermore, most of the bulge testing theories in the literature assume that the film has negligible thickness and deformations due to shear along the transverse direction are, thus, not accounted for.

Using the theory of low *Re* FSI, it is also possible to formulate an expression for friction factor for a deformable channel or tube, and thus extend the Moody's chart to hitherto unknown domains. The friction factor is a dimensionless representation of the pressure drop due to fully-developed flow through a rigid conduit. The traditional visual representation of the friction factor, and its dependence upon other key dimensionless parameters, is the Moody diagram [119], featured in every undergraduate textbooks on fluid mechanics [120]. The friction factor represented in the Moody diagram is obtained under the assumptions of isothermal flow of an incompressible, Newtonian fluid in a rigid tube (for both laminar and turbulent flows). It has been of interest to extend the calculation and prediction of the friction factor beyond the "ideal" (textbook) cases. For example, the compressible flow of gases, at large Mach number, engenders a pressure drop that cannot be accurately pre-

dicted by the incompressible friction factor from the classical Moody diagram and therefore the expression for friction factor should be modified to account for the flow compressibility [76, 78]. Similarly, the flow rate–pressure drop relationship for deformable channels and tubes may also be re-formulated as an expression for friction factor. Besides being a theoretical innovation, a novel expression for friction factor which takes into account the deformation of the flow conveying conduits, may find practical uses in microscale rheometry, for estimating the viscosity of a flowing fluid [121, 122].

1.4   Knowledge gaps and organization of the thesis

The literature survey presented in the previous section identifies the following key gaps in the research on low Reynolds number FSI:

- While there have been limited experimental measurements of FSI of non-Newtonian fluids in microchannel [42], the theoretical treatment has been restricted to Newtonian fluids. Thus, a clear gap remains in the non-Newtonian fluid mechanics literature: *What is the flow rate–pressure drop relation when FSI, due to a non-Newtonian fluid flow in a compliant rectangular microchannel, is taken into account?* This question has been addressed in Chapter 2 of this thesis.

- Beyond the fundamental knowledge gained about FSIs in microchannels through the theory and simulations in Chapters 2, there remain some open questions about how FSIs could be used in practice. A knowledge gap in the literature on materials property characterization at the microscale exists regarding: *How can we determine the elastic properties of thin sheets of materials, without the need for a precise microscale deformation measurement? How can we take into account residual pre-stresses in the membrane?* To address these questions, in Chapter 3 of this thesis, we demonstrate how to characterize the elastic properties of a soft material using a mathematical model derived to relate the *total* pressure drop, at steady state, over the length of the elastic sheet to the imposed volumetric flow rate of the fluid flow underneath it.

- Then, as far as non-Newtonian FSIs in microtubes go, the current theory captures transient FSIs only, at the leading order ; the corresponding steady state theory is still missing. Moreover, there has been few detailed validations of the existing theory against either simulations or experiments. Therefore, a clear gap remains in the literature pertaining to steady-state FSI in tubes: *What is the corresponding flow rate–pressure drop relationship due to non-Newtonian fluid flow in microtubes? Are simple expression of the latter in textbooks valid when compared to direct numerical simulations? How do we account for bending layers in the deformation profile near clamped edges?* These questions are addressed in Chapter 4 of this thesis.

- Since most biological tissues are hyperelastic, not linearly elastic, the flow rate–pressure drop relation derived for elastic tubes in Chapter 4 may be suitable for analyzing FSI in such tissues conveying low *Re* flows. Therefore, this gap in the literature pertains to: *How does hyperelastic response of the elastic vessel, conveying a non-Newtonian fluid, affect its hydrodynamic resistance?* This question has been addressed in Chapter 5 of this thesis.

- Many studies carried out pertaining to FSI, including the earlier chapters of this thesis, so far have tackled the incompressible flow problem. At the same time, compressible flow has always been analyzed when interacting with linearly elastic channels and tubes. Under unsteady conditions, linear viscoelasticity of tube can be important in determining the dynamic response. Therefore, the gap in the literature remains regarding our understanding of transient low *Re* compressible fluid flow in viscoelastic tubes. Specifically, *How do transient gas flow and viscoelastic tube deformation couple under transient conditions? What novel dynamical phenomena can be uncovered by analyzing such FSIs?* These questions are addressed in Chapter 6 of this thesis.

2. DEFORMABLE MICROCHANNELS: STATIC RESPONSE TO NON-NEWTONIAN FLOW

SUMMARY

We study fluid–structure interactions (FSIs) in a long and shallow microchannel, conveying a non-Newtonian fluid, at steady state. The microchannel has a linearly elastic and compliant top wall, while its three other walls are rigid. The fluid flowing inside the microchannel has a shear-dependent viscosity described by the power-law rheological model. We employ lubrication theory to solve for the flow problem inside the long and shallow microchannel. For the structural problem, we employ two plate theories, namely Kirchhoff–Love theory of thin plates and Reissner–Mindlin first-order shear deformation theory. The hydrodynamic pressure couples the flow and deformation problem by acting as a distributed load onto the soft top wall. Within our perturbative (lubrication theory) approach, we determine the relationship between the flow rate and the pressure gradient, which is a nonlinear first-order ordinary differential equation for the pressure. From the solution of this differential equation, all other quantities of interest in non-Newtonian microchannel FSIs follow. Through illustrative examples, we show the effect of FSI coupling strength and the plate thickness on the pressure drop across the microchannel. Through direct numerical simulation of non-Newtonian microchannel FSIs using commercial computational engineering tools, we benchmark the prediction from our mathematical theory for the flow rate–pressure drop relation and the structural deformation profile of the top wall. In doing so, we also establish the limits of applicability of our perturbative theory.

The material in this chapter was published in [V. Anand, J. David JR, and I. C. Christov, "Non-Newtonian fluid–structure interactions: Static response of a microchannel due to internal flow of a power-law fluid," *J. Non-Newtonian Fluid Mech.*, vol. 264, pp. 62–72, 2019] [60]

2.1 Problem formulation and mathematical analysis

2.1.1 Fluid flow problem

The key assumptions imposed on the fluid flow problem are that an incompressible viscous fluid flows in a channel that is (a) shallow (width w much greater than its undeformed height h_0) and (b) long (undeformed height h_0 much smaller than its length ℓ); see Fig. 2.1 for notation. These assumptions lead to an ordering of length scales:

$$h_0 \ll w \ll \ell, \tag{2.1}$$

and the emergence of *two* small dimensionless parameters in the problem, i.e., $\epsilon := h_0/\ell$ and $\delta := h_0/w$. Then, as shown in [37], for steady, fully developed conditions, the flow obeys the classical lubrication approximation [3, 123] for $\epsilon \ll \delta \ll 1$. Specifically, to the leading order in ϵ and δ, the flow field is unidirectional

$$\boldsymbol{v} \sim v_z(x, y)\hat{\boldsymbol{k}}, \tag{2.2}$$

and the $\hat{\boldsymbol{\imath}}$ and $\hat{\boldsymbol{\jmath}}$ flow components can be thus neglected. (Here, we use the standard notation of $\hat{\boldsymbol{\imath}}$, $\hat{\boldsymbol{\jmath}}$ and $\hat{\boldsymbol{k}}$ being the unit normal vectors in the x, y and z coordinate directions.) Such a flow automatically satisfies the conservation of mass (continuity) equation $\boldsymbol{\nabla} \cdot \boldsymbol{v} = 0$ for an incompressible fluid.[1]

Similarly, the lubrication approximation dictates that we may neglect inertial forces in comparison to viscous and pressure forces in the fluid. Then, as a consequence of the kinematics, i.e., Eq. (2.2), the pressure becomes independent of x and y. This result is a well known consequence of the flow geometry being "long and thin" [124]. Lubrication flows of non-Newtonian fluids have been studied extensively, for example in the context of *rivulets* [125, 126], but not as much in the microfluidics and FSI contexts.

Next, the fluid's only nontrivial momentum balance is in the z-direction:

$$0 = -\frac{\mathrm{d}p}{\mathrm{d}z} + \frac{\partial \tau_{yz}}{\partial y} \qquad \Rightarrow \qquad \tau_{yz} = \frac{\mathrm{d}p}{\mathrm{d}z} y + C_1. \tag{2.3}$$

---

[1]This statement is true subject to the caveat that, due to FSI, v_z will "pick up" a weak dependence on z, which is still valid within the lubrication approximation [3, 123].
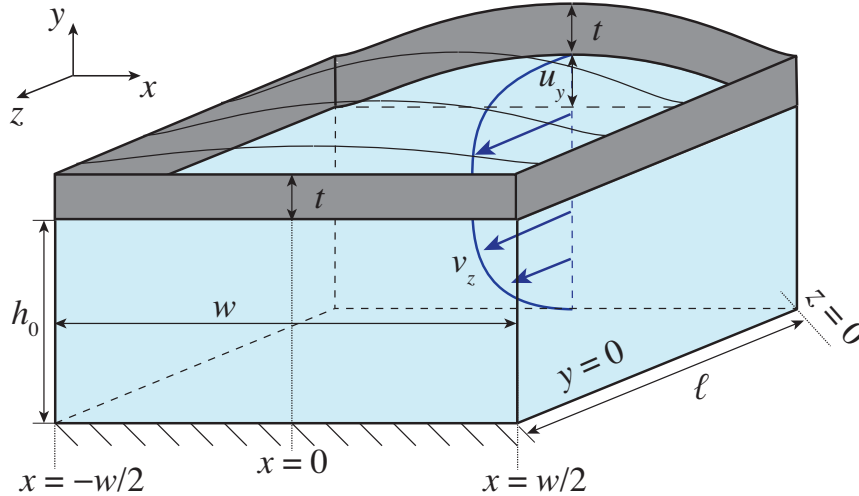
Fig. 2.1. Schematic of the chosen microchannel geometry with three rigid and one soft (top) wall. Notation used in the main text is labeled in the schematic. Clamping of the plate along the inlet ($z = 0$) plane is not shown for clarity.

To fix the constant of integration, we must specify τ_{yz} somewhere. Consider the following: for a rigid channel the centerline is at $y = h_0/2$, however, after the deformation of the upper wall, the centerline shifts to $y = (h_0 + u_y)/2$. Here, $u_y(x, z)$ is the absolute deformation of the top wall in the y-direction, while $h_0 = const.$ is the undeformed (initial) height of the channel (see Fig. 2.1). We require that the shear stress vanish at the centerline, $\tau_{yz}|_{y=(h_0+u_y)/2} = 0$. Hence,

$$C_1 = -\frac{\mathrm{d}p}{\mathrm{d}z}\left(\frac{h_0 + u_y}{2}\right). \tag{2.4}$$

Next, we must specify the constitutive equation between stress and shear rate-of-strain. The rheological behavior of most biofluids is non-Newtonian [56]. Specifically, human blood has been shown to exhibit a shear-thinning behavior [127], which can be described by the *power-law* (also known as Ostwald–de Waele) model [128]. Under the lubrication approximation [3, 123], it can be shown that the dominant term in the deviatoric stress tensor is the shear stress. Under the latter approximation, the power-law rheological model reduces to:

$$\tau_{zy} = \eta \frac{\partial v_z}{\partial y} = m \left|\frac{\partial v_z}{\partial y}\right|^{n-1} \left(\frac{\partial v_z}{\partial y}\right), \tag{2.5}$$

where $\eta = m|\partial v_z/\partial y|^{n-1}$ is the *apparent viscosity* [129]. Here m is the consistency factor, which reduces to the dynamic viscosity for a Newtonian fluid, and n is the power-law index with a value of $n = 1$ for the special case of a Newtonian fluid.

Now, for the lower half of the channel, i.e., for $0 \leq y \leq (h_0 + u_y)/2$, we expect the velocity gradient to be positive under our chosen sign convention:

$$\frac{\partial v_z}{\partial y} > 0 \qquad \Rightarrow \qquad \left|\frac{\partial v_z}{\partial y}\right| = \frac{\partial v_z}{\partial y}. \tag{2.6}$$

Then, combining the momentum Eq. (2.3) with the appropriate simplification of the constitutive Eq. (2.5) yields

$$m\left(\frac{\partial v_z}{\partial y}\right)^n = \left(\frac{\mathrm{d}p}{\mathrm{d}z}\right)\left(y - \frac{h_0 + u_y}{2}\right) \qquad \Rightarrow \qquad \frac{\partial v_z}{\partial y} = \left(-\frac{1}{m}\frac{\mathrm{d}p}{\mathrm{d}z}\right)\left(\frac{h_0 + u_y}{2} - y\right)^{1/n}. \tag{2.7}$$

Integration of the last equation subject to no slip on the lower wall, i.e., $v_z = 0$ at $y = 0$, yields the expression for velocity profile in the *lower* half of the channel, i.e., $0 \leq y \leq (h_0 + u_y)/2$:

$$v_z(x, y, z) = \frac{1}{1 + 1/n}\left(-\frac{1}{m}\frac{\mathrm{d}p}{\mathrm{d}z}\right)^{1/n}\left(\frac{h_0 + u_y}{2}\right)^{1+1/n}\left\{1 - \left[1 - \frac{y}{(h_0 + u_y)/2}\right]^{1+1/n}\right\}. \tag{2.8}$$

Now, for the upper half of the channel, i.e., for $(h_0 + u_y)/2 \leq y \leq (h_0 + u_y)$, the velocity gradient is negative:

$$\frac{\partial v_z}{\partial y} < 0 \qquad \Rightarrow \qquad \left|\frac{\partial v_z}{\partial y}\right| = -\frac{\partial v_z}{\partial y}. \tag{2.9}$$

Consequently,

$$-m\left(-\frac{\partial v_z}{\partial y}\right)^n = \frac{\mathrm{d}p}{\mathrm{d}z}\left(y - \frac{h_0 + u_y}{2}\right) \qquad \Rightarrow \qquad -\frac{\partial v_z}{\partial y} = \left(-\frac{1}{m}\frac{\mathrm{d}p}{\mathrm{d}z}\right)^{1/n}\left(y - \frac{h_0 + u_y}{2}\right)^{1/n}. \tag{2.10}$$

Integration of the last equation subject to no slip at the upper wall, i.e., $v_z = 0$ at $y = h_0 + u_y$ yields the expression for velocity profile in the *upper* half of the channel, i.e., $(h_0 + u_y)/2 \leq y \leq h_0 + u_y$:

$$v_z(x, y, z) = \frac{1}{1 + 1/n}\left(-\frac{1}{m}\frac{\mathrm{d}p}{\mathrm{d}z}\right)^{1/n}\left(\frac{h_0 + u_y}{2}\right)^{1+1/n}\left\{1 - \left[\frac{y}{(h_0 + u_y)/2} - 1\right]^{1+1/n}\right\}. \tag{2.11}$$

This completes the derivation of the velocity profile, which is piecewise defined by Eqs. (2.8) and (2.11), of a power-law fluid in a microchannel with a deformed top wall shape given by

$$h(x, z) = h_0 + u_y(x, z). \tag{2.12}$$

Nondimensionalization

To make the governing equations dimensionless, we introduce the following dimensionless variables:

$$\bar{p} = p/\mathcal{P}_c, \quad \bar{v}_{\bar{z}} = v_z/\mathcal{V}_c, \quad \bar{x} = x/w, \quad \bar{y} = y/h_0, \quad \bar{z} = z/\ell,$$

$$\bar{u}_{\bar{y}} = u_y/u_c, \quad \beta = u_c/h_0, \quad \epsilon = h_0/\ell, \quad \delta = h_0/w. \tag{2.13}$$

Here, h_0, w and ℓ are, respectively, the undeformed height, fixed width and constant length of the microchannel as in Fig. 2.1. Making the fluid's momentum equation (2.3) dimensionless and ensuring all terms are of order one, we can determine how the characteristic velocity scale is related to the characteristic pressure scale, namely $\mathcal{V}_c = [\mathcal{P}_c h_0/(m\ell)]^{1/n} h_0$. Then, the pressure scale can be taken to be $\mathcal{P}_c = \Delta p$ if Δp is known (pressure-controlled experiment/simulation) or estimated as $\mathcal{P}_c = [q/(h_0^2 w)]^n m\ell/h_0$ if q is known (flow-rate-controlled experiment/simulation). Each choice then yields a corresponding velocity scale $\mathcal{V}_c = [\Delta p\, h_0/(m\ell)]^{1/n} h_0$ or $\mathcal{V}_c = q/(h_0 w)$, respectively. The characteristic scale of deflection u_c will be determined self-consistently below by coupling the flow and structural deformation problems, from which we will then determine the ratio β. The two length ratios, ϵ and δ, are key to satisfying the asymptotic requirements of the lubrication approximation. Specifically, we require that a separation of scales exists, i.e., $0 < \epsilon \ll \delta \ll 1$, meaning the microchannel is *long* and *shallow*.

In terms of the dimensionless variables from Eq. (2.13), the velocity profile from Eqs. (2.8) and (2.11) above now takes the form:

$$
\bar{v}_{\bar{z}}(\bar{x}, \bar{y}, \bar{z}) = \frac{1}{2^{1+1/n}} \left(-\frac{\mathrm{d}\bar{p}}{\mathrm{d}\bar{z}} \right)^{1/n} \frac{(1 + \beta \bar{u}_{\bar{y}})^{1+1/n}}{1 + 1/n}
$$

$$
\times \begin{cases} 1 - \left[1 - \dfrac{\bar{y}}{(1 + \beta \bar{u}_{\bar{y}})/2} \right]^{1+1/n} , & \bar{y} < [1 + \beta \bar{u}_{\bar{y}}(\bar{x}, \bar{z})]/2, \\[2em] 1 - \left[\dfrac{\bar{y}}{(1 + \beta \bar{u}_{\bar{y}})/2} - 1 \right]^{1+1/n} , & \bar{y} \geq [1 + \beta \bar{u}_{\bar{y}}(\bar{x}, \bar{z})]/2, \end{cases} \tag{2.14}
$$

while the dimensionless microchannel height is

$$
\bar{h}(\bar{x}, \bar{z}) \equiv h(x, z)/h_0 = 1 + \beta \bar{u}_{\bar{y}}(\bar{x}, \bar{z}). \tag{2.15}
$$

It is straightforward to verify that the velocity profile is continuous at $\bar{y} = (1 + \beta \bar{u}_{\bar{y}})/2$.

2.1.2 Coupling flow and deformation: Finding the flow rate

We study steady flow, thus conservation of mass then requires that the volumetric flow rate $q = const$. This flow rate is, by definition, given by

$$
q = \int_{-w/2}^{+w/2} \int_0^{h_0+u_y} v_z(x, y, z) \, \mathrm{d}x \, \mathrm{d}y
$$

$$
= \int_{-w/2}^{+w/2} \int_0^{(h_0+u_y)/2} v_z \, \mathrm{d}x \, \mathrm{d}y + \int_{-w/2}^{+w/2} \int_{(h_0+u_y)/2}^{h_0+u_y} v_z \, \mathrm{d}x \, \mathrm{d}y, \tag{2.16}
$$

where we have split the integral over y to account for the velocity profile's slope change at $y = (h_0 + u_y)/2$. A switch to dimensionless variables turns Eq. (2.16) into

$$
q = \mathcal{V}_c h_0 w \left\{ \int_{-1/2}^{+1/2} \int_0^{(1+\beta \bar{u}_{\bar{y}})/2} \bar{v}_{\bar{z}} \, \mathrm{d}\bar{x} \, \mathrm{d}\bar{y} + \int_{-1/2}^{+1/2} \int_{(1+\beta \bar{u}_{\bar{y}})/2}^{1+\beta \bar{u}_{\bar{y}}} \bar{v}_{\bar{z}} \, \mathrm{d}\bar{x} \, \mathrm{d}\bar{y} \right\}. \tag{2.17}
$$

Substituting the expressions for $\bar{v}_{\bar{z}}$ from Eq. (2.14) into Eq. (2.17) and re-arranging:

$$\frac{q}{\mathcal{V}_c h_0 w} = \frac{1}{2^{1+1/n}(1+1/n)}\left(-\frac{d\bar{p}}{d\bar{z}}\right)^{1/n}\int_{-1/2}^{+1/2}(1+\beta\bar{u}_{\bar{y}})^{1+1/n}$$

$$\times\left\{\int_0^{(1+\beta\bar{u}_{\bar{y}})/2}\left(1-\left[1-\frac{\bar{y}}{(1+\beta\bar{u}_{\bar{y}})/2}\right]^{1+1/n}\right)d\bar{y}\right.$$

$$\left.+\int_{(1+\beta\bar{u}_{\bar{y}})/2}^{1+\beta\bar{u}_{\bar{y}}}\left(1-\left[\frac{\bar{y}}{(1+\beta\bar{u}_{\bar{y}})/2}-1\right]^{1+1/n}\right)d\bar{y}\right\}d\bar{x}. \quad (2.18)$$

Let us now introduce the dimensionless flow rate $\bar{q} = q/(\mathcal{V}_c h_0 w)$.[2] Then, performing the integration in Eq. (2.18) along with the requisite substitution of limits yields

$$\bar{q} = \frac{1}{2^{1+1/n}(2+1/n)}\left(-\frac{d\bar{p}}{d\bar{z}}\right)^{1/n}\int_{-1/2}^{+1/2}(1+\beta\bar{u}_{\bar{y}})^{2+1/n}\,d\bar{x}. \quad (2.19)$$

To complete the calculation, we must specify the cross-sectional displacement profile $\bar{u}_{\bar{y}} = \bar{u}_{\bar{y}}(\bar{x},\bar{z})$.

2.1.3 Structural mechanics problem

Typical manufacturing techniques for PDMS-based microfluidics yield microchannels and top walls that are rectangular [130]. Thus, assuming isotropic and quasi-static plate-bending under steady fluid flow, the governing equations of the solid mechanics problems can be taken to be those of either the zeroth-order (i.e., Kirchhoff–Love (KL) [131, 132]) or the first-order shear-deformation (i.e., Reissner–Mindlin (RM) [39, 133]) plate theory. Kirchhoff–Love plate theory, which preserves all the assumptions of Love's first postulate, is the straightforward extension of Euler beam theory to two spatial dimensions. Thus, KL theory only accounts for plane stress and plane strain condition inside the plate. More specifically, the KL theory applies when the maximum top wall deformation $u_{y,\mathrm{max}}$ is such

---

[2]Of course, since $\mathcal{V}_c = q/(h_0 w)$ for a flow-rate-controlled experiment or simulation, this definition of $\bar{q}$ would yield $\bar{q} = 1$ in this case. Nevertheless, we keep $\bar{q}$ in the equations that follow to allow the reader to easily use them under a pressure-drop-controlled situation, or with a different $\mathcal{V}_c$ expression.

that $u_{y,\max} \ll t \ll w$, i.e., the KL theory is a *thin-plate theory*. On the other hand, Reissner–Mindlin theory allows for shear deformations (and strains) across a plate of finite thickness. More specifically, the RM theory applies when $u_{y,\max} \ll t \simeq w$, i.e., the RM theory is a *thick-plate theory*. Both these theories are *linear*, in the sense that strains ($\sim u_{y,\max}/w$) are assumed small, so that the strain–displacement relations are linear, and the constitutive equation relating the stress to the strain is also linear.

Under the same lubrication scaling ($h_0 \ll w \ll \ell$) as for the fluid mechanics problem, it was shown in [37, 38], that the flow-wise and span-wise displacements *decouple*. Then, to the leading order in ϵ and δ, the displacement of the top wall is given by the solution of a beam equation in the (x, y) cross-section (fixed z) subject to the applied (constant in the cross-section) load $p(z)$. In terms of the dimensionless variables from Eq. (2.13), the displacement profile is thus given by either

$$\text{KL}: \quad \bar{u}_{\bar{y}}(\bar{x}, \bar{z}) = \frac{1}{24} \left(\frac{1}{4} - \bar{x}^2 \right)^2 \bar{p}(\bar{z}), \tag{2.20a}$$

$$\text{RM}: \quad \bar{u}_{\bar{y}}(\bar{x}, \bar{z}) = \frac{1}{24} \left(\frac{1}{4} - \bar{x}^2 \right) \left[\frac{2(t/w)^2}{\kappa(1 - \nu_{\rm s})} + \left(\frac{1}{4} - \bar{x}^2 \right) \right] \bar{p}(\bar{z}). \tag{2.20b}$$

Notice that Eq. (2.20a) can be understood simply as the $t/w \to 0^+$ limit of Eq. (2.20b), which captures the effect of finite plate thickness t. In Eq. (2.20b), κ is a *shear-deformation factor* [134,135], which must be taken as unity (i.e., $\kappa = 1$) based on previous mathematical analysis [136] that was further justified in [38] through comparisons with simulations and experiments.

From Eq. (2.20b), it is clear that $\bar{u}_{\bar{y}}$ increase with t/w (at a *fixed* load $\bar{p}$). To understand this observation, we recall that RM plate theory allows the normal to the plate's reference surface to change direction (and, thus, no longer remain normal, as it would in the KL theory) during deformation. Shear strains in the transverse (to the surface) direction are thus allowed and accounted for. Then, since shear deformations are integrals of shear strains along the thickness, increasing the thickness leads to larger shear strains and, thereby, larger overall deformation in the normal direction, (see also [137, Ch. 13]).

An important feature of the asymptotic decoupling introduced in [37] is that the structural deformation equations, and the resulting deflection profiles, are *not explicitly* depen-

dent on the fluid's rheology! The only fluid quantity that enters Eqs. (2.20a) and (2.20b) is the pressure $\bar{p}$. Of course, the latter is computed from the flow profile, which depends on the rheological model at hand, but none of this information is required to write down the deflection profiles explicitly. Here, we shall not expend any more effort on the structural mechanics problem as it is already developed in full detail in [37, 38].

In both of the analyses [37, 38], the characteristic deformation scale turns out to be $u_c = w^4 \mathcal{P}_c / B$, where $B = Et^3/[12(1 - v_s^2)]$ is the *bending rigidity* of a plate [132]. This choice ensures a leading-order asymptotic balance [37]. Hence, we can now express $\beta\,(> 0)$ defined in Eq. (2.13) explicitly as

$$\beta := \frac{u_c}{h_0} = \frac{w^4 \mathcal{P}_c}{B h_0} \equiv \frac{w^{4-n} \ell m q^n}{B h_0^{2(1+n)}}. \tag{2.21}$$

Since β is a dimensionless ratio of the hydrodynamic forces applied on the solid ($\mathcal{P}_c \propto \Delta p$) to its bending rigidity, we term β the *FSI parameter*. It should be clear from Eq. (2.15) that $\beta = 0$ corresponds to a rigid (undeformable) top wall.

2.1.4 Completing the calculation

Although $\bar{u}_{\bar{y}}$, as given by Eqs. (2.20a) and (2.20b), is "simply" a quartic polynomial in $\bar{x}$, the remaining integral in the flow rate expression from Eq. (2.19) cannot be performed in terms of elementary functions for arbitrary n because $2 + 1/n$ is a *fractional* power, even for integer n. On the other hand, a binomial expansion of the integrand yields

$$(1 + \beta\bar{u}_{\bar{y}})^{2+1/n} = \sum_{k=0}^{\infty} C_{k,n}(\beta\bar{u}_{\bar{y}})^k, \qquad C_{k,n} := \frac{\Gamma(3 + 1/n)}{\Gamma(k + 1)\Gamma(1/n - k + 3)}, \tag{2.22}$$

where $C_{k,n}$ is the binomial coefficient [138], and $\Gamma(\zeta) := \int_0^{\infty} s^{\zeta-1}\mathrm{e}^{-s}\,\mathrm{d}s$ is the Gamma function. Clearly, if $2 + 1/n$ is an integer, then the expansion must terminate for $k - 1$ such that $1/n - k + 3 = 0$; for example, it terminates at $k = 3$ for $n = 1$.

For non-integer $2 + 1/n$, the expansion in Eq. (2.22) is exact if taken as a convergent infinite sum, which is the case only if $\beta\bar{u}_{\bar{y}} < 1$. We expect (and the results below confirm) that for the typical displacements and values of β relevant to microchannel FSI, the convergence criterion is satisfied. Finally, in practice, the infinite sum in Eq. (2.22) must be

truncated. We now undertake the endeavor of determining how and when this truncation can be done.

Negligible plate thickness $(t/w \to 0)$

Although it is possible to unify the cases of thin and thick plates from the start, by using Eq. (2.20a) for the displacement, it is quite illustrative to perform the thin and thick plate calculations separated, due to the simplifications arising in the integration of various terms. To this end, substituting the expression for $\bar{u}_{\bar{y}}$ from Eq. (2.20a) into Eq. (2.22) yields

$$(1 + \beta \bar{u}_{\bar{y}})^{2+1/n} = \sum_{k=0}^{\infty} C_{k,n} \left(\frac{\beta \bar{p}}{24} \right)^k (\bar{x} + 1/2)^{2k} (\bar{x} - 1/2)^{2k}. \tag{2.23}$$

Now, let us consider just the integral

$$\begin{aligned}
\int_{-1/2}^{+1/2} & (1 + \beta \bar{u}_{\bar{y}})^{2+1/n} \, \mathrm{d}\bar{x} \\
&= \int_{-1/2}^{+1/2} \sum_{k=0}^{\infty} C_{k,n} \left(\frac{\beta \bar{p}}{24} \right)^k (\bar{x} + 1/2)^{2k} (\bar{x} - 1/2)^{2k} \, \mathrm{d}\bar{x} \\
&= \sum_{k=0}^{\infty} C_{k,n} \left(\frac{\beta \bar{p}}{24} \right)^k \int_{-1/2}^{+1/2} (\bar{x} + 1/2)^{2k} (\bar{x} - 1/2)^{2k} \, \mathrm{d}\bar{x} \\
&= \sum_{k=0}^{\infty} C_{k,n} \left(\frac{\beta \bar{p}}{24} \right)^k \frac{k \sqrt{\pi} \, \Gamma(2k)}{2^{4k} \, \Gamma(3/2 + 2k)}.
\end{aligned} \tag{2.24}$$

Then, Eq. (2.19) becomes

$$\bar{q} = \frac{1}{2^{1+1/n}(2 + 1/n)} \left(-\frac{\mathrm{d}\bar{p}}{\mathrm{d}\bar{z}} \right)^{1/n} \sum_{k=0}^{\infty} C_{k,n} \left(\frac{\beta \bar{p}}{24} \right)^k \frac{k \sqrt{\pi} \, \Gamma(2k)}{2^{4k} \, \Gamma(3/2 + 2k)}. \tag{2.25}$$

Finally, we re-express the latter equation as a first-order ODE:

$$\frac{\mathrm{d}\bar{p}}{\mathrm{d}\bar{z}} = -\bar{q}^n \left\{ \frac{1}{2^{1+1/n}(2 + 1/n)} \sum_{k=0}^{\infty} C_{k,n} \left[\frac{\beta}{24} \bar{p}(\bar{z}) \right]^k \frac{k \sqrt{\pi} \, \Gamma(2k)}{2^{4k} \, \Gamma(3/2 + 2k)} \right\}^{-n}. \tag{2.26}$$

All quantities, except $\bar{p}$, on the right-hand side of the latter equation are given constants, thus Eq. (2.26) is indeed a first-order *nonlinear* ODE.

The ODE (2.26) is obviously separable but the integration cannot be carried out, even with special functions, due to the infinite sum over k. Instead, below we will integrate the ODE (2.26) numerically, checking to see how many terms in the k-summation are needed to obtain results insensitive to the truncation of the infinite sum.

Consistency checks

Although verifying that a mathematical expression reduces to a previous result in a special case cannot speak to the veracity of said mathematical expression, considering some limiting cases of our theory is of pedagogical value.

First, the rigid-channel limit is easy to take from Eq. (2.25) by letting $\beta \to 0^+$:

$$\bar{q} = \frac{1}{2^{1+1/n}(2+1/n)} \left(-\frac{\mathrm{d}\bar{p}}{\mathrm{d}\bar{z}}\right)^{1/n}. \tag{2.27}$$

This flow rate–pressure gradient expression for a power-law fluid in a slot can be matched to the one given in the first row of Table 4.2-1 in [129].

Second, the Newtonian limit is also easy to take, starting from Eq. (2.25) and noting that the sum terminates at $k = 3$ when $n = 1$, to obtain:

$$\bar{q} = -\frac{1}{12}\frac{\mathrm{d}\bar{p}}{\mathrm{d}\bar{z}} \left[\sum_{k=0}^{3} C_{k,1} \left(\frac{\beta\bar{p}}{24}\right)^k \frac{k\sqrt{\pi}\,\Gamma(2k)}{2^{4k}\,\Gamma(3/2+2k)}\right]. \tag{2.28}$$

Subjecting Eq. (2.28) to the outlet boundary condition $\bar{p}(1) = 0$, it can be separated and integrated to yield:

$$\bar{q} = \frac{1}{12}\frac{\bar{p}(\bar{z})}{(1-\bar{z})} \left\{\sum_{k=0}^{3} \frac{C_{k,1}}{k+1} \left[\frac{\beta}{24}\bar{p}(\bar{z})\right]^k \frac{k\sqrt{\pi}\,\Gamma(2k)}{2^{4k}\,\Gamma(3/2+2k)}\right\}. \tag{2.29}$$

The implicit algebraic relation for $\bar{p}(\bar{z})$ in Eq. (2.29) can be compared to [37, Eq. (4.3)], matching the coefficients of $\bar{p}^k$, $k = 0, 1, 2, 3$ (see 2.1.4 for more details).

Third, letting $\beta \to 0^+$ in Eq. (2.29) means that only the $k = 0$ term in the summation "survives," and we obtain

$$\bar{q} = \frac{1}{12}\frac{\bar{p}(\bar{z})}{(1-\bar{z})} \lim_{k \to 0} \left[\frac{C_{k,1}}{k+1}\frac{k\sqrt{\pi}\,\Gamma(2k)}{2^{4k}\,\Gamma(3/2+2k)}\right]. \tag{2.30}$$

The limit on the right-hand side can be shown to equal 1. Hence, we have recovered the pressure profile for unidirectional flow in a slot of height h_0 and width w: $\bar{p}(\bar{z}) = 12\bar{q}(1 - \bar{z})$. The latter, evaluated at $\bar{z} = 0$ along with the definition of $\mathcal{V}_c$ substituted back in, yields $\Delta p = 12\mu\ell q/(h_0^3 w)$, where $\Delta p := p(0) - p(1)$ is the full pressure drop across the microchannel, as expected [3, §3.4.2].

Plates with considerable thickness (finite t/w)

As in Sec. 2.1.4, let us consider just the integral in Eq. (2.19) but with the top-wall deformation from Eq. (2.20b) under the binomial series expansion from Eq. (2.22):

$$\int_{-1/2}^{+1/2} (1 + \beta\bar{u}_{\bar{y}})^{2+1/n} \, d\bar{x} = \sum_{k=0}^{\infty} C_{k,n} \left(\frac{\beta\bar{p}}{24}\right)^k \int_{-1/2}^{+1/2} \left(1/4 - \bar{x}^2\right)^k \left[\frac{2(t/w)^2}{\kappa(1 - \nu_s)} + \left(\frac{1}{4} - \bar{x}^2\right)\right]^k d\bar{x}$$

$$= \sum_{k=0}^{\infty} C_{k,n} \left(\frac{\beta\bar{p}}{24}\right)^k 2^{-1-4k} \left(1 + \frac{8(t/w)^2}{\kappa(1 - \nu_s)}\right)^k$$

$$\times \sqrt{\pi}\, \Gamma(k + 1) \, {}_2\tilde{F}_1\left(\frac{1}{2}, -k; \frac{3}{2} + k; \frac{1}{1 + \frac{8(t/w)^2}{\kappa(1-\nu_s)}}\right), \quad (2.31)$$

where ${}_2\tilde{F}_1$ is the *regularized hypergeometric function* [139]. Therefore, the flow rate becomes

$$\bar{q} = \frac{1}{2^{1+1/n}(2 + 1/n)} \left(-\frac{d\bar{p}}{d\bar{z}}\right)^{1/n} \left\{ \sum_{k=0}^{\infty} C_{k,n} \left(\frac{\beta\bar{p}}{24}\right)^k 2^{-1-4k} \right.$$

$$\left. \times \left[1 + \frac{8(t/w)^2}{\kappa(1 - \nu_s)}\right]^k \sqrt{\pi}\, \Gamma(k + 1) \, {}_2\tilde{F}_1\left(\frac{1}{2}, -k; \frac{3}{2} + k; \frac{1}{1 + \frac{8(t/w)^2}{\kappa(1-\nu_s)}}\right) \right\}. \quad (2.32)$$

Again, Eq. (2.32) can be put in the form of an ODE for the pressure:

$$
\frac{\mathrm{d}\bar{p}}{\mathrm{d}\bar{z}} = -\bar{q}^n \left\{ \frac{1}{2^{1+1/n}(2+1/n)} \sum_{k=0}^{\infty} C_{k,n} \left[\frac{\beta}{24} \bar{p}(\bar{z}) \right]^k 2^{-1-4k} \left[1 + \frac{8(t/w)^2}{\kappa(1-\nu_s)} \right]^k \right.
$$

$$
\left. \times \sqrt{\pi}\, \Gamma(k+1)\, {}_2\tilde{F}_1\left(\frac{1}{2}, -k; \frac{3}{2}+k; \frac{1}{1+\frac{8(t/w)^2}{\kappa(1-\nu_s)}} \right) \right\}^{-n}. \quad (2.33)
$$

Consistency checks

First, the rigid-channel limit is obtained exactly as in Sec. 2.1.4 to yield Eq. (2.27).

Second, the Newtonian limit is easy to take starting from Eq. (2.32), noting that the sum terminates at $k = 3$ when $n = 1$:

$$
\bar{q} = -\frac{1}{12} \frac{\mathrm{d}\bar{p}}{\mathrm{d}\bar{z}} \left\{ \sum_{k=0}^{3} C_{k,1} \left(\frac{\beta\bar{p}}{24} \right)^k 2^{-1-4k} \left[1 + \frac{8(t/w)^2}{\kappa(1-\nu_s)} \right]^k \right.
$$

$$
\left. \times \sqrt{\pi}\, \Gamma(k+1)\, {}_2\tilde{F}_1\left(\frac{1}{2}, -k; \frac{3}{2}+k; \frac{1}{1+\frac{8(t/w)^2}{\kappa(1-\nu_s)}} \right) \right\}. \quad (2.34)
$$

For a pressure distribution subject to the outlet boundary condition $\bar{p}(1) = 0$, Eq. (2.34) can be separated and integrated to yield:

$$
\bar{q} = \frac{1}{12} \frac{\bar{p}(\bar{z})}{(1-\bar{z})} \left\{ \sum_{k=0}^{3} \frac{C_{k,1}}{k+1} \left[\frac{\beta}{24} \bar{p}(\bar{z}) \right]^k 2^{-1-4k} \left[1 + \frac{8(t/w)^2}{\kappa(1-\nu_s)} \right]^k \right.
$$

$$
\left. \times \sqrt{\pi}\, \Gamma(k+1)\, {}_2\tilde{F}_1\left(\frac{1}{2}, -k; \frac{3}{2}+k; \frac{1}{1+\frac{8(t/w)^2}{\kappa(1-\nu_s)}} \right) \right\}. \quad (2.35)
$$

Equation (2.35) is an implicit algebraic equation for $\bar{p}(\bar{z})$. It can be compared to [38, Eqs. (17)–(20)], matching the coefficients of $\bar{p}^k$, $k = 0, 1, 2, 3$ (see 2.1.4 for more details).

Third, the thickness contribution can be neglected by setting $t/w \equiv 0$. Then, Eq. (2.32) reduces to Eq. (2.26), derived for a thin-plate top wall, upon taking into account the appropriate limiting behaviors of ${}_2\tilde{F}_1$ [139].

The special case of a Newtonian fluid

For a Newtonian fluid, $n = 1$. Then, the summation in Eq. (2.29) can be shown to terminate at $k = 2 + 1/n = 3$. The non-zero coefficient in the summation are:

$$k = 0 : \quad \lim_{k \to 0} C_{k,1} \frac{k \sqrt{\pi} \Gamma(2k)}{2^{4k} \Gamma(3/2 + 2k)} = 1, \tag{2.36a}$$

$$k = 1 : \quad \frac{C_1}{2} \frac{\sqrt{\pi} \Gamma(2)}{2^4 \Gamma(3/2 + 2)} \left(\frac{\beta}{24}\right) = \frac{\beta}{480}, \tag{2.36b}$$

$$k = 2 : \quad \frac{C_2}{3} \frac{2 \sqrt{\pi} \Gamma(4)}{2^8 \Gamma(3/2 + 4)} \left(\frac{\beta}{24}\right)^2 = \frac{\beta^2}{362880}, \tag{2.36c}$$

$$k = 3 : \quad \frac{C_3}{4} \frac{6 \sqrt{\pi} \Gamma(6)}{2^{12} \Gamma(3/2 + 6)} \left(\frac{\beta}{24}\right)^3 = \frac{\beta^3}{664215552}, \tag{2.36d}$$

as expected [37, Eq. (4.3)].

The non-zero coefficient in the summation in Eq. (2.35) for the thick-plate theory, in the limit of a Newtonian fluid, are calculated similarly. However, we must further show how the regularized hypergeometric function reduces to the functions denoted by f_1, f_2 and f_3 in [38, Eqs. (18)–(20)]. To this end, consider the factor multiplying $\frac{1}{k+1} \left(\frac{\beta \bar{p}}{24}\right)^k$ in a representative term in the series in Eq. (2.35):

$$C_{k,n} 2^{-1-4k} \left[1 + \frac{8(t/w)^2}{\kappa(1 - \nu_s)}\right]^k \sqrt{\pi} \Gamma(k + 1) \, _2\tilde{F}_1 \left(\frac{1}{2}, -k; \frac{3}{2} + k; \frac{1}{1 + \frac{8(t/w)^2}{\kappa(1-\nu_s)}}\right). \tag{2.37}$$

For integer k, the expression in the last equation evaluates to a polynomial in

$$\xi = \frac{(t/w)^2}{\kappa(1 - \nu_s)} \tag{2.38}$$

via the properties of the regularized hypergeometric function $_2\tilde{F}_1$. Specifically, we may verify, e.g., using MATHEMATICA, that for $k = 0$, Eq. (2.37) reduces to 1. Then for $k = 1$, Eq. (2.37) becomes

$$\frac{1}{10} + \xi, \tag{2.39}$$

which is precisely the factor in the brackets multiplying $p(z)$ in [38, Eqs. (17)] after $1/48$ is factored out. Likewise, for $k = 1$, Eq. (2.37) becomes

$$\frac{1}{210} + \frac{3}{35}\xi + \frac{2}{5}\xi^2, \tag{2.40}$$

which is precisely the factor in the brackets multiplying $p(z)^2$ in [38, Eqs. (17)] after 1/1728 is factored out, and so on.

2.2 Results and discussion

2.2.1 Illustrative examples of the theoretical results

The ultimate objective of this chapter is to investigate steady-state FSIs due to internal flow of a power-law fluid within a microchannel with a soft top wall. In this subsection, we discuss and illustrate the interplay between the FSI parameter β [recall Eq. (2.21)], the fluid's power-law index n, and the thickness-to-width ratio t/w of the top wall. Specifically, we address how the latter interplay sets the dimensionless pressure drop $\Delta \bar{p}$ over the microchannel for a given dimensionless flow rate $\bar{q}$.

Our mathematical analysis in Sec. 2.1.4 culminated in Eq. (2.33), an ODE for the dimensionless pressure profile $\bar{p}(\bar{z})$. We integrate this ODE numerically using the `odeint` subroutine in Python's SciPy module [140]. Forty terms are taken in the series in Eq. (2.32) to ensure an accurate estimate of the infinite series. It was verified that taking any more than forty terms does not influence the numerical values for the pressure thus calculated.

In Fig. 2.2, we show the complete dimensionless pressure drop $\Delta \bar{p}$ for different values of β but a fixed t/w. We note that $\Delta \bar{p}$ is larger for smaller values of β. This trend is similar to one observed in [37, 38] for Newtonian fluids. We understand that, because a large value of β corresponds to stronger fluid–structure coupling and larger absolute deformations, the flow impedance is lower, which culminates in a smaller $\Delta \bar{p}$.

We also see that shear-thickening fluids (solid curves) lead to a larger $\Delta \bar{p}$ than shear-thinning fluids (dashed curves) for larger $\bar{q}$, and vice versa for small $\bar{q}$. This cross-over is due to the shear-rate-dependent apparent viscosity of power-fluids. As discussed above, the shear stress scales as $\sim m \left(\mathcal{V}_c / h_0 \right)^n$ and $\mathcal{V}_c \propto q$. Therefore, depending on whether $\mathcal{V}_c / h_0 \gtrsim 1 \text{ s}^{-1}$ or $\mathcal{V}_c / h_0 \lesssim 1 \text{ s}^{-1}$ (1 s^{-1} for the sake of this argument), the shear stress will increase or decrease with q, respectively. Therefore, in the first case, the shear stress in the flow of a shear-thickening fluid ($n > 1$) is higher than the corresponding one in a shear-
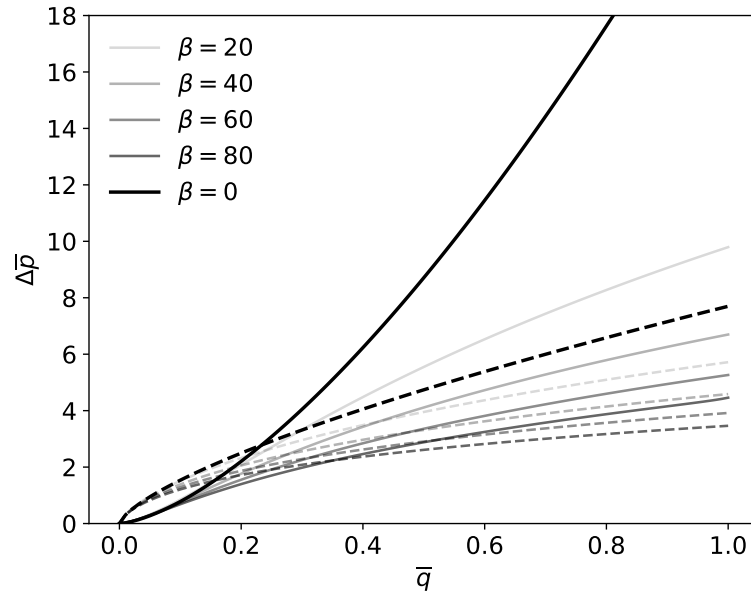
Fig. 2.2. The dimensionless pressure drop $\Delta\bar{p}$ across the microchannel for different values of the FSI parameters β and a fixed top wall thickness-to-width ratio of $t/w = 0.2$. The dashed curves correspond to a shear-thinning fluid ($n = 0.7$), while the solid curves correspond to a shear-thickening fluid ($n = 1.5$).

thinning fluid ($n < 1$), resulting in a higher pressure drop; and, vice versa in the second case. The precise cross-over is difficult to predict due to the coupled nature of the FSI problem. For $\beta = 0$, however, we can immediately predict this cross-over from Eq. (2.27) by solving $[2^{1+1/n_1}(2+1/n_1)\bar{q}]^{n_1} = [2^{1+1/n_2}(2+1/n_2)\bar{q}]^{n_2}$ for $\bar{q}$ with $n_1 = 0.5$ and $n_2 = 1.5$, yielding $\bar{q} \approx 0.22964$, in perfect agreement with Fig. 2.2.

Figure 2.3 shows $\Delta\bar{p}$ across the microchannel for different values of t/w but fixed β. Clearly, $\Delta\bar{p}$ decreases with t/w because a thicker top wall has a larger absolute deformation at steady state [e.g., compare Figs. 2.5 and 2.8 below, and recall Eq. (2.20b)], thus increasing the cross-sectional area, posing a lower impedance to the flow, and requiring a smaller $\Delta\bar{p}$ for the same β.
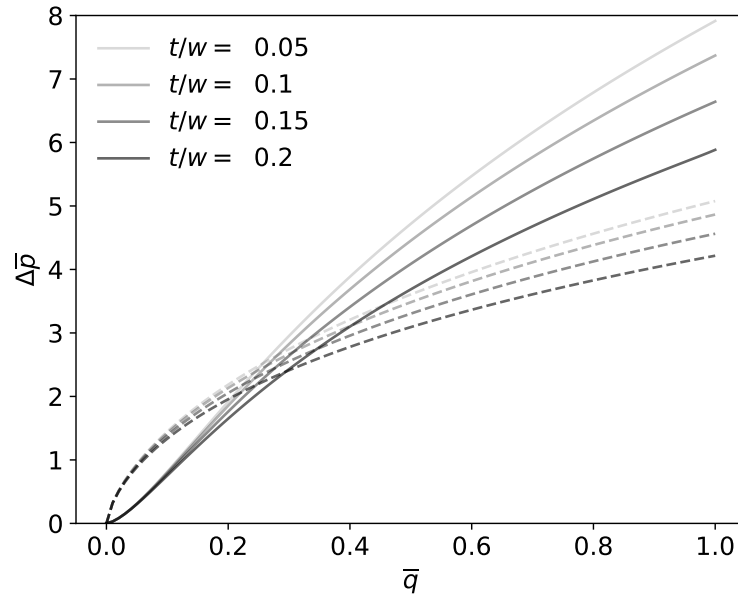
Fig. 2.3. The dimensionless pressure drop $\Delta\bar{p}$ across the microchannel for different values of the top wall's thickness-to-width ratio t/w and a fixed FSI parameter of $\beta = 50$. The dashed curves correspond to a shear-thinning fluid ($n = 0.7$), while the solid curves correspond to a shear-thickening fluid ($n = 1.5$).

2.2.2 Comparisons between theory and 3D direct numerical simulations of FSI

In this subsection, we compare the results of our mathematical theory with those of "full" three-dimensional (3D) direct numerical simulations of non-Newtonian FSI in a microchannel. We carry out simulations using the commercial software suite by AN-SYS [141], building upon the success of previous computational analyses of microchannel FSIs using ANSYS' software [38, 142]. To ensure that the simulations capture all the physics of the problem, a two-way coupling approach is employed. Specifically, the two domains—fluid and solid—are separately meshed and each set of appropriate governing equations (mass and momentum conservation for the fluid and force balance for the solid) is solved separately. A coupling module transfers information between the two solvers to ensure a fully two-way-coupled solution procedure. Although the "full" set of governing

equations in the fluid and solid is solved, they are still assumed steady (i.e., time indepen-
dent), as above.

The governing equations of the solid mechanics problem are the force balance for a
linearly elastic continuum characterized by a Young's modulus E and Poisson ratio v_s;
however, strains are computed from their "full" nonlinear (in terms of displacements) def-
inition. The bottom and two side walls of the microchannel (see Fig. 2.1) are considered
rigid (undeformable), and the solid mechanics problem for the soft (deformable) top wall is
initialized with a flat rectangular plate configuration. No displacements are allowed along
the planes $x = \pm w/2$ and $z = 0, \ell$ to enforce clamping. For all the example cases in this
subsection, the microchannel's top wall is considered to be made from PDMS, which is
modeled as a nearly incompressible linearly elastic isotropic solid with $E = 1.6$ MPa and
$v_s = 0.499$, along the lines of [38].

The governing equations of the fluid mechanics problem are the (steady) Navier–Stokes
equations with a variable (apparent) viscosity (i.e., the tensorial form of Eq. (2.5), see
[129]) with consistency factor m and power-law index n to account for the assumed power-
law rheology. To capture the flow behavior of human blood in a microchannel, we take
$m = 0.018$ Pa·s^n, $n = 0.7$ [143], which are estimates obtained by fitting blood rheology to
the power-law model, and $\varrho = 1060$ kg/m^3 (in line with typical estimates for whole blood
(see, e.g., [144, Ch. 11]). The fluid mechanics problem is initialized with a *fully-developed*
flow profile. This velocity profile is obtained by performing a separate simulation in AN-
SYS Fluent of just the flow in an equivalent *rigid* microchannel with the same cross-section.
The equivalent microchannel was chosen to be sufficiently long to allow the flow to develop
fully from an initially uniform (in the cross-section) velocity with the imposed flow rate q.
The fully developed velocity profile at the outlet of the rigid microchannel is then extracted
and imposed along the inlet plane ($z = 0$) of the deformable microchannel, while the pres-
sure is set to gauge at the outlet: $p(\ell) = 0$. No slip (zero velocity in this steady problem)
boundary conditions are imposed on all solid and elastic channel walls.

The governing equations of fluid mechanics and structural mechanics are solved using
a finite volume and a finite element method (FEM), respectively. The finite volume solu-

Table 2.1.
Force (F_x, F_y, F_z) transfer and pressure drop Δp across the microchannel for different values of the diffusion-based smoothing algorithm's parameter α in ANSYS Fluent.

α	F_x (μN)	F_y (N)	F_z (N)	Δp (Pa)
0	-16.4	21827	295.38	1622.16
1.0	-15.5	21813	295.38	1622.12
1.5	-15.5	21809	295.39	1621.99

tion is provided by ANSYS Fluent, while the FEM solution is provided by the ANSYS Static Structural module within ANSYS Mechanical. An iterative procedure couples the two domains/solvers and ensures that traction forces from the flow simulation are imposed onto the structural simulation as boundary conditions. Then, the displacements of the microchannel walls are calculated from the FEM analysis and transferred to the fluid problem as changes in the domain (and mesh) shape. This two-way transfer of data between the fluid and structural solvers continues till a specified (default) convergence criterion is reached.

The displacement of the nodes on the fluid-solid interface are calculated from the FEM solution, then they are imposed onto the finite volume mesh for the fluid domain. Therefore, in each iteration of the two-way coupling loop, the fluid mesh deforms. The deformed fluid mesh requires *smoothing* to preserve its overall quality, and thereby the quality of the solution to the fluid mechanics problem. Various mesh smoothing algorithms are available in ANSYS Fluent: diffusion-based smoothing, Laplace smoothing and spring-based smoothing. For FSI simulations, with hexahedral meshes, ANSYS recommends the diffusion-based smoothing algorithm. This smoothing algorithm has a parameter, denoted α, which determines how *deep* (roughly speaking) into the fluid domain mesh the effects of the deformed interface should be felt. In order to determine an optimal value of α, we ran several test FSI simulation with different values of α. The results are shown in Table 2.1. For different values of α, the pressure drop across the microchannel Δp and the force transfers (F_x in the x-direction, and so on) across the interface do not vary by more than 1%. There-

fore, for our FSI simulations, the choice of α is not important in obtaining accurate results. Thus, we choose $\alpha = 1$ for all of our simulations reported in this channel.

Hexahedral elements were used for meshing the fluid and the solid domains of each benchmark case above. The aspect ratio of the elements was kept close to 1. For the case given in Table 2.2, the number of divisions of the grid was set to be 800 and 50 for the fluid domain, and 500 and 40 for the solid domain, along the length and width dimensions, respectively. Similarly, for the case given in Table 2.3, the number of divisions was set to be 1000 and 80 for the fluid domain, and 500 and 40 for the solid domain, along the length and width dimensions, respectively. The total simulation run time for the highest flow rate in each benchmark case was approximately 2 hours using 8 cores on our computational server (with, specifically, Intel Xeon E5-2680 v4 processors with 14 cores each at 2.4GHz). We also carried out various grid-independence tests, the details of which are similar to the ones reported in [38].

The goal of a comparison between direct numerical simulation and theory is to validate our mathematical results and to ascertain their range of validity. To explore the applicability of the theory over a wide portion of the parameter space, we separate the simulations into those suitably described by (a) thin-plate theory (Sec. 2.2.2), for which the thickness-to-width ratio of the microchannel's top wall is small ($t/w = 0.075$), and (b) thick-plate theory (Sec. 2.2.2), for which the thickness-to-width ratio is not as small ($t/w = 0.36$). For each of the latter cases, multiple numerical simulations are performed under the methodology just described above. The material and geometric properties are fixed but the inlet flow rate is varied from $q = 7$ mL/min to 20 mL/min for the thin-plate example and from $q = 30$ mL/min to 70 mL/min for the thick-plate example. These values were chosen to generally represent the ranges in a typical experiment (e.g., [34, 42]).

Thin-plate example and validation

Consider a case in which the deformable top wall of the microchannel (see Fig. 2.1) is a "thin" plate. The geometric parameters of this model microchannel are given in Table 2.2.

Table 2.2.
Dimensions and geometric parameters for the thin-plate benchmark. All lengths are given in mm.

h_0	w	ℓ	t	δ	ϵ	t/w
0.244	2.44	24.4	0.183	0.1	0.01	0.075

These values were chosen to emulate the PDMS-based microchannels (labeled "S4" for the thinner top wall and "S5" for the thicker top wall) manufactured in the experimental study [34], which were also two of the examples for our Newtonian benchmark simulation study [38].

Specifically, by thin we mean that that the plate's thickness-to-width ratio is $t/w = 0.075 \ll 1$, and the plate's bending rigidity can be calculated to be $B = 7.36 \ \mu$J. Furthermore, as shown in Table 2.2, the lubrication theory separation of scales is respected, i.e., $\epsilon \ll \delta \ll 1$, which validates the assumptions of shallowness and slenderness, respectively, imposed on the theory developed above. For the flow rates chosen, we can calculate a maximum $\epsilon Re \approx 0.8$, which is small enough to justify the lubrication approximation. Here, $Re = \varrho \mathcal{V}_c^2 / \tau_c$, $\tau_c = m(\mathcal{V}_c/h_0)^n$ is the stress scale for a power-law fluid, leading to $Re = \varrho \mathcal{V}_c^{2-n} h_0^n / m = \varrho q^{2-n} h_0^{2n-2} w^{n-2} / m$.

Now, we are ready to validate our theory against direct numerical simulations. To this end, in Fig. 2.4, we show the full dimensional pressure drop across Δp the microchannel as a function of the imposed inlet dimensional flow rate q. For the range of parameters chosen, significant FSI occurs in this microchannel with a soft top wall as the differences between the ideal Hagen–Poiseuille (dashed), the theory curve (solid), and the simulation data in Fig. 2.4 clearly show. More importantly, however, there is good quantitative agreement between the theoretical prediction for the q–Δp relation under FSI and the direct numerical simulation results. Overall, Fig. 2.4, shows that our mathematical model for the q–Δp relation, i.e., the solution to the ODE (2.26), accurately captures the pressure drop due to non-Newtonian FSI in a microchannel with a thin top wall, within 7% maximum pointwise

error in this example. Also observe that FSI has a significant effect on the flow, reducing Δp up to 40% compared to a rigid channel. Clearly, it is crucial to accurately capture this quantitative difference between a deformable and a rigid microchannel when designing microfluidic systems.
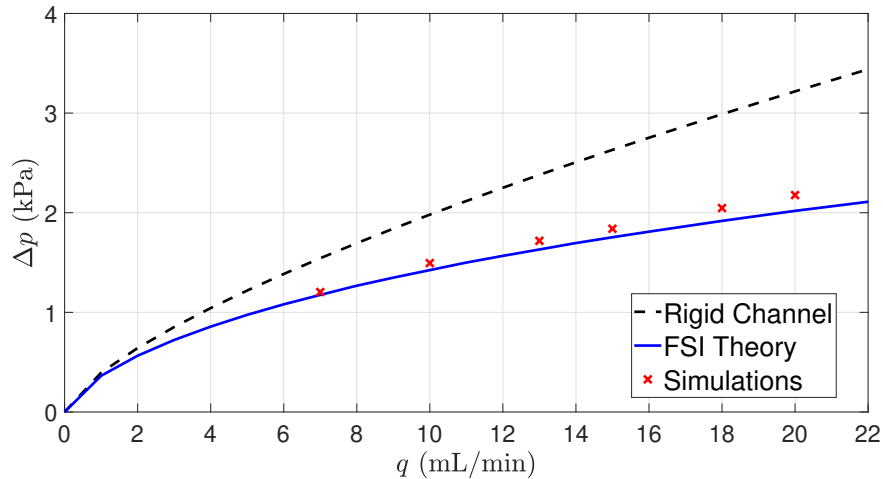
Fig. 2.4. Flow rate–pressure drop relationship for a thin-plate top wall: comparison between non-Newtonian FSI theory [i.e., Δp computed from Eq. (2.26)], direct numerical simulation, and the rigid microchannel expression [i.e., Δp computed from Eq. (2.27)].

Switching to the structural domain, in Fig. 2.5, we show the *self-similar collapse* of the ratio of the dimensionless transverse deflection to the dimensionless pressure, i.e., $\bar{u}_{\bar{y}}/\bar{p}$, for different q and at different axial positions z. This self-similar form, in which the ratio $\bar{u}_{\bar{y}}/\bar{p}$ is a *universal* function of $\bar{x}$ alone is immediately apparent from the structural deformation prediction in Eq. (2.20a). Figure 2.5 shows that there is good agreement between the collapsed data points and the theoretical shape predicted by Eq. (2.20a). At higher flow rates, however, the simulation data begins to "dip" below the theory curve, resulting in a maximum error of 11%.

For a different perspective, and to further examine the collapse (or lack thereof), in Fig. 2.6, we plot the same data but at a *fixed-z* cross-section, as a function of the FSI

parameter β [recall Eq. (2.21)]. Again there is good agreement between the results from direct numerical simulation and the theoretical prediction from Eq. (2.20a), with deviations (and the "dip" below the theory curve) now clearly being attributable to β being large.[3]

Therefore, we have not only shown the high accuracy of our theory through this comparison with direct numerical simulations, but we have also outlined the extent of the theory's applicability. Specifically, we observe that the systematic deviations from the theoretical prediction in Figs. 2.5 and 2.6 occur at high q and, equivalently, large β, irrespective of the axial position. This observation is attributed to the fact that at higher q, the deformation of the top wall enters a nonlinear stretching regime, which cannot be described by classical plate theories, as also discussed in [38]. This hypothesis is corroborated by Fig. 2.6, in which the collapse worsens as the FSI parameter β increases—i.e., the load imposed onto the plate by the fluid becomes larger compared to the plate's bending rigidity. In other words, as β increases, so does the effect of FSI, and the deformation of the top wall becomes more significant, leaving the range of validity of our "linear" FSI model.

Thick-plate example and validation

Our benchmark microchannel for a thick-plate top wall has dimensions as given in Table 2.3. The thickness-to-width ratio for this microchannel is $t/w = 0.36$, which is a large enough value to warrant the deployment of the Reissner–Mindlin thick-plate theory. This plate's bending rigidity can be calculated to be $B = 266 \ \mu$J. Then, the displacement of the top wall is predicted to obey Eq. (2.20b). As before, to ensure the proper asymptotic regime of a long and shallow microchannel, we must have $\epsilon \ll \delta \ll 1$, which is indeed the case for this microchannel as shown in Table 2.3.

For the flow rates chosen, we calculate a maximum $\epsilon Re \approx 8.7$, which is larger than the corresponding value for the thin-plate example above. Although, strictly speaking, this value of ϵRe (and not $\epsilon^2 Re$ as in two-dimensional lubrication theory [37]) is beyond the expected applicability of the lubrication approximation, we nevertheless obtain good agree-

---

[3]As discussed in [37, Appendix B], this type of "linear FSI" theory holds for β large, up to at least $\beta = O(1/\delta)$.
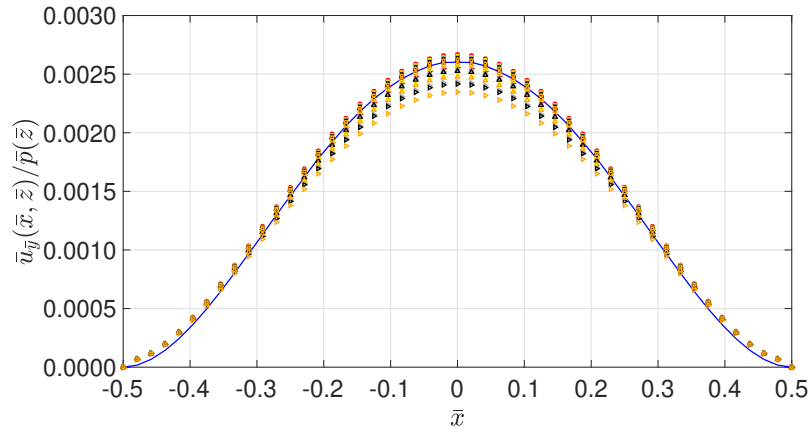
Fig. 2.5. Self-similar collapse of the scaled dimensionless cross-sectional displacement profiles, $\bar{u}_{\bar{y}}(\bar{x}, \bar{z})/\bar{p}(\bar{z})$, for different flow rates of the example thin-plate case. The solid curve corresponds to the theoretical profile from Eq. (2.20a), while the symbols correspond to direct numerical simulation. Colors: red = 7 mL/min, yellow = 10 mL/min, gray = 13 mL/min, black = 15 mL/min, and orange = 18 mL/min; shapes: □ is $z = 21.4$ mm, ○ is $z = 19.4$ mm, △ is $z = 16.4$ mm, and ▷ is $z = 12.4$ mm.

Table 2.3.
Dimensions and geometric parameters for the thick-plate benchmark. All lengths are given in mm.

h_0	w	ℓ	t	δ	ϵ	t/w
0.155	1.7	15.5	0.605	0.09	0.01	0.36

ment between the theoretical prediction and direct numerical simulations. This highlights the extent to which lubrication theory can be "pushed beyond" its strict $\epsilon Re \ll 1$ validity range.

First, we compare the flow rate–pressure drop relation predicted by our theory, i.e., the solution of Eq. (2.33), to the results of direct numerical simulation. To this end, in Fig. 2.7, we plot the pressure drop Δp across the microchannel for different values of the imposed inlet flow rate q. The mathematical prediction for Δp, which is found from
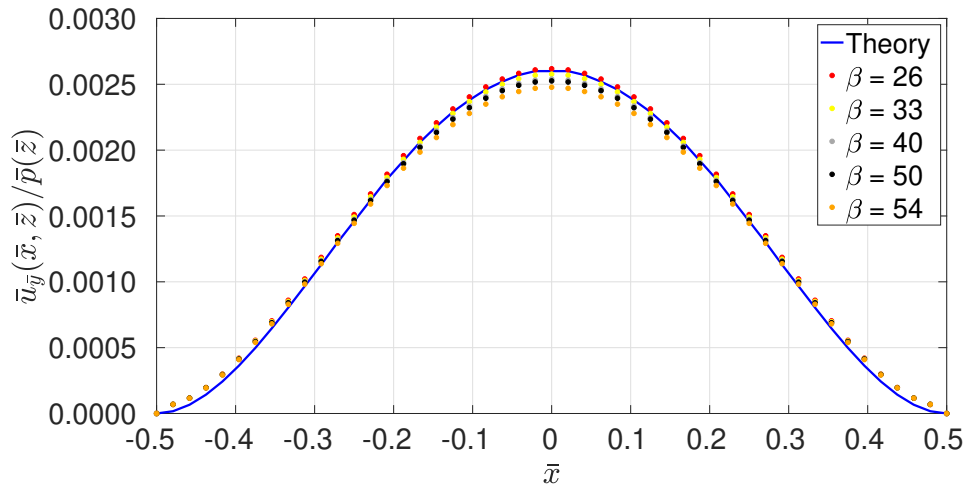
Fig. 2.6. Self-similar collapse of the scaled dimensionless cross-sectional displacement profiles, $\bar{u}_{\bar{y}}(\bar{x}, \bar{z})/\bar{p}(\bar{z})$, from Fig. 2.6 for different values of the FSI parameter β but at the fixed flow-wise cross-section $z = 16.4$ mm. Symbols correspond to the computational results from two-way FSI simulations. The solid curve corresponds to the theoretical profile from Eq. (2.20a).

integrating the ODE (2.33), is in excellent agreement with the direct numerical simulation results within 2% maximum pointwise error, across a half a decade of range in the flow rate. In this case, the pressure drops are significantly larger than in Sec. 2.2.2 because of the much smaller (undeformed) cross-sectional area (see Table 2.3). Thus, while the thick top wall deforms more than an equivalent thin one, which increases the cross-sectional area and lowers the resistance to flow, the deformation in this case is not so large as to make the pressure drops in this section comparable to those in Sec. 2.2.2, in which the channel has larger (undeformed) cross-sectional area. Nevertheless, once again, FSI decreases Δp in the microchannel, by up to 12% compared to an equivalent rigid conduit, through the increase in the cross-sectional area engendered by the deformation of the top wall.

Next, we plot the ratio of dimensionless deflection to dimensionless pressure, i.e., $\bar{u}_{\bar{y}}/\bar{p}$, for different values the imposed inlet flow rate q in our simulations. Figure 2.8 shows the self-similar collapse of $\bar{u}_{\bar{y}}/\bar{p}$ across q and axial positions z in the flow-wise direction. There
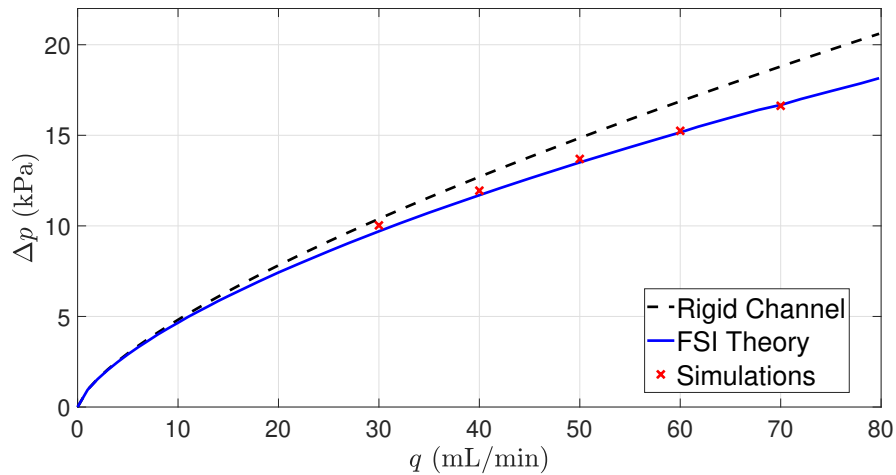
Fig. 2.7. Flow rate–pressure drop relationship for a thick-plate top wall: comparison between non-Newtonian FSI theory [i.e., Δp computed from Eq. (2.33)], direct numerical simulations, and the rigid microchannel expression [i.e., Δp computed from Eq. (2.27)].

is excellent collapse of the data in Fig. 2.8, with all data points being almost indistinguishable, onto the mathematically predicted dimensionless displacement profile is given by Eq. (2.20b). In parallel, Fig. 2.9 shows the same data but at a fixed value of z and as a function of the FSI parameter β. Given the smaller range of β values compared to the case in Sec. 2.2.2 (well within the "linear" FSI theory developed herein), we cannot visually distinguish any variation with β in Fig. 2.9.

In both Figs. 2.8 and 2.9, we observe good quantitative agreement between the theoretical predictions and direct numerical simulation results across the range of q, equivalently β values chosen. Nevertheless, there are systematic deviations between the collapsed simulation data and the $\bar{u}_{\bar{y}}/\bar{p}$ profile from Eq. (2.20b) predicted by thick-plate theory. These deviations are due to the fact that, in the direct numerical simulation, the 3D equations of linear elasticity are solved, while our mathematical results are based on the assumptions of the Reissner–Mindlin plate theory, which is necessarily approximate. Specifically, the Reissner–Mindlin plate theory assumes that the normal strains, along the thickness of the
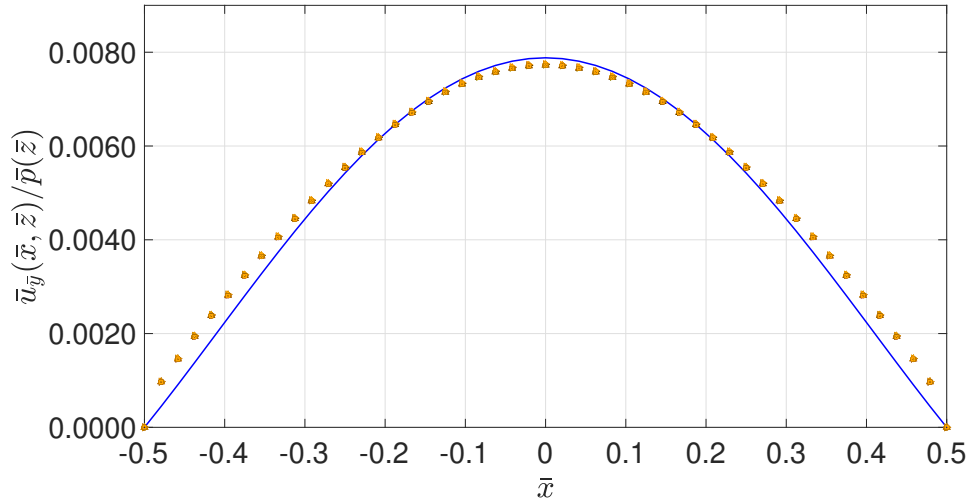
Fig. 2.8. Self-similar collapse of the scaled dimensionless cross-sectional displacement profiles, $\bar{u}_{\bar{y}}(\bar{x}, \bar{z})/\bar{p}(\bar{z})$, for different flow rates of the example thick-plate case. The solid curve corresponds to the theoretical profile from Eq. (2.20b), while the symbols correspond to direct numerical simulation. Colors: red = 30 mL/min, yellow = 40 mL/min, gray = 50 mL/min, black = 60 mL/min, and orange = 70 mL/min; shapes: □ is z = 12.5 mm, ○ is z = 10.5 mm, △ is z = 7.5 mm, and ▷ is z = 3.5 mm. Symbols might be hard to distinguish due to the excellent collapse of the data.

plate, are small, while the shear deformations are not negligible. Therefore, every material point along the thickness of the plate undergoes the same displacement in the normal direction. This kinematic assumption may not always hold true, especially for plates that are very thick. Then, a systematic deviations from Eq. (2.20b) (for the vertical displacements) are expected, and an even-higher-order plate theory would be required to capture them.

2.3 Conclusion

In this chapter, we presented a theory of low Reynolds number fluid–structure interactions (FSIs) between a generalized non-Newtonian fluid with shear-dependent viscosity and a rectangular microchannel with a top compliant wall. The power-law model of shear-dependent viscosity was employed for the fluid. The structural mechanics of the mi-

crochannel's top wall were modeled using two classical plate theories: the Kirchhoff–Love theory of quasi-static flexural deformations of thin plates and the first-order shear deformation Reissner–Mindlin theory applicable to thick plates. Specifically, we showed that the deformation of the structure is coupled to the fluid mechanics only through the hydrodynamic pressure, and the fluid's rheology does not explicitly affect the previously derived displacement profiles [37, 38]. Then, through a perturbative analysis under the lubrication approximation (i.e., a long and shallow microchannel), we reduced the coupled problem to a single ordinary differential equation (ODE) for the hydrodynamic pressure:

$$
\frac{dp}{dz} = -\frac{m}{h_0}\left(\frac{q}{wh_0^2}\right)^n \left\{\frac{1}{2^{1+1/n}(2+1/n)}\sum_{k=0}^{\infty} C_{k,n}\left[\frac{w^4}{24Bh_0}p(z)\right]^k\right.
$$

$$
\left. \times\, 2^{-1-4k}\left[1+\frac{8(t/w)^2}{\kappa(1-\nu_s)}\right]^k \sqrt{\pi}\,\Gamma(k+1)\;{}_2\tilde{F}_1\left(\frac{1}{2},-k;\frac{3}{2}+k;\frac{1}{1+\frac{8(t/w)^2}{\kappa(1-\nu_s)}}\right)\right\}^{-n}. \quad (2.41)
$$

Once the pressure $p(z)$ is determined via Eq. (2.41), the deformed channel shape is given by

$$
h(x,z) = h_0 + \frac{w^4}{24B}\left[\frac{1}{4}-\left(\frac{x}{w}\right)^2\right]\left\{\frac{2(t/w)^2}{\kappa(1-\nu_s)}+\left[\frac{1}{4}-\left(\frac{x}{w}\right)^2\right]\right\}p(z). \quad (2.42)
$$

Equations (2.41) and (2.42), technically derived under the Reissner–Mindlin plate theory, unify both the plate theories considered herein because letting $t/w \to 0^+$ (recall Sec. 2.1.4) reduces Eqs. (2.41) and (2.42) to the ones derived under the Kirchhoff–Love thin-plate theory.

Next, we illustrated some trends predicted by our theory. A microchannel with a thicker top wall is more compliant in the sense that the absolute deformation is larger for the same undeformed cross-section. Therefore, the pressure drop, at a fixed inlet flow rate, decreases with the thickness-to-width ratio t/w. The same trend was shown with respect to the dimensionless FSI parameter

$$
\beta = \frac{w^4 \mathcal{P}_c}{Bh_0}, \quad (2.43)
$$

which quantifies the strength of the FSI coupling in the problem with β large corresponding to significant compliance of the top wall. Recall that the choice of pressure scale $\mathcal{P}_c$ was discussed after Eq. (2.13) above.
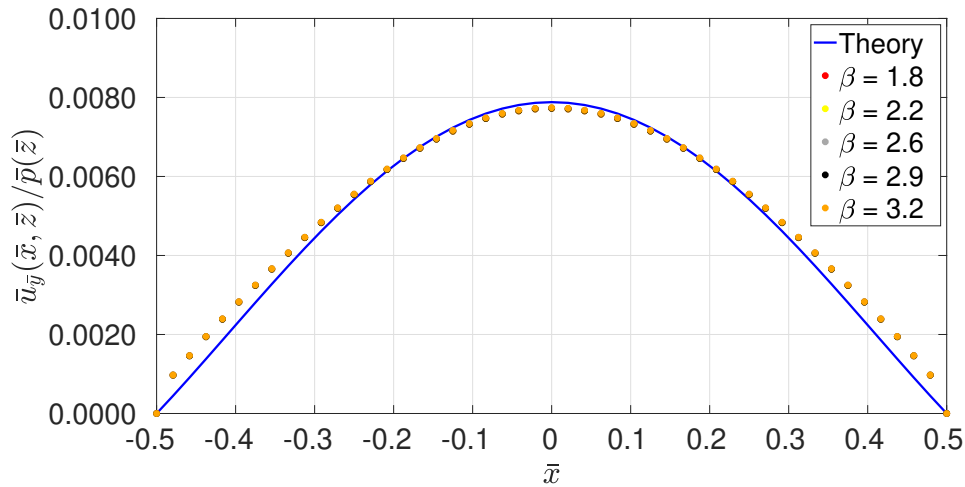
Fig. 2.9. Self-similar collapse of the scaled dimensionless cross-sectional displacement profiles, $\bar{u}_{\bar{y}}(\bar{x}, \bar{z})/\bar{p}(\bar{z})$, from Fig. 2.8 for different values of the FSI parameter β but at the fixed flow-wise cross-section $z = 7.5$ mm. Symbols correspond to the computational results from two-way FSI simulations. The solid curve corresponds to the theoretical profile from Eq. (2.20b). Symbols might be hard to distinguish due to the excellent collapse of the data.

Full-scale direct numerical simulations of non-Newtonian microfluidic FSI were carried out using the commercial computer-aided engineering (CAE) platform by ANSYS [141]. The numerical simulations were used to confirm our theoretical predictions for flow and deformation, and to also ascertain the theory's range of validity. Specifically, the pressure drop across the microchannel predicted by our theory was shown to closely match the predictions of CAE simulations, across a range of flow rates, with an accuracy of 2% in the best case and 7% in the worst case. Deviations between theory and simulations emerge only when the structural response of the top wall of the microchannel enters a nonlinear regime (β not small), i.e., when the deformation is too large to be adequately described within the framework of the linear strain–displacement relationships of classical plate theories. Perhaps more importantly, we note that pressure drop across the microchannel decreases significantly, up to 40% in some cases, due to the presence of FSI. This result provides

concrete new evidence for the early observations in [30] toward the fact that FSI must be accurately accounted for, when formulating flow rate–pressure drop relationships for compliant microchannels.

3. HYDRODYNAMIC BULGE TEST FOR MATERIAL PROPERTY CHARACTERIZATION OF LINEARLY ELASTIC THICK PLATES

SUMMARY

Characterizing the elastic properties of soft materials through bulge testing relies on accurate measurement of deformation, which is experimentally challenging. To avoid measuring deformation, we propose a hydrodynamic bulge test for characterizing the material properties of thick, pre-stressed elastic sheets via their fluid–structure interaction with a steady viscous fluid flow. Specifically, the hydrodynamic bulge test relies on a pressure drop measurement across a rectangular microchannel with a deformable top wall. We develop a mathematical model using first-order shear-deformation theory of plates with stretching, and the lubrication approximation for Newtonian fluid flow. Specifically, a relationship is derived between the imposed flow rate and the total pressure drop. Then, this relationship is inverted numerically to yield estimates of the Young's modulus (given the Poisson ratio), if the pressure drop is measured (given the steady flow rate). Direct numerical simulations of two-way-coupled fluid–structure interaction are carried out in ANSYS to determine the cross-sectional membrane deformation and the hydrodynamic pressure distribution. Taking the simulations as "ground truth," a hydrodynamic bulge test is performed using the simulation data to ascertain the accuracy and validity of the proposed methodology for estimating material properties. An error propagation analysis is performed via Monte Carlo simulation to characterize the susceptibility of the hydrodynamic bulge test estimates to noise. We find that, while a hydrodynamic bulge test is less accurate in characterizing material properties, it is less susceptible to noise, in the input (measured) variable, than a hydrostatic bulge test.

The material in this chapter has been published in [V. Anand, S. C. Machundinath, and I. C. Christov, "Hydrodynamic Bulge Testing: Materials Characterization Without Measuring Deformation," *ASME J. Appl. Mech.*, vol. 87, pp. 051012, 2020] [145]

3.1 Preliminaries

Consider the geometry depicted in Fig. 3.1. An elastic plate, clamped on all its edges, is placed as the top wall over a rectangular channel that is long and wide. The plate's thickness is smaller than its spanwise width ($t/w < 1$), but it is not negligible ($t/w \not\to 0$). Furthermore, the reference configuration of the plate is assumed to have an uniform (isotropic) pre-tension T, defined as a force per unit length (stress resultant). The structure mechanics problem is analyzed using *first-order shear deformation theory* (FOSDT), also known as thick-plate theory or the Reissner–Mindlin plate theory, that also accounts for the
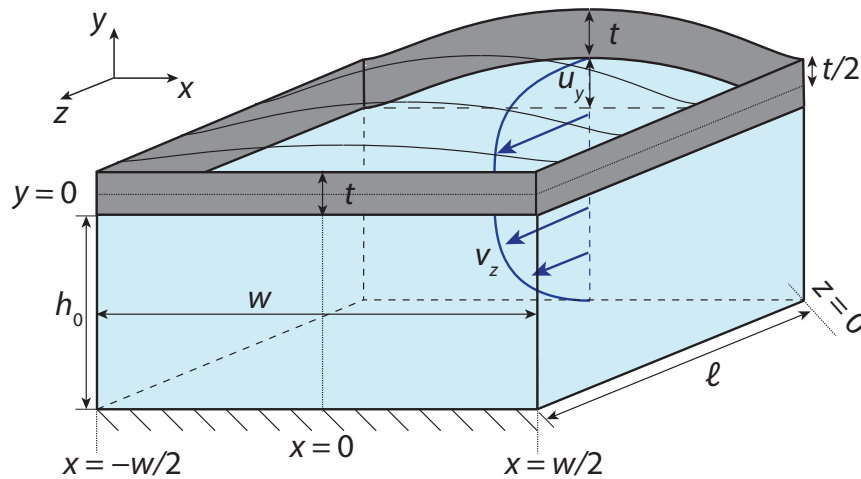
Fig. 3.1. Geometry of the problem and notation. A slender elastic membrane (plate) represents the top wall of an otherwise rigid channel. A steady flow is established in the z-direction, which gives rise to a pressure gradient that leads to a deformation of the membrane in the y-direction. The membrane is clamped on all ends (not shown at $z = 0$ for clarity).

pre-tension/pre-stress/stretching in the elastic body (see the recent historical overview of the development of these theories by Challamel and Elishakoff [146])

3.2 Structural mechanics

3.2.1 Kinematics

In FOSDT, the assumption that the transverse normals are straight and inextensible leads to the following displacement field within the plate [147]:

$$u_x(x, y, z) = u_{x0}(x, z) + y\phi_x(x, z), \tag{3.1a}$$

$$u_z(x, y, z) = u_{z0}(x, z) + y\phi_z(x, z), \tag{3.1b}$$

$$u_y(x, z, y) = u_{y0}(x, z). \tag{3.1c}$$

Here, u_{x0} and u_{z0} are the in-plane displacements, u_{y0} is the transverse displacement (henceforth denoted just as u_y for simplicity and without fear of confusion), and ϕ_x and ϕ_z are the rotations of the normal to the plate about the x- and the z-axis, respectively. Equations (3.1) are written assuming $y = 0$ is the mid-plane (neutral surface) of the plate, as shown in Fig. 3.1. In FOSDT, the nonlinear terms in the strain tensor, which arise from von Kármán strains, are neglected and the strain tensor is written in the column vector form as:

$$\underbrace{\begin{pmatrix} \gamma_{xx} \\ \gamma_{zz} \\ \gamma_{yy} \\ \gamma_{xz} \\ \gamma_{xy} \\ \gamma_{zy} \end{pmatrix}}_{\underline{\underline{\gamma}}} = \underbrace{\begin{pmatrix} \frac{\partial u_{x0}}{\partial x} \\ \frac{\partial u_{z0}}{\partial z} \\ 0 \\ \frac{\partial u_{x0}}{\partial z} + \frac{\partial u_{z0}}{\partial x} \\ \frac{\partial u_y}{\partial x} + \phi_x \\ \frac{\partial u_y}{\partial z} + \phi_z \end{pmatrix}}_{\underline{\underline{\gamma}}^0} + y \underbrace{\begin{pmatrix} \frac{\partial \phi_x}{\partial x} \\ \frac{\partial \phi_z}{\partial z} \\ 0 \\ \frac{\partial \phi_x}{\partial z} + \frac{\partial \phi_z}{\partial x} \\ 0 \\ 0 \end{pmatrix}}_{\underline{\underline{\Phi}}}. \tag{3.2}$$

Here, $\underline{\underline{\Phi}}$ is the curvature strain tensor, which arises from bending, while $\underline{\underline{\gamma}}^0$ represents the in-plane stretching and deformation due to transverse shear. It is a feature of FOSDT that

the transverse shear strains remain constant across the thickness, while the in-plane strains vary linearly with y.

3.2.2 Equations of static equilibrium

As is standard in plate theory, we integrate the stresses across the thickness and define the corresponding stress resultants as

$$
\begin{pmatrix} N_{xx} \\ N_{zz} \\ N_{xz} \\ Q_x \\ Q_z \end{pmatrix} = \int_{-t/2}^{+t/2} \begin{pmatrix} \sigma_{xx} \\ \sigma_{zz} \\ \sigma_{xz} \\ \sigma_{xy} \\ \sigma_{zy} \end{pmatrix} dy,
\tag{3.3}
$$

and the bending moments as

$$
\begin{pmatrix} M_{xx} \\ M_{zz} \\ M_{xz} \end{pmatrix} = \int_{-t/2}^{+t/2} \begin{pmatrix} \sigma_{xx} \\ \sigma_{zz} \\ \sigma_{xz} \end{pmatrix} y \, dy.
\tag{3.4}
$$

There are only two independent variables in the plate theory: the in-plane coordinates x and z. Thus, here, N_{xx} and N_{zz} are the normal stress resultants in these, x and z directions, respectively. Likewise, Q_x and Q_z are the transverse shear stress resultants acting on the planes which have their outward normals in the x and z directions, respectively. Meanwhile, N_{xz} is the in-plane shear stress resultant. Similarly, M_{xx} and M_{zz} are bending moments, while M_{xz} is the twisting moment. There are no moments due to the transverse stresses σ_{xy} and σ_{zy}. Additionally, the assumption of a plane-stress state means that $\sigma_{yy} = 0$, and σ_{yy} does not contribute to any stress resultants.

The equations of equilibrium, written in terms of the stress resultants [147, Ch. 10], are

$$
\frac{\partial N_{xx}}{\partial x} + \frac{\partial N_{xz}}{\partial z} = 0,
\tag{3.5a}
$$

$$\frac{\partial N_{xz}}{\partial x} + \frac{\partial N_{zz}}{\partial z} = 0, \tag{3.5b}$$

$$\frac{\partial Q_x}{\partial x} + \frac{\partial Q_z}{\partial z} + \mathcal{N} + p = 0, \tag{3.5c}$$

$$\frac{\partial M_{xx}}{\partial x} + \frac{\partial M_{xz}}{\partial z} - Q_x = 0, \tag{3.5d}$$

$$\frac{\partial M_{xz}}{\partial x} + \frac{\partial M_{zz}}{\partial z} - Q_z = 0, \tag{3.5e}$$

where

$$\mathcal{N} := \frac{\partial}{\partial x}\left(N_{xx}\frac{\partial u_y}{\partial x} + N_{xz}\frac{\partial u_y}{\partial z}\right) + \frac{\partial}{\partial z}\left(N_{xz}\frac{\partial u_y}{\partial x} + N_{zz}\frac{\partial u_y}{\partial z}\right) \tag{3.6}$$

couples the displacement in the transverse direction (bending) to the in-plane displacements (stretching). This term accounts for moderate rotations and originates from employing von Kármán strains in the derivation of the equations of equilibrium [147].

Thus, we have neglected the nonlinear terms in the kinematics of the problem, but opted to retain these terms in the equations of static equilibrium. Neglecting $\mathcal{N}$ in Eq. (3.5c), would decouple the bending response from the stretching response. In other words, the transverse deflection would not be affected by stretching (pre-stress) at all, which is valid only when the stretching is negligible. Retaining $\mathcal{N}$ in the equations of static equilibrium thus enlarges the scope of application of the theory, and allows for the consideration of pre-stressed (pre-stretched) plates. On the other hand, if we had also incorporated the nonlinear (moderate rotation) terms in the kinematics, and employed the von Kármán strains, then we would have obtained the *nonlinear* von Kármán plate theory [148], which is difficult (if not impossible) to solve analytically [147, 148]. In the von Kármán plate theory, stretching and bending responses are tightly coupled, unlike a linear plate theory in which $\mathcal{N}$ is dropped altogether from the analysis.

To summarize: in this chapter, the coupling between stretching and bending is one-way; stretching influences bending but the converse is not true. The influence of stretching in the bending response is accounted for by incorporating $\mathcal{N}$, given by Eq. (3.6), which appears in Eq. (3.5c). On the other hand, however, Eqs. (3.5a) and (3.5b) that govern the in-plane equilibrium (stretching) are decoupled from Eqs. (3.5c)–(3.5e) and do not contain any terms corresponding to the bending response. The current theory may thus be regarded

as "weakly nonlinear" in a sense, providing a suitable trade-off between the nonlinear von Kármán plate theory (with stretching) and a linear FOSDT theory (in which stretching decouples).

3.2.3 Constitutive equations

For the condition of plane stress, the constitutive equations reduce (see [147, 149]) to

$$
\begin{pmatrix} \sigma_{xx} \\ \sigma_{zz} \\ \sigma_{xz} \end{pmatrix} = \frac{E}{(1 - v^2)} \begin{pmatrix} 1 & v & 0 \\ v & 1 & 0 \\ 0 & 0 & \frac{1-v}{2} \end{pmatrix} \begin{pmatrix} \gamma_{xx} \\ \gamma_{zz} \\ \gamma_{xz} \end{pmatrix},
\tag{3.7}
$$

where v is the Poisson ratio and E is the Young's modulus of the linearly elastic material. Next, we substitute the expressions for the strains in terms of displacements from Eq. (3.2) into Eq. (3.7), the result of which, upon being employed in Eq. (3.3), yields:

$$
\begin{pmatrix} N_{xx} \\ N_{zz} \\ N_{xz} \end{pmatrix} = \frac{Et}{(1 - v^2)} \begin{pmatrix} 1 & v & 0 \\ v & 1 & 0 \\ 0 & 0 & \frac{1-v}{2} \end{pmatrix} \begin{pmatrix} \frac{\partial u_{x0}}{\partial x} \\ \frac{\partial u_{z0}}{\partial z} \\ \frac{\partial u_{x0}}{\partial z} + \frac{\partial u_{z0}}{\partial x} \end{pmatrix}.
\tag{3.8}
$$

Note that due to the assumption about linear strains, the in-plane stress resultants are only functions of the in-plane strains, and they are independent of the transverse deflections and rotations. Similarly, the bending moments from Eq. (3.4) are calculated to be

$$
\begin{pmatrix} M_{xx} \\ M_{zz} \\ M_{xz} \end{pmatrix} = \frac{Et^3}{12(1 - v^2)} \begin{pmatrix} 1 & v & 0 \\ v & 1 & 0 \\ 0 & 0 & \frac{1-v}{2} \end{pmatrix} \begin{pmatrix} \frac{\partial \phi_x}{\partial x} \\ \frac{\partial \phi_z}{\partial z} \\ \frac{\partial \phi_x}{\partial z} + \frac{\partial \phi_z}{\partial x} \end{pmatrix},
\tag{3.9}
$$

where we observe that the bending moments are only a function of the rotations.

Next, the constitutive equations for the shear stresses are modified as:

$$
\sigma_{xy} \approx \kappa G \gamma_{xy},
\tag{3.10a}
$$

$$
\sigma_{zy} \approx \kappa G \gamma_{zy},
\tag{3.10b}
$$

where $G = E/[2(1 + \nu)]$ is the shear modulus, and κ is Timoshenko's "shear correction factor" [150], which is commonly introduced to account for nonuniform distribution of the transverse shear strain across the thickness [135, 136, 151]. Now, we substitute the expressions for σ_{xy} and σ_{zy} from Eqs. (3.10) into Eq. (3.3) to relate the shear stress resultants to the deformation and rotation of the normal:

$$Q_x = \kappa \int_{-t/2}^{+t/2} G\gamma_{xy} \, \mathrm{d}y = \kappa G t \left[\frac{\partial u_y}{\partial x} + \phi_x \right], \tag{3.11a}$$

$$Q_z = \kappa \int_{-t/2}^{+t/2} G\gamma_{zy} \, \mathrm{d}y = \kappa G t \left[\frac{\partial u_y}{\partial z} + \phi_z \right]. \tag{3.11b}$$

Zhang [136] proved mathematically that the equations of linear elasticity and those of the RM plate theory, both in the limit of $t/w \rightarrow 0$, agree only when $\kappa = 1$. Therefore, as in our previous works [38, 60], we take $\kappa = 1$ when generating our results below. However, we keep the variable κ throughout our equations for consistency with the applied mechanics literature. This completes the derivation of the stress resultants in terms of the displacements under the FOSDT.

3.2.4 Differential equations for the displacement

To define a FOSDT with both stretching and bending, one substitutes the stress resultants from Eqs. (3.8), (3.9) and (3.11) into the equations of equilibrium (3.5), to obtain a set of differential equations for the displacements (u_{x0}, u_y, u_{z0}) and the rotations of the normal (ϕ_x, ϕ_z):

$$D_s \left(\frac{\partial^2 u_{x0}}{\partial x^2} + \nu \frac{\partial^2 u_{z0}}{\partial x \partial z} \right) + \kappa G t \left(\frac{\partial^2 u_{x0}}{\partial z^2} + \frac{\partial^2 u_{z0}}{\partial x \partial z} \right) = 0, \tag{3.12a}$$

$$\kappa G t \left(\frac{\partial^2 u_{z0}}{\partial x^2} + \frac{\partial^2 u_{x0}}{\partial x \partial z} \right) + D_s \left(\frac{\partial^2 u_{z0}}{\partial z^2} + \nu \frac{\partial^2 u_{x0}}{\partial x \partial z} \right) = 0, \tag{3.12b}$$

$$\kappa G t \left[\left(\frac{\partial^2 u_y}{\partial x^2} + \frac{\partial^2 u_y}{\partial z^2} \right) + \frac{\partial \phi_x}{\partial x} + \frac{\partial \phi_z}{\partial z} \right] + \mathcal{N} + p = 0, \tag{3.12c}$$

$$D_b \left(\frac{\partial^2 \phi_x}{\partial x^2} + \nu \frac{\partial^2 \phi_z}{\partial x \partial z} \right) + D_b \left(\frac{1 - \nu}{2} \right) \left(\frac{\partial^2 \phi_x}{\partial z^2} + \nu \frac{\partial^2 \phi_z}{\partial x \partial z} \right) - \kappa G t \left(\frac{\partial u_y}{\partial x} + \phi_x \right) = 0, \tag{3.12d}$$

$$D_b \left(\nu \frac{\partial^2 \phi_x}{\partial x \partial z} + \frac{\partial^2 \phi_z}{\partial z^2} \right) + D_b \left(\frac{1 - \nu}{2} \right) \left(\frac{\partial^2 \phi_x}{\partial x \partial z} + \frac{\partial^2 \phi_z}{\partial x^2} \right) - \kappa G t \left(\frac{\partial u_y}{\partial z} + \phi_z \right) = 0, \quad (3.12e)$$

where $D_b := Et^3 / [12(1 - \nu^2)]$ is the bending rigidity, and $D_s := Et/(1 - \nu)$ is the extensional rigidity, of the plate with Young's modulus E and Poisson ratio ν [148, 152].

Equations (3.12a) and (3.12b) completely describe the in-plane displacement field, which is independent of the transverse deflection and/or rotations. In the analysis below, this in-plane displacement field will not be necessary, thus we discard these two equations.

Finally, in this chapter, we assume that the stretching response of the plate is due to a known isotropic, uniform pre-tension T, i.e., the normal stress and in-plane shear stress resultants are simply given by

$$\begin{pmatrix} N_{xx} \\ N_{zz} \\ N_{xz} \end{pmatrix} = T \begin{pmatrix} 1 \\ 1 \\ 0 \end{pmatrix}. \tag{3.13}$$

Then, Eq. (3.12c) becomes,

$$\kappa G t \left(\frac{\partial \phi_x}{\partial x} + \frac{\partial \phi_z}{\partial z} \right) + (T + \kappa G t) \left(\frac{\partial^2 u_y}{\partial x^2} + \frac{\partial^2 u_y}{\partial z^2} \right) = -p. \tag{3.14}$$

Together, Eqs. (3.14), (3.12d) and (3.12e) describe the transverse deflection and rotations of the normal to the mid-plane of a thick, pre-stressed plate. A subtle consequence of imposing the pre-stress on the model *a priori*, rather than computing it through internal strains, is that the equations of the present weakly nonlinear theory become equivalent to equations of von Kármán's plate theory with given constant isotropic pre-tension [148,149].

3.2.5   Shallow, slender plates: Regimes of deformation

First, we rewrite the governing differential equations (3.14), (3.12d) and (3.12e) using the following dimensionless variables:

$$X = x/w, \quad Z = z/\ell, \quad U = u_y/\mathcal{U}_c, \Phi_x = \phi_x/\mathcal{F}_x, \quad \Phi_z = \phi_z/\mathcal{F}_z \quad P = p/\mathcal{P}_c, \quad (3.15)$$

Here, $\mathcal{F}_x$, $\mathcal{F}_z$ and $\mathcal{U}_c$ are the characteristic scales for the rotation of the normal in the x and z directions, and the characteristic scale for the deformation itself, respectively. These

scales will be determined self-consistently through the mathematical analysis below. The characteristic pressure scale is $\mathcal{P}_c$, which will be obtained from the analysis of the fluid mechanics problem. For a long and wide microchannel, following [37], assume that

$$h_0 \ll w \ll \ell \qquad \Rightarrow \qquad \epsilon \ll \delta \ll 1, \tag{3.16}$$

where $\epsilon := h_0/\ell$ and $\delta := h_0/w$, and h_0 is the undeformed height of the channel (recall Fig. 3.1). Substituting the dimensionless variables from Eq. (3.15) into Eqs. (3.14), (3.12d) and (3.12e) yields a dimensionless set of governing equations:

$$\kappa Gt \left(\frac{\mathcal{F}_x}{w} \frac{\partial \Phi_x}{\partial X} + \frac{\mathcal{F}_z}{\ell} \frac{\partial \Phi_z}{\partial Z} \right) + (T + \kappa Gt) \left(\frac{\mathcal{U}_c}{w^2} \frac{\partial^2 U}{\partial X^2} + \frac{\mathcal{U}_c}{\ell^2} \frac{\partial^2 U}{\partial Z^2} \right) = -\mathcal{P}_c P, \tag{3.17a}$$

$$\frac{D_b}{w^2} \mathcal{F}_x \frac{\partial^2 \Phi_x}{\partial X^2} + \frac{1}{2} \frac{D_b(1-\nu)}{\ell^2} \mathcal{F}_x \frac{\partial^2 \Phi_x}{\partial Z^2} + \frac{1}{2} \frac{D_b(1+\nu)}{w\ell} \mathcal{F}_z \frac{\partial^2 \Phi_z}{\partial X \partial Z} - \kappa Gt \left(\mathcal{F}_x \Phi_x + \frac{\mathcal{U}_c}{w} \frac{\partial U}{\partial X} \right) = 0, \tag{3.17b}$$

$$\frac{D_b}{\ell^2} \mathcal{F}_z \frac{\partial^2 \Phi_z}{\partial Z^2} + \frac{1}{2} \frac{D_b(1-\nu)}{w^2} \mathcal{F}_z \frac{\partial^2 \Phi_z}{\partial X^2} + \frac{1}{2} \frac{D_b(1+\nu)}{w\ell} \mathcal{F}_x \frac{\partial^2 \Phi_x}{\partial X \partial Z} - \kappa Gt \left(\mathcal{F}_z \Phi_z + \frac{\mathcal{U}_c}{\ell} \frac{\partial U}{\partial Z} \right) = 0. \tag{3.17c}$$

In Eqs. (3.17b) and (3.17c), the terms involving $\partial U/\partial X$ and $\partial U/\partial Z$ arise from the transverse shear resultant, meaning they are a key aspect of the FOSDT. To retain these terms asymptotically, we take

$$\mathcal{F}_x = \frac{\mathcal{U}_c}{w}, \qquad \mathcal{F}_z = \frac{\mathcal{U}_c}{\ell} = \frac{w}{\ell} \mathcal{F}_x. \tag{3.18}$$

Next, we substitute the expressions for $\mathcal{F}_x$ and $\mathcal{F}_x$ from Eq. (3.18) into Eq. (3.17b) and multiply by h_0^2 to obtain:

$$\delta^2 D_b \mathcal{F}_x \frac{\partial^2 \Phi_X}{\partial X^2} + \frac{1}{2} D_b (1-\nu) \mathcal{F}_x \epsilon^2 \frac{\partial^2 \Phi_X}{\partial Z^2}$$
$$+ \frac{1}{2} \mathcal{F}_x D_b (1+\nu) \epsilon^2 \frac{\partial^2 \Phi_Z}{\partial X \partial Z} - \kappa Gt h_0^2 \mathcal{F}_x \left(\Phi_X + \frac{\partial U}{\partial X} \right) = 0. \tag{3.19}$$

Under the assumed asymptotic scaling given in Eq. (3.16), we retain terms of $O(\delta^2)$ in the last equation, while dropping the terms of $O(\epsilon^2)$ in Eq. (3.19), to obtain:

$$\delta^2 D_b \frac{\partial^2 \Phi_X}{\partial X^2} - \kappa Gt h_0^2 \left(\Phi_X + \frac{\partial U}{\partial X} \right) = 0. \tag{3.20}$$

To balance all terms in the last equation, we must require that $\delta^2 D_b \sim \kappa G t h_0^2$. This scaling can be interpreted in two ways. First, in the "stiffness space," it can be rewritten as

$$\delta^2 \sim \frac{\kappa G t h_0^2}{D_b} = \frac{\text{transverse shear stiffness}}{\text{bending stiffness}}, \qquad (3.21)$$

which means that the ratio of the transverse shear stiffness to the bending stiffness, though small, is still finite, unlike "thin-plate" (Kirchhoff–Love) theory [132, 153] (referred to as "classical plate theory" in [147]), in which it is identically zero. Second, by using the definition of the bending stiffness D_b and the shear modulus G given above, Eq. (3.21) can be rewritten as

$$6\kappa(1 - \nu) \sim (t/w)^2, \qquad (3.22)$$

which is an equivalent relation in the "dimensions space," and portrays the relationship between the thickness and the width of the plate in an order of magnitude sense.

Next, Eq. (3.20) can be rewritten as

$$\mathscr{T}\frac{\partial^2 \Phi_X}{\partial X^2} - \left(\Phi_X + \frac{\partial U}{\partial X}\right) = 0, \qquad \mathscr{T} := \frac{(t/w)^2}{6\kappa(1 - \nu)}, \qquad (3.23)$$

where a scaled dimensionless thickness $\mathscr{T}$ has been defined for convenience.

Similarly, for Eq. (3.17a), we substitute $\mathscr{F}_x$ and $\mathscr{F}_z$ from Eq. (3.18) and multiply by $h_0^2 w^2 / D_b$ to obtain:

$$\frac{1}{\mathscr{T}}\left(\delta^2 \frac{\partial \Phi_X}{\partial X} + \epsilon^2 \frac{\partial \Phi_Z}{\partial Z}\right) + \left(\frac{Tw^2}{D_b} + \frac{1}{\mathscr{T}}\right)\left(\delta^2 \frac{\partial^2 U}{\partial X^2} + \epsilon^2 \frac{\partial^2 U}{\partial Z^2}\right) = -\frac{h_0^2 w^2 \mathcal{P}_c}{D_b \mathcal{U}_c}P. \qquad (3.24)$$

Again, we neglect terms of $O(\epsilon^2)$ and retain terms of $O(\delta^2)$, arriving at

$$\frac{1}{\mathscr{T}}\left(\delta^2 \frac{\partial \Phi_X}{\partial X}\right) + \left(\lambda + \frac{1}{\mathscr{T}}\right)\left(\delta^2 \frac{\partial^2 U}{\partial X^2}\right) = -\frac{h_0^2 w^2 \mathcal{P}_c}{D_b \mathcal{U}_c}P, \qquad (3.25)$$

where $\lambda := Tw^2 / D_b$ has been defined as a dimensionless tension-to-bending number. Although $\lambda < 0$ is possible as well (pre-compressed plate), we restrict ourselves to the case of $\lambda > 0$ to avoid potentially having to deal with buckled states of the membrane [116].

To summarize, the FOSDT equations (in terms of the deformation U and the rotation of the normal Φ_X) for bending of a long and wide plate, initially subject to a uniform isotropic pretension, are

$$\mathscr{T} \frac{\partial^2 \Phi_X}{\partial X^2} - \left(\Phi_X + \frac{\partial U}{\partial X} \right) = 0, \tag{3.26a}$$

$$\frac{1}{\mathscr{T}} \frac{\partial \Phi_X}{\partial X} + \left(\lambda + \frac{1}{\mathscr{T}} \right) \frac{\partial^2 U}{\partial X^2} = -\frac{h_0^2 w^2 \mathcal{P}_c}{\delta^2 D_b \mathcal{U}_c} P. \tag{3.26b}$$

The corresponding (four) clamping boundary conditions (BCs) at the channel's lateral sidewalls are

$$U|_{X=\pm 1/2} = 0, \qquad \Phi_X|_{X=\pm 1/2} = 0. \tag{3.27}$$

The characteristic deformation scale $\mathcal{U}_c$ remains unknown. It will be determined by considering appropriate balances in Eq. (3.26b), depending on the order of magnitude of λ.

3.2.6 Solution of the deformation equations

It was shown in [37] (see also Sec. 3.3 below) that, under the lubrication approximation, the hydrodynamic pressure load can vary *at most* in the flow-wise direction; i.e., $P = P(Z)$ only. Then, the governing differential equations Eqs. (3.26) for Φ_X and U are a set of coupled, inhomogeneous, *ordinary* differential equations (ODEs) in X with constant coefficients.

Based on the definition of λ from Eq. (3.26b), we can delineate four regimes of structural deformation:

- Regime 1 ($\lambda \ll 1$): Pre-tension is negligible compared to transverse shear and bending, i.e., $T w^2 / D_b \ll 1$.

- Regime 2 ($\lambda = \mathcal{O}(1)$): Pre-tension and transverse shear are comparable to bending: $T w^2 / D_b = \mathcal{O}(1)$, or $T h_0^2 / D_b = \mathcal{O}(\delta^2)$.

- Regime 3a ($\lambda = \mathcal{O}(1/\delta^2)$): Pre-tension is much stronger that transverse shear and bending: $T w^2 / D_b = \mathcal{O}(1/\delta^2)$, or $T h_0^2 / D_b = \mathcal{O}(1)$.

- Regime 3b ($\lambda \gg 1/\delta^2$): Again, pre-tension is much stronger that transverse shear and bending, but there are no longer dominant balances involving λ in the governing equation: $T h_0^2 / D_b \gg 1$.

Regime 1 is bending dominated, and the problem reduces to the no-pre-tension case considered in previous work [38, 60]. In Regime 3b, the problem reduces to the trivial case of biaxial stretching of a bar, without any FSI, which is not of interest either. In Regime 2, both pre-tension and bending effects are important. Thus, Regime 2 is of primary interest in this chapter, and a solution will be sought for the displacement in this regime. Then, the displacement under Regimes 1 and 3a can be easily found from the solution in Regime 2 as special/limiting cases.

Next, Eq. (3.26b) can be solved for $\partial \Phi_X / \partial X$:

$$\frac{\partial \Phi_X}{\partial X} = -\mathcal{T} \left[\frac{w^4 \mathcal{P}_c}{D_b \mathcal{U}_c} P + \left(\lambda + \frac{1}{\mathcal{T}} \right) \frac{\partial^2 U}{\partial X^2} \right], \tag{3.28}$$

which, in turn, can be differentiated twice with respect to X, to obtain:

$$\frac{\partial^3 \Phi_X}{\partial X^3} = -\mathcal{T} \left(\lambda + \frac{1}{\mathcal{T}} \right) \frac{\partial^4 U}{\partial X^4}. \tag{3.29}$$

Taking $\partial / \partial X$ of Eq. (3.26a) and substituting into it the results from Eq. (3.28) and (3.29), yields a single ODE for U:

$$- (\lambda \mathcal{T} + 1) \frac{\partial^4 U}{\partial X^4} + \lambda \frac{\partial^2 U}{\partial X^2} + \frac{w^4 \mathcal{P}_c}{D_b \mathcal{U}_c} P = 0, \tag{3.30}$$

Thus, to balance all terms (and account for bending, stretching and pressure loading), we must choose the scale of deformation to be

$$\mathcal{U}_c = \frac{w^4 \mathcal{P}_c}{D_b}. \tag{3.31}$$

Equation (3.30) is subject to the four BCs from Eq. (3.27). Again, two of them need to be converted from BCs on Φ_X to corresponding BCs on U. To that end, differentiate Eq. (3.28) to obtain an expression for $\partial^2 \Phi_x / \partial X^2$, which is then substituted into Eq. (3.26a). Next, evaluate the result at $X = \pm 1/2$ and impose the BCs $\Phi_X|_{X=\pm 1/2} = 0$ to obtain the new BCs

$$\left[\frac{1}{\mathcal{T}} \frac{\partial U}{\partial X} + (\lambda \mathcal{T} + 1) \frac{\partial^3 U}{\partial X^3} \right]\Bigg|_{X=\pm 1/2} = 0. \tag{3.32}$$

By inspection, the particular solution of Eq. (3.30) is $-\frac{1}{2\lambda}P(Z)X^2$. For the homogeneous problem, the characteristic polynomial is $(\lambda\mathcal{T}+1)r^4 - \lambda r^2 = 0$, the roots of which are $r = \left\{0, \pm\sqrt{\lambda/(\lambda\mathcal{T}+1)}\right\}$, where $r = 0$ is a double root. Thus, the general solution of Eq. (3.30) is

$$U(X,Z) = -\frac{P(Z)}{2\lambda}X^2 + C_1(Z)\exp\left(X\sqrt{\frac{\lambda}{\lambda\mathcal{T}+1}}\right)$$
$$+ C_2(Z)\exp\left(-X\sqrt{\frac{\lambda}{\lambda\mathcal{T}+1}}\right) + C_3(Z) + C_4(Z)X, \quad (3.33)$$

where $C_{1,2,3,4}(Z)$ are arbitrary functions of integration.

The $X \mapsto -X$ symmetry of the boundary-value problem (BVP) specified by Eq. (3.30) and its BCs requires that $C_1(Z) = C_2(Z)$ and $C_4(Z) = 0$. Thus, the general solution (3.33) can be rewritten as

$$U(X,Z) = 2C_1(Z)\cosh\left(X\sqrt{\frac{1}{\lambda\mathcal{T}+1}}\right) + C_3(Z) - \frac{P(Z)}{2\lambda}X^2, \quad (3.34)$$

The BCs in Eq. (3.32) require that

$$C_1(Z) = \frac{P(Z)}{4\lambda\sqrt{\lambda(\lambda\mathcal{T}+1)}\sinh\left(\frac{1}{2}\sqrt{\frac{\lambda}{\lambda\mathcal{T}+1}}\right)}. \quad (3.35)$$

Then, the BCs $U|_{X=\pm 1/2} = 0$ require that

$$C_3(Z) = \frac{P(Z)}{2\lambda}\left[\frac{1}{4} - \frac{1}{\sqrt{\lambda(\lambda\mathcal{T}+1)}}\coth\left(\frac{1}{2}\sqrt{\frac{\lambda}{\lambda\mathcal{T}+1}}\right)\right]. \quad (3.36)$$

Thus, the complete solution for the cross-sectional deformation profile of the prestressed plate is

$$U(X,Z) = \frac{P(Z)}{2\lambda}\left\{\left(\frac{1}{4} - X^2\right) - \left[\frac{\cosh\left(\frac{1}{2}\sqrt{\frac{\lambda}{\lambda\mathcal{T}+1}}\right) - \cosh\left(X\sqrt{\frac{\lambda}{\lambda\mathcal{T}+1}}\right)}{\sqrt{\lambda(\lambda\mathcal{T}+1)}\sinh\left(\frac{1}{2}\sqrt{\frac{\lambda}{\lambda\mathcal{T}+1}}\right)}\right]\right\}. \quad (3.37)$$

As a consistency check, we also note that, in the limit of negligible thickness ($\mathcal{T} \to 0$), Eq. (3.37) reduces to the deformation profile of a pre-stressed thin membrane [116, Eq. (8)] (see also [110, Eq. (10)]).

On the other hand, in the limit $\lambda \to 0$, Eq. (3.37) reduces to the solution for thick plate without pre-tension, i.e., the solution for Regime 1 from [38],

In Regime 3a, $\lambda = O(1/\delta^2)$, i.e., $\lambda \gg 1$, and a straightforward Taylor series expansion of Eq. (3.37) for $\lambda \to \infty$ gives

$$U(X, Z) = \frac{P(Z)}{2\lambda} \left\{ \left(\frac{1}{4} - X^2 \right) - \frac{1}{\lambda} \frac{\cosh \left(\frac{1}{2\sqrt{\mathscr{T}}} \right) - \cosh \left(\frac{X}{\sqrt{\mathscr{T}}} \right)}{\sqrt{\mathscr{T}} \sinh \left(\frac{1}{2\sqrt{\mathscr{T}}} \right)} + O \left(\frac{1}{\lambda^2} \right) \right\}. \tag{3.38}$$

For future reference, Eq. (3.37) can be put back into its dimensional form:

$$u(x, z) = \frac{w^2 p(z)}{2T} \left\{ \left[\frac{1}{4} - \left(\frac{x}{w} \right)^2 \right] - \left[\frac{\cosh \left(\frac{1}{2} \sqrt{\frac{\lambda}{\lambda \mathscr{T}+1}} \right) - \cosh \left(\frac{x}{w} \sqrt{\frac{\lambda}{\lambda \mathscr{T}+1}} \right)}{\sqrt{\lambda(\lambda \mathscr{T}+1)} \sinh \left(\frac{1}{2} \sqrt{\frac{\lambda}{\lambda \mathscr{T}+1}} \right)} \right] \right\}. \tag{3.39}$$

Then, by $x \mapsto -x$ symmetry, the maximum deformation over the cross-section is its value at $x = 0$:

$$u_{\max}(z) = u(0, z) = \frac{w^2 p(z)}{2T} \left\{ \frac{1}{4} - \frac{\cosh \left(\frac{1}{2} \sqrt{\frac{\lambda}{\lambda \mathscr{T}+1}} \right) - 1}{\sqrt{\lambda(\lambda \mathscr{T}+1)} \sinh \left(\frac{1}{2} \sqrt{\frac{\lambda}{\lambda \mathscr{T}+1}} \right)} \right\}. \tag{3.40}$$

3.2.7 Deformation profile in other regimes

In this subsection, we derive the expression for deformation profile in Regime 1 and Regime 3a directly, that is to say without considering the limits of Eq. (3.37).

Regime 1

In this regime, as $\lambda \ll 1$, we simply take the formal limit $\lambda \to 0$, and Eq. (3.26b) reduces to

$$\frac{1}{\mathscr{T}} \left(\frac{\partial \Phi_X}{\partial X} + \frac{\partial^2 U}{\partial X^2} \right) = -\frac{w^4 \mathcal{P}_c}{D_b \mathcal{U}_c} P(Z). \tag{3.41}$$

Eliminating Φ_X between Eqs. (3.41) and (3.26a), we obtain a single ODE in U:

$$\frac{\partial^4 U}{\partial X^4} = \frac{w^4 \mathcal{P}_c}{D_b \mathcal{U}_c} P(Z). \tag{3.42}$$

Clearly, the appropriate choice for the deformation scale is

$$\mathcal{U}_c = \frac{w^4 \mathcal{P}_c}{D_b}, \tag{3.43}$$

and, therefore, Eq. (3.42) becomes:

$$\frac{\partial^4 U}{\partial X^4} = P(Z). \tag{3.44}$$

Next, the BCs $\Phi_X|_{X=\pm 1/2} = 0$ need to be converted to appropriate BCs on U. To this end, differentiate Eq. (3.41) with respect to X to obtain an expression for $\partial^2 \Phi_x / \partial X^2$, which can be evaluated at $X = \pm 1/2$. Then, substituting the latter, along with imposing $\Phi_X|_{X=\pm 1/2} = 0$, into Eq. (3.26a) evaluated at $X = \pm 1/2$ yields:

$$\left(\frac{\partial U}{\partial X} + \frac{1}{\mathcal{T}} \frac{\partial^3 U}{\partial X^3} \right)\Bigg|_{X=\pm 1/2} = 0. \tag{3.45}$$

The solution of Eq. (3.44) subject to Eq. (3.45) and $U|_{X=\pm 1/2} = 0$ is easily found to be

$$U(X, Z) = \frac{P(Z)}{24} \left[X^4 - \left(\mathcal{T} + \frac{1}{2} \right) X^2 + \frac{1}{4} \left(\mathcal{T} + \frac{1}{4} \right) \right]. \tag{3.46}$$

This profile was already obtained in [38, Eq. (21)] in the absence of pre-tension.

Regime 3a

For Regime 3a, $\lambda = O(1/\delta^2)$, thus $\lambda \gg 1$ for $\delta \ll 1$. Keeping only the largest terms in Eq. (3.30) for $\lambda \gg 1$, we obtain

$$\mathcal{T} \frac{\partial^4 U}{\partial X^4} - \frac{\partial^2 U}{\partial X^2} = \frac{1}{\lambda \delta^2} P(Z). \tag{3.47}$$

Retaining the pressure on the right-hand side of the last equation can be justified by arguing that, in Regime 3a, we should choose the scale deformation

$$\mathcal{U}_c = \frac{h_0^2 w^2 \mathcal{P}_c}{D_b}, \tag{3.48}$$

so that the coefficient of $P(Z)$ is now $1/(\lambda \delta^2) = O(1)$.

The ODE (3.47) is still subject to the boundary conditions given in Eq. (3.27), which means that, as before, we need to convert the BCs on Φ_X to appropriate BCs on U. To that end, we first insert $\Phi_X|_{X=\pm 1/2} = 0$ in Eq. (3.26a) to obtain:

$$\left(\mathcal{T} \frac{\partial^2 \Phi_X}{\partial X^2} - \frac{\partial U}{\partial X} \right)\Bigg|_{X=\pm 1/2} = 0. \tag{3.49}$$

Next, we differentiate Eq. (3.26b), evaluate it at $X = \pm 1/2$, and insert the expression for $\partial^2 \Phi_X / \partial X^2$ from Eq. (3.49) into it to obtain:

$$\left[\left(\frac{\delta^2}{\mathcal{T}} \right) \frac{\partial U}{\partial X} + (\lambda \mathcal{T} + 1)\delta^2 \frac{\partial^3 U}{\partial X^3} \right]\Bigg|_{X=\pm 1/2} = 0. \tag{3.50}$$

Now, since $\lambda = O(1/\delta^2)$, the above equation to the leading order in $\delta \ll 1$ is

$$\frac{\partial^3 U}{\partial X^3}\Bigg|_{X=\pm 1/2} = 0. \tag{3.51}$$

The solution of Eq. (3.47) subject to Eq. (3.51) and $U|_{X=\pm 1/2} = 0$ is easily found to be

$$U(X, Z) = \frac{P(Z)}{2\lambda \delta^2} \left(\frac{1}{4} - X^2 \right), \tag{3.52}$$

where, due to the differing choice in $\mathcal{U}_c$, the last equation contains a δ^2 not present in Eq. (3.38). Note that neglecting bending rendered the deformation profile given in Eq. (3.52) independent of the thickness of the structure. Thus, Eq. (3.52) is suitable for both thin and thick plates. Equation (3.52) has been used in the literature to characterize the material properties of thin membranes undergoing strong compression ($\lambda < 0$) and buckling (see Eq. (8) and Table II in [116]).

3.3 Fluid mechanics

The slenderness of the channel allows us to invoke the lubrication approximation [154], according to which the dimensionless velocity field (see [37] for details) is

$$V_Z(X, Y, Z) = \frac{1}{2} \left(-\frac{\mathrm{d}P}{\mathrm{d}Z} \right) \left[-\frac{t}{2h_0} + \beta U(X, Z) - Y \right] \left[Y + \frac{t}{2h_0} + 1 \right] \tag{3.53}$$

for no-slip boundary conditions at the rigid bottom $Y = -t/(2h_0) - 1$ and at the deformed top $Y = -t/(2h_0) + \beta U(X, Z)$ walls. The pressure P varies only in the flow-wise $+Z$-direction (meaning, $dP/dZ < 0$), thus a complete (not partial) derivative is featured in Eq. (3.53); however, due to FSI, $dP/dZ \neq const.$ as it would be in pipe flow [154]. Observe also that in FOSDT, the vertical displacement U does not depend on Y, thus it is the same at $Y = -t/(2h_0)$ (the fluid–solid interface) and at $Y = 0$ (the plate's mid-plane).

In Eq. (3.53), $V_Z(X, Y, Z) = v_z(x, y, z)/\mathcal{V}_z$ is the dimensionless velocity in the streamwise direction (recall Fig. 3.1), while $U(X, Z) = u_y(x, z)/\mathcal{U}_c$ is the dimensionless deformation of the top wall, as per Eq. (3.15). Here, on using Eq. (3.31), we have defined

$$\beta := \frac{\mathcal{U}_c}{h_0} = \frac{w^4 \mathcal{P}_c}{D_b h_0} \tag{3.54}$$

as a dimensionless group, which we term the *FSI parameter*. This parameter quantifies the compliance of the plate compared to the characteristic magnitude of the applied hydrodynamic pressure load. Then, the height of the deformed fluid domain is

$$H(X, Z) = \frac{h(x, z)}{h_0} = \frac{h_0 + u_y(x, z)}{h_0} = 1 + \beta U(X, Z). \tag{3.55}$$

The dimensionless flow rate is evaluated as the area integral of the streamwise velocity from Eq. (3.53), then written solely in terms of $U(X, Z)$ and $P(Z)$ via Eqs. (3.55) and (3.37):

$$1 = \int_{-1/2}^{+1/2} \int_{-\frac{t}{2h_0}-1}^{-\frac{t}{2h_0}-1+H(X,Z)} V_Z(X, Y, Z) \, dY \, dX \tag{3.56a}$$

$$= -\frac{1}{12} \frac{dP}{dZ} \int_{-1/2}^{1/2} H(X, Z)^3 \, dX \tag{3.56b}$$

$$= -\frac{1}{12} \frac{dP}{dZ} \int_{-1/2}^{+1/2} \Big[1 + 3\beta \mathfrak{U}(X) P(Z) + 3\beta^2 \mathfrak{U}(X)^2 P(Z)^2$$

$$+ \beta^3 \mathfrak{U}(X)^3 P(Z)^3 \Big] dX, \tag{3.56c}$$

where we have introduced the dimensionless deformation-to-pressure ratio

$$\mathfrak{U}(X) = \frac{U(X, Z)}{P(Z)} = \frac{1}{2\lambda} \left\{ \left(\frac{1}{4} - X^2 \right) - \left[\frac{\cosh\left(\frac{1}{2} \sqrt{\frac{\lambda}{\lambda \mathcal{T}+1}} \right) - \cosh\left(X \sqrt{\frac{\lambda}{\lambda \mathcal{T}+1}} \right)}{\sqrt{\lambda(\lambda \mathcal{T}+1)} \sinh\left(\frac{1}{2} \sqrt{\frac{\lambda}{\lambda \mathcal{T}+1}} \right)} \right] \right\}. \tag{3.57}$$

The left-hand side of Eqs. (3.56) is unity because we have employed a flow-rate-based velocity scale $\mathcal{V}_z = q/(h_0 w)$ as in prior work [37, 60], yielding a dimensionless flow rate $\mathcal{Q} = q/q = 1$ under steady flow with imposed inlet $q = const$.

Performing the integration in Eq. (3.56c) reduces it to a first-order nonlinear ODE in $P(Z)$:

$$-12 = \frac{dP}{dZ} \left[1 + 3\beta \mathcal{I}_1 P(Z) + 3\beta^2 \mathcal{I}_2 P(Z)^2 + \beta^3 \mathcal{I}_3 P(Z)^3 \right], \tag{3.58}$$

where, following [40], we have defined

$$\mathcal{I}_i := \int_{-1/2}^{+1/2} \mathfrak{U}(X)^i \, dX. \tag{3.59}$$

Note that $\{\mathcal{I}_i\}_{i=1,2,3}$ are known functions of λ and $\mathcal{T}$ (but not X or Z), even if obtaining them analytically might be challenging. As a further guide to the reader, the variation of $\mathcal{I}$s with λ for different values of $\mathcal{T}$, has been plotted in Fig. 3.2.

Now, the ODE (3.58) is solved subject to the boundary condition that $P(1) = 0$ (outlet gauge pressure) to obtain an implicit dimensionless relation for $P(Z)$:

$$12(1 - Z) = P(Z) \left[1 + \frac{3}{2}\beta \mathcal{I}_1 P(Z) + \beta^2 \mathcal{I}_2 P(Z)^2 + \frac{1}{4}\beta^3 \mathcal{I}_3 P(Z)^3 \right]. \tag{3.60}$$

Finally, the steady flow rate–pressure relation can be put in dimensional form by taking $\mathcal{P}_c = \mathcal{V}_c \mu \ell / h_0^2 = q\mu\ell/(wh_0^3)$ [37] to be the viscous flow pressure scale for an imposed flow rate:

$$q = \frac{wh_0^3 p(z)}{12\mu(\ell - z)} \left[1 + \frac{3}{2}\left(\frac{w^4}{D_b h_0}\right) \mathcal{I}_1 p(z) + \left(\frac{w^4}{D_b h_0}\right)^2 \mathcal{I}_2 p(z)^2 + \frac{1}{4}\left(\frac{w^4}{D_b h_0}\right)^3 \mathcal{I}_3 p(z)^3 \right], \tag{3.61}$$

where μ is the (constant) dynamic viscosity of the Newtonian fluid.

3.4 Results

The previous sections were devoted to the derivation of the theory of steady-state fluid–structure interaction (FSI) in a microchannel between the viscous fluid flow within and a pre-stressed elastic top wall clamped on all edges. In this section, we compare the latter theoretical results to direct numerical simulations (DNS) of FSI performed using the commercial software suite by ANSYS [155]. The simulations are two-way coupled to ensure
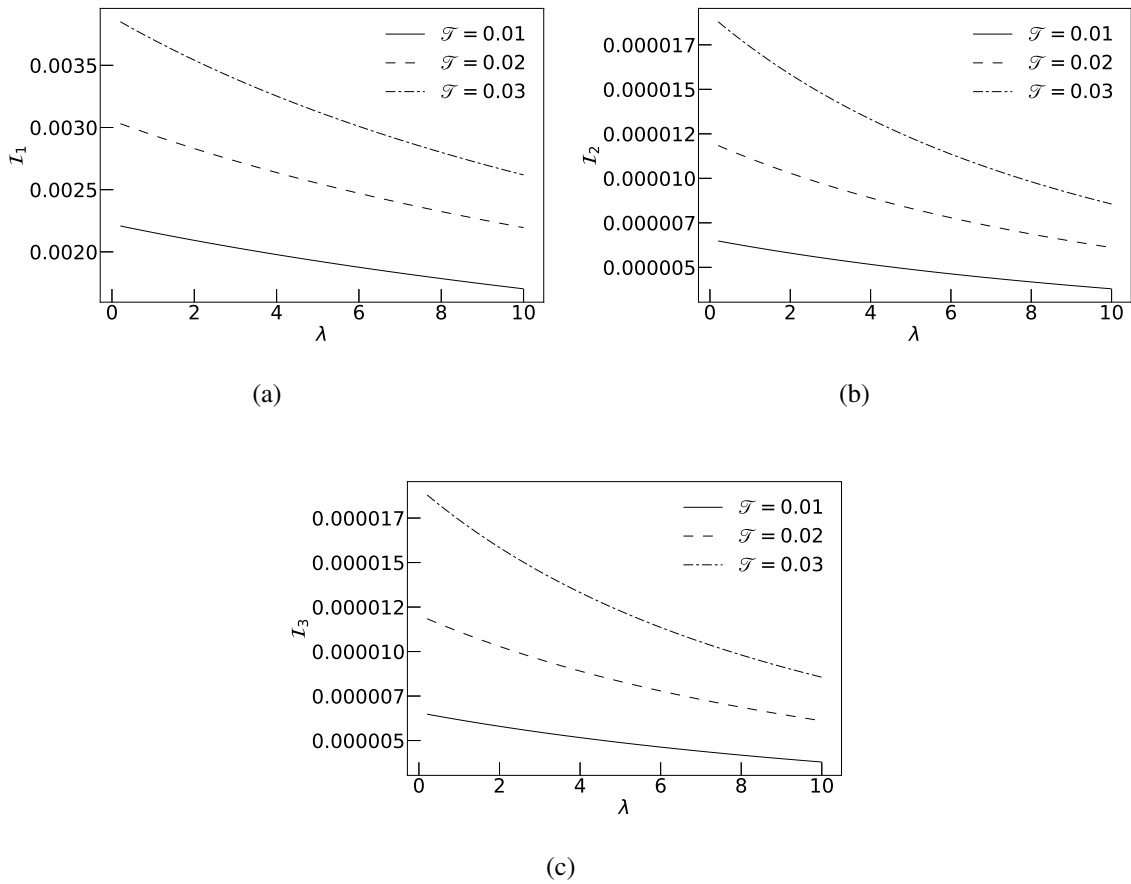
Fig. 3.2. Dependence of (a) $\mathcal{I}_1$, (b) $\mathcal{I}_2$, and (c) $\mathcal{I}_3$ on the dimensionless stretch parameter λ for different values of the dimensionless plate thickness $\mathcal{T}$.

full fidelity. Many of the details of such simulations have been presented in previous publications [37, 38, 60, 142]. Nevertheless, to ensure that this chapter is self-contained, a short summary is provided next.

3.4.1 Computational approach

ANSYS employs a segregated solution procedure to perform FSI simulations, wherein the mechanical deformation field is solved in the 'Static Structural' module, using the fi-

nite element method (FEM), while the fluid flow field is solved separately in the 'Fluent' module, using the finite volume method (FVM).

In the Static Structural module, we have switched on the option of 'large deformations.' Therefore:

- The difference between deformed and undeformed coordinates is maintained.

- The logarithmic (Henky) strain and the true (Cauchy) stress are employed as the strain and stress measures, respectively, instead of engineering strain and engineering stress, which would have been employed in a small-strain analysis.

- The stiffness matrix in the FEM formulation is a function of the displacements and results in a nonlinear governing equation for each node, which is solved by iterative methods.

Importantly, the assumptions of the plate theory, from which the mathematical model in Sec. 3.2 was derived, are *not* imposed on the numerical solution. Similarly, Fluent solves the steady 3D incompressible Navier–Stokes equation on a deforming domain without any *a priori* approximations. Previously, we carried out mesh refinement studies [38], and we explored choices of algorithms for mesh smoothing [60], in similar FSI problems. We carry over the lessons learned to the present study to obtain the right blend of numerical accuracy and computational effort.

The distinguishing feature of the FSI simulations carried out in this chapter is the inclusion of pre-stress in the elastic wall. To this end, we employed two Static Structural modules, instead of one. In the first Static Structural module, forces were imposed on the edges of the structure to induce pre-stress in the elastic wall. The resulting pre-stress distribution was then written to a file. This file containing the information about pre-stress at every node was then read into the second Static Structural module using the 'inistate' command.

The geometric details of the model are given in Table 3.1. The channel has a linearly elastic top wall characterized by a Young's modulus $E = 1.6$ MPa and a Poisson ratio $\nu = 0.4999$, similar to PDMS [38]. Three values of the uniform pre-tension of the elastic

Table 3.1.

Dimensions and relevant geometric parameters for DNS of FSI in ANSYS. All lengths are given in mm.

h_0	w	ℓ	t	δ	ϵ	t/w
0.155	1.7	15.5	0.605	0.09	0.01	0.36

top wall were considered: T = 13.62, 27.24 and 68.11 N·mm, which correspond to $\lambda \equiv Tw^2/D_b$ = 1, 2 and 5, respectively. The remaining three walls of the channel are rigid. The fluid inside the channel was taken to be water with a constant density ρ = 997.3 kg/m^3 and dynamic viscosity μ = 9.14 × 10^{-4} Pa·s. The dimensions of the channel were chosen so that the assumptions of a long and slender geometry, as stated in Eq. (3.16), are satisfied, and thus the simulations may be compared to the theory.

3.4.2   Cross-sectional deformation profile

A major result of the proposed theory is the self-similar form of the dimensionless cross-sectional deformation profiles scaled by the hydrodynamic pressure, i.e., the ratio $U(X, Z)/P(Z)$ from Eq. (3.37) is independent of the flow-wise coordinate Z. This result connects the local deformation with the local pressure, forming the theoretical foundation for the hydrostatic bulge test. To verify this result of the theory, in Fig. 3.3 we plot the results from ANSYS FSI simulations for $U(X, Z)/P(Z)$ as a function of X alongside the prediction from from Eq. (3.37). We observe that the simulations (represented by symbols and colors, corresponding to the different flow rates q and evaluated at different flow-wise locations z) collapse neatly onto a single curve, which closely matches the theoretical profile (solid curve). In practice, validation of this prediction cannot be carried out in a noninvasive manner due to the need to measure the deformation at several flow-wise locations.
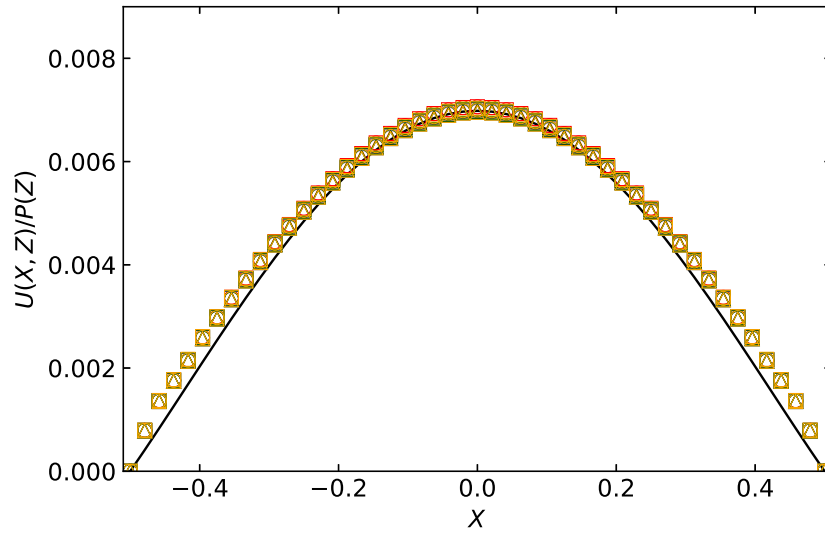
Fig. 3.3. Self-similar collapse of the scaled dimensionless deformation of the channel's elastic plate top wall, across the width of the channel, for different flow rates q and axial locations z; $\lambda = 2$. The solid curve represents the theoretical prediction from Eq. (3.37), the symbols correspond to the results of DNS of FSI in ANSYS. Colors correspond to flow rates: red is $q = 10$ mL/min, yellow is $q = 20$ mL/min, gray is $q = 30$ mL/min, black is $q = 40$ mL/min, green is $q = 50$ mL/min, and orange is $q = 60$ mL/min. Symbols correspond to different axial locations: $\square$ is at $z = 4$ mm, $\bigcirc$ is at $z = 8$ mm, and $\triangle$ is at $z = 12$ mm. Note that many symbols overlap due to the high quality of the collapse.

Next, we carried out the simulations for fixed q but different values of the pre-tension T. In Fig. 3.4, the profile $U(X, Z)/P(Z)$ from ANSYS simulation is compared to the theoretical profile from Eq. (3.37), for different values of the bending-to-tension ratio λ. We observe good match between the theoretical prediction and the results of simulation, but it worsens as λ increases. A possible explanation may be that significant stretching occurs in the structure at high λ, which invalidates the small strain assumption employed in the FOSDT of plates. Also, the agreement is better at the center of the cross-section, compared to the sides, which can be attributed to the use of clamped boundary conditions in the theory, while a 3D zero-displacement boundary condition for the nodes along the $x = \pm w/2$ planes
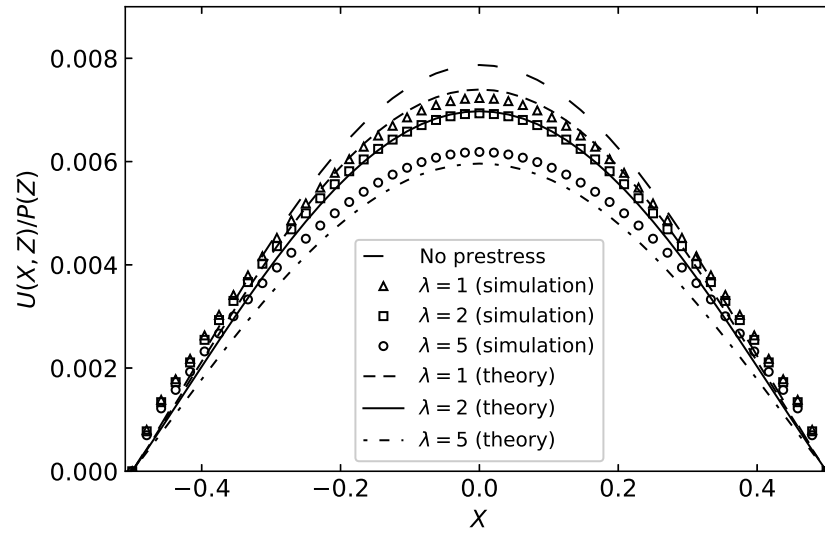
Fig. 3.4. Self-similar scaled dimensionless deformation of the elastic plate top wall of the channel, for different bending-to-tension ratios λ, at an inlet flow rate of $q = 30$ mL/min. The curves represents the theoretical prediction from Eq. (3.37), while the symbols correspond to the results of DNS of FSI in ANSYS.

is imposed in simulations. Others have used the so-called "elastically clamped" boundary conditions [109, 110] to improve the agreement near the edges. However, the elastically clamped boundary conditions involve a free parameter, whose value must be determined from additional numerical simulation of the particular plate geometry [156]. Therefore, the use of elastically clamped boundary conditions pose their own set of challenges, while yielding at a best a modest improvement in the already quite good match between the theoretical and simulated deformation profiles.

3.4.3 Flow rate–pressure drop relationship

Next, we shift our focus to the flow rate–pressure drop relationship obtained in closed-form from the theory as Eq. (3.61). This result involves variables that need to be measured only at the inlet and/or the outlet of the microchannel; these measurements can be done non-
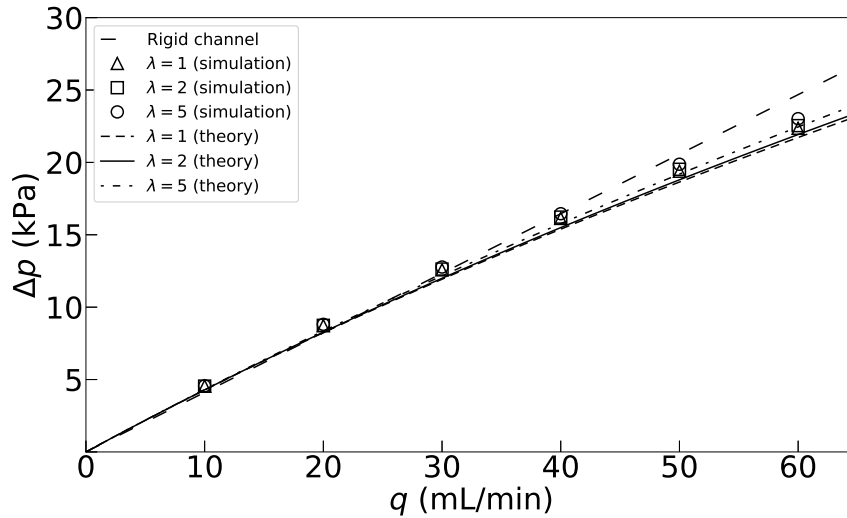
Fig. 3.5. Comparison of flow rate–pressure drop relationship from numerical simulation (markers) and the theoretical dependence found from inverting Eq. (3.61) (solid curves), for different values of the tension-to-bending ratio λ to highlight the effect of pre-tension in the plate.

invasively. Therefore, there is no need to measure quantities inside the system (channel) to obtain an estimate of the material properties from Eq. (3.61). The latter idea underpins the proposed hydrodynamic bulge test, which renders the system a "black box" for experimental materials characterization, unlike the hydrostatic bulge test, which requires measuring $u_{\max}(z)$ at some axial position z and inverting Eq. (3.40) to determine E (via D_b in λ).

To illustrate our FSI theory, in Fig. 3.5, we plot the full pressure drop $\Delta p = p(0) - p(\ell) = p(0)$, as calculated from Eq. (3.61), as a function of the volumetric flow rate q, for different tension-to-bending ratios λ. Additionally, the corresponding results from our ANSYS FSI simulations are shown as symbols. Clearly, the theory agrees with the simulations for the range of q and λ considered. An increase in λ causes the pressure drop to increase, because of the decrease in deformation as pre-tension "stiffens" the plate. The match worsens at larger q and λ due to "stronger" FSI. For each λ, the maximum error between theory and simulation occurs at the maximum flow rate $q = 60$ mL/min; still, this maximum relative error is just $\approx 2.53\%$ for $\lambda = 5$.

3.4.4 Characterization of material properties and range of validity of the theory

The goal of this chapter is to introduce a theory of hydrodynamic bulge testing, wherein the material properties of a finite-thickness elastic membrane (plate) are characterized using a pressure drop measurement and the relationship in Eq. (3.61), without measuring the membrane's transverse deformation. To achieve this goal, the measured pressure drop, the imposed flow rate, and the known geometric dimensions are substituted into Eq. (3.61), which is then solved using the bisection method [157, Ch. 5] in a Python script using SciPy [140], to obtain the Young's modulus E given the Poisson ratio ν.

To demonstrate how a hydrodynamic bulge test might work, we carried out FSI simulations for different values of the elastic modulus E of the top wall. The simulations were carried out for flow rates of $q = 60$ mL/min, 80 mL/min, and 100 mL/min for $\lambda = 1, 2$, and 5. The resulting pressure drop from the simulation was used to predict the value of E by inverting Eq. (3.61). The results of this analysis are shown in Fig. 3.6.

Clearly, there is acceptable match between the actual (here, simulation) values and the estimated (here, theoretical) values of E, for the chosen range that is typical of PDMS. The quality of this match is gauged by the closeness of the symbols to the line with slope 1 passing through the origin. The maximum error is about 43% for the case of $q = 60$ mL/min and $E = 2.4$ MPa. We note that the match is better for stiffer walls (larger values of E) at higher flow rates, and for softer walls (smaller values of E) at lower flow rates.

This observation can be explained by considering the regime of validity of our theory, which is given in mathematical terms as:

$$\{t \lesssim w \sim \mathcal{U}_c\} \ll \ell, \tag{3.62}$$

where

$$\mathcal{U}_c = \frac{w^4 \mathcal{P}_c}{D_b} = \frac{q\mu\ell w^3}{D_b h_0^3} = \frac{12q\mu\ell(1 - \nu^2)w^3}{Et^3 h_0^3}. \tag{3.63}$$

Here, the inequality $t \lesssim w$ means that we have accounted for moderate (rather than vanishing, $t \ll w$) plate thickness. The scaling $\mathcal{U}_c \sim w$ means that we have accounted for moderate rotations in the equilibrium equations, by inclusion of $\mathcal{N}$ and, thus, the plate's bending response is coupled with its stretching response. The inequality of $w \ll \ell$ is necessary to

ensure that the lubrication approximation is valid (for the fluid mechanics problem), so that cross-section deformation profiles are decoupled from each other in the flow-wise direction (for the structural mechanics problem). Therefore, if the characteristic deformation $\mathcal{U}_c$ is large compared to the dimensions of the channels, i.e., $\mathcal{U}_c > w$, the structural mechanics problem is no longer linear and our FSI theory breaks down. On the other hand, if $\mathcal{U}_c$ is extremely small, i.e., $\mathcal{U}_c \ll w$, and the FSI in the system is "weak," the estimate of E deteriorates. In the limiting case of a rigid channel, in which there is obviously no FSI, it would not be possible to estimate E at all because there is no deformation.

To quantify the above-identified requirement of "sufficient FSI" via deformation that is still in the linearly elastic regime, we can employ Eq. (3.62) to restrict the range of $\mathcal{U}_c/w$ values for which the hydrodynamic bulge test is expected to be accurate. Observing that $\beta\delta = \mathcal{U}_c/w$, it is more convenient to write this restriction as one on the FSI parameter β introduced in Eq. (3.54). Based on applying the hydrodynamic bulge test idea to simulation data from the present study, as well as previous simulations [38] and experiments [158] without pre-stress, we suggest the order-of-magnitude guideline:

$$1 \lesssim \beta \equiv \frac{12q\mu\ell(1 - v^2)w^3}{Et^3h_0^4} \lesssim 10, \tag{3.64}$$

where the upper range of values is suitable for non-pre-stressed plates ($\lambda = 0$), while the lower range of values should be preferred in the case of a plate stiffened by pre-stress ($\lambda = O(1)$). This guideline is an important result in practice. Since one can control q, μ, ℓ, t, w and h_0, then it always possible to set up a sample, to be characterized by the proposed hydrodynamic bulge test, such that the bulge test is accurate. However, since Eq. (3.64) already contains E, it must be applied in a recursive manner to design the hydrodynamic bulge test experiment, as show in Fig. 3.7. Importantly, the iteration process only requires updating the flow rate q in the experiment (easily controlled by a pump), thus it does *not* require modification of the microchannel geometry, once it is manufactured.
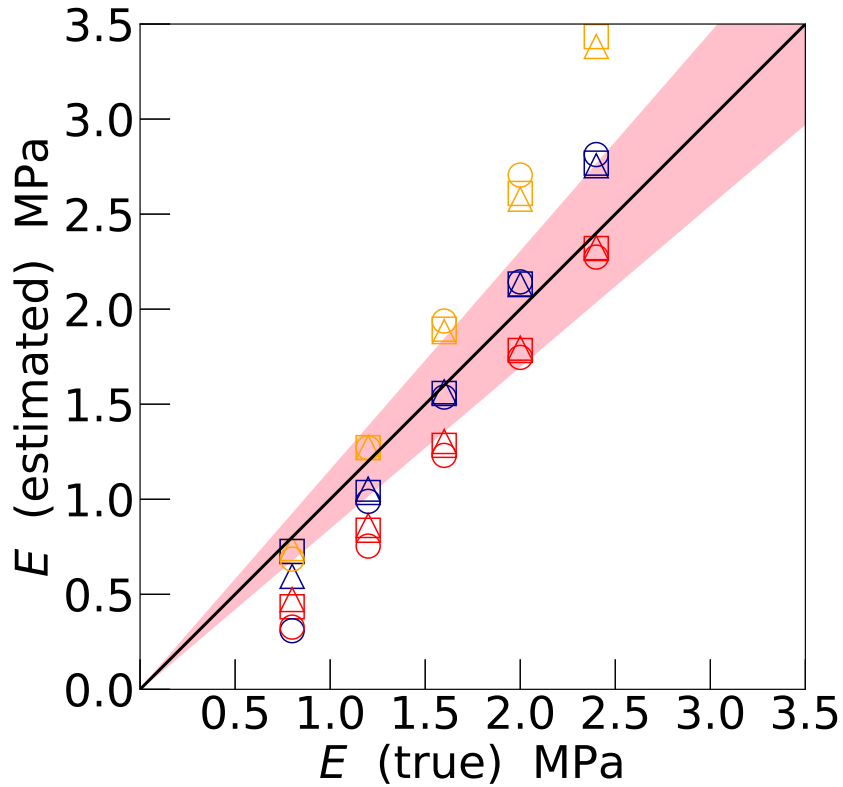
Fig. 3.6. Estimation of the elastic modulus E from a hydrodynamic bulge test versus its "true" value (used in the simulations). Colors correspond to different flow rates: orange is $q = 60$ mL/min, blue is $q = 80$ mL/min, and red is $q = 100$ mL/min. Symbols correspond to different values of the tension-to-bending ratio λ: $\bigcirc$ is $\lambda = 5$, $\square$ is $\lambda = 2$, and $\triangle$ is $\lambda = 1$. All other quantities are as given in Table 3.1. The shaded area corresponds to an uncertainty of $\pm 15\%$ in E.

3.5 Error propagation and sensitivity analysis

It is important to compare the hydrostatic and hydrodynamic bulge tests with respect to error propagation via a sensitivity analysis. Due to measurement errors [159], any experimental observation has an uncertainty associated with it. The uncertainty in the independent (measured) variable propagates to an uncertainty in the dependent (estimated) variable. In this section, we discuss examples of how errors propagate in the hydrostatic
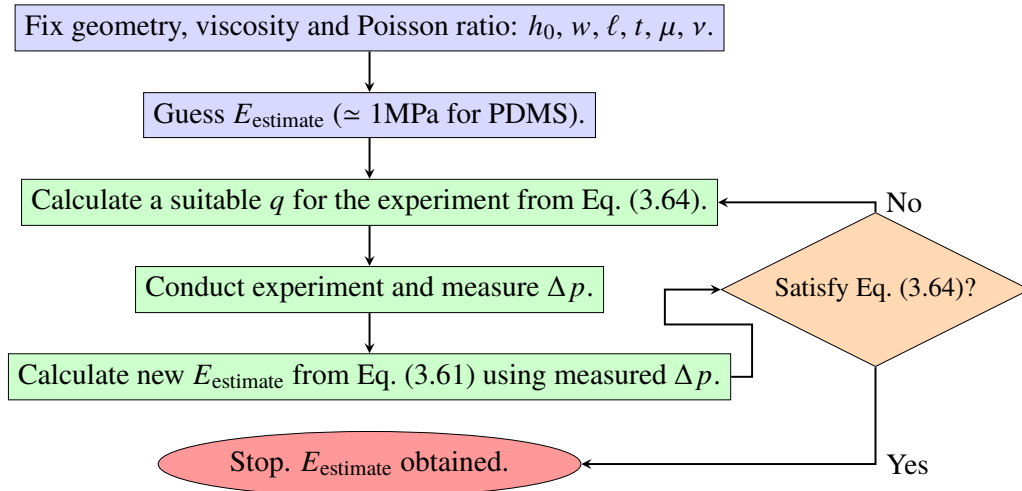
Fig. 3.7. Flow chart of how to iteratively apply the hydrodynamic bulge testing methodology to estimate the Young's modulus E of a plate, starting from a guess.

and the hydrodynamic bulge testing theories. Specifically, we simulate how uncertainty in the corresponding independent variables (Δp in the hydrodynamic case and $u_{\max}$ in the hydrostatic case) leads to an uncertainty in the dependent variable, the Young's modulus E, and compare the two cases to each other.

In our theory from Sec. 3.3, the relationship between the dependent variable and the independent variables is given by Eq. (3.61) in conjunction with Eqs. (3.57) and (3.59). These set of coupled equations is not amenable to a standard uncertainty quantification by analytical means, such as a Taylor series-based root-mean-squared error propagation [159, Sec. 4.7]. This situation is unlike the hydrostatic case in which E is determined (via D_b in λ) by measuring $u_{\max}(z)$ at some axial position z and inverting Eq. (3.40), which is amenable to an error propagation analysis. Hence, we take a statistical approach and perform Monte Carlo simulations of error propagation.

The Monte Carlo simulation of error propagation is straightforward. The independent variables $u_{\max}$ and Δp are replaced by random variables, which are sampled from a normal distribution. The normal distribution is, in turn, determined from a nominal value, the
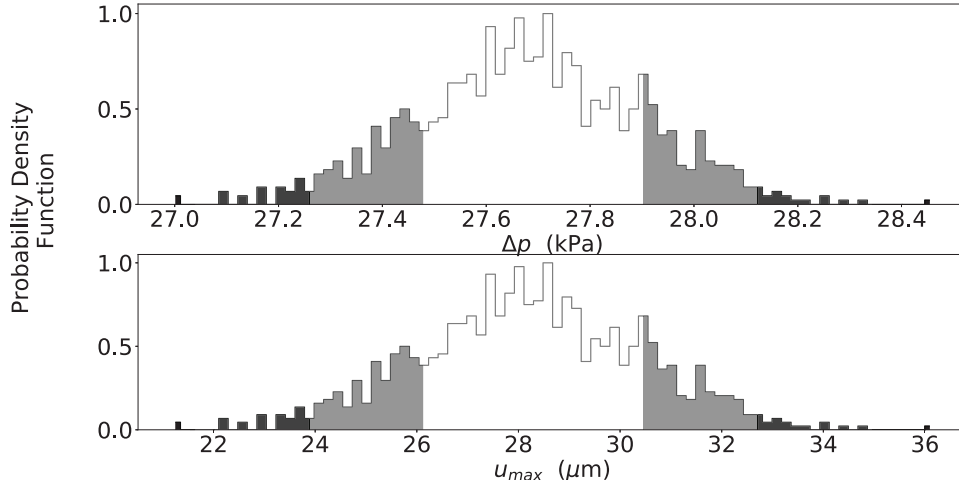
Fig. 3.8. Realizations of the noisy distributions of the total pressure drop Δp (top) and the maximum deformation u_{max} (bottom) as an input to the Monte Carlo simulation for error propagation under the hydrostatic and hydrodynamic bulge test, respectively. Each shaded band has a width of one standard deviation.

given mean $\overline{u_{\mathrm{max}}}$ or $\overline{\Delta p}$ in Table 3.2, and the upper and lower limits on uncertainty $\pm \Upsilon$ as a percentage, from which the standard deviations ς of the distributions are

$$\varsigma_{u_{\mathrm{max}}} = \left[\frac{\Upsilon_{u_{\mathrm{max}}}}{F^{-1}(0.9)} \right] \overline{u_{\mathrm{max}}}, \qquad \varsigma_{\Delta p} = \left[\frac{\Upsilon_{\Delta p}}{F^{-1}(0.9)} \right] \overline{\Delta p}. \tag{3.65}$$

The factor $\Upsilon/F^{-1}(0.9)$ in Eqs. (3.65), where $F^{-1}(0.9)$ is the inverse of the normal cumulative density function at the 90th quantile, ensures that 90% of the area under probability density function is below the specified upper limit $(+\Upsilon\%)$ and similarly 90% of the area under probability density function is above the specified lower limit $(-\Upsilon\%)$. A total of 1000 samples were taken of the input random variables, as a trade-off between the computational effort expended and the desired accuracy of probabilistic models. Example distributions of the input variables are shown in Fig. 3.8.

The mean and the standard deviation of the output samples for E were computed for both models. The results are shown in Fig. 3.9 and in Table 3.3. To gauge the sensitivity of the estimate of E to the input distributions of u_{max} and Δp, we employed a statistical rank order correlation, specifically Kendall's tau rank correlation coefficient, available in

Table 3.2.

Statistics of the input distribution for the Monte Carlo simulation of error propagation under the hydrostatic and hydrodynamic bulge tests. The mean values of the independent variables are the ones used in the ANSYS simulation for $q = 80$ mL/min, $\lambda = 2$ and $E = 1.60$ MPa.

Bulge Test	Input	Mean $\overline{(\cdot)}$	Uncertainty Υ
Hydrostatic	$u_{\max}$	28.296 μm	$\pm 10\%$
Hydrodynamic	Δp	27.691 kPa	$\pm 1\%$

Python's SciPy module [140]. The value of Kendall's tau rank correlation lies between -1 and $+1$; a value of $+1$ denotes strong positive correlation, a value of -1 denotes strong negative correlation, while a value of 0 denotes no correlation at all. From Fig. 3.9 and Table 3.3, we conclude that estimates of elastic modulus obtained from the hydrostatic bulge test are more accurate compared to those obtained from the hydrodynamic bulge test, though the difference is not very large ($\approx 2.5\%$). However, the noise in the estimates E is much larger for the hydrostatic bulge test than for the hydrodynamic bulge test, as evidenced by the larger standard deviation of the hydrostatic bulge test's output distribution. The higher noise in the estimated variable E is attributed to the higher noise in the measured variable $u_{\max}$, as the absolute value of the rank correlation coefficient (Kendall's τ) is approximately the same for both models.

The means match the deterministic values used in the ANSYS simulations corresponding to a flow rate $q = 80$ mL/min, a tension-to-bending ratio $\lambda = 2$, and Young's modulus $E = 1.6$ MPa. The uncertainty in the pressure drop measurement corresponds to that of a standard off-the-shelf pressure measurement device like Omega PXM409-007BDWUI. On the other hand, the uncertainty in the deformation has been taken to be an order of magnitude larger, at 10%, which is close to the uncertainty in deformation measurements extracted from the experimental data in [42, 108].
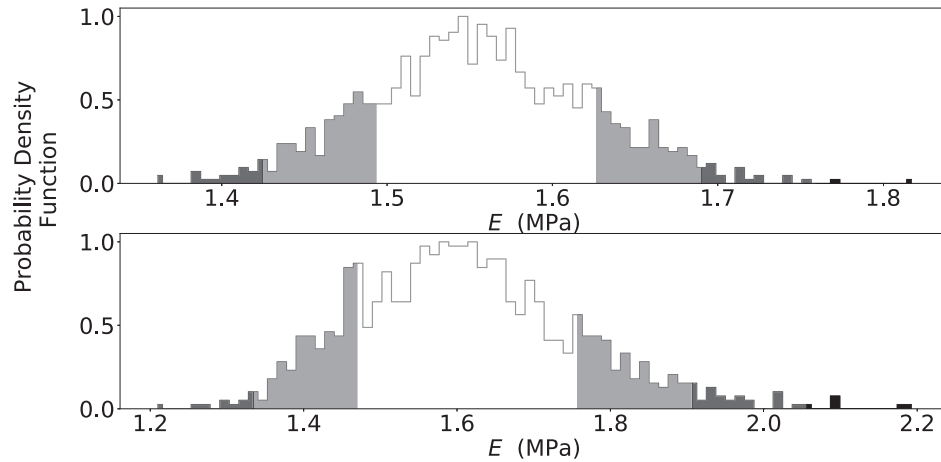
Fig. 3.9. Distribution of the estimate of E obtained from the Monte Carlo simulation of the hydrodynamic (top) and hydrostatic (bottom) bulge test. Each shaded band has a width of one standard deviation.

Table 3.3.

Statistics for the estimate of the Young's modulus E obtained from the Monte Carlo simulation of the hydrostatic and hydrodynamic bulge tests; $q = 80$ mL/min and $\lambda = 2$. $\bar{E}$ is the mean, and ς_E is the standard deviation.

Bulge Test	$\bar{E}$ (MPa)	ς_E (MPa)	$\varsigma_E/\bar{E}$	Kendall's τ
Hydrostatic	1.61	0.14	0.087	-0.99
Hydrodynamic	1.57	0.07	0.045	1.0

3.6 Conclusion

In this chapter, we proposed a hydrodynamic bulge testing technique for soft materials characterization problems relevant to design of microfluidic systems and devices. Specifically, we derived a theory of the fluid–structure interaction (FSI) between a pre-stressed linearly elastic plate with finite thickness and a viscous fluid flow underneath it. The flow rate–pressure drop relationship for the case when the elastic plate is clamped as the top

wall of a rectangular microchannel conveying a "slow" viscous Newtonian fluid flow (low Reynolds number), was obtained in the form of Eq. (3.61). Then, we showed that this relationship can be inverted numerically to characterize the material properties of the elastic plate, specifically its Young's modulus E, by only measuring the total pressure drop across its length. We argued that, in microfluidics, a measurement of the pressure drop is easier and/or more accurate than a measurement of the membrane deflection due to the (hydrodynamic) pressure of the flow underneath it.

We also carried out three-dimensional direct numerical simulations of fluid–structure interactions using the commercial computational engineering platform by ANSYS. These simulations did not require any of the assumptions used to derive the mathematical model. The deformation profile and pressure drop obtained from the simulations showed favorable agreement with the predictions of our model, thus validating it.

Overall, from the mechanics point of view, pre-stressing the membrane makes it appear "stiffer," thus its deformation (induced by either hydrodynamic or hydrostatic pressure) is smaller than a corresponding initially stress-free plate. To sustain the same flow rate in a microchannel with an initially pre-stressed top wall thus requires a larger pressure drop. These conclusions were drawn from the general displacement profile, Eq. (3.37), which we believe is a novel result because the expression accounts for the non-negligible thickness of the membrane ($t/w \nrightarrow 0$), while the current literature on bulge testing concerns thin-film membranes ($t/w \rightarrow 0$) [116, Eq. (8)].

Next, the simulations were used as "ground truth" (in lieu of experiments) to establish the predictive power of hydrodynamic bulge tests. Specifically, a region in the parameter space was identified and represented as Eq. (3.62). Through Fig. 3.6, this parameter space region of validity was quantified Eq. (3.64) was proposed as a guideline to the experimentalist for obtaining accurate results from the hydrodynamic bulge test. Furthermore, a sensitivity analysis, performed through Monte Carlo simulation, showed that the hydrodynamic bulge test's estimate is only slightly less precise than a hydrostatic bulge test, while allowing a greater degree of "control" over error propagation.

4. DEFORMABLE MICROTUBES: STATIC RESPONSE TO NON-NEWTONIAN FLOW

SUMMARY

A flow vessel with an elastic wall can deform significantly due to viscous fluid flow within it, even at vanishing Reynolds number (no fluid inertia). Deformation leads to an enhancement of throughput due to the change in cross-sectional area. The latter gives rise to a non-constant pressure gradient in the flow-wise direction and, hence, to a nonlinear flow rate–pressure drop relation (unlike the Hagen–Poiseuille law for a rigid tube). Many biofluids are non-Newtonian, and are well approximated by generalized Newtonian (say, power-law) rheological models. Consequently, we analyze the problem of steady low Reynolds number flow of a generalized Newtonian fluid through a slender elastic tube by coupling fluid lubrication theory to a structural problem posed in terms of Donnell shell theory. A perturbative approach (in the slenderness parameter) yields analytical solutions for both the flow and the deformation. Using matched asymptotics, we obtain a uniformly valid solution for the tube's radial displacement, which features both a boundary layer and a corner layer caused by localized bending near the clamped ends. In doing so, we obtain a "generalized Hagen–Poiseuille law" for soft microtubes. We benchmark the mathematical predictions against three-dimensional two-way coupled direct numerical simulations (DNS) of flow and deformation performed using the commercial computational engineering platform by ANSYS. The simulations show good agreement and establish the range of validity of the theory. Finally, we discuss the implications of the theory on the problem of the flow-induced deformation of a blood vessel, which is featured in some textbooks.

The material in this chapter has been submitted for publication as [V. Anand and I. C. Christov, "Revisiting steady viscous flow of a generalized Newtonian fluid through a slender elastic tube using shell theory"] [160]
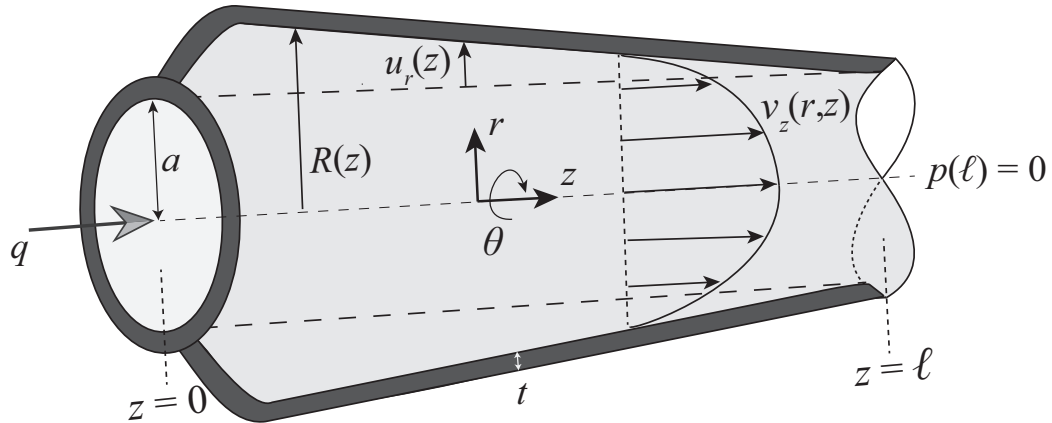
Fig. 4.1. Schematic of the slender and thin tube geometry in its deformed configuration. The notation for the flow and the deformation is also labeled.

4.1 Preliminaries

We consider an initially cylindrical flow conduit geometry. As shown in Fig. 4.1, the geometry of the tube is *slender*, i.e., its streamwise dimension is much larger than its cross-sectional dimension, and *shallow* (or, *thin*), i.e., its wall thickness is much smaller than its cross-sectional dimension. The cylindrical coordinate system has its origin at the center of the inlet of the tube but it is displaced in Fig. 4.1 for clarity. The wall of the tube has a finite thickness, and it is soft; hence, it deforms elastically due to the fluid flow within it. Specifically, the tube has an undeformed radius a, a constant length ℓ, and constant (within the classical shell theories to be discussed below) thickness t. The radial deformation of the tube is denoted by $u_r(z)$ so that the radius of the deformed tube is $R(z) = a + u_r(z)$. Axisymmetry ensures that the latter only depends on the streamwise coordinate z. The tube's wall is composed of a linearly elastic material with constant modulus of elasticity (Young's modulus) E and a constant Poisson ratio ν.

Fully-developed steady flow of a non-Newtonian fluid enters the tube across the inlet ($z = 0$ plane) at a constant flow rate q. The non-Newtonian behavior of the fluid is due to its shear-dependent viscosity. Our main objective is to determine the relation between the pressure drop Δp, across the length of the tube, and the imposed flow rate q. In other words,

we seek to derive, mathematically, the Hagen–Poiseuille law for steady non-Newtonian flow in a deformable tube. To this end, we simplify the fluid flow (§4.2) and structural mechanics (§4.3) problems independently in the appropriate asymptotic limit(s). Then, we solve the two sets of governing equations, which are coupled together by the hydrodynamic pressure (the normal forces exerted by the fluid), which act as a load on the structure.

4.2   Fluid mechanics problem

The assumptions made pertaining to the fluid flow problem are:

1. Steady flow: $\partial(\,\cdot\,)/\partial t = 0$.

2. Axisymmetric flow without swirl: $\partial(\,\cdot\,)/\partial\theta = 0$ and $v_\theta = 0$.

3. Slender tube: $\ell \gg a \iff \lambda := a/\ell \ll 1$.

Assumption 3 is key to our analysis. Davis [124] highlights the "importance of being thin" in making analytical progress on nonlinear fluid mechanics problems.

First, we determine the kinematics of the flow. In the cylindrical coordinates labeled in Fig. 4.1, and under assumption 2 above, the fluid's equation of continuity (conservation of mass) is

$$\frac{1}{r}\frac{\partial}{\partial r}(rv_r) + \frac{\partial v_z}{\partial z} = 0. \tag{4.1}$$

Let us now introduce the following dimensionless variables:

$$\bar{r} = r/a, \qquad \bar{z} = z/\ell, \qquad \bar{v}_{\bar{r}} = v_r/\mathcal{V}_r, \qquad \bar{v}_{\bar{z}} = v_z/\mathcal{V}_z, \qquad \bar{p} = p/\mathcal{P}_c, \tag{4.2}$$

Here, $\mathcal{V}_z$ and $\mathcal{V}_r$ are characteristic velocity scales in the axial and radial directions respectively, while $\mathcal{P}_c$ is the characteristic pressure (stress) scale: e.g., the full pressure drop in pressure-controlled scenarios or the viscous pressure scale in flow-rate-controlled situations. $\mathcal{P}_c$ can be determined from the velocity scale [see Eq. (4.17) below]. Introducing the dimensionless variables from Eq. (4.2), Eq. (4.1) becomes

$$\frac{\mathcal{V}_r}{a}\frac{1}{\bar{r}}\frac{\partial}{\partial\bar{r}}(\bar{r}\bar{v}_{\bar{r}}) + \frac{\mathcal{V}_z}{\ell}\frac{\partial\bar{v}_{\bar{z}}}{\partial\bar{z}} = 0. \tag{4.3}$$

Balancing all terms in Eq. (4.3) yields the characteristic radial velocity scale: $\mathcal{V}_r \equiv \lambda \mathcal{V}_z$. Consequently, to the leading order in λ, the velocity field is *unidirectional*: $\bar{\boldsymbol{v}} = \bar{v}_{\bar{z}}(\bar{r})\hat{\boldsymbol{k}}$, where $\hat{\boldsymbol{k}}$ is the unit normal vector in the z-direction. Below, we show that, due to FSI, the unidirectional profile "picks up" a weak $\bar{z}$ dependence as well, which is "allowed" under the *lubrication approximation* [3].

Next, we consider the dynamics of the flow field. Since we are dealing with flow at the microscale, the Reynolds number Re (to be properly defined below upon introducing the fluid's rheology) is assumed to be small (i.e., $Re \ll 1$), and the lubrication approximation applies. Consequently, inertial forces in fluid are negligible in comparison to pressure and viscous forces, and we begin our analysis with the following simplified equations express-ing the momentum conservation in the (radial) r- and (axial) z-directions [129]:

$$0 = \frac{1}{r}\frac{\partial}{\partial r}(r\tau_{rr}) + \frac{\partial \tau_{zr}}{\partial z} - \frac{\partial p}{\partial r}, \tag{4.4a}$$

$$0 = \frac{1}{r}\frac{\partial}{\partial r}(r\tau_{rz}) + \frac{\partial \tau_{zz}}{\partial z} - \frac{\partial p}{\partial z}. \tag{4.4b}$$

Here, $\underline{\underline{\tau}}$ is the fluid's shear stress tensor, and p is the hydrodynamic pressure. We have already made use of the assumptions of axisymmetry in Eqs. (4.4), by neglecting the cir-cumferential stress and any derivatives with respect to θ. The same assumption also leads to the momentum equation in θ direction being reduced to zero *identically*.

Now, we need to express the rate-of-strain tensor $\underline{\underline{\dot{\gamma}}}$ in terms of the velocity components. For axisymmetric flow with no swirl, the only non-vanishing rate-of-strain components are

$$\dot{\gamma}_{rr} = \frac{\partial v_r}{\partial r} \qquad\qquad = \frac{\lambda \mathcal{V}_z}{a}\frac{\partial \bar{v}_r}{\partial \bar{r}}, \tag{4.5a}$$

$$\dot{\gamma}_{zz} = 2\frac{\partial v_z}{\partial z} \qquad\qquad = 2\frac{\lambda \mathcal{V}_z}{a}\frac{\partial \bar{v}_{\bar{z}}}{\partial \bar{z}}, \tag{4.5b}$$

$$\dot{\gamma}_{rz} = \dot{\gamma}_{zr} = \frac{\partial v_r}{\partial z} + \frac{\partial v_z}{\partial r} = \frac{\lambda^2 \mathcal{V}_z}{a}\frac{\partial \bar{v}_r}{\partial \bar{z}} + \frac{\mathcal{V}_z}{a}\frac{\partial \bar{v}_{\bar{z}}}{\partial \bar{r}}, \tag{4.5c}$$

having used the dimensionless variables from Eq. (4.2). Clearly, $(a/\mathcal{V}_z)\dot{\gamma}_{zz} = O(\lambda)$ and $(a/\mathcal{V}_z)\dot{\gamma}_{rr} = O(\lambda)$, while $(a/\mathcal{V}_z)\dot{\gamma}_{rz} = (a/\mathcal{V}_z)\dot{\gamma}_{zr}$ have one $O(1)$ term. Therefore, to the leading order in λ, the rate-of-strain tensor has two components, consistent with the

kinematic reduction to unidirectional flow; v_r and its derivatives, as well as $\partial v_z / \partial z$, are negligible.

Next, we move onto the constitutive equations for the fluid under consideration. Keeping biofluid mechanics applications in mind, we consider the fluid to be non-Newtonian [161]. Blood is known to exhibit shear-dependent viscosity at steady state, and it is often modeled as a *Casson fluid*, which captures both a yields stress and a shear-dependent viscosity [57, Ch. 3]. However, detecting the yield stress (at zero shear rate) in a suspension of blood cells is extremely difficult (perhaps even "controversial" [162]), and some experiments [127] show it to be vanishing; see also [57, p. 65]. Therefore, we consider the special case of zero yield stress, which reduces the Casson fluid model to the *power-law fluid* (also known as Ostwald–de Waele [128]) model, which connects the stress tensor $\underline{\underline{\tau}}$ to the rate-of-strain tensor $\underline{\underline{\dot{\gamma}}}$ as

$$\underline{\underline{\tau}} = \eta \underline{\underline{\dot{\gamma}}}. \tag{4.6}$$

For an incompressible shear flow, the apparent viscosity η is a function of the invariants of the rate-of-strain tensor [129]. Specifically, it depends solely on the second invariant $\frac{1}{2} II$ (see, e.g., [163, §8.8]):

$$\eta(\underline{\underline{\dot{\gamma}}}) = m \left| \frac{1}{2} II \right|^{(n-1)/2}, \tag{4.7}$$

where m is the *consistency factor* (a non-negative quantity), and n is the *power-law index* (also a non-negative quantity). Under the condition of axisymmetry, the second invariant takes the form

$$
\begin{aligned}
\frac{1}{2} II &= 2 \left(\frac{\partial v_r}{\partial r} \right)^2 + \left(\frac{\partial v_z}{\partial z} \right)^2 + \left(\frac{\partial v_r}{\partial z} + \frac{\partial v_z}{\partial r} \right)^2 \\
&= 2 \left(\frac{\lambda \mathcal{V}_z}{a} \right)^2 \left[\left(\frac{\partial \bar{v}_{\bar{r}}}{\partial \bar{r}} \right)^2 + \left(\frac{\partial \bar{v}_{\bar{z}}}{\partial \bar{z}} \right)^2 \right] + \left(\frac{\mathcal{V}_z}{a} \right)^2 \left(\lambda^2 \frac{\partial \bar{v}_{\bar{r}}}{\partial \bar{z}} + \frac{\partial \bar{v}_{\bar{z}}}{\partial \bar{r}} \right)^2 \\
&= \left(\frac{\mathcal{V}_z}{a} \right)^2 \left(\frac{\partial \bar{v}_{\bar{z}}}{\partial \bar{r}} \right)^2 + O(\lambda^2).
\end{aligned}
\tag{4.8}
$$

Now, the shear stress components are

$$\tau_{rz} = \tau_{zr} = \eta(\underline{\underline{\dot{\gamma}}}) \left(\frac{\partial v_z}{\partial r} + \frac{\partial v_r}{\partial z} \right). \tag{4.9}$$

Introducing $\mathcal{T}_c$ as the scale for the shear stress, Eq. (4.9) can be written in dimensionless form:

$$
\begin{aligned}
\tau_{rz} = \mathcal{T}_c \bar{\tau}_{\bar{r}\bar{z}} = \tau_{zr} = \mathcal{T}_c \bar{\tau}_{\bar{z}\bar{r}} &= m \left| \frac{1}{2} II \right|^{(n-1)/2} \left(\frac{\lambda^2 \mathcal{V}_z}{a} \frac{\partial \bar{v}_r}{\partial \bar{z}} + \frac{\mathcal{V}_z}{a} \frac{\partial \bar{v}_{\bar{z}}}{\partial \bar{r}} \right) \\
&= m \left(\frac{\mathcal{V}_z}{a} \right)^n \left| \frac{\partial \bar{v}_{\bar{z}}}{\partial \bar{r}} \right|^{n-1} \frac{\partial \bar{v}_{\bar{z}}}{\partial \bar{r}} + O(\lambda^{n-1}),
\end{aligned}
\tag{4.10}
$$

which suggest the choice of stress scale:

$$
\mathcal{T}_c = m \left(\frac{\mathcal{V}_z}{a} \right)^n .
\tag{4.11}
$$

Similarly, to the leading order in λ, the normal stress components are

$$
\bar{\tau}_{\bar{z}\bar{z}} = \lambda \mathcal{T}_c \left| \frac{\partial \bar{v}_{\bar{z}}}{\partial \bar{r}} \right|^{n-1} \frac{\partial \bar{v}_{\bar{z}}}{\partial \bar{z}},
\tag{4.12a}
$$

$$
\bar{\tau}_{\bar{r}\bar{r}} = \lambda \mathcal{T}_c \left| \frac{\partial \bar{v}_{\bar{z}}}{\partial \bar{r}} \right|^{n-1} \frac{\partial \bar{v}_{\bar{r}}}{\partial \bar{r}},
\tag{4.12b}
$$

which are of order $O(\lambda)$ and, clearly, negligible compared to the shear stress components in Eq. (4.10).

Next, we nondimensionalize the z-momentum equation (4.4b):

$$
0 = \mathcal{T}_c \frac{1}{\bar{r}} \frac{\partial}{\partial \bar{r}} (\bar{r} \bar{\tau}_{\bar{r}\bar{z}}) + \lambda^2 \mathcal{T}_c \frac{\partial \bar{\tau}_{\bar{z}\bar{z}}}{\partial \bar{z}} - \lambda \mathcal{P}_c \frac{\partial \bar{p}}{\partial \bar{z}},
\tag{4.13}
$$

and observe that this equation has a leading-order balance only if

$$
\mathcal{P}_c = \frac{\mathcal{T}_c}{\lambda},
\tag{4.14}
$$

i.e., $\mathcal{P}_c \gg \mathcal{T}_c$, as expected under lubrication theory [123, Ch. 21]. It follows that the gradient of the normal stress is negligible to the leading order in $\lambda \ll 1$.

Next, we employ all the information deduced so far to render the radial momentum equation (4.4a) dimensionless:

$$
0 = \lambda^2 \mathcal{T}_c \frac{1}{\bar{r}} \frac{\partial}{\partial \bar{r}} (\bar{r} \bar{\tau}_{\bar{r}\bar{r}}) + \lambda^2 \mathcal{T}_c \frac{\partial \bar{\tau}_{\bar{r}\bar{z}}}{\partial \bar{z}} - \mathcal{T}_c \frac{\partial \bar{p}}{\partial \bar{r}},
\tag{4.15}
$$

where we have used Eq. (4.14) to replace $\mathcal{P}_c$ with $\mathcal{T}_c / \lambda$. No undetermined scales remain to attempt to balance the last equation; to the leading order in λ, it simply becomes

$$
0 = \frac{\partial \bar{p}}{\partial \bar{r}}.
\tag{4.16}
$$

Therefore, the pressure is a function of neither $\bar{r}$, from the last equation, nor θ, by assumption 2, hence it is at most a function of $\bar{z}$, i.e., $\bar{p} = \bar{p}(\bar{z})$. From Eqs. (4.14) and (4.11), we can re-express $\mathcal{P}_c$ in terms of $\mathcal{V}_z$ as

$$\mathcal{P}_c = \frac{m\ell\mathcal{V}_z^n}{a^{n+1}}. \tag{4.17}$$

In a flow-rate-controlled experiment/simulation, we can choose a velocity scale $\mathcal{V}_z = q/(\pi a^2)$ based on the constant inlet flow rate q, then $\mathcal{P}_c = m\ell q^n/(a^{3n+1}\pi^n)$.

For axisymmetric flow, we expect that the axial velocity will attain its maximum along the centerline ($r = 0$), decreasing with the radius until it reaches zero at the tube wall (due to no slip) in this steady flow. Consequently, the velocity gradient is negative and $\left|\partial\bar{v}_{\bar{z}}/\partial\bar{r}\right| = -\partial\bar{v}_{\bar{z}}/\partial\bar{r}$. Then, Eq. (4.10) becomes

$$\bar{\tau}_{\bar{r}\bar{z}} = -\left(-\frac{\partial\bar{v}_{\bar{z}}}{\partial\bar{r}}\right)^n. \tag{4.18}$$

Substituting the latter expression for into the z-momentum equation (4.13), having neglected the normal stresses of $O(\lambda^2)$, yields

$$\frac{1}{\bar{r}}\frac{\partial}{\partial\bar{r}}\left[\bar{r}\left(-\frac{\partial\bar{v}_z}{\partial\bar{r}}\right)^n\right] = -\frac{d\bar{p}}{d\bar{z}}. \tag{4.19}$$

Next, substituting Eq. (4.17) into Eq. (4.19) and integrating the resulting equation with respect to $\bar{r}$ and requiring that $\bar{v}_{\bar{z}}$ be finite along the centerline, as well as enforcing no slip along the tube's inner wall, $\bar{v}_{\bar{z}}(\bar{r} = \bar{R}) = 0$, yields

$$\bar{v}_{\bar{z}} = \left(-\frac{1}{2}\frac{d\bar{p}}{d\bar{z}}\right)^{1/n}\left(\frac{\bar{R}^{1+1/n} - \bar{r}^{1+1/n}}{1 + 1/n}\right), \tag{4.20}$$

where $\bar{R} = R/a$ is the dimensionless deformed tube radius. Note that $\bar{R}$ is not necessarily unity because we allow the tube to deform due to FSI, as discussed in the next section. As a result, while $\bar{p}$ is at most a function of $\bar{z}$, $\bar{v}_{\bar{z}}$ can depend upon both $\bar{r}$ and $\bar{z}$.

4.3 Structural mechanics problem

In §4.2, the momentum conservation equations for a power-law fluid were reduced to unidirectional flow. They explicitly depend only on the radial coordinate, up to the leading

order under the assumptions of axisymmetry and the lubrication approximation. In a similar manner, we now model the structural mechanics of the tube. To make the problem tractable analytically, the equations stating the equilibrium of forces in the solid are simplified under the following assumptions:

1. The tube is thin; its thickness is negligible compared to its radius: $t \ll a$.

2. The tube is slender; its radius is small compared to its length: $a \ll \ell$.

3. The material from which the tube is composed is isotropic and linearly elastic, with elasticity (Young's) modulus E and Poisson ratio ν, so the relationship between stress and strain is linear.

4. The strains are small, so the relationship between strain and displacement is linear.

5. The characteristic radial deformation $\mathcal{U}_c$ is small compared to the (smallest) characteristic dimension of the tube: $\mathcal{U}_c \ll t$.

Here, assumptions 3 and 4 ensure that the relation between stress and displacement is linear. Thus, the corresponding theory developed in this chapter pertains to what we shall term *linear* FSI. The ramifications of assumptions 1 and 2 will be discussed in the context of shell theories. Assumption 5 implies our theory is a *small-deformation* FSI theory, thus we may work the problem in Eulerian coordinates. In general, soft elastic structures (e.g., blood vessels) can exhibit a nonlinear material (hyperelastic) response, as well as viscoelasticity and even anisotropy (see, e.g., [57, Ch. 8 and 9]). Therefore, the linear FSI theory developed in the present work, under the above five assumptions, must be understood as the simplest mathematical model with the key FSI features.

A shell theory models the dynamics of a 3D entity in two dimensions, thus it by definition an approximate theory. Approximations are introduced in every facet of shell theory: in the strain–displacement relation (*kinematics*), in the stress equilibrium relation (*statics*), and in the stress–strain relation (*constitutive*). There are many shell theories, of varying degree of approximation, as discussed in the classic monographs by Kraus [164],

Flugge [165], and Timoshenko and Woinowsky-Krieger [132]. We focus only on the "simplest" shell theories capable of describing the FSI problem posed above.

4.3.1 Membrane theory

The thinness assumption ($t \ll a$) allows us to analyze the tube using membrane theory for sufficiently small t/a. Membrane theory of shells pertains to structures that sustain only tension (in the axial and/or in the circumferential directions) but cannot support bending or twisting moments [165, Ch. 3]. Furthermore, the radial stress developed inside the structure is negligible, at the leading order in t/a, compared to the hoop and axial stress.

Owing to the slenderness of the geometry, i.e., $\lambda = a/\ell \ll 1$, we start our exposition of the membrane theory by assuming a state of plane strain. In other words, $\varepsilon_{zz} = \partial u_z/\partial z = 0$. Next, since the edges are clamped, we conclude that $u_z = 0$ along the length of the tube. Indeed, most tubes in physiology, like arteries, tracheoles, urethra are longitudinally constrained *in situ* [87,166]. Note that neglecting the axial displacement is a fairly common assumption in the hemodynamics literature [167–170]; for a more rigorous derivation, see [171].

From the constitutive equation of linear elasticity [see, e.g., Eqs. (3.17) and (3.18a) in [165]], we then have:

$$\varepsilon_{zz} = \frac{1}{E}(\sigma_{zz} - \nu\sigma_{\theta\theta}) = 0 \qquad \Rightarrow \qquad \sigma_{zz} = \nu\sigma_{\theta\theta}, \tag{4.21}$$

where $\sigma_{\theta\theta}$ is the hoop stress, while σ_{zz} and ε_{zz} are the axial stress and strain, respectively. To find an expression for $\sigma_{\theta\theta}$, we appeal to the equation of static equilibrium in the radial direction:

$$N_\theta = ap, \tag{4.22}$$

where N_θ is the stress resultant in the azimuthal direction of the tube. Here, the hydrodynamic pressure $p(z)$ provides the load, and we have shown in §4.2 that p is, at most, a function of z. Next, membrane theory assumes that due to the cylinder being thin, the stress

across the thickness is uniform. Therefore, $\sigma_{\theta\theta}$ is simply the corresponding stress resultant divided by the cylinder's thickness t:

$$\sigma_{\theta\theta} = \frac{N_\theta}{t} = \left(\frac{a}{t}\right) p. \tag{4.23}$$

Finally, under the assumption of axisymmetric deformation [165, Eq. (3.18b)] and Eqs. (4.21) and (4.23), we obtain

$$u_r(z) = \varepsilon_{\theta\theta} a = \frac{1}{E}(\sigma_{\theta\theta} - \nu\sigma_{zz})a = (1 - \nu^2)\left(\frac{a^2}{Et}\right) p(z) \tag{4.24}$$

for the radial displacement. The most important conclusion to be drawn from the analysis in this subsection is that, under the membrane theory, the tube's radial displacement is simply proportional to the local hydrodynamic pressure, with the geometric and elasticity parameters setting the proportionality constant.

4.3.2   Donnell shell theory

From the several theories for thin shells of revolution based on the Love–Kirchhoff hypothesis [131], perhaps the earliest and most "popular" is Donnell's shell theory [172]. Donnell's shell theory is a straightforward extension of thin-plate theory to shells [164], which itself is an extension of Euler-beam theory to two dimensions. Furthermore, for the special case of axisymmetric loads with zero curvature, Donnell's shell theory reduces identically to the Kirchhoff–Love thin-plate theory [164], which we have successfully employed to analyze microchannel FSIs [37, 60]. Improving upon the membrane theory of §4.3.1, Donnell's shell theory takes into account bending moments and the variation of the stresses across the shell's thickness [164, 165].

To be consistent with the membrane theory of §4.3.1, we again neglect the axial displacement ($u_z \equiv 0$). Then, following Dym [173, Ch. V], the equation expressing the momentum balance (for axisymmetric deformation and loading) of a Donnell shell is

$$\frac{d^2 M_z}{dz^2} - \frac{N_\theta}{a} = -p(z). \tag{4.25}$$

Here, the bending moment M_z is expressed through the linear elastic law as

$$M_z = -K \frac{\mathrm{d}^2 u_r}{\mathrm{d}z^2}, \tag{4.26}$$

where $K = Et^3/[12(1 - v^2)]$ is the *bending (flexural) rigidity* of the shell. The stress resultant in the circumferential direction is

$$N_\theta = D \left(\frac{u_r}{a} \right), \tag{4.27}$$

where $D = Et/(1 - v^2)$ is the *extensional rigidity* of the shell. Then, Eq. (4.25), when written in terms of the displacement using Eqs. (4.26) and (4.27), and simplified by substituting the expressions for D and K, becomes an ordinary differential equation (ODE) for the radial deflection $u_r(z)$ forced by the hydrodynamic pressure $p(z)$:

$$\frac{Et^3}{12(1 - v^2)} \left(\frac{\mathrm{d}^4 u_r}{\mathrm{d}z^4} + \frac{12}{a^2 t^2} u_r \right) = p. \tag{4.28}$$

To understand the dominant balance(s) in Eq. (4.28), we introduce dimensionless variables, some of which are restated from Eq. (4.2), as follows:

$$\bar{z} = z/\ell, \qquad \bar{u}_{\bar{r}} = u_r/\mathcal{U}_c, \qquad \bar{p} = p/\mathcal{P}_c. \tag{4.29}$$

The characteristic scale for the radial deflection of the tube, $\mathcal{U}_c$, is to be determined self-consistently as part of this analysis. Substituting the dimensionless variables from Eq. (4.29) into Eq. (4.28) yields

$$\left(\frac{t}{a} \right)^2 \left(\frac{a}{\ell} \right)^4 \frac{\mathrm{d}^4 \bar{u}_{\bar{r}}}{\mathrm{d}\bar{z}^4} + 12 \bar{u}_{\bar{r}} = \frac{12(1 - v^2) a^2 \mathcal{P}_c}{Et \, \mathcal{U}_c} \bar{p}. \tag{4.30}$$

For a thin and slender shell we can neglect, in an order of magnitude sense to the leading order in t/a and a/ℓ, the first term on the left-hand side of Eq. (4.30) to obtain:

$$\bar{u}_{\bar{r}} = \frac{a^2 \mathcal{P}_c}{Et \, \mathcal{U}_c} (1 - v^2) \bar{p}. \tag{4.31}$$

Since Eq. (4.31) represents a leading-order balance, we are free to choose the deformation scale in terms of the pressure scale as

$$\mathcal{U}_c = \frac{a^2 \mathcal{P}_c}{Et}. \tag{4.32}$$

Hence, the deformed tube radius is

$$\bar{R}(\bar{z}) \equiv \frac{a + u_r(z)}{a} = 1 + \beta \bar{u}_{\bar{r}}(\bar{z}), \tag{4.33}$$

where $\beta := \mathcal{U}_c/a$ is a dimensionless parameter that "controls" the fluid–structure interaction. It is a measure of the magnitude of the characteristic radial deformation $\mathcal{U}_c$ compared to the undeformed radius a. A larger value of β corresponds to "stronger" fluid–structure coupling and, thus, a larger deformation.

Thus, at the leading order in t/a and a/ℓ, Eq. (4.30) yields a simple deformation–pressure relation:

$$\bar{u}_{\bar{r}}(\bar{z}) = (1 - \nu^2)\bar{p}(\bar{z}). \tag{4.34}$$

Note that Eq. (4.34) is identically the dimensionless version of our membrane theory result in Eq. (4.24). Also, in obtaining Eq. (4.34), we have *singularly perturbed* Eq. (4.30), a point that we revisit in §4.4.3.

Remark 4.3.1 *Mathematical analogues to Eq. (4.28) exist in at least two different domains of structural mechanics. First is the governing equation of bending of a beam placed on an elastic foundation due to Winkler [174] (see also the book [175] and recent review article [176]). The force generated by the elastic foundation is directly proportional to the local displacement of the beam and this leads to the linear term in Eq. (4.28). The fourth-order derivative term is due to the beam's bending resistance. Second, is the governing equation of the quasi-static planar spreading of a fluid under an elastic beam (ignoring tension) driven by gravity—a problem that arises in geophysical fluid dynamics; see [29, Eq. (4.2)] and [177, 178]. In this example, the fourth-order derivative term is again due to bending resistance, but the term that is linear in the displacement arises from the hydrostatic pressure due to gravity.*

Remark 4.3.2 *To the leading order in t/a and a/ℓ, bending in Donnell's shell theory is negligible and this theory leads to the same result as the membrane theory, namely Eq. (4.24) [and its dimensionless counterpart, Eq. (4.34)], which dictates that the radial*

deflection of the tube is directly proportional to the pressure at a given flow-wise cross-section. This result is also in agreement with the results of Elbaz and Gat [63, 64], taking into account, of course, the different boundary conditions employed therein.

4.4 Coupling the fluid mechanics and structural problems: Flow rate–pressure drop relation

We now turn to the main task, which is evaluating the pressure drop and thus generalizing the Hagen–Poiseuille law to deformable tubes. The flow rate in the tube is by definition

$$q = \int_0^{2\pi} \int_0^{R(z)} v_z(r, z)\, r\, \mathrm{d}r\, \mathrm{d}\theta = \mathcal{V}_z 2\pi a^2 \int_0^{\bar{R}(\bar{z})} \bar{v}_{\bar{z}}(\bar{r}, \bar{z})\, \bar{r}\, \mathrm{d}\bar{r}, \tag{4.35}$$

where the second equality follows from performing the (trivial) azimuthal integration and introducing the dimensionless variables from Eq. (4.2). Now, substituting the expression for $\bar{v}_{\bar{z}}$ from Eq. (4.20) into Eq. (4.35) yields:

$$\frac{q}{\mathcal{V}_z \pi a^2} = \left(-\frac{1}{2} \frac{\mathrm{d}\bar{p}}{\mathrm{d}\bar{z}} \right)^{1/n} \frac{[\bar{R}(\bar{z})]^{3+1/n}}{3 + 1/n}. \tag{4.36}$$

In a steady incompressible flow, conservation of mass requires that the volumetric flow rate is a constant independent of z. Then, owing to our choice of axial velocity scale, $q/(\mathcal{V}_z \pi a^2) = 1$ [recall the discussion after Eq. (4.17)], and the above equation can be rewritten as:

$$\frac{\mathrm{d}\bar{p}}{\mathrm{d}\bar{z}} = -2[(3 + 1/n)]^n [\bar{R}(\bar{z})]^{-(3n+1)}. \tag{4.37}$$

This is an ODE for $\bar{p}(\bar{z})$, subject to an appropriate closure relation for $\bar{R}(\bar{z})$.

4.4.1 Rigid tube

First, for completeness and future reference, consider the case of $\bar{R} = 1$ (rigid tube of uniform radius). Equation (4.37) can be immediately integrated, subject to an outlet boundary condition [$\bar{p}(1) = 0$], to yield the usual linear pressure profile:

$$\bar{p}(\bar{z}) = 2[(3 + 1/n)]^n (1 - \bar{z}). \tag{4.38}$$

Since it is our convention that $\bar{p}(\bar{z} = 0) = \Delta\bar{p}$ is the full pressure drop across the length of the tube, then $\Delta\bar{p} = 2[(3 + 1/n)]^n$, which is the well-known Hagen–Poiseuille law for a power-law fluid [129].

4.4.2 Leading-order-in-thickness (membrane) theory

Next, inserting the relation $\bar{R} = 1 + (1 - v^2)\beta\bar{p}$ [having employed Eqs. (4.33) and (4.34)] into Eq. (4.37) yields:

$$\frac{d\bar{p}}{d\bar{z}} = -2[(3 + 1/n)]^n[1 + (1 - v^2)\beta\bar{p}]^{-(3n+1)}. \tag{4.39}$$

Separating variables and integrating subject to $\bar{p}(1) = 0$, we have:

$$\bar{p}(\bar{z}) = \frac{1}{(1 - v^2)\beta}\left\{\left[1 + 2(3n + 2)(1 - v^2)\beta[(3 + 1/n)]^n(1 - \bar{z})\right]^{1/(3n+2)} - 1\right\}. \tag{4.40}$$

Again, the full dimensionless pressure drop is obtained by evaluating Eq. (4.40) at $\bar{z} = 0$:

$$\Delta\bar{p} = \frac{1}{(1 - v^2)\beta}\left\{\left[1 + 2(3 + 1/n)^n(3n + 2)(1 - v^2)\beta\right]^{1/(3n+2)} - 1\right\}. \tag{4.41}$$

Notice that Eqs. (4.40) and (4.41) are explicit relations for $\bar{p}$ and $\Delta\bar{p}$, respectively, which is unlike the case of microchannels [37, 38, 60].

Remark 4.4.1 *Equation* (4.39)*, when written in dimensional form, can be inverted to yield the flow rate in terms of the pressure gradient:*

$$q = \varsigma(p)\left(-\frac{dp}{dz}\right)^{1/n}, \qquad \varsigma(p) := \frac{1}{3 + 1/n}\left(\frac{a}{2m}\right)^{1/n}\left[1 + (1 - v^2)\frac{a}{Et}p\right]^{3+1/n}. \tag{4.42}$$

This equation is, clearly, a generalization of the classic result of Rubinow and Keller [179] for steady low Re, Newtonian flow in a deformable tube. Importantly, we have self-consistently derived the function $\varsigma(p)$ that accounts for steady non-Newtonian FSI in a tube.

Remark 4.4.2 *The maximum radial displacement of the tube wall over its length is $\beta\bar{u}_{\bar{r}}(0)$ [recall Eq. (4.33)]. Using Eqs. (4.34) and (4.40), it can then computed to be*

$$\max_{0 \leq \bar{z} \leq 1}\beta\bar{u}_{\bar{r}}(\bar{z}) = \left\{1 + 2(3n + 2)(1 - v^2)\beta[(3 + 1/n)]^n\right\}^{1/(3n+2)} - 1. \tag{4.43}$$

Note that, once the solid and fluid properties (ν and n) are fixed, the maximum displacement is solely a function of the FSI parameter β.

Remark 4.4.3 *To perform the consistency check of recovering the rigid-tube pressure profile in Eq. (4.38) as the $\beta \to 0^+$ limit of the deformable-tube pressure profile in Eq. (4.40), we must realize that $\beta \to 0^+$ in Eq. (4.40) is a "0/0" limit. L'Hôpital's rule or a Taylor series in $\beta \ll 1$ easily shows that Eq. (4.38) is indeed the $\beta \to 0^+$ limit of Eq. (4.40).*

Remark 4.4.4 *For the special case of a Newtonian fluid (i.e., $n = 1$ and $m = \mu$), Eq. (4.40) reduces to:*

$$\bar{p}(\bar{z}) = \frac{1}{(1 - \nu^2)\beta} \left\{ \left[1 + 40(1 - \nu^2)\beta(1 - \bar{z}) \right]^{1/5} - 1 \right\}. \tag{4.44}$$

A Taylor series expansion in $\beta \ll 1$ of Eq. (4.44) yields the pressure distribution in Poiseuille flow: $\bar{p}(\bar{z}) = 8(1 - \bar{z}) + O(\beta)$.

4.4.3 Beyond leading-order-in-thickness theory

In §4.4.2, we obtained the flow rate–pressure drop relationship considering only the leading-order deformation profile as given by Eq. (4.34). In this subsection, we venture beyond the leading-order approximation by solving the "full" ODE, namely Eq. (4.30) for the deformation under Donnell's shell theory. Equation (4.30) is coupled to Eq. (4.37), which relates the pressure gradient and the tube's radial deformation. Taking $\mathrm{d}/\mathrm{d}\bar{z}$ of Eq. (4.30), eliminating $\mathrm{d}\bar{p}/\mathrm{d}\bar{z}$ using Eq. (4.37), substituting $\bar{R}$ and $\mathcal{U}_c$ from Eqs. (4.33) and (4.32), respectively, we obtain a single *nonlinear fifth-order* ODE in the deformation:

$$\left(1 + \beta \bar{u}_{\bar{r}} \right)^{3n+1} \left[\underbrace{\left(\frac{t}{a} \right)^2 \left(\frac{a}{\ell} \right)^4 \frac{\mathrm{d}^5 \bar{u}_{\bar{r}}}{\mathrm{d}\bar{z}^5}}_{\text{bending}} + \underbrace{12 \frac{\mathrm{d}\bar{u}_{\bar{r}}}{\mathrm{d}\bar{z}}}_{\text{stretching}} \right] = \underbrace{-24(1 - \nu^2)^2 \left[(3 + 1/n) \right]^n}_{\text{loading}}. \tag{4.45}$$

The ODE (4.45) is subject to the following boundary conditions expressing clamping of the shell at the inlet and outlet planes [Eqs. (4.46a) and (4.46b), respectively] and zero gauge pressure at the outlet [Eq. (4.46c)]:

$$\bar{u}_{\bar{r}}|_{\bar{z}=0} = \left. \frac{\mathrm{d}\bar{u}_{\bar{r}}}{\mathrm{d}\bar{z}} \right|_{\bar{z}=0} = 0, \tag{4.46a}$$

$$\bar{u}_{\bar{r}}|_{\bar{z}=1} = \left.\frac{\mathrm{d}\bar{u}_{\bar{r}}}{\mathrm{d}\bar{z}}\right|_{\bar{z}=1} = 0, \tag{4.46b}$$

$$\left.\frac{\mathrm{d}^4\bar{u}_{\bar{r}}}{\mathrm{d}\bar{z}^4}\right|_{\bar{z}=1} = 0. \tag{4.46c}$$

Equations (4.45) and (4.46) represent a nonlinear *two-point* (TP) *boundary value problem* (BVP) [180], the solution of which fully characterizes the physics of steady FSI in an elastic tube conveying a non-Newtonian fluid.

As alluded to in §4.3.2, for a slender ($a \ll \ell$) and thin ($t \ll a$) structure, Eq. (4.45) becomes an example of a *singular perturbation problem* in the limit of vanishing t/a and a/ℓ. Physically, "boundary layers" develop near the inlet and outlet of the tube, where the bending due to clamping becomes significant, as opposed to the rest of the tube where stretching dominates. A similar story unfolds for gravity-driven spreading of a viscous fluid under an elastic beam [178]: an elasto-gravity length scale divides the domain into an inner region, in which pressure is hydrostatic and due to gravity, and a peripheral region, in which bending is also important.

As a singular perturbation problem, Eq. (4.45) is now amenable to treatment via *matched asymptotics* [181, Ch. 2]. First, we introduce a dimensionless small parameter $\epsilon = \sqrt{ta/\ell^2}$, such that $\epsilon \ll 1$, then Eq. (4.45) can be rewritten as:

$$\left(1 + \beta\bar{u}_{\bar{r}}\right)^{3n+1}\left(\epsilon^4\frac{\mathrm{d}^5\bar{u}_{\bar{r}}}{\mathrm{d}\bar{z}^5} + 12\frac{\mathrm{d}\bar{u}_{\bar{r}}}{\mathrm{d}\bar{z}}\right) = -24(1 - \nu^2)^2[(3 + 1/n)]^n. \tag{4.47}$$

As is standard, we first let $\epsilon \to 0^+$, thus singularly perturbing the ODE, and obtain the governing equation for the solution in the *outer region*:

$$\left(1 + \beta\bar{u}_{\bar{r}}\right)^{3n+1}\frac{\mathrm{d}\bar{u}_{\bar{r}}}{\mathrm{d}\bar{z}} = -2(1 - \nu^2)^2[(3 + 1/n)]^n. \tag{4.48}$$

The outer solution must "respect" the first part of the clamping condition at $\bar{z} = 1$, i.e., $\bar{u}_{\bar{r}}|_{\bar{z}=1} = 0$ from Eq. (4.46b). Then, the solution to the ODE (4.48) is

$$\bar{u}_{\bar{r}}(\bar{z}) = \frac{1}{\beta}\left(\left\{1 + 2\beta(3n + 2)(1 - \nu^2)^2[(3 + 1/n)]^n(1 - \bar{z})\right\}^{1/(3n+2)} - 1\right). \tag{4.49}$$

Note that Eq. (4.49) can also be obtained by combining Eqs. (4.34) and (4.40) from the membrane theory, showing the consistency of our two structural mechanics models.

To satisfy the clamped boundary condition at $\bar{z} = 0$, i.e., Eq. (4.46a), we must introduce a *boundary layer* near $\bar{z} = 0$ wherein the highest-order derivative in Eq. (4.47) is dominant and is retained. Then, an inner solution can be obtained. To this end, we introduce a scaled spatial coordinate ζ such that for $\bar{z} \ll 1$, $\zeta = O(1)$. A straightforward balancing argument leads us to define $\zeta = \bar{z}/\epsilon$. Then, the nonlinear ODE (4.47) becomes

$$\frac{\mathrm{d}^5\bar{u}_{\bar{r}}}{\mathrm{d}\zeta^5} + 12\frac{\mathrm{d}\bar{u}_{\bar{r}}}{\mathrm{d}\zeta} = -\epsilon \left\{ \frac{24(1 - v^2)^2[(3 + 1/n)]^n}{\left(1 + \beta\bar{u}_{\bar{r}}\right)^{3n+1}} \right\}. \tag{4.50}$$

At the leading order in $\epsilon \ll 1$, we have

$$\frac{\mathrm{d}^5\bar{u}_{\bar{r}}}{\mathrm{d}\zeta^5} + 12\frac{\mathrm{d}\bar{u}_{\bar{r}}}{\mathrm{d}\zeta} = 0 \tag{4.51}$$

subject to the following boundary conditions:

$$\bar{u}_{\bar{r}}|_{\zeta=0} = \left.\frac{\mathrm{d}\bar{u}_{\bar{r}}}{\mathrm{d}\zeta}\right|_{\zeta=0} = 0, \tag{4.52a}$$

$$\bar{u}_{\bar{r}}|_{\zeta\to\infty} = \bar{u}_{\bar{r}}^{\text{outer}}\big|_{\bar{z}=0}, \tag{4.52b}$$

where $\bar{u}_{\bar{r}}^{\text{outer}}$ denotes the outer solution from Eq. (4.49). Here, the first two boundary conditions (at $\zeta = 0$) are due to clamping, while the remaining boundary condition (as $\zeta \to \infty$) is necessary to *match* the inner solution to the outer solution.

The general solution to Eq. (4.51) that decays as $\zeta \to \infty$ is

$$\bar{u}_{\bar{r}}(\zeta) = \mathrm{e}^{-\zeta\sqrt[4]{3}}\left[\tilde{C}_2 \sin\left(\zeta\sqrt[4]{3}\right) + \tilde{C}_4 \cos\left(\zeta\sqrt[4]{3}\right)\right] + C_0, \tag{4.53}$$

Now, we apply the boundary condition $\bar{u}_{\bar{r}}|_{\zeta=0} = 0$ to obtain $\tilde{C}_4 = -C_0$. Next, we use the boundary condition $(\mathrm{d}\bar{u}_{\bar{r}}/\mathrm{d}\zeta)|_{\zeta=0} = 0$ to find that $\tilde{C}_2 = \tilde{C}_4$. Finally, from the matching condition in Eq. (4.52b), we find

$$\tilde{C}_4 = \frac{1}{\beta}\left(1 - \left\{1 + 2\beta(3n + 2)(1 - v^2)^2[(3 + 1/n)]^n\right\}^{1/(3n+2)}\right). \tag{4.54}$$

Thus, the final expression for the inner solution in the boundary layer near $\bar{z} = 0$, to the leading order in ϵ, is

$$\bar{u}_{\bar{r}}(\zeta) \sim \tilde{C}_4\left\{\mathrm{e}^{-\zeta\sqrt[4]{3}}\left[\sin\left(\zeta\sqrt[4]{3}\right) + \cos\left(\zeta\sqrt[4]{3}\right)\right] - 1\right\}. \tag{4.55}$$

Next, another boundary layer must exist near the outlet at $\bar{z} = 1$ because, although $\bar{u}_{\bar{r}}^{\text{outer}} \to 0$ as $\bar{z} \to 1$, $d\bar{u}_{\bar{r}}^{\text{outer}}/d\bar{z} \not\to 0$ as $\bar{z} \to 1$, i.e., the clamping boundary condition is not fully satisfied. Thus, we expect both the dependent (deformation) and the independent (axial position) variables to be small in this layer. That is, we conjecture that the boundary layer at $\bar{z} = 1$ is actually a *corner layer* [181, §2.6] (sometimes termed a *derivative layer* [182, pp. 85–93]). Indeed, [29] also observed boundary and corner layers in the related problem of gravity-driven spreading of a viscous fluid under an elastic beam. The boundary layers in their study were the result of the need for "regularization" of the contact line at the advancing fluid front, accomplished by introducing a pre-wetting film. Unlike the present model, however, the differential equation in the inner and outer regions, along with the pertinent matching conditions, had to be solved numerically by [29], due to their complexity.

Now, introducing the rescalings $\zeta = (1 - \bar{z})/\epsilon^{\alpha_1}$ and $\hat{u}(\zeta) = \bar{u}_{\bar{r}}(\bar{z})/\epsilon^{\alpha_2}$ into Eq. (4.47), we can balance all three terms if and only if $\alpha_1 = \alpha_2 = 1$. The first and last terms can be balanced for any $4 - 5\alpha_1 + \alpha_2 = 0$ as long as $\alpha_1 < \alpha_2$ but then there is a non-uniqueness of the boundary layer thickness, so we discard this possibility. Thus, the nonlinear ODE (4.47) becomes

$$\frac{d^5\hat{u}}{d\zeta^5} + 12\frac{d\hat{u}}{d\zeta} = \frac{24(1 - \nu^2)^2[(3 + 1/n)]^n}{(1 + \beta\epsilon\hat{u})^{3n+1}}. \tag{4.56}$$

Expanding in $\epsilon \ll 1$, we have, at the leading order,

$$\frac{d^5\hat{u}}{d\zeta^5} + 12\frac{d\hat{u}}{d\zeta} = 12\mathcal{A}, \tag{4.57}$$

where for convenience we have defined $\mathcal{A} := 2(1 - \nu^2)^2[(3 + 1/n)]^n$. The ODE (4.57) must satisfy the remaining boundary conditions at $\bar{z} = 1$, from Eqs. (4.46b) and (4.46c), that are not satisfied by the outer solution, namely

$$\left.\frac{d\hat{u}}{d\zeta}\right|_{\zeta=0} = \left.\frac{d^4\hat{u}}{d\zeta^4}\right|_{\zeta=0} = 0, \tag{4.58a}$$

$$\hat{u}|_{\zeta\to\infty} = \left.\bar{u}_{\bar{r}}^{\text{outer}}\right|_{\bar{z}=1}. \tag{4.58b}$$

The general solution to Eq. (4.57) that decays as $\zeta \to \infty$ is

$$\hat{u}(\zeta) = e^{-\zeta\sqrt[4]{3}}\left[\tilde{C}_2 \sin\left(\zeta\sqrt[4]{3}\right) + \tilde{C}_4 \cos\left(\zeta\sqrt[4]{3}\right)\right] + C_0 + \mathcal{A}\zeta. \tag{4.59}$$

Now, we impose the boundary condition $(d\hat{u}/d\zeta)|_{\zeta=0} = 0$ to find that $\tilde{C}_2 = \tilde{C}_4 - \mathcal{A}/\sqrt[4]{3}$. Finally, the boundary condition $(d^4\hat{u}/d\zeta^4)|_{\zeta=0} = 0$ requires that $\tilde{C}_4 = 0$. Thus, we have obtained a fully-specified corner layer (inner) solution:

$$\hat{u}(\zeta) \sim \mathcal{A}\left[\zeta - \frac{e^{-\zeta\sqrt[4]{3}}}{\sqrt[4]{3}}\sin\left(\zeta\sqrt[4]{3}\right)\right] + C_0. \tag{4.60}$$

The inner solution in Eq. (4.60) must still be matched to the outer solution in Eq. (4.49), which goes to zero as $\bar{z} \to 1$. Thus, we immediately conclude that $C_0 = 0$, and the common part of the inner and outer solutions is $\mathcal{A}\zeta$ [as can be confirmed by a Taylor series expansion of Eq. (4.49) for $\bar{z} \approx 1$]. This argument can be made even more rigorous using an intermediate variable matching procedure as in [181, §2.6].

Finally, adding together Eqs. (4.49), (4.55) and (4.60) (expressed in the original variables) and subtracting their mutual common parts, we obtain a *composite solution* uniformly valid on $\bar{z} \in [0, 1]$, to the leading order in ϵ:

$$\begin{aligned}
\bar{u}_{\bar{r}}(\bar{z}) \sim{}& \frac{1}{\beta}\left(\left\{1 + 2\beta(3n+2)(1-v^2)^2[(3+1/n)]^n(1-\bar{z})\right\}^{1/(3n+2)} - 1\right) \\
&+ \tilde{C}_4 e^{-\sqrt[4]{3}\bar{z}/\epsilon}\left[\sin\left(\sqrt[4]{3}\,\frac{\bar{z}}{\epsilon}\right) + \cos\left(\sqrt[4]{3}\,\frac{\bar{z}}{\epsilon}\right)\right] \\
&- \epsilon\frac{2(1-v^2)^2[(3+1/n)]^n}{\sqrt[4]{3}}e^{-\sqrt[4]{3}(1-\bar{z})/\epsilon}\sin\left(\sqrt[4]{3}\frac{(1-\bar{z})}{\epsilon}\right), \quad (4.61)
\end{aligned}$$

where the constant $\tilde{C}_4$ is given in Eq. (4.54).

Remark 4.4.5 *Čanić and Mikelić [53] discussed the formation of deformation "boundary layers" in the context of viscous incompressible flow through a long elastic tube, as the aspect ratio $a/\ell \to 0^+$. Their approach was based on* a priori *estimates of the coupled PDEs. Here, we have actually constructed the boundary (and corner) layers explicitly through a matched asymptotic expansion, further showing that the relevant small parameter also involves the tube's thickness: $\epsilon = \sqrt{ta/\ell^2}$. Our result, then, is closer to some of the discussion in textbooks on shell theory, wherein the (dimensional) thickness of boundary layers (near the clamped ends of a Donnell shell subject to uniform internal pressure) is estimated to be $O(\sqrt{ta})$ (see [173, Ch. V]).*

4.5 Results and discussion

4.5.1 Deviations from the Hagen–Poiseuille law due to FSI

Our objective is to quantify the deviation from the Hagen–Poiseuille law caused by FSI in a tube. To this end, we plot the dimensionless pressure $\bar{p}(\bar{z})$ across the tube for different values of the FSI parameter β in Fig. 4.2(a) for Newtonian fluid and in Fig. 4.2(b) for a shear-thinning fluid. Clearly, "stronger" FSI (increasing values of β) leads to a decrease in the pressure everywhere, but especially near the inlet ($\bar{z} = 0$). The decrease in pressure is due to the increase in the flow area, which reduces the resistance to flow.

4.5.2 Comparison between analytical and numerical solutions for the flow-induced deformation

Our results in §4.4, suggest the following possible ways for solving the coupled problem of flow and deformation in an elastic tube: (i) using leading-order-in-thickness membrane theory (§4.4.2), (ii) using a matched asymptotic expansion for beyond-leading-order-in-thickness (i.e., Donnell shell) theory to capture bending and clamping (§4.4.3), and (iii) by numerical integration of the nonlinear TPBVP for the displacement given by Eqs. (4.45) and (4.46). We may conceptualize these approaches as a hierarchy: the leading-order perturbative solution is a less accurate version of the solution obtained by the matched asymptotic expansion, which in itself is a less accurate version of the solution found by solving the TPBVP numerically.

Let us now compare the deformation profile obtained via matched asymptotic expansion, i.e., Eq. (4.61) to the numerical solution of the original nonlinear TPBVP. The latter profile is obtained using the `solve_bvp` method in Python's SciPy module [140] to solve the TPBVP numerically. Figure 4.3 shows the results of such a comparison for different values of the small parameter $\epsilon = \sqrt{ta/\ell^2}$ but fixed β, n, and ν. There is very good agreement between the composite solution obtained via a matched asymptotic expansion and the numerical solution of the nonlinear TPBVP. As expected, the error in the composite solu-
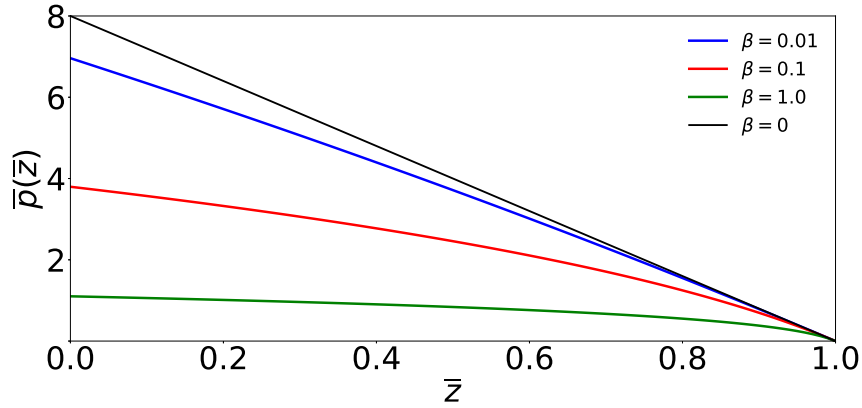
(a) Newtonian fluid.
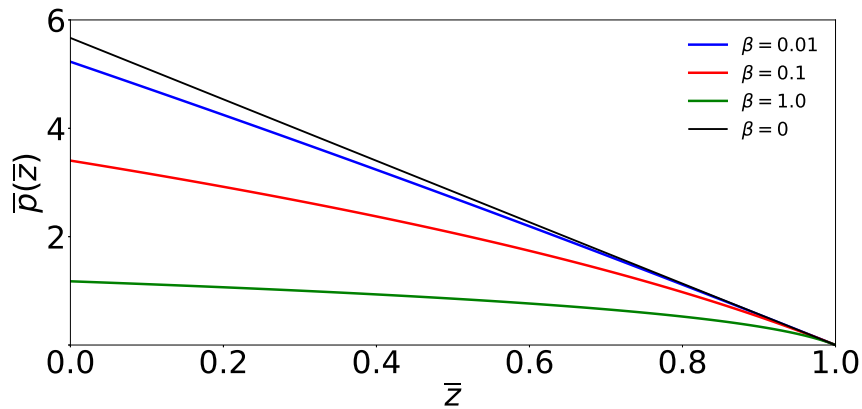
(b) Shear-thinning fluid.

Fig. 4.2. The dimensionless hydrodynamic pressure $\bar{p}$ in a elastic tube as a function of the dimensionless axial coordinate $\bar{z}$ for different values of the FSI parameter β for (a) Newtonian fluid ($n = 1$) and (b) shear-thinning fluid ($n = 0.7$). Both plots have been produced using Eq. (4.40) for an incompressible solid ($\nu = 1/2$). Note the different scales on the vertical axes for both the plots. Compliance of the tube reduces the pressure required to maintain steady flow.

tion increases with ϵ, especially in the corner layer at $\bar{z} = 1$. Nevertheless, the asymptotic expression is clearly very accurate.

In addition, observe that the radial displacement profile exhibits an overshoot near the inlet due to clamping. A similar profile has also been reported by Heil and Pedley [183] in their numerical study of large-deformation, small-strain FSI in a *collapsible* tube, which
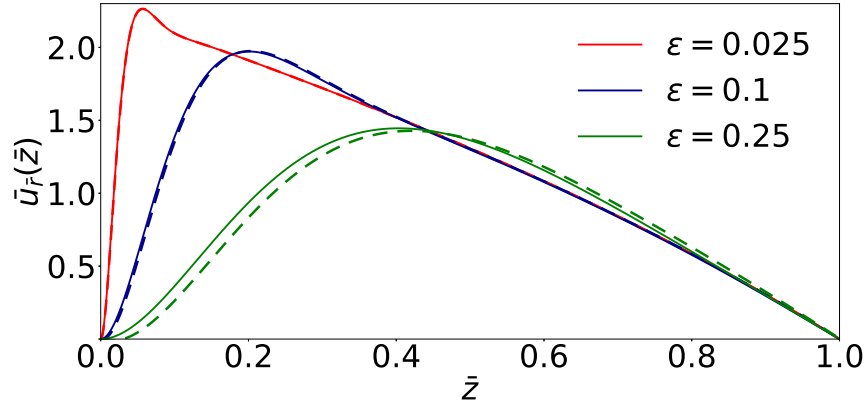
(a)
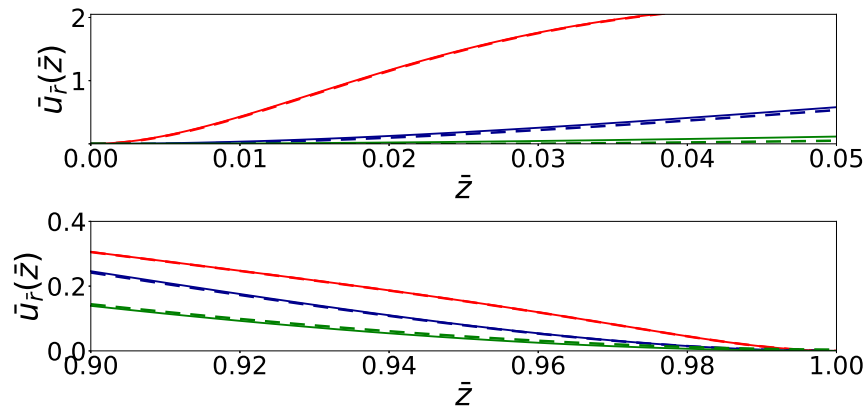
(b)

Fig. 4.3. The dimensionless radial displacement $\bar{u}_{\bar{r}}(\bar{z})$ as a function of the dimensionless axial position $\bar{z}$ in the elastic microtube for $\beta = 0.11$, $n = 0.7$, and $\nu = 1/2$. The solid curves are the numerical solution of TPBVP given by Eqs. (4.45) and (4.46), while dashed curves are the matched asymptotic solution from Eq. (4.61). Panel (a) shows the displacement over the whole tube, while panels (b) and (c) show zoom-ins near the clamped ends. The matched asymptotic solution is highly accurate, capturing the displacement overshoot near the inlet as $\epsilon \to 0^+$.

they modeled using Poiseuille's law and geometrically nonlinear shell theory (accounting for axial pre-stretch). However, since Heil and Pedley [183] modelled buckling of collapsible tubes, as opposed to the inflated tubes studied herein, the deformation profile actually exhibits an undershoot (compare [183, Fig. 6] with Fig. 4.3 above). Perhaps more impor-

tantly, even though Heil and Pedley [183] accounted for bending stiffness of the tube, their analysis does not yield an analytical solution to the deformation profile, i.e., a counterpart to Eq. (4.61) derived above. We also observe that the deformation profile of a beam due to quasi-static gravity-driven spreading of a viscous fluid underneath it exhibits this overshoot near the edge [see the inset of [178, Fig. 2(a)(ii)]], as should be expected from the structure of solutions to Eq. (4.28).

4.5.3 Comparison between theory and direct numerical simulations: Flow and deformation

To ascertain the validity of the theory developed in this chapter, we now compare our theoretical results against 3D direct numerical simulations (DNS) of coupled flow and deformation in an elastic tube. To this end, we choose an illustrative set of physical and geometric parameters, given in Table 4.1. The tube is assumed to be made of elastin, which is a highly elastic protein found in all vertebrates and is major constituent of arteries [26]. Here, along the lines of the work in [26, 184, 185], elastin is modeled as an isotropic linearly elastic solid with a constant Young's modulus of $E = 0.5$ MPa and a Poisson ratio of $\nu = 0.499$ (i.e., a nearly incompressible material). The dimensions have been chosen to ensure that the assumptions of shallowness and slenderness are satisfied. Specifically, the thickness-to-radius ratio of the tube is fixed at $t/a = 0.1$, consistent with the hemodynamics literature [166, p. 60]. The radius-to-length ratio is chosen to be sufficiently smaller, $a/\ell = 0.025 \ll t/a$, and the length $\ell = 3.2$ mm is chosen to be similar to microchannel studies (see, e.g., [38]), from which the values of a and t in Table 4.1 follow.

The generalized Newtonian fluid inside the tube is assumed to be human blood. Blood rheology is a topic of active research, as the rheological properties of blood depend on various factors such as a patient's age, health, concentration of plasma, etc. [55, 143]. Here, for the sake of simplicity, without sacrificing any physics, and to validate our theory for both Newtonian and non-Newtonian rheology, blood plasma is chosen as our example of a Newtonian fluid with constant shear viscosity of $\mu = 0.0012$ Pa·s (i.e., $m = \mu$ and

Table 4.1.
Geometric and material properties for a sample tube FSI problem.

a (mm)	ℓ (mm)	a/ℓ (–)	t (mm)	t/a (–)	E (MPa)	ν (–)
0.08	3.2	0.025	0.008	0.1	0.5	0.499

μ (Pa·s)	n (–)	m (Pa·s^n)	ϱ (kg/m^3)
0.0012	0.7	0.0185	1 060

$n = 1$) [87], while whole blood is chosen as our example of a shear-thinning fluid with a power-law index of $n = 0.7$ and a consistency index of $m = 0.0185$ Pa·s^n [143]. In both cases, a density of $\rho = 1060$ kg/m^3 is used, which is within the range for both blood plasma and whole blood (see, e.g., [186, Table 2.1.1]). Simulations were carried out for flow rates up to $q = 2.00$ mL/min, which corresponds to a maximum $Re \approx 150$ [$\Rightarrow \lambda Re \approx 3.75$, which is reasonably small within the lubrication approximation and well below the onset of unsteady effects closer to $Re \approx 300$ [187]] and a maximum FSI parameter value of $\beta \approx 0.12 \ll 1$.

For our computational approach, we employ a segregated solution strategy, as opposed to a monolithic one (see, e.g., [188]). That is, the solid (resp. fluid) problem is solved independently of the fluid (resp. solid) problem, each on its own computational domain. The displacements (resp. forces) from the solid (resp. fluid) domain are then transferred to the fluid (resp. solid) domain via a surface traction boundary condition. Based on previous successful computational microscale FSI studies [38, 60, 142], we have used the commercial computer-aided engineering (CAE) software from ANSYS [141] to perform such two-way coupled FSI DNS via a segregated approach. The domain geometry was created in ANSYS SpaceClaim, and the computational grid was generated in ANSYS ICEM CFD. The steady incompressible mass and momentum equations for the power-law fluid were solved using ANSYS Fluent as the computational fluid dynamics (CFD) solver based on the finite volume method. The structural mechanics solver, based on the finite element method (FEM),

under ANSYS Mechanical was employed for the structural problem, which solved the static force-equilibrium equations for a linearly elastic isotropic solid with geometrically nonlinear strains. In the static structural module, the option of "large deformations" had been turned on. This feature allows the distinction between the deformed and undeformed coordinates to be retained. Additionally, this feature means that that the Henky strain and Cauchy stress are used as the strain and stress measures, respectively. Consequently, the stiffness matrix in the resultant finite element method (FEM) formulation is not constant, and it is a function of displacements, leading to a nonlinear algebraic problem. However, there is no material nonlinearity in this problem, and the relationship between the stress and strain tensors is described by linear elasticity with two material parameters (E and v). The exchange of forces and displacements along the inner surface of the tube was achieved by declaring the surface as an "FSI interface." A nonlinear iterative procedure transfers the loads and displacements incrementally until convergence is reached, ensuring two-way coupling. Most importantly, beyond assuming a steady state, this DNS approach *does not* make any of the approximations that the theory does, e.g., lubrication, Donnell shell, and the various smallness assumptions.

To ensure that the numerical solutions computed are independent of the grid choice, we performed a grid-independence (convergence) study. Two grids each were defined for the fluid and the solid solvers, thus bringing the total number of grid arrangements to four. The details of the grids are shown in Table 4.2. For the fluid grid, grid 2 was generated by scaling the number of edge divisions across the model in grid 1 by a factor of 2. Similarly, grid 2 for the FEM grid was generated by increasing the number of divisions on the lateral surfaces from 500 to 800. The simulations were performed for the fluid and solid models on all four grids described above, under the conditions in Table 4.1. However, for the grid refinement study, the simulations were carried out only for a single flow rate of $q = 1$ mL/min.

The results of the grid convergence study are shown in Table 4.3 for the displacement at the midsection of the tube (averaged over the circumference) and the pressure drop over the length of the microtube. The insignificant variation of these values across grid combi-

Table 4.2.
Details for the four grids used for the grid-convergence study.

	fluid grid 1	fluid grid 2	solid grid 1	solid grid 2
Number of nodes	1 348 768	10 626 967	1 090 584	1 743 984
Number of elements	1 387 365	10 467 576	198 000	316 800

Table 4.3.
Grid-independence (convergence) study for the ANSYS simulations, using the circumferentially averaged displacement $\langle u_r \rangle$ at the tube wall's midsection and the full pressure drop Δp as the metrics. The percent difference is computed with respect to the reference values from the simulation on the combination of fluid grid 2 and solid grid 2.

fluid grid/solid grid	1/1	2/1	1/2	2/2
$\langle u_r \rangle$ % difference	0.2	−0.4	−0.6	–
Δp % difference	−0.08	0.08	0.04	–

nations shows that our simulation results, which were computed on the combination fluid grid 1 and solid grid 1, are indeed grid independent and accurate.

Fluid mechanics benchmark

First, we benchmark the q–Δp relationships predicted by our mathematical models: the leading-order FSI from the membrane theory [Eq. (4.41)] and the Donnell shell FSI [Eqs. (4.45) and (4.46)]. The dimensional full pressure drop Δp as a function of the dimensional flow rate q is shown in Fig. 4.4 for (a) a Newtonian fluid (blood plasma) and (b) a shear-thinning fluid (whole blood). There is good agreement between theory and simulation, particularly for the smaller flow rates. The maximum relative error, over the shown range of q, is $\approx 10\%$ for the Newtonian fluid and $\approx 5\%$ for the shear-thinning fluid. The higher relative error for the same flow rate for Newtonian fluid flow is attributed to the

larger pressure (note the different vertical axis scales in the two plots). At larger q, small but systematic differences emerge between theory and simulation because, at these flow rates, the deformation of the tube starts to exhibit significant strains, which are beyond the applicability of the linear shell theory employed herein. We also observe that there is hardly any perceptible difference in Δp predicted by the membrane and Donnell shell theories, which shows that, indeed, bending has a negligible effect on the total pressure drop.

To justify the use of the power-law rheological model in the fluid mechanics problem, we post-processed our simulation results, and we verified that the maximum shear stress in the flow is much larger than the yield stress of the Casson model for blood. For example, for the flow rate of 1 mL/min, the maximum wall shear stress on the tube was found to be 35.14 Pa, which is two orders of magnitude higher than the 0.05 Pa yield stress of the Casson model for blood [189].

Next, it is important to evaluate the theory developed herein in the context of the classical results, namely the law of Laplace [171, 190] and the model proposed by Fung in his *Biomechanics* textbook [87, §3.4], which is often quoted in newer texts on biofluid mechanics [191, pp. e25–e27]. Fung's model and that of Laplace take a large-deformation approach, writing the stress equilibrium equations in the *deformed* configuration of the tube, which requires reconsidering the structural mechanics calculation from §4.3.1. In order not to belabor the discussion in this section, we have relegated the large-deformation re-derivation of our main mathematical result [i.e., Eq. (4.40)] to Sec. 4.5.5.

Structural mechanics benchmark

Having compared and validated the theoretical prediction for the hydrodynamics portion of the FSI problem, we now shift our focus to the solid domain. In Fig. 4.5, we plot the ratio of dimensionless radial tube deformation, $\bar{R}(\bar{z}) - 1$, to the dimensionless pressure $\bar{p}(\bar{z})$ along the tube's length. Again, the results have been shown for both our chosen (a) Newtonian and (b) shear-thinning fluid. Equations (4.33) and (4.34) predict this ratio to be
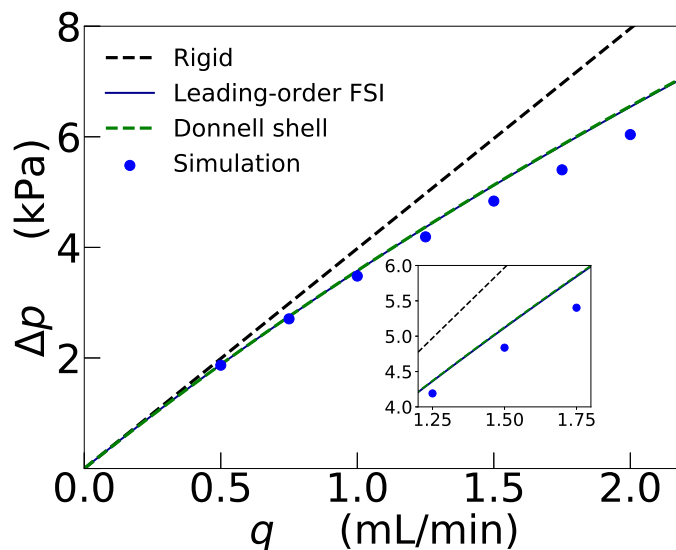
(a) Newtonian fluid.
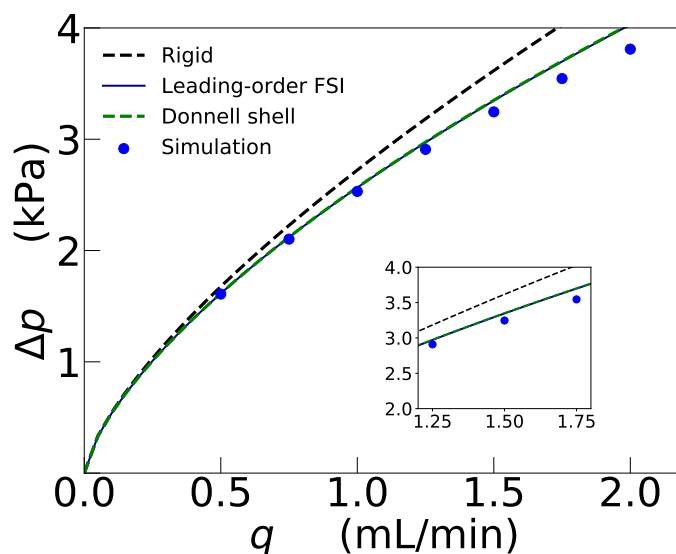
(b) Shear-thinning fluid.

Fig. 4.4. Full pressure drop $\Delta p = p(0)$ vs. flow rate q in a deformable tube. Fluid–structure interaction causes the pressure drop to decrease in the deformable tube compared to the rigid one. The perturbative analysis developed herein, culminating in Eqs. (4.40) [power-law, (b)] and (4.44) [Newtonian, (a)] captures the latter effect quite accurately, when compared to 3D direct numerical simulations. Note the different scales on the vertical axes for both the plots.

$[\bar{R}(\bar{z}) - 1]/\bar{p}(\bar{z}) = \beta(1 - \nu^2)$ (interestingly, a constant independent of $\bar{z}$), to the leading order in $\epsilon = \sqrt{ta/\ell^2}$. For the beyond-leading-order analysis, we integrated the fifth-order nonlinear BVP from Donnell's shell theory, i.e., Eq. (4.45) subject to Eqs. (4.46), using the TPBVP solver method in Python's SciPy module [140]. (We could have also plotted the matched asymptotic solution to Eq. (4.45), i.e., Eq. (4.61), but it would be indistinguishable for this value of $\epsilon = 6.25 \times 10^{-5}$ based on Table 4.1.)

Figure 4.5 shows good agreement between the results of DNS and the two proposed mathematical models (i.e., leading-order FSI and the Donnell shell FSI). As predicted in §4.4.3 there are extremely narrow regions (boundary layers) near the inlet ($\bar{z} = 0$) and outlet ($\bar{z} = 1$) planes in which the full ODE solution deviates from the leading-order perturbative solution. The thinness of these boundary layers, in comparison with the tube's length, leads us to conclude that almost the entire tube, except a sliver near each end, is in a membrane state with negligible bending.

To verify our assumption about negligible (no) axial displacement, which was used to arrive at Eq. (4.21), we post-processed the axial σ_{zz} and hoop $\sigma_{\theta\theta}$ stresses from our ANSYS simulations. For a Newtonian fluid, the ratio of the hoop stress to the axial stress at the middle of the tube, where the effect of clamping at the edges and the resultant bending is negligible, is $(\sigma_{\theta\theta}/\sigma_{zz})|_{\bar{z}=0.5} \approx 2.20$ for $q = 0.5$ mL/min and $(\sigma_{\theta\theta}/\sigma_{zz})|_{\bar{z}=0.5} \approx 2.45$ for $q = 2$ mL/min. These two values, for the smallest and largest flow rates considered, can be compared to the theoretical value of $1/\nu = 2$ [from Eq. (4.21)], leading to a relative error of 10% for $q = 0.5$ mL/min and 22% for $q = 0.5$ mL/min. Similarly, the ratio of axial deformation to radial deformation at the middle of the tube is ≈ 0.004 for $q = 0.5$ mL/min and ≈ 0.2 for $q = 2$ mL/min. While nonzero, these errors are small enough to justify having employed Eq. (4.21) in the mathematical analysis above.

4.5.4 Region of validity in the parameter space

The proposed theory of steady non-Newtonian FSI in slender elastic tubes hinges upon on a set of intertwined assumptions:
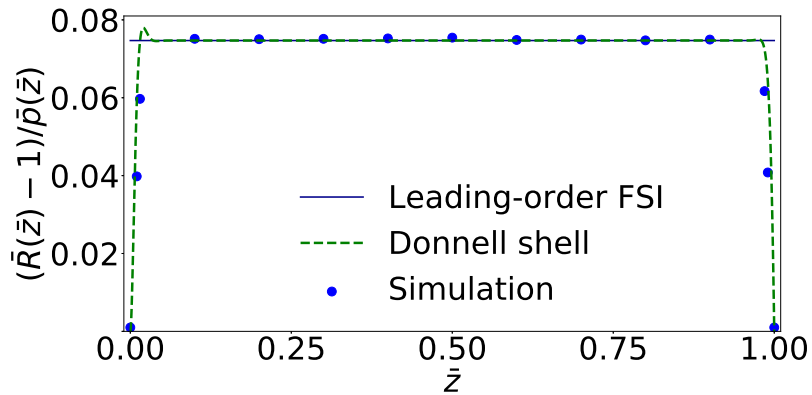
(a) Newtonian fluid.
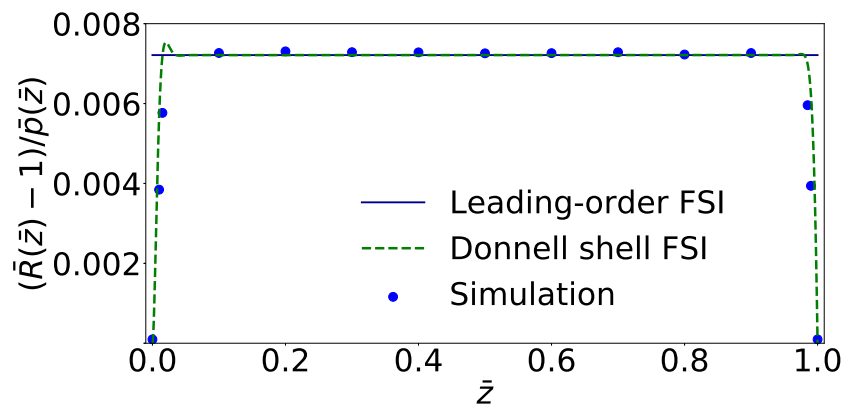
(b) Shear-thinning fluid.

Fig. 4.5. Ratio of the dimensionless radial deformation $\bar{R} - 1$ to the hydrodynamic pressure $\bar{p}$, as a function of the axial position $\bar{z}$ in the tube. The leading-order FSI theory is given by Eq. (4.34) (solid), the Donnell shell FSI theory is the numerical solution of the TPBVP given by Eqs. (4.45) and (4.46) (dashed), the simulation results are from ANSYS (symbols). Note the different vertical scale of these plots. For both the plots, the results of the simulations correspond to a flow rate of $q = 1$ mL/min.

1. $t/a \ll 1$: This requirement allows us to use thin-shell theory.

2. $\mathcal{U}_c/a \ll 1$: This requirement represents the small-strain assumption of the shell theory.

3. $a/\ell \ll 1$: This slender-geometry requirement allows us to simplify both the fluid mechanics and the structural mechanics problems. This requirement also ensures the rotation of a shell element is negligible.

4. $\mathcal{U}_c/t \ll 1$: This requirement allows us to refer the analysis to the undeformed (Eulerian) coordinates and also restricts the theory to small deformations.

A natural ordering of the length scales associated with FSI in a tube thus follows:

$$\mathcal{U}_c \ll t \ll a \ll \ell, \tag{4.62}$$

which must hold for the present linear, small-deformation FSI theory to apply. Importantly, our DNS results form §4.5.2 show that this regime is accessible under realistic flow conditions.

4.5.5 Large-deformation formulation and connections to the law of Laplace and to Fung's model

In §4.3, we termed the proposed FSI theory as *small deformation* due to our assumptions on the structural mechanics aspect of the FSI. We used small-deformation classical shell theories, which assume that the (radial) deformation is considerably smaller than the (smallest) characteristic dimension of the tube, i.e., $\mathcal{U}_c/t \ll 1$. This assumption ensures the equivalence between the deformed and undeformed coordinates (i.e., between the Langrangian and Eulerian frames). Then, the equations of static equilibrium, which are strictly valid only when written in terms of deformed coordinates, can be written in terms of the undeformed coordinates, as done above and in classical shell theory. However, some prior work in the literature has used a mixture of frames of references by posing the equilibrium equations of a small-deformation shell theory in the deformed configuration, while using the undeformed coordinates in the subsequent calculation of deformations from strains. Thus, in this section, we offer a critical discussion of this issue. The resulting theory may be termed "large-deformation" theory.

The membrane theory of §4.3.1, when referred to the tube's deformed coordinates, leads us to reformulate Eqs. (4.22) and (4.23) as

$$N_\theta = R(z)p(z) \quad \Rightarrow \quad \sigma_{\theta\theta} = \frac{R(z)}{t}p(z). \tag{4.63}$$

The assumption of no axial displacement leads to Eq. (4.21), which still applies and whence the hoop strain (from the linear elastic law) is $\varepsilon_{\theta\theta} = (1 - v^2)\sigma_{\theta\theta}/E$. Then, the radial deformation, under the assumption of axisymmetry, is

$$u_r(z) = \varepsilon_{\theta\theta}a = (1 - v^2)\frac{R(z)a}{Et}p(z). \tag{4.64}$$

Equation (4.64) is the so-called *law of Laplace*, which relates the pressure at a given cross-section to its radius in the *deformed* state [171, 190]. This result, in mixing frames of reference without rigorous motivation for doing so, is not without criticism in the biomechanics literature [192]. Furthermore, observe that u_r appears on both sides of Eq. (4.64) because $R(z) = a + u_r(z)$.

Using the dimensionless variables from Eq. (4.29), Eq. (4.64) becomes

$$\mathcal{U}_c\bar{u}_{\bar{r}}(\bar{z}) = (1 - v^2)\frac{(a + \mathcal{U}_c\bar{u}_{\bar{r}})a}{Et}\mathcal{P}_c\bar{p}(\bar{z}). \tag{4.65}$$

Now, for large deformations, the appropriate scale is $\mathcal{U}_c = t$, which ensures consistency with the results above by keeping the FSI parameter defined as $\beta = a\mathcal{P}_c/(Et)$. Thus, solving for $\bar{u}_{\bar{r}}$ from Eq. (4.65), we obtain the pressure–deformation relationship:

$$\bar{u}_{\bar{r}}(\bar{z}) = \left(\frac{a}{t}\right)\left[\frac{(1 - v^2)\beta\bar{p}(\bar{z})}{1 - (1 - v^2)\beta\bar{p}(\bar{z})}\right]. \tag{4.66}$$

Note that, unlike the case of small-deformation theory leading to Eq. (4.34), this last relationship between deformation and pressure is not linear in $p(z)$. Next, substituting $\bar{R}(\bar{z}) = 1 + (t/a)\,\bar{u}_{\bar{r}}(\bar{z})$ and Eq. (4.66) into Eq. (4.37) yields an ODE for the pressure $\bar{p}(\bar{z})$. Solving this ODE subject to $\bar{p}(1) = 0$, we obtain

$$\bar{p}(\bar{z}) = \frac{1}{(1 - v^2)\beta}\left(1 - \left\{1 + 6n(1 - v^2)\beta[(3 + 1/n)]^n(1 - \bar{z})\right\}^{-1/3n}\right). \tag{4.67}$$

Next, we evaluate the full pressure drop $\Delta\bar{p} = \bar{p}(0)$ from Eq. (4.67) and perform a Taylor series expansion for $\beta \ll 1$, to obtain:

$$\Delta\bar{p} = \left\{ 2\left(3 + 1/n\right)^n - \frac{(1 + 3n)}{2}[(1 - \nu^2)\beta]\left[2\left(3 + 1/n\right)^n\right]^2 \right.$$
$$\left. - \frac{(1 + 3n)(1 + 6n)}{6}[(1 - \nu^2)\beta]^2\left[2\left(3 + 1/n\right)^n\right]^3 + O(\beta^3) \right\}. \quad (4.68)$$

On the other hand, a Taylor series expansion of Eq. (4.41) leads to

$$\Delta\bar{p} = \left\{ 2\left(3 + 1/n\right)^n - \frac{(1 + 3n)}{2}[(1 - \nu^2)\beta]\left[2\left(3 + 1/n\right)^n\right]^2 \right.$$
$$\left. - \frac{(1 + 3n)(3 + 6n)}{6}[(1 - \nu^2)\beta]^2\left[2\left(3 + 1/n\right)^n\right]^3 + O(\beta^3) \right\}. \quad (4.69)$$

Equations (4.68) and (4.69) agree to *two* terms, with the first discrepancy being the relatively minor change of $1 + 6n$ becoming $3 + 6n$ in the coefficient of β^2. This shows that the pressure drop predicted by the law of Laplace is almost indistinguishable from the corresponding one obtained from small-deformation theory given by Eq. (4.41).

Now, writing the pressure drop computed from Eq. (4.67) in dimensional variables and specializing it to a Newtonian fluid ($n = 1$, $m = \mu$), we obtain

$$\Delta p = \frac{Et}{(1 - \nu^2)a}\left\{ 1 - \left[1 + \frac{24\mu q\ell(1 - \nu^2)}{\pi a^3 Et}\right]^{-1/3} \right\}. \quad (4.70)$$

Equation (4.70) can be compared to the corresponding flow rate–pressure drop relation from Fung's textbook [87, §3.4, Eq. (8)]:

$$\Delta p = \frac{Et}{a}\left\{ 1 - \left[1 + \frac{24\mu q\ell}{\pi a^3 Et}\right]^{-1/3} \right\}. \quad (4.71)$$

Clearly, Eqs. (4.70) and (4.71) are quite similar with Eq. (4.71) simply being the case of $\nu = 0$ of Eq. (4.70). The physical reason for this mathematical fact is that, in Fung's analysis, the cylinder's axial stresses and deformation are neglected (yielding a state of *uniaxial* stress), which means that Fung's result is a so-called *independent-ring model*. This approximation is distinct from the shell models considered herein, in which both $\sigma_{\theta\theta}$

and σ_{zz} are taken into account. Therefore, Fung's result, being independent of the Poisson ratio, is strictly applicable only to highly compressible solids such as cork, rather than rubber-like elastomers such as PDMS microtubes or blood vessels.

In Fig. 4.6, we compare the results of Fung's model and the law of Laplace, alongside those of our leading-order (membrane) and Donnell-shell FSI theories. The full dimensional pressure drops Δp predicted by the different mathematical theories considered are quite close. While Fung's model first overpredicts then underpredicts the pressure drop, the other theories over-predict the pressure drop with increasing error as q increases, consistent with the perturbation approach under which they were derived. As expected, given the small deformation of the tube, the use of a large-deformation membrane theory does not influence the predicted pressure drop. Therefore, we conclude that the assumptions about the deformation and the stress made in Fung's classic treatment of the problem *coincidentally* yield good agreement at large q, while Fung's model reduces to the theory derived herein for small q.

We also carry out a comparison of the structural mechanics prediction, in Fig. 4.7, by comparing the ratio $[\bar{R}(\bar{z}) - 1]/\bar{p}(\bar{z})$ of dimensionless deformation and pressure obtained across the models. Here, the conflicting assumptions used to obtain the law of Laplace and Fung's model are quite apparent in this comparison. For both Newtonian and power-law fluids, Fung's model overpredicts $[\bar{R}(\bar{z}) - 1]/\bar{p}(\bar{z})$. As explained above, Fung's model is an "independent ring" model that neglects the stress and strains in the streamwise direction. These assumptions, in conjunction with those of large-deformation FSI, lead both Fung's model and the law of Laplace to predict an incorrect displacement profile for which $[\bar{R}(\bar{z}) - 1]/\bar{p}(\bar{z})$ slowly varies with z (outside the boundary and corner layers).

4.6 Conclusions and outlook

In this chapter, we formulated a theory of the low Reynolds number axisymmetric fluid–structure interaction (FSI) between a generalized Newtonian fluid and an elastic tube enclosing the flow. Specifically, we derived an analytical relation between the pressure
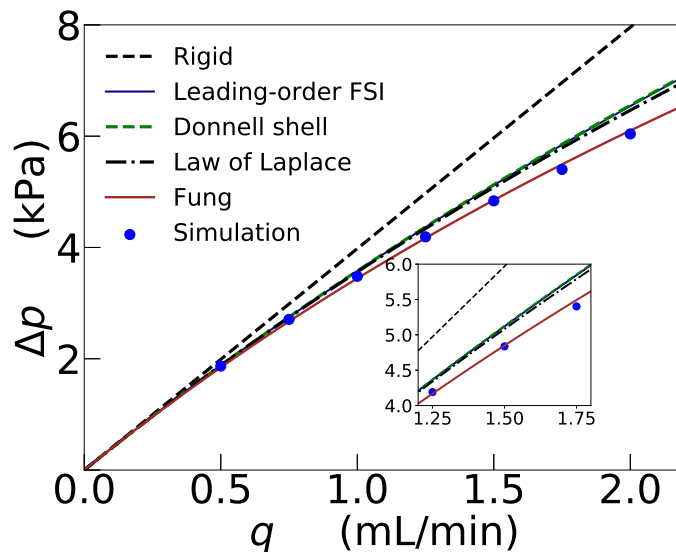
(a) Newtonian fluid.
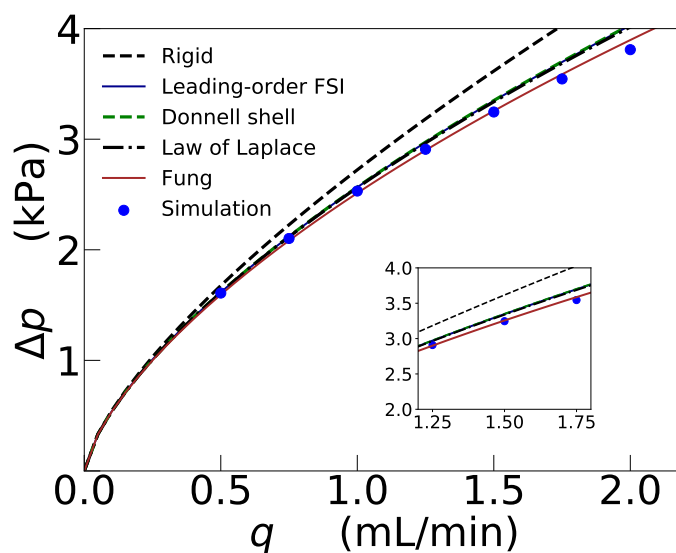
(b) Shear-thinning fluid.

Fig. 4.6. Flow rate–pressure drop relation for FSI in an elastic tube. The difference between the results from the law of Laplace [large-deformation theory, Eq. (4.67)] and the leading-order FSI theory [small-deformation theory, Eq. (4.40)] is minute. Meanwhile, the results from Fung's relation given by Eq. (4.71) deviate significantly from the results of other theories. Note the different the vertical scales in the plots.
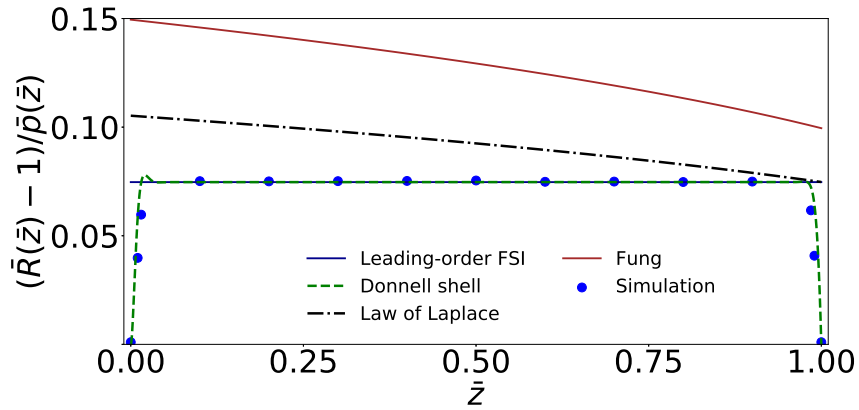
(a) Newtonian fluid.
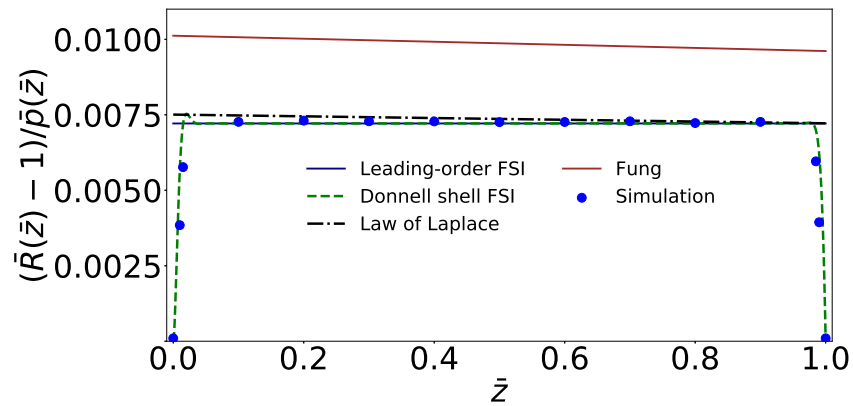
(b) Shear-thinning fluid.

Fig. 4.7. Ratio of the dimensionless radial deformation $\bar{R} - 1$ to the dimensionless hydrodynamic pressure $\bar{p}$, as a function of the dimensionless axial position $\bar{z}$ in the elastic tube for $q = 1$ mL/min. The leading-order FSI theory is given by Eq. (4.34), the Donnell shell FSI theory is the numerical solution of the TP-BVP given by Eqs. (4.45) and (4.46), the law of Laplace is given by Eq. (4.66), Fung's result is given by Eq. (4.66) with $\nu = 0$, and the simulation results are from ANSYS. Note the different vertical scales in the plots.

drop across the tube and the imposed steady flow rate through it, taking into account both the fluid's shear-dependent viscosity (such as, e.g., whole blood) and the compliance of the conduit (such as, e.g., a blood vessel). Although physiological flows occur across a range of flow regimes (Reynolds numbers) [44–46, 50], previous research has focused on

moderate-to-high Reynolds number phenomena, including collapse of the vessel, unlike the present context. The proposed theory is also applicable to problems in microfluidics, wherein soft (e.g., PDMS-based) microchannels of circular cross-section and microtubes are now manufactured and FSI becomes relevant [59, 61].

Under the lubrication approximation for low Reynolds number flow, we showed how to analytically couple a unidirectional flow field to an appropriate linear shell theory. This led us to a fifth-order nonlinear ordinary differential equation (ODE), namely Eq. (4.45) for the radial displacement, which fully describes the FSI. In a perturbative sense, we showed that, at the leading order in slenderness and shallowness of the tube, the shell theory reduces to membrane theory and a *linear* relationship, given by Eq. (4.34), emerges between the local radial deformation and the local hydrodynamic pressure at a given cross-section. Then, a dimensionless "generalized Poiseuille law" was obtained in Eq. (4.41), which *explicitly* gives the pressure drop in terms of the solid and fluid properties. This relationship rationalizes and updates certain arguments found in textbook discussions of physiological flow [87, 191]. Specifically, Eq. (4.41) can be put into dimensional form to yield the total pressure drop Δp due to flow of a generalized Newtonian (power-law) fluid in a slender deformable tube:

$$\Delta p = \frac{Et}{(1-v^2)a} \left\{ \left[1 + 2(3+1/n)^n (3n+2)(1-v^2) \left(\frac{m\ell}{Et} \right) \left(\frac{q}{\pi a^3} \right)^n \right]^{1/(3n+2)} - 1 \right\}. \quad (4.72)$$

The most important observation is that, due to FSI, Eq. (4.72) is *nonlinear* in q, even for a Newtonian fluid ($n = 1$), in contrast to the Hagen–Poiseuille law.

Furthermore, we showed that a boundary layer (at the inlet) and a corner layer (at the outlet) of the tube are required to enforce the clamping conditions on the structure. Using the method of matched asymptotics, we obtained a uniformly valid (closed-form) expression, given by Eq. (4.61), for the deformation profile. The ability to solve for the tube's deformation as a function of the axial coordinate via a matched-asymptotics calculation is in contrast with the case of low Reynolds number FSI in a microchannel of rectangular cross-section [37, 60] (see also §4.6.1), but similar to planar low Reynolds number flow under an elastic beam [29].
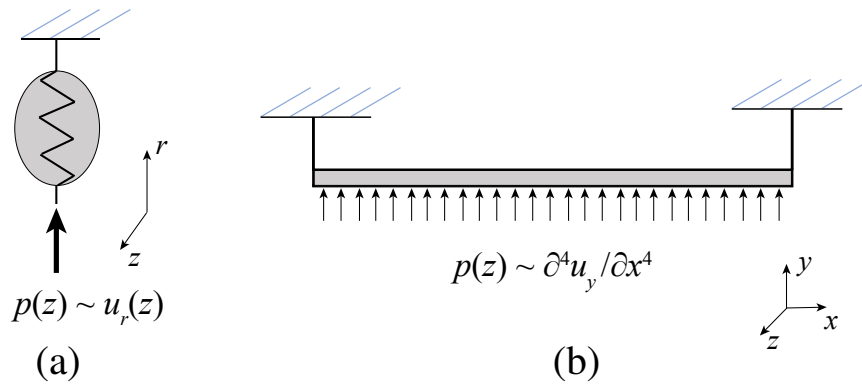
Fig. 4.8. Shells versus plates in viscous FSI. (a) A slice of a soft microtube represented as a Hookean spring. (b) A slice of a microchannel's soft top wall represented as an Euler beam. Under the perturbation theory, each slice is uniformly loaded by the hydrodynamic pressure p at flow-wise cross-section z.

To ascertain the validity of our mathematical results, we carried out two-way-coupled 3D simulations using the commercial computer-aided engineering suite by ANSYS [141]. We showed that good agreement can be obtained between predictions from the theory (for both the pressure drop and the radial deformation) and the corresponding direct numerical simulations. Then, we specified, through Eq. (4.62), the region in the physical and geometric parameter space in which our FSI theory applies.

4.6.1 Comparison between viscous FSI in a rectangular microchannel and an axisymmetric microtube

As mentioned previously, the deformation of any infinitesimal transverse slice in the streamwise direction of the elastic tube considered herein is akin to a Hookean spring because of the direct *linear* proportionality between the deformation and the pressure expressed by Eq. (4.34). This deformation is independent of neighboring slices, just as for a slender microchannel with a soft top wall [37, 38, 60]. The mathematical reason for this decoupling is the same for both geometries: the streamwise length scale of the micro-

tube/channel is much larger than its cross-sectional dimension. However, the two cases should also be contrasted: for a long and shallow microchannel, each slice of the top wall acts like an Euler beam in the cross-sectional direction (due to clamping at the sidewalls); while, for a slender microtube, each slice acts as a Hookean spring (due to axisymmetric deformation), as illustrated schematically in Fig. 4.8. The maximum cross-sectional deformation of the microtube, from the dimensional versions of Eqs. (4.33) and (4.34), is $u_{\max}(z) = (1 - \nu^2)a^2 p(z)/(Et)$, while it is $u_{\max}(z) = (1/2)(1 - \nu^2)a^4 p(z)/(Et^3)$ for a microchannel with equivalent width $w = 2a$ [37]. Consequently, a microtube is more compliant (and thus deforms more than a similar microchannel), with all other conditions being the same, if $t < a/\sqrt{2}$. This condition is satisfied in the distinguished limit considered herein: $t/a \ll 1$.

5. DEFORMABLE MICROTUBES: HYPERELASTIC RESPONSE AT STEADY STATE

SUMMARY

In this chapter, we analyze the steady-state microscale fluid–structure interaction (FSI) between a generalized Newtonian fluid and a hyperelastic tube. Physiological flows, especially in hemodynamics, serve as primary examples of such FSI phenomena. The small scale of the physical system renders the flow field, under the power-law rheological model, amenable to a closed-form solution using the lubrication approximation. On the other hand, negligible shear stresses on the walls of a long vessel allow the structure to be treated as a pressure vessel. The constitutive equation for the microtube is prescribed via the strain energy functional for an incompressible, isotropic Mooney–Rivlin material. We employ both the thin- and thick-walled formulations of the pressure vessel theory, and derive the static relation between the pressure load and the deformation of the structure. We harness the latter to determine the flow rate–pressure drop relationship for non-Newtonian flow in thin- and thick-walled soft hyperelastic microtubes. Through illustrative examples, we discuss how a hyperelastic tube supports the same pressure load as a linearly elastic tube with smaller deformation, thus requiring a higher pressure drop across itself to maintain a fixed flow rate.

The material in this chapter has been published as [V. Anand and I. C. Christov, "On the Deformation of a Hyperelastic Tube Due to Steady Viscous Flow Within," in *Dynamical Processes in Generalized Continua and Structures* (H. Altenbach, A. Belyaev, V. A. Eremeyev, A. Krivtsov, and A. V. Porubov, Eds.), Springer Nature (Cham, Switzerland), 2019, vol. 103, ch. 2, pp. 17–35] [193]
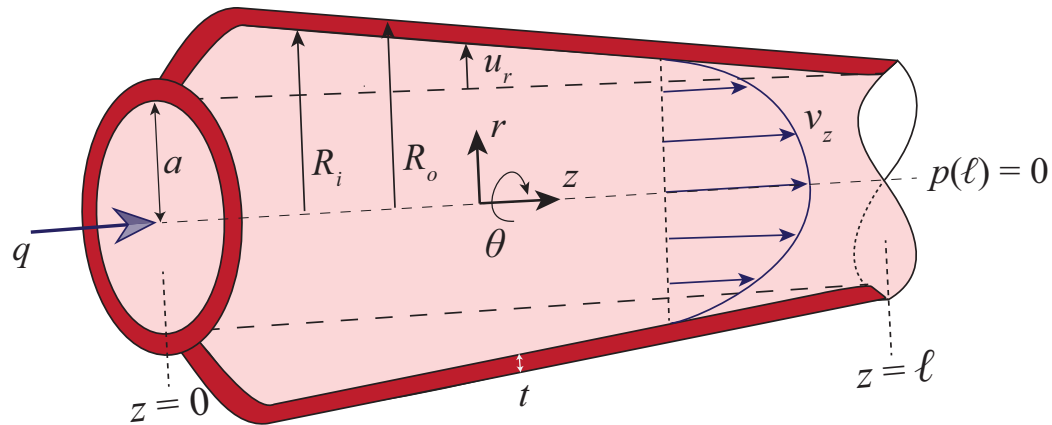
Fig. 5.1. Schematic of the microtube geometry, including notation used in this chapter.

5.1 Fluid mechanics problem: Solving for the axial velocity

Consider a fluid flow $\boldsymbol{v} = v_r \hat{\boldsymbol{r}} + v_\theta \hat{\boldsymbol{\theta}} + v_z \hat{\boldsymbol{z}}$ in cylindrical coordinates. A diagram of the deformed microtube geometry is shown in Fig. 5.1, specifically the tube has uniform thickness t, undeformed inner radius a, and length ℓ. Now, following [160], let us assume that

1. The flow is steady: $\frac{\partial}{\partial t}(\cdot) = 0$.

2. The flow is axisymmetric without swirl: $\frac{\partial}{\partial \theta}(\cdot) = 0$ and $v_\theta = 0$.

3. The geometry of the flow vessel is a slender tube: $\ell \gg a \iff a/\ell = \epsilon \ll 1$.

Assumption 3. is key to the mathematical analysis below. Specifically, this assumption leads us to the appeal to the *lubrication approximation* of fluid mechanics (see, e.g., [123, 154]), which will allow us to solve for the flow profile analytically.

As shown with due diligence in our previous work [160], to the leading order in a/ℓ, the velocity field is *unidirectional* [154]: $\bar{\boldsymbol{v}} = \bar{v}_{\bar{z}} \hat{\boldsymbol{z}}$ but weakly varying with the (long)

flow-wise direction i.e., $\bar{v}_{\bar{z}} = \bar{v}_{\bar{z}}(\bar{r}, \bar{z})$. Here, and henceforth, bars over quantities denote dimensionless variables according to the following scheme:

$$\bar{r} = r/a, \qquad \bar{z} = z/\ell, \qquad \bar{v}_{\bar{r}} = v_r/\mathcal{V}_r, \qquad \bar{v}_{\bar{z}} = v_z/\mathcal{V}_z, \qquad \bar{p} = p/\mathcal{P}_c, \qquad (5.1)$$

where the characteristic radial velocity scale is $\mathcal{V}_r \equiv \epsilon \mathcal{V}_z$, the characteristic axial velocity scale is $\mathcal{V}_z$, and $\mathcal{P}_c$ is the characteristic pressure scale. Upon specifying the rheology of the fluid (see below), $\mathcal{P}_c$ and $\mathcal{V}_z$ will be related to each other.

Next, we specify the fluid's rheological behavior. We are interested in biofluid mechanics applications such as blood flow through a deformable artery or vein. Blood is known to have a shear-dependent viscosity due to the fact that red blood cells deform. Haemorheology is a complex topic [57, Ch. 3], nevertheless experiments suggest [143] that blood flow can be accurately fit to a power-law fluid model (a generalized Newtonian rheology often going by the name Ostwald–de Waele [128]) at steady state. Now, the dominant shear stress component is τ_{rz}; likewise the corresponding rate-of-strain tensor component is just $\dot{\gamma}_{rz} = \partial v_z/\partial r$ to the leading order in a/ℓ (i.e., under the slenderness assumption). Thus the fluid's rheological model takes the "simple shear" form:

$$\tau_{rz} = \underbrace{m \left| \frac{\partial v_z}{\partial r} \right|^{n-1}}_{=\eta} \frac{\partial v_z}{\partial r}, \qquad (5.2)$$

where η is the *apparent viscosity*, $m(> 0)$ is the *consistency factor*, and $n(> 0)$ is the *power-law index*. On making Eq. (5.2) dimensionless using the variables from Eq. (5.1), we obtain the relationship between the axial velocity $\mathcal{V}_z$ scale and the pressure scale $\mathcal{P}_c$: $\mathcal{V}_z = \left[a^{n+1} \mathcal{P}_c / (m\ell) \right]^{1/n}$.

The power-law rheological model captures the flow behavior of fluids that are shear thinning (η decreases with $\dot{\gamma}_{rz}$), such as blood [127, 143] as mentioned above, for $n < 1$. It also captures the flow behavior of shear-thickening fluids (η increases with $\dot{\gamma}_{rz}$) such as as woven Kevlar fabrics impregnated with a colloidal suspension of silica particles [194] used for ballistic armors, for $n > 1$. The viscous Newtonian fluid is obtained as the special case of $n = 1$ in Eq. (5.2). Our motivation is mainly fluid mechanics of blood vessels, so our examples consider $n < 1$, but the theory applies to both cases.

Finally, considering the dynamics of the flow under the constitutive relationship in Eq. (5.2), we found that the dimensionless axial velocity profile is [160]:

$$\bar{v}_{\bar{z}} = \left(-\frac{1}{2}\frac{\mathrm{d}\bar{p}}{\mathrm{d}\bar{z}}\right)^{1/n}\left(\frac{\bar{R}_i^{1+1/n} - \bar{r}^{1+1/n}}{1 + 1/n}\right), \tag{5.3}$$

where $\bar{R}_i = R_i/a$ is the dimensionless *inner* radius of the deformed microtube. More importantly, $\bar{R}_i$ is not necessarily equal to unity because we allow the microtube to deform due to FSI, as discussed in the next section. Likewise, the pressure gradient $\mathrm{d}\bar{p}/\mathrm{d}\bar{z}$ is *not* constant but, rather, varies with $\bar{z}$. As a result, while $\bar{p}$ is at most a function of $\bar{z}$ (but not a linear function), $\bar{v}_{\bar{z}}$ can depend upon both $\bar{r}$ and $\bar{z}$.

5.2 Structural mechanics problem: Solving for the deformation

In this section, we address the structural mechanics aspect of the coupled FSI problem posed above. To this end, we treat the structure as a *pressure vessel*, wherein the only load acting on the structure is the hydrodynamic pressure from the fluid, and the load due to viscous and shear stresses is neglected. This assumption stems from the lubrication approximation for the fluid flow, wherein the viscous shear stress scale is $\approx \epsilon$ times the hydrodynamic pressure scale [123, Ch. 22]. We begin our discussion by first analyzing a *thin-walled* pressure vessel, then we move onto its *thick-walled* counterpart.

5.2.1 Thin-walled cylinder

Let us consider the case of a thin-walled initially cylindrical microtube with thickness $t \ll a$. This assumption allows us to consider the cylinder in a state of plane stress and plane strain, thus simplifying the analysis of the structural mechanics problem. As a consequence, the walls of the cylinder act like a membrane, which does not sustain any bending or twisting moments. There is no variation of stress and deformation throughout the thickness of the cylinder.

Deformation

In the undeformed material coordinate system, the coordinates of a material point are given by $r = a$, $\theta \in [0, 2\pi]$, and $z \in [0, \ell]$. Upon *axisymmetric* deformation, the coordinates of the same material point become

$$R = R(r), \qquad \Theta = \theta, \qquad Z = \alpha z. \tag{5.4}$$

We further assume that the deformation is homogeneous along the axial direction, thus $\alpha = L/\ell$, with L being the deformed cylinder's length and ℓ being the undeformed cylinder's length (as in Fig. 5.1). Now, since the cylinder is clamped at both its ends, its length does not change and $L = \ell$. Hence, $\alpha = 1$. The foregoing discussion reduces the coordinates of the point in the spatial coordinate system to:

$$R = R(r), \qquad \Theta = \theta, \qquad Z = z. \tag{5.5}$$

As the shell is considered (infinitesimally) thin in this theory, we denote the inner radius R_i by R (in this section) without fear of confusion.

For the case of a deformation defined by Eq. (5.5), the deformation gradient tensor $\underline{\underline{\mathcal{F}}}$ can be easily computed:

$$\underline{\underline{\mathcal{F}}} = \begin{pmatrix} \partial R/\partial r & 0 & 0 \\ 0 & R/r & 0 \\ 0 & 0 & 1 \end{pmatrix}. \tag{5.6}$$

Since $\underline{\underline{\mathcal{F}}}$ is a diagonal tensor, then its principal axes are just the r, θ, and z axes of the cylindrical coordinate system. Indeed, we deduce from the deformation field introduced in Eq. (5.5) that a line segment oriented along either the r, θ or z coordinate directions will, at most, only *stretch* and cannot rotate.

Consequently, for this type of deformation, the rotation tensor $\underline{\underline{\mathcal{R}}} = \underline{\underline{\mathcal{I}}}$ (the identity tensor) and the stretch tensor is simply

$$\underline{\underline{\mathcal{U}}} = \underline{\underline{\mathcal{F}}} = \begin{pmatrix} \lambda_1 & 0 & 0 \\ 0 & \lambda_2 & 0 \\ 0 & 0 & \lambda_3 \end{pmatrix}. \tag{5.7}$$

Here, λ_1, λ_2, λ_3 are the principal stretches, which one can immediately write down by comparison of Eqs. (5.6) and (5.7). Now, since the material is incompressible, $\det \underline{\underline{\mathcal{F}}} = \lambda_1 \lambda_2 \lambda_3 = 1$, we can determine λ_1, and thus

$$\lambda_1 = r/R, \qquad \lambda_2 = R/r, \qquad \lambda_3 = 1. \tag{5.8}$$

Constitutive equation

We consider the material from which the cylindrical tube is composed to be an isotropic, incompressible, *hyperelastic* material. For such a material, the constitutive equation is specified through a strain energy functional W [195, 196], which depends upon the principal stretches λ_i, i.e., $W = W(\lambda_1, \lambda_2, \lambda_3)$. Specifically, we assume that the hyperelastic material is defined by the *incompressible* Mooney–Rivlin constitutive equation [195–197] with strain energy given by

$$W = \mathbb{C}_1 \left(\lambda_1^2 + \lambda_2^2 + \lambda_3^2 \right) + \mathbb{C}_2 \left(\lambda_1^2 \lambda_2^2 + \lambda_2^2 \lambda_3^2 + \lambda_3^2 \lambda_1^2 \right) \qquad (\lambda_1 \lambda_2 \lambda_3 = 1). \tag{5.9}$$

Here, $\mathbb{C}_1$ and $\mathbb{C}_2$ are two material constants characterizing the structural response of the hyperelasic material; they are determined empirically by comparison to experiments [198]. Equation (5.9) is traditionally invoked to describe the response of highly elastic, i.e., rubber like, materials under isothermal conditions [198]. In particular, setting $\mathbb{C}_2 = 0$ reduces the Mooney–Rivlin model to the neo-Hookean solid. For most "rubber-like" materials, $\mathbb{C}_1 > 0$ and $\mathbb{C}_2 \leq 0$ [199–201]. For compatibility with linear (i.e., small-strain) elasticity theory (see [196, Eq. (6.11.29)]), we must have

$$G = 2(\mathbb{C}_2 + \mathbb{C}_1) \tag{5.10}$$

as the shear modulus of elasticity. We also recall that, for a linearly elastic material,

$$2G(1 + \nu) = E, \tag{5.11}$$

where ν is the Poisson ratio, and E is Young's modulus.

Now, for isotropic materials, the principal Cauchy stresses are coaxial with the principal stretches and are given by

$$\sigma_1 - \sigma_3 = \lambda_1 \frac{\partial W}{\partial \lambda_1} - \lambda_3 \frac{\partial W}{\partial \lambda_3}, \tag{5.12a}$$

$$\sigma_2 - \sigma_3 = \lambda_2 \frac{\partial W}{\partial \lambda_2} - \lambda_3 \frac{\partial W}{\partial \lambda_3}. \tag{5.12b}$$

Substituting Eq. (5.9) into Eqs. (5.12), we obtain

$$\sigma_1 - \sigma_3 = 2\mathbb{C}_1 \left(\lambda_1^2 - \lambda_3^2 \right) - 2\mathbb{C}_2 \left(\lambda_1^{-2} - \lambda_3^2 \right), \tag{5.13a}$$

$$\sigma_2 - \sigma_3 = 2\mathbb{C}_1 \left(\lambda_2^2 - \lambda_3^2 \right) - 2\mathbb{C}_2 \left(\lambda_2^{-2} - \lambda_3^2 \right). \tag{5.13b}$$

Static equilibrium

As mentioned above, our exemplar thin-walled cylinder acts as a pressure vessel, i.e., a structure that sustains only stretching and tension but no bending or twisting. For such a structure, the equations of static equilibrium take the form:

$$\sigma_1 = \sigma_{rr} = -p, \tag{5.14a}$$

$$\sigma_2 = \sigma_{\theta\theta} = \frac{pR}{t}, \tag{5.14b}$$

$$\sigma_3 = \sigma_{zz} = \frac{pR}{2t}. \tag{5.14c}$$

Since the tube is thin, i.e., $t \ll a$ and $R = O(a)$, then $\sigma_1 \ll \sigma_2 \approx \sigma_3$. Substituting Eqs. (5.14) (stress balance) into Eqs. (5.13) (constitutive) and employing Eqs. (5.8) (deformation), we obtain

$$-\frac{pR}{2t} = 2\mathbb{C}_1 \left(\frac{a^2}{R^2} - 1 \right) - 2\mathbb{C}_2 \left(\frac{R^2}{a^2} - 1 \right), \tag{5.15a}$$

$$\frac{pR}{2t} = 2\mathbb{C}_1 \left(\frac{R^2}{a^2} - 1 \right) - 2\mathbb{C}_2 \left(\frac{a^2}{R^2} - 1 \right). \tag{5.15b}$$

Combining the last two equations, we arrive at the pressure–radius relation

$$\frac{pa}{2t(\mathbb{C}_1 + \mathbb{C}_2)} = \frac{R}{a} - \frac{a^3}{R^3}, \tag{5.16}$$

where $R = a + u_r$ is the deformed tube radius, and u_r is the radial deformation (recall Fig. 5.1).

Notice that the cross-sectional area of the tube at some fixed axial location, z, is $A = \pi R^2$ [here, $R = R(z)$ due to FSI]. Then, Eq. (5.16) can be rewritten as a *pressure–area* relationship:

$$p(\bar{A}) = 2(\mathbb{C}_1 + \mathbb{C}_2)\frac{\bar{t}}{\sqrt{\bar{A}}}\left(\bar{A} - \frac{1}{\bar{A}}\right), \tag{5.17}$$

where $\bar{t} = t/a$ is the dimensionless (reduced) thickness of the tube, and $\bar{A} = A/(\pi a^2)$ is the dimensionless (reduced) area of the deformed tube under axisymmetric conditions (initial circular cross-section remains circular under deformation). Equation (5.17) represent a *tube law* [49] for microscale FSI in a hyperelastic pressure vessel. This "law" is often used as a "constitutive" equation (closure) in unsteady FSI problems in which the flow is cross-sectionally averaged [47]. Of interest is to note that $p(\bar{A})$ in Eq. (5.17) is *nonlinear*.

Finally, let us make Eq. (5.16) dimensionless using the following dimensionless variables

$$\bar{u}_{\bar{r}} = u_r/a, \qquad \bar{p} = p/\mathcal{P}_c, \tag{5.18}$$

to yield

$$\gamma\bar{p} = (1 + \bar{u}_{\bar{r}}) - \frac{1}{(1 + \bar{u}_{\bar{r}})^3}, \qquad \gamma := \frac{\mathcal{P}_c}{2(\mathbb{C}_1 + \mathbb{C}_2)\bar{t}}, \tag{5.19}$$

where $\bar{t} = t/a$ as above, and we have defined γ as a dimensionless parameter that captures the "strength" of fluid–structure coupling, i.e., the so-called *FSI parameter*. In our previous work on linearly elastic incompressible microtubes [160], the FSI parameter was defined as $\beta = \mathcal{P}_c/(E\bar{t})$. To connect the hyperelastic theory to the linearly elastic theory, we can use Eqs. (5.10) and (5.11), taking $\nu = 1/2$ for an incompressible material, to find that

$$\gamma = \beta/3. \tag{5.20}$$

A few remarks are in order. Equation (5.19) represents the final dimensionless form of the pressure–deformation relation for a thin-walled incompressible hyperelastic cylinder. Second, note that, being a quartic (polynomial) equation in $(1 + \bar{u}_{\bar{r}})$, Eq. (5.19) can be solved explicitly for $\bar{u}_{\bar{r}}$ as a function of $\bar{p}$ using, e.g., MATHEMATICA. However, the resulting

expression is too lengthy to be worth including here. Third, observe that both $\bar{p}$ and $\bar{u}_{\bar{r}}$ can (and do) depend on the dimensionless flow-wise coordinate $\bar{z}$, but $\bar{z}$ does not feature explicitly in the pressure–deformation relationship in Eq. (5.19).

5.2.2 Thick-walled cylinder

In this section, we account for the non-negligible thickness of a cylinder, i.e., the case of thick-walled pressure vessel, also known as *Lamé's first problem* (see, e.g., [202]).

Unlike the case of a thin-walled cylinder, the inner and outer radii of the thick-walled cylinder differ. They are, thus, denoted by r_i and r_o before deformation, and by R_i and R_o after deformation. Specifically,

$$r_i = a, \tag{5.21a}$$

$$r_o = a + t, \tag{5.21b}$$

$$R_i = a + u_r, \tag{5.21c}$$

where u_r is the radial displacement of the inner surface of the cylinder. For the problem that we have posed, the displacement of the outer surface is of no consequence to the flow within the cylinder, hence we do not discuss it; then, denoting the displacement of the inner surface by u_r is unambiguous. Since the cylinder's wall is assumed to be composed of an incompressible material (constant volume), and it is clamped at both its ends (constant length), its cross sectional area remains constant. Therefore,

$$R_o^2 - R_i^2 = r_o^2 - r_i^2. \tag{5.22}$$

The cylinder kinematics (Sec. 5.2.1) and the hyperelastic constitutive equations (Sec. 5.2.1) developed for the thin-walled cylinder also apply to the thick-walled one. However, unlike the previously discussed case, the stress and deformation fields are not constant for a thick-walled cylinder. Specifically, the stress and deformation vary across the thickness of the cylinder. Consequently, the equations for static equilibrium of a thick-walled tube are differential equations. Neglecting body forces (due to the small scale of the posed FSI

problem) and shear stresses, the equations for static equilibrium [164, 165, 173, 197] are thus:

$$\frac{\partial \sigma_{rr}}{\partial R} + \frac{1}{R}(\sigma_{rr} - \sigma_{\theta\theta}) = 0, \tag{5.23a}$$

$$\frac{\partial \sigma_{zz}}{\partial Z} = 0. \tag{5.23b}$$

The latter equations, when written in terms of material coordinates in association with the deformation field described in Eq. (5.5), reduce to

$$\frac{\partial (R\sigma_{rr})}{\partial r} + \frac{r}{R}\sigma_{\theta\theta} = 0, \tag{5.24a}$$

$$\frac{\partial \sigma_{zz}}{\partial z} = 0. \tag{5.24b}$$

Note that Eq. (5.24b) is satisfied identically.

As above, $\sigma_{rr}(= \sigma_1)$ and $\sigma_{\theta\theta}(= \sigma_2)$ are also related by Eq. (5.13), i.e., the principal stress relations for an isotropic, hyperelastic Mooney–Rivlin material. Thus, we can eliminate $\sigma_{\theta\theta}$ from the constitutive equation (5.13) and the static equilibrium equations (5.24). Then, employing the expressions for the principal stretches λ_1 and λ_2 from Eq. (5.8), we obtain the following differential equation governing σ_{rr}:

$$\frac{\partial (R\sigma_{rr})}{\partial r} + \frac{r}{R}\left\{\sigma_{rr} + 2(\mathbb{C}_1 + \mathbb{C}_2)\left[\left(\frac{R}{r}\right)^2 - \left(\frac{r}{R}\right)^2\right]\right\} = 0. \tag{5.25}$$

We solve Eq. (5.25) for σ_{rr} subject to the loading boundary conditions

$$\sigma_{rr}|_{r=r_o} = 0, \tag{5.26a}$$

$$\sigma_{rr}|_{r=r_i} = -p, \tag{5.26b}$$

to obtain the pressure–radius relation

$$p = \left[f\left(\frac{r_1^2}{R_1^2}\right) - f\left(\frac{r_i^2}{R_i^2}\right)\right](\mathbb{C}_1 + \mathbb{C}_2), \tag{5.27}$$

where, for convenience, the function f is defined (see also [197]) as

$$f(\xi) := \xi + \ln \xi. \tag{5.28}$$

Note that Eq. (5.27) is equivalent to Eq. (3.4.3) in [197, Ch. 9]. It is relevant to remind the reader that $p \neq p(r)$, so the integration of Eq. (5.25) is straightforward.

Finally, substituting the geometric relationships from Eqs. (5.21) and (5.22) into Eq. (5.27), we obtain

$$\frac{p}{\mathbb{C}_1 + \mathbb{C}_2} = \left[f \left(\frac{(1+t/a)^2}{(1+t/a)^2 - 1 + (1+u_r/a)^2} \right) - f \left(\frac{1}{(1+u_r/a)^2} \right) \right]. \tag{5.29}$$

The last equation can be re-written in dimensionless form using the variables from Eq. (5.18) as

$$2\bar{t}\gamma\bar{p} = \left[f \left(\frac{(1+\bar{t})^2}{(1+\bar{t})^2 - 1 + (1+\bar{u}_{\bar{r}})^2} \right) - f \left(\frac{1}{(1+\bar{u}_{\bar{r}})^2} \right) \right], \tag{5.30}$$

where γ is the FSI parameter as defined in Eq. (5.19) above. Equation (5.30) represents the final dimensionless form of the pressure–deformation relation for a thick-walled incompressible hyperelastic cylinder.

5.3 Coupling of the fluid and structural mechanics problems

We now turn to the main task, which is coupling the flow and deformation. As shown in our previous work [160], this task is accomplished by computing the flow rate q explicitly using its definition for an axisymmetric cylindrical tube:

$$q = \int_0^{2\pi} \int_0^{R_i} v_z \, r \, dr \, d\theta = \mathcal{V}_z 2\pi a^2 \int_0^{\bar{R}_i} \bar{v}_{\bar{z}} \, \bar{r} \, d\bar{r}, \tag{5.31}$$

where we have also introduced the dimensionless variables from Eq. (5.1). Now, substituting the expression for $\bar{v}_{\bar{z}}$ from Eq. (5.3) into Eq. (5.31), we obtain the *dimensionless* flow rate

$$\bar{q} \equiv \frac{q}{\mathcal{V}_z \pi a^2} = \left(-\frac{1}{2} \frac{d\bar{p}}{d\bar{z}} \right)^{1/n} \frac{\bar{R}_i^{3+1/n}}{3+1/n}, \tag{5.32}$$

where $\bar{R}_i = 1 + \bar{u}_{\bar{r}}$ is the dimensionless *inner* radius of the deformed tube.

Thus, since $\bar{q} = const.$ by conservation of mass in a steady flow [123], Eq. (5.32) becomes an ordinary differential equation (ODE) for $\bar{p}(\bar{z})$:

$$\frac{d\bar{p}}{d\bar{z}} = -2[(3+1/n)\bar{q}]^n [1 + \bar{u}_{\bar{r}}(\bar{z})]^{-(1+3n)}. \tag{5.33}$$

Now, we must specify the deformation profile $\bar{u}_{\bar{r}}$ to complete the calculation. Even in the special case of a Newtonian fluid ($n = 1$), Eq. (5.33) represents a strongly nonlinear pressure gradient–deformation coupling.

5.3.1 Thin-walled cylinder

To finish the derivation of the coupled FSI theory for a thin-walled cylinder, we differentiate the pressure–deformation relation from Eq. (5.19) with respect to $\bar{z}$ to obtain

$$\gamma \frac{\mathrm{d}\bar{p}}{\mathrm{d}\bar{z}} = \left[1 + \frac{3}{(1 + \bar{u}_{\bar{r}})^4}\right] \frac{\mathrm{d}\bar{u}_{\bar{r}}}{\mathrm{d}\bar{z}}. \tag{5.34}$$

Then, we eliminate $\mathrm{d}\bar{p}/\mathrm{d}\bar{z}$ between Eqs. (5.33) and (5.34) to obtain an ODE for $\bar{u}_{\bar{r}}$:

$$-2\gamma[(3 + 1/n)\bar{q}]^n = \left[(1 + \bar{u}_{\bar{r}})^{3n+1} + (1 + \bar{u}_{\bar{r}})^{3n-3}\right] \frac{\mathrm{d}\bar{u}_{\bar{r}}}{\mathrm{d}\bar{z}}. \tag{5.35}$$

Since conservation of mass dictates that $\bar{q} = const.$, and γ and n are known constants, the ODE (5.35) can be separated and directly integrated, subject to the boundary condition (BC) $\bar{u}_{\bar{r}}(\bar{z} = 1) = 0$,[1] to yield:

$$2\gamma[(3 + 1/n)\bar{q}]^n(1 - \bar{z}) = \frac{[1 + \bar{u}_{\bar{r}}(\bar{z})]^{3n+2}}{(3n + 2)} + \frac{[1 + \bar{u}_{\bar{r}}(\bar{z})]^{3n-2}}{(3n - 2)} - \frac{6n}{(3n + 2)(3n - 2)}. \tag{5.36}$$

Equations (5.19) and (5.36) fully specify (albeit implicitly) the static response of a thin hyperelastic cylinder due to internal flow of a generalized Newtonian fluid within it. For example, the displacement at $\bar{z} = 0$ found from Eq. (5.36) can be used in Eq. (5.19) to determine $\bar{p}(0)$ from which the full dimensionless pressure drop follows: $\Delta\bar{p} := \bar{p}(0) - \bar{p}(1)$, where $\bar{p}(1) = 0$ is our chosen pressure gauge for the pressure at the outlet and also in the surrounding medium exterior to the cylinder. Thus, the flow rate–pressure drop relationship ($\bar{q}$ as a function of $\Delta\bar{p}$, or vice versa), i.e., a generalized Hagen–Poiseuille law, in the presence of FSI can be obtained analytically.

---

[1]Note, more importantly, that although in general we cannot expect to satisfy *clamping* BCs, i.e., $\bar{u}_{\bar{r}} = \mathrm{d}\bar{u}_{\bar{r}}/\mathrm{d}\bar{z} = 0$ at $\bar{z} = 0$ and $\bar{z} = 1$ in this leading-order analysis of deformation, we *must* respect the pressure outlet BC, i.e., $\bar{p}(\bar{z} = 1) = 0$. From Eq. (5.19), it is then clear that the pressure BC requires that $\bar{u}_{\bar{r}}(\bar{z} = 1) = 0$ as assumed.

5.3.2 Thick-walled cylinder

For a thick-walled cylinder, we differentiate Eq. (5.30) with respect to $\bar{z}$ to obtain

$$\gamma \frac{\mathrm{d}\bar{p}}{\mathrm{d}\bar{z}} = -\left\{ \frac{2(1+\bar{t})^2(1+\bar{u}_{\bar{r}})}{[(1+\bar{t})^2 + (\bar{u}_{\bar{r}})^2 + 2\bar{u}_{\bar{r}}]^2} + \frac{2(1+\bar{u}_{\bar{r}})}{(1+\bar{t})^2 + (\bar{u}_{\bar{r}})^2 + 2\bar{u}_{\bar{r}}} \right.$$
$$\left. -\frac{2}{(1+\bar{u}_{\bar{r}})} - \frac{2}{(1+\bar{u}_{\bar{r}})^3} \right\} \frac{\mathrm{d}\bar{u}_{\bar{r}}}{\mathrm{d}\bar{z}}. \quad (5.37)$$

Then, we eliminate $\mathrm{d}\bar{p}/\mathrm{d}\bar{z}$ between Eqs. (5.33) and (5.37) to obtain an ODE for the dimensionless transverse deflection $\bar{u}_{\bar{r}}$:

$$\left\{ \frac{2(1+\bar{t})^2(1+\bar{u}_{\bar{r}})}{[(1+\bar{t})^2 + (\bar{u}_{\bar{r}})^2 + 2\bar{u}_{\bar{r}}]^2} + \frac{2(1+\bar{u}_{\bar{r}})}{(1+\bar{t})^2 + (\bar{u}_{\bar{r}})^2 + 2\bar{u}_{\bar{r}}} - \frac{2}{(1+\bar{u}_{\bar{r}})} \right.$$
$$\left. -\frac{2}{(1+\bar{u}_{\bar{r}})^3} \right\} \frac{\mathrm{d}\bar{u}_{\bar{r}}}{\mathrm{d}\bar{z}} = \bar{t}\gamma[(3+1/n)\bar{q}]^n (1+\bar{u}_{\bar{r}})^{-(1+3n)}, \quad (5.38)$$

subject to the BC that $\bar{u}_{\bar{r}}(1) = 0$, as before. Unlike, Eq. (5.35), Eq. (5.38) cannot be integrated directly, thus it must be solved numerically. We employ the `odeint` subroutine of the Python package SciPy [140], with default error tolerances, for this integration.

Equations (5.30) and (5.38) fully specify the static FSI response of the thick-walled hyperelastic cylinder due to the flow of the generalized Newtonian fluid within. Together these two equations can be used to develop the flow rate–pressure relationship for a thick-walled hyperelastic tube, however the calculation must be done via numerical quadratures, unlike the case of the thin-walled cylinder (Sec. 5.3.1).

5.4 Linearly elastic thick-walled cylinder

In this section, we derive the flow rate–pressure drop relationship for steady flow of a power-law fluid within a linearly elastic, thick-walled pressure vessel of thickness t, and inner radius $r_i = a$. The pressure vessel is subject only to an internal distributed pressure

load p, with zero external pressure. Then, the state of stress evaluated at the inner radius (see [203]) is:

$$\sigma_{\theta\theta} = \left(\frac{r_o^2 + r_i^2}{r_o^2 - r_i^2}\right) p, \tag{5.39a}$$

$$\sigma_{rr} = -p, \tag{5.39b}$$

$$\sigma_{zz} = \left(\frac{r_i^2}{r_o^2 - r_i^2}\right) p. \tag{5.39c}$$

The hoop strain is given by the constitutive equations of linear elasticity as:

$$\varepsilon_{\theta\theta} = \frac{u_r}{r_i} = \frac{1}{E}\left[\sigma_{\theta\theta} - \nu(\sigma_{zz} + \sigma_{rr})\right]. \tag{5.40}$$

Using Eqs. (5.39) and (5.40) yields

$$\frac{u_r}{r_i} = \frac{1}{E}\left[\left(\frac{r_o^2 + r_i^2}{r_o^2 - r_i^2}\right) p - \nu\left(\frac{r_i^2}{r_o^2 - r_i^2} - 1\right) p\right], \tag{5.41}$$

which, upon using Eqs. (5.18) and (5.21), becomes

$$\frac{u_r}{r_i} = \bar{t}\left[\frac{(1 + \bar{t})^2(1 + \nu) + (1 - 2\nu)}{(1 + \bar{t})^2 - 1}\right]\beta\bar{p}; \qquad \beta = \frac{\mathcal{P}_c}{E\bar{t}}. \tag{5.42}$$

After deformation, the inner radius is $R_i = r_i + u_r$ (where, initially, $r_i = a$). Thus, the dimensionless inner radius is

$$\bar{R}_i = \frac{r_i + u_r}{r_i} = 1 + \frac{u_r}{r_i} = 1 + \left[\frac{(1 + \bar{t})^2(1 + \nu) + (1 - 2\nu)}{2 + \bar{t}}\right]\beta\bar{p}. \tag{5.43}$$

Substituting the expression for $\bar{R}_i$ from Eq. (5.43) into Eq. (5.33), we obtain an ODE for the dimensionless pressure $\bar{p}$:

$$\frac{\mathrm{d}\bar{p}}{\mathrm{d}\bar{z}} = -2[(3 + 1/n)\bar{q}]^n \left(1 + \mathfrak{K}\beta\bar{p}\right)^{-(1+3n)}, \tag{5.44}$$

where we have defined $\mathfrak{K} := [(1 + \bar{t})^2(1 + \nu) + (1 - 2\nu)]/(2 + \bar{t})$ for convenience. As usual, the ODE (5.44) is separable and subject to a pressure outlet BC [i.e., $\bar{p}(1) = 0$], thus we obtain:

$$\bar{p}(\bar{z}) = \frac{1}{\mathfrak{K}\beta}\left(\left\{1 + 2(2 + 3n)\mathfrak{K}\beta[(3 + 1/n)\bar{q}]^n(1 - \bar{z})\right\}^{1/(2+3n)} - 1\right). \tag{5.45}$$

Then, the full pressure drop is simply $\Delta\bar{p} = \bar{p}(\bar{z} = 0)$. Note that $\mathfrak{K} = (1 - \nu/2) + O(\bar{t})$, thus the expression for $\Delta\bar{p}$ based on Eq. (5.45) [i.e., Eq. (5.47) above] reduces to Eq. (5.46) (based on [160]) identically for thin shells ($\bar{t} \ll 1$).

5.5 Results and discussion

Let us now illustrate the deformation–pressure and flow rate–pressure drop relationships predicted by our FSI theory for the interaction between the steady flow of a power-law fluid within a soft hyperelastic cylindrical vessel containing it. Specifically, in this section, we wish to highlight the effect of hyperelasticity on the structural response of the microtube.

In Fig. 5.2, we plot the dimensionless pressure drop $\Delta \bar{p}$ across a thin-walled microtube as a function of the dimensionless inlet flow rate $\bar{q}$ for different values of the FSI parameter $\beta (= 3\gamma)$. The curves (solid) for the thin-walled hyperelastic tube are obtained from the present theory, namely Eqs. (5.19) and (5.36), while the curves (dashed) pertaining to the thin-walled linearly elastic tube are calculated based on the results from our previous study [160], namely:

$$\Delta \bar{p} = \frac{1}{(1 - \nu/2)\beta} \left(\left\{ 1 + 2(2 + 3n)(1 - \nu/2)\beta [(3 + 1/n)\bar{q}]^n \right\}^{1/(2+3n)} - 1 \right), \qquad (5.46)$$

We note that, for both linearly elastic and hyperelastic tubes, the pressure drop decreases with $\beta (= 3\gamma)$. This observation is attributed to the very definition of β as the parameter symbolizing the strength of the FSI coupling. For large β values, there is "stronger" FSI coupling than at small β values and, hence, there is larger deformation of the tube. Consequently, the cross-sectional area increases, lowers the resistance to the flow, and culminates in a smaller pressure drop for large β compared to small β.

Perhaps more attuned to the thesis of this chapter is the difference in the response of a hyperelastic and the responce of a linearly elastic tube for the *same* FSI coupling strength. Thus, comparing the solid and dashed curves, respectively, in Fig. 5.2 at fixed γ (i.e., same color), we observe that a hyperelastic tube supports a higher pressure drop than a linearly elastic tube. We explain this trend by noting that a hyperelastic tube, in general, is stiffer and has a higher tendency to preserve its original configuration compared to a linearly elastic tube. In other words, a hyperelastic material requires higher pressure than a linearly elastic material to sustain the same deformations (see also [204, 205]).
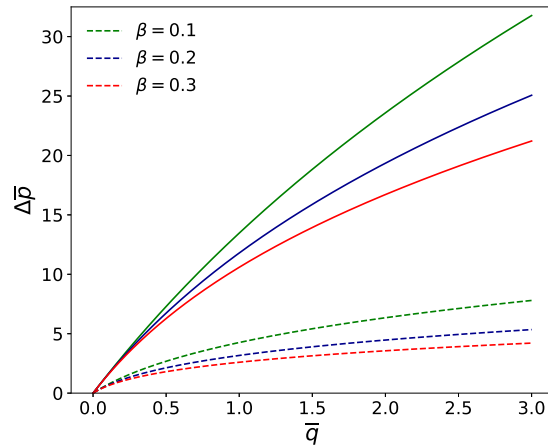
(a) $n = 1$ (Newtonian)
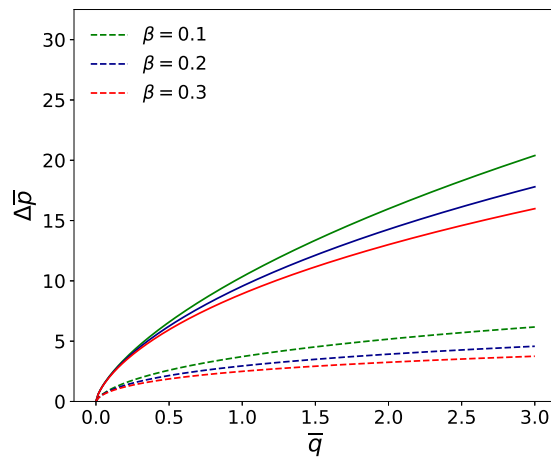
(b) $n = 0.7$ (pseudoplastic)

Fig. 5.2. The dimensionless (full) pressure drop across a thin-walled microtube as a function of the dimensionless inlet flow rate $\bar{q}$ for different values of FSI parameter $\beta = 3\gamma$. Hyperelastic thin-walled tubes correspond to solid curves, while linearly elastic thin-walled tubes correspond to dashed curves for (a) a Newtonian fluid with $n = 1.0$ (e.g., blood plasma), and (b) a shear-thinning fluid with $n = 0.7$ (e.g., whole blood). For the hyperelastic tube, the corresponding theory has been presented in Sec. 5.3.1, while for linearly elastic tubes the predicted pressure drop is given by Eq. (5.46) derived in [160].

Next, we move on to the case of thick-walled tubes and compare, in Fig. 5.3, the flow rate–pressure drop relation in a thick-walled hyperelastic tube obtained from the present theory, namely Eqs. (5.30) and (5.38), with the corresponding relationship for a thick-walled linearly elastic tube calculated based on

$$\Delta\bar{p} = \frac{1}{\mathfrak{K}\beta}\left(\left\{1 + 2(2+3n)\mathfrak{K}\beta[(3+1/n)\bar{q}]^n\right\}^{1/(2+3n)} - 1\right), \qquad (5.47)$$

which was derived from Eq. (5.45) ; $\mathfrak{K} = [(1+\bar{t})^2(1+\nu) + (1-2\nu)]/(2+\bar{t})$ and $\bar{t} = t/a$. For the same reason as above, an increase in $\beta(= 3\gamma)$ causes $\Delta\bar{p}$ to decrease.

Things become more interesting, however, when the curves corresponding to same value of the FSI parameter β are compared (solid vs. dashed) in Fig. 5.3. For small $\bar{q}$ and small β, the linearly elastic tube deforms less and sustains a larger $\Delta\bar{p}$ compared to the hyperelastic one. However, this trend is reversed for large $\bar{q}$ and large β, for which the hyperelastic tube sustains a higher $\Delta\bar{p}$ than the linearly elastic one. This interesting observation can be explained by the very nature of hyperelasticity. It is more difficult to deform a hyperelastic material as the deformation increases, i.e., hyperelastic materials exhibit *strain-stiffening* [199–201]. Mathematically, this resistance to deformation can be measured through the rate of change of the stress with respect to the strain (or deformation). To this end, when we differentiate the constitutive equation for a hyperelastic material, namely Eq. (5.13), with respect to the principal deformation along the "1" direction, whilst keeping the deformations in the other directions constant for simplicity, to obtain:

$$\frac{\partial\sigma_1}{\partial\lambda_1} = 4\mathbb{C}_1\lambda_1 + 4\mathbb{C}_2/\lambda_1^3. \qquad (5.48)$$

From the latter equation it follows that the resistance to deformation increases with deformation (keeping in mind that $\mathbb{C}_2 < 0$). On the other hand, for a linearly elastic material, the resistance to deformation is given by Young's modulus E (at least for a uniaxial load), which is a constant!

One could also interpret the much larger $\Delta\bar{p}$ in hyperelastic (over linearly elastic) thin-wall cylinders in Fig. 5.2 as a consequence of strain-hardening. However, in that case, due to significant resistance to deformation of the thin-walled hyperelastic vessel (there is

almost one order of magnitude difference in the vertical scales between Figs. 5.2 and 5.3), the interplay between $\bar{q}$ and β values just described is not present.

Finally, we also note that an increase in the cylinder thickness will lead to a corresponding decrease in the pressure drop, although this is not shown in Fig. 5.3, in which all the curves have been plotted for a constant ratio $\bar{t} = t/a = 0.3$. This result is similar to the one for thick linearly elastic plates, which was discussed in our previous work [60], and it can be attributed to an increase in the normal stress throughout the structure's thickness as $\bar{t}$ increases.

5.6 Conclusion

In this chapter, we have solved the problem of steady-state low Reynolds number fluid–structure interaction (FSI) between a generalized Newtonian fluid and a hyperelastic cylindrical tube. The hydrodynamic pressure, which is needed to maintain a unidirectional flow in a deformed cylindrical pipe, was transferred as a load onto the elastic structure, the mechanics of which were analyzed using the *thin* and *thick* pressure vessels theories for isotropic, incompressible Mooney–Rivlin materials. The fluid and solid mechanics were brought together to yield a coupled equation relating the constant inlet flow rate q to the tube's radial deformation $u_r(z)$. For a thin-walled pressure vessel, the latter relation takes the *implicit* dimensional form

$$\frac{m\left[(3 + 1/n)q\right]^n}{(\mathbb{C}_1 + \mathbb{C}_2)t}(\ell - z) = \frac{[a + u_r(z)]^{(3n+2)}}{a^2(3n + 2)} + \frac{a^2[a + u_r(z)]^{(3n-2)}}{(3n - 2)}$$
$$- \frac{6na^{3n}}{(3n + 2)(3n - 2)}. \quad (5.49)$$

As a special case, we have also found the flow rate–deformation relation for a Newtonian fluid ($n = 1$, and $m = \mu$ is the shear viscosity):

$$\frac{4\mu q}{(\mathbb{C}_1 + \mathbb{C}_2)t}(\ell - z) = \frac{[a + u_r(z)]^5}{5a^2} + a^2[a + u_r(z)] - \frac{6a^3}{5}, \quad (5.50)$$
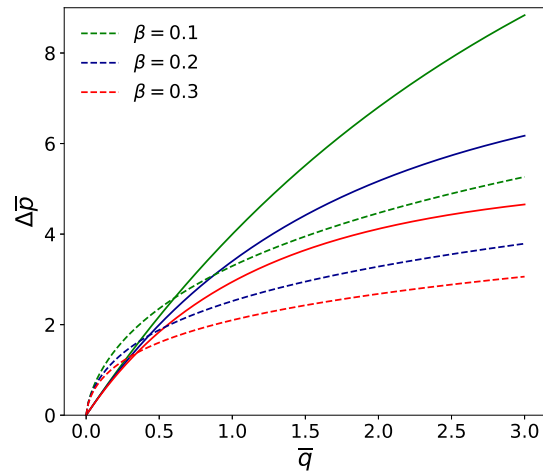
(a) $n = 1$ (Newtonian)
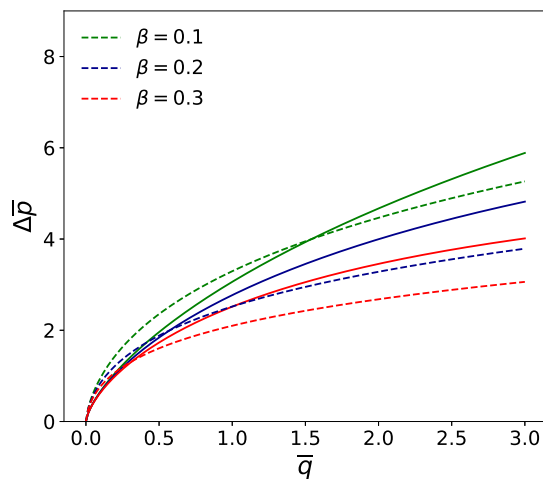
(b) $n = 0.7$ (pseudoplastic)

Fig. 5.3. The dimensionless (full) pressure drop across a thick-walled micro-tube as a function of the dimensionless inlet flow rate $\bar{q}$ for different values of FSI parameter $\beta = 3\gamma$ and $\bar{t} = t/a = 0.3$. Hyperelastic thick-walled tubes correspond to solid curves, while linearly elastic thick-walled tubes correspond to dashed curves, for (a) a Newtonian fluid with $n = 1.0$ (e.g., blood plasma), and (b) a shear-thinning fluid with $n = 0.7$ (e.g., whole blood). For a thick-walled hyperelastic tube, the corresponding theory was presented in Sec. 5.3.2, while for thick-walled linearly elastic tubes the predicted pressure drop is given by Eq. (5.47).

which is an implicit relation for $u_r(z)$ given q. Whence, the equation relating the pressure $p(z)$ at an axial location z with the deformation $u_r(z)$ is

$$p(z) = 2(\mathbb{C}_1 + \mathbb{C}_2)\left(\frac{t}{a}\right)\left\{[1 + u_r(z)/a] - \frac{1}{[1 + u_r(z)/a]^3}\right\}. \tag{5.51}$$

Consonant with our previous FSI results [60, 160], the pressure–deformation relationship is set by the structural mechanics alone, hence it *does not explicitly depend* upon the fluid's rheology.

Equations (5.49) [or (5.50)] and (5.51) fully specify the FSI problem for a thin-walled hyperelastic cylinder. In deriving these equations, we arrived at the dimensionless *FSI parameter γ*, which determines the "strength" of the coupling between flow and deformation fields:

$$\gamma := \frac{\mathcal{P}_c}{2(\mathbb{C}_1 + \mathbb{C}_2)}\left(\frac{a}{t}\right) \tag{5.52}$$

for a hyperelastic cylinder with material constants $\mathbb{C}_1$ and $\mathbb{C}_2$. Here, the pressure scale $\mathcal{P}_c$ depends on the nature of the physical scenario at hand. For a flow-rate-controlled experiment and/or simulation, as considered in this chapter for example, we set $\mathcal{P}_c = [q/(\pi a^2)]^n m\ell/a^{n+1}$, as dictated by the fluid's momentum balance. On the other hand, for a pressure-drop-controlled experiment or simulation, we can directly set $\mathcal{P}_c = \Delta p$, which means the fluids velocity scale $\mathcal{V}_z$ discussed above becomes a function of the dimensional pressure drop Δp.

We compared the predicted q–Δp relation due to the hyperelastic FSI theory developed in this chapter with the corresponding relation due to linearly elastic FSI theory form previous work [160]. In particular, we concluded that a hyperelastic microtube supports smaller deformations than a linearly elastic microtube for the same hydrodynamic pressure, or conversely a hyperelastic microtube can sustain a higher pressure drop than a linearly elastic one, for the same deformation. Finally, our observation in Sec. 5.5 that the pressure drop across a soft microtube *decreases* with the wall thickness is in agreement with the case of rectangular microchannels with a plate for a top wall, which we considered in our previous work [60].

6. DEFORMABLE MICROTUBES: TRANSIENT VISCOELASTIC RESPONSE TO COMPRESSIBLE FLOW

SUMMARY

Motivated by problems arising in the pneumatic actuation of controllers (for MEMS, labs-on-a-chip or biomimetic soft robots) and the study of microrheology of both gases and soft solids, we analyze the transient fluid–structure interactions (FSIs) in an viscoelastic tube conveying compressible flow at low. Under the lubrication approximation, the density of the fluid is expressed as a linear function of the pressure. For small compressibility numbers, the flow is coupled to a structural mechanical problem, in which the correspondence principle allows us to modify Donnell shell theory and account for Kelvin–Voigt-type linear viscoelastic response. The resulting fluid and structural mechanics equations are coupled through the deformed radius and the hydrodynamic pressure. For weak coupling, the equations are solved analytically via a perturbation expansion. Three illustrative sub-problems are analyzed. First is steady flow, in which the structure behaves like a linearly elastic tube, without inertia or dissipation. Second is the transient problem of impulsive pressurization of the tube's inlet. Third is the transient response to an oscillatory inlet pressure. We show that the low Reynolds number flow in the tube requires a finite time to adjust to transient forcing due to FSI. An oscillatory inlet pressure leads to acoustic streaming in the tube, attributed to the nonlinear pressure gradient induced by FSI and compressibility. We demonstrate an enhancement in the volumetric flow rate due to the coupling of compressibility and FSI, which has a low-pass frequency response (when averaged over the period of oscillations). On the other hand, the corresponding frequency response of the tube deformation is similar to that of a band-pass filter.

6.1 Mathematical formulation of the problem

6.1.1 Preliminaries

The flow domain of interest consists of an initially cylindrical tube (see Fig. 6.1) of undeformed radius a, thickness h and length ℓ. The tube is assumed to be thin ($h \ll a$) and slender ($a \ll \ell$). The tube is made of an isotropic, homogeneous, and linearly viscoelastic material that obeys the KV material model, also sometimes referred to as just the 'Voigt model' [57, Ch. 2].

Both the structural mechanical and fluid mechanical fields are considered axisymmetric in θ. The tube conveys a Newtonian gas. Since this gas flow can be (in general) both unsteady and compressible, the flow rate $\bar{q}$ is a function of both axial location $\bar{z}$ and time $\bar{t}$, i.e., $\bar{q} = \bar{q}(\bar{z}, \bar{t})$. The density of the gas at the outlet is ρ_0 corresponding to the (reference) pressure at the outlet $\bar{p} = p_0$. At the inlet, the pressure is imposed as a boundary condition. Due to the hydrodynamic pressure exerted by the transient compressible flow, the tube deforms, and the deformed radius is $\bar{R}(\bar{z}, \bar{t}) = a + \bar{u}_{\bar{r}}(\bar{z}, \bar{t})$, where $\bar{u}_{\bar{r}}$ is the radial displacement of the structure.

Through a perturbative approach, we aim to establish a predictive relationship between the key fluid mechanical and structural mechanical quantities: $\bar{q}(\bar{z}, \bar{t})$, $\bar{p}(\bar{z}, \bar{t})$, $\bar{R}(\bar{z}, \bar{t})$, and $\bar{u}_{\bar{r}}(\bar{z}, \bar{t})$, as well as their spatiotemporal variations due to unsteady flow conditions.

Assumptions:

1. Newtonian gas, with zero bulk viscosity (exact for monoatomic gases).[1]

2. Axisymmetric flow without swirl: $\partial(\,\cdot\,)/\partial\theta = 0$ and $v_\theta = 0$.

3. Slender tube: $\ell \gg a \iff \epsilon = a/\ell \ll 1$.

4. Isothermal flow.

---

[1]The assumption of zero bulk viscosity is not crucial as the terms in the momentum equation dealing with bulk viscosity are negligible under the lubrication approximation [73, 84].
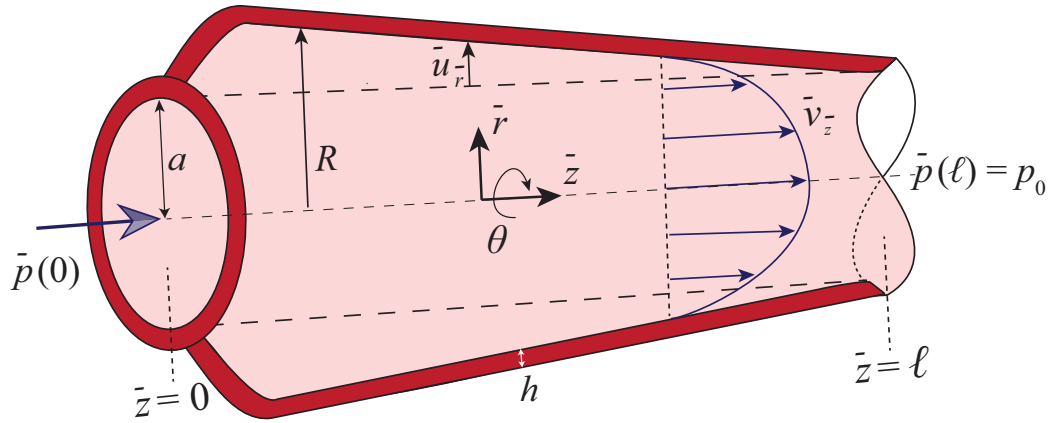
Fig. 6.1. Schematic of the microtube geometry. The origin of the coordinate system is at the inlet of the tube, however, it has been displaced from the inlet in the figure for clarity.

Continuity equation

For axisymmetric, transient flow of a gas, the equation of continuity in cylindrical co-ordinates takes the form [123, 207]:

$$\frac{\partial \bar{\rho}}{\partial \bar{t}} + \frac{1}{\bar{r}} \frac{\partial}{\partial \bar{r}} (\bar{r} \bar{\rho} \bar{v}_{\bar{r}}) + \frac{\partial}{\partial \bar{z}} (\bar{\rho} \bar{v}_{\bar{z}}) = 0, \tag{6.1}$$

where $\bar{\rho}(\bar{r}, \bar{z}, \bar{t})$ is the density of the gas and $v(\bar{r}, \bar{z}, \bar{t}) = (\bar{v}_{\bar{r}}, 0, \bar{v}_{\bar{z}})$ is its axisymmetric velocity field. We introduce the following dimensionless variables:

$$t = \bar{t}/\mathcal{T}_f, \quad r = \bar{r}/a, \quad z = \bar{z}/\ell, \quad v_z = \bar{v}_{\bar{z}}/\mathcal{V}_z, \quad v_r = \bar{v}_{\bar{r}}/\mathcal{V}_r,$$

$$\rho = \bar{\rho}/\rho_0, \quad p = (\bar{p} - p_0)/\mathcal{P}_c, \tag{6.2}$$

where $\bar{p}$ is the absolute pressure. Here, $\mathcal{P}_c$ is the characteristic pressure scale to be determined from the boundary condition, since it is a pressure controlled system. $\mathcal{V}_z$ and $\mathcal{V}_r$ are characteristic velocity scales in the axial and radial directions respectively, connected by the conservation of mass, and related to the pressure scale by the conservation of momentum equation. $\mathcal{T}_f$ is characteristic time scale, ρ_0 is characteristic scale for density, which

is the density at the outlet, where the (absolute) pressure is p_0. Substituting the variables from Eqs. (6.2) into Eq. (6.1) yields

$$\frac{\rho_0}{\mathcal{T}_f} \frac{\partial \rho}{\partial t} + \frac{\rho_0 \mathcal{V}_r}{a} \frac{1}{r} \frac{\partial}{\partial r}(\rho r v_r) + \frac{\rho_0 \mathcal{V}_z}{\ell} \frac{\partial}{\partial z}(\rho v_z) = 0. \tag{6.3}$$

Balancing the latter equation (in an order-of-magnitude sense), we obtain

$$\mathcal{V}_r = \epsilon \mathcal{V}_z, \qquad \mathcal{T}_f = \ell/\mathcal{V}_z. \tag{6.4}$$

Momentum equation

For the compressible flow of a Newtonian gas with zero bulk viscosity, the conservation of linear momentum equation in the axial, z-direction takes the form [123, 207]:

$$\bar{\rho}\left(\frac{\partial \bar{v}_{\bar{z}}}{\partial \bar{t}} + \bar{v}_{\bar{r}}\frac{\partial \bar{v}_{\bar{z}}}{\partial \bar{r}} + \bar{v}_{\bar{z}}\frac{\partial \bar{v}_{\bar{z}}}{\partial \bar{z}}\right)$$
$$= \frac{1}{\bar{r}} \frac{\partial}{\partial \bar{r}}\left(\mu \bar{r} \frac{\partial \bar{v}_{\bar{z}}}{\partial \bar{r}} + \mu \bar{r} \frac{\partial \bar{v}_{\bar{r}}}{\partial \bar{z}}\right) + \frac{\partial}{\partial \bar{z}}\left(2\mu \frac{\partial \bar{v}_{\bar{z}}}{\partial \bar{z}} - \frac{2}{3}\mu \bar{\nabla} \cdot \bar{v}\right) - \frac{\partial \bar{p}}{\partial \bar{z}}. \tag{6.5}$$

By using the scales introduced in Eqs. (6.2) and (6.4), the dimensionless form of Eq. (6.5) is

$$\frac{\rho_0 \mathcal{V}_z^2}{\ell}\rho\left(\frac{\partial v_z}{\partial t} + v_r\frac{\partial v_z}{\partial r} + v_z\frac{\partial v_z}{\partial z}\right)$$
$$= \frac{\mu \mathcal{V}_z}{a^2}\frac{1}{r}\frac{\partial}{\partial r}\left(r\frac{\partial v_z}{\partial r} + r\epsilon^2\frac{\partial v_r}{\partial z}\right) + \frac{\mu \mathcal{V}_z}{\ell^2}\frac{\partial}{\partial z}\left(2\frac{\partial v_z}{\partial z} - \frac{2}{3}\nabla \cdot v\right) - \frac{\mathcal{P}_c}{\ell}\frac{\partial p}{\partial z}. \tag{6.6}$$

As the flow is isothermal and compressible, a constitutive equation must be specified to relate $\bar{\rho}$ and $\bar{p}$. We use a linear equation of state [79, 80]:

$$\bar{\rho} = \rho_0\left(1 + \frac{\bar{p} - p_0}{\mathcal{B}_T}\right), \qquad \mathcal{B}_T = \rho_0\left(\frac{\partial \bar{p}}{\partial \bar{\rho}}\right)_T, \tag{6.7}$$

where $\mathcal{B}_T = const.$ is the isothermal bulk modulus of the gas. The dimensionless form of Eq. (6.7) is then

$$\rho = 1 + \alpha p, \qquad \alpha = \mathcal{P}_c/\mathcal{B}_T, \tag{6.8}$$

where the dimensionless parameter α is termed the compressibility number. The chosen equation of state (6.8) (and its dimensional counterpart, Eq. (6.7)) can be interpreted as a

Taylor-series expansion of the density about the outlet value, in terms of the gauge pressure. Compressibility effects are important in the flow if $\mathcal{P}_c \sim \mathcal{B}_T$, i.e., $\alpha = O(1)$. Therefore, α herein fulfills the same role, for low-Re viscous flow, as Ma does for high-Re inertial flow.[2]

Using Eq. (6.8), Eq. (6.6) can be rewritten as:

$$
\epsilon Re(1 + \alpha p) \left(\frac{\partial v_z}{\partial t} + v_r \frac{\partial v_z}{\partial r} + v_z \frac{\partial v_z}{\partial z} \right)
$$

$$
= \frac{1}{r} \frac{\partial}{\partial r} \left(r \frac{\partial v_z}{\partial r} + \epsilon^2 r \frac{\partial v_r}{\partial z} \right) + \epsilon^2 \frac{\partial}{\partial z} \left(2 \frac{\partial v_z}{\partial z} - \frac{2}{3} \nabla \cdot v \right) - \frac{\mathcal{P}_c a^2}{\ell \mathcal{V}_z \mu} \frac{\partial p}{\partial z}, \quad (6.9)
$$

where

$$
Re = \frac{\rho_0 \mathcal{V}_z a}{\mu} \quad (6.10)
$$

is the Reynolds number. To the leading order in $O(\epsilon^2, \epsilon Re)$, Eq. (6.9) reduces to:

$$
0 = \frac{1}{r} \frac{\partial}{\partial r} \left(r \frac{\partial v_z}{\partial r} \right) - \frac{\mathcal{P}_c a^2}{\ell \mathcal{V}_z \mu} \frac{\partial p}{\partial z}. \quad (6.11)
$$

Balancing the last equation yields the axial velocity scale

$$
\mathcal{V}_z = \frac{\mathcal{P}_c a^2}{\mu \ell}. \quad (6.12)
$$

We study pressure-controlled systems in which $\mathcal{P}_c$ is set by the boundary conditions, so $\mathcal{V}_z$ can be, in principle, calculated from Eq. (6.12).[3] Thus, Eq. (6.11) is finally written as:

$$
0 = \frac{1}{r} \frac{\partial}{\partial r} \left(r \frac{\partial v_z}{\partial r} \right) - \frac{\partial p}{\partial z}. \quad (6.13)
$$

Using Eqs. (6.2), (6.4), (6.8), (6.10) and (6.12), the dimensionless r-momentum equation [123, 207] is

$$
\epsilon^3 Re(1 + \alpha p) \left(\frac{\partial v_r}{\partial t} + v_r \frac{\partial v_r}{\partial r} + v_z \frac{\partial v_r}{\partial z} \right)
$$

$$
= \epsilon^2 \frac{1}{r} \frac{\partial}{\partial r} \left(2r \frac{\partial v_r}{\partial r} - \frac{2}{3} r \nabla \cdot v \right) + \epsilon^2 \frac{\partial}{\partial z} \left(\frac{\partial v_z}{\partial r} + \epsilon^2 \frac{\partial v_r}{\partial z} \right) - \frac{\partial p}{\partial r}. \quad (6.14)
$$

Neglecting small terms, we obtain:

$$
0 = \frac{\partial p}{\partial r}. \quad (6.15)
$$

---

[2]Commensurate with the definition of Ma in terms of speed of sound, we can also express α in terms of speed of sound c as $\alpha = \gamma \mathcal{P}_c / \rho_0 c^2$, where γ is the ratio of specific heats and $c = \sqrt{\gamma \mathcal{B}_T / \rho_0}$.

[3]We can also consider a system in which the inlet mass flow rate $\dot{m}$ is specified. Then, $\mathcal{V}_z \equiv \dot{m} / (\rho_0 \pi a^2)$, in which case $\mathcal{P}_c$ can be, in principle, calculated from Eq. (6.12).

Velocity boundary conditions

We account for rarefaction effects by introducing a slip velocity boundary condition in the flow-wise direction. This condition, which holds only at the tube's deformed radius $\bar{r} = \bar{R}$ is given by Navier's slip equation [208–210]:

$$
\begin{aligned}
\bar{v}_z|_{\bar{r}=\bar{R}} &= \left(\frac{2 - \sigma_v}{\sigma_v} \right) \frac{\lambda}{\mu} \bar{\tau}_s \\
&= - \left(\frac{2 - \sigma_v}{\sigma_v} \right) \frac{\lambda}{\mu} \left[\mu \left(\frac{\partial \bar{v}_{\bar{z}}}{\partial \bar{r}} + \frac{\partial \bar{v}_{\bar{r}}}{\partial \bar{z}} \right) \right]_{\bar{r}=\bar{R}}.
\end{aligned}
\tag{6.16}
$$

Here, σ_v is the tangential momentum accommodation coefficient (dimensionless), λ is the mean free path (length) of the gas and $\bar{\tau}_s$ is the shear stress on the wall surface.

We also introduce $Kn_0 = \lambda_0/a$ as the characteristic Knudsen number [208] corresponding to the characteristic mean free path λ_0, which itself is related to the characteristic pressure $\mathcal{P}_c$. Since the mean free path is inversely proportional to the pressure, we can write:

$$
\lambda = \frac{\lambda_0 \mathcal{P}_c}{\bar{p}} = \frac{\lambda_0}{p} \qquad \Rightarrow \qquad Kn = \frac{\lambda}{a} = \frac{\lambda_0}{pa} = \frac{Kn_0}{p}.
\tag{6.17}
$$

Therefore, the velocity boundary condition (6.16) can be re-expressed as:

$$
v_z|_{r=R} = - \left(\frac{2 - \sigma_v}{\sigma_v} \right) \frac{Kn_0}{p} \frac{\partial v_z}{\partial r} \bigg|_{r=R} + O(\epsilon^2).
\tag{6.18}
$$

Next, no-slip in the radial direction leads us to the kinematic boundary condition [123], which in dimensionless form is

$$
v_r|_{r=R} = \beta \left(\frac{\partial u_r}{\partial t} + v_z \frac{\partial u_r}{\partial z} \right)_{r=R},
\tag{6.19}
$$

where u_r is the (dimensionless) radial deformation of the tube, and we have neglected axial displacements (to be justified in Sec. 6.1.2 below). Here, $\beta = \mathcal{U}_c/a$ can be termed the *FSI parameter*; $\mathcal{U}_c$ is the characteristic deformation scale, which is to be determined upon analyzing the mechanical force balance on the structure. Then, the deformed radius $\bar{R}$, can be written in terms of the dimensionless variables as:

$$
R(z,t) = \frac{\bar{R}(\bar{z},\bar{t})}{a} = \frac{a + \bar{u}_{\bar{r}}(\bar{z},\bar{t})}{a} = 1 + \beta u_r(z,t).
\tag{6.20}
$$

Velocity field

We solve Eq. (6.11) subject to Eq. (6.18) to obtain the axial velocity field:

$$v_z(r, z, t) = -\frac{1}{2}\frac{\partial p}{\partial z}\left[\frac{(1 + \beta u_r)^2 - r^2}{2} + \left(\frac{2 - \sigma_v}{\sigma_v}\right)\frac{Kn_0}{p}(1 + \beta u_r)\right]. \qquad (6.21)$$

Observe the flow is primarily axial but it is two-dimensional. Here, β, $u_r(z, t)$, and $p(z, t)$ are independent of r. The volumetric flow rate is the area integral of the axial velocity from Eq. (6.21):

$$q(z, t) \equiv \frac{\bar{q}(\bar{z}, \bar{t})}{\mathcal{V}_z \pi a^2} = \int_0^{R(z,t)} v_z(r, z, t)\, r\, dr = -\frac{\partial p}{\partial z}\left[\frac{1}{8}(1 + \beta u_r)^4 + \frac{\sigma Kn_0}{2p}(1 + \beta u_r)^3\right]. \quad (6.22)$$

As a consistency check, observe that for $Kn_0 \to 0$ and $\beta \to 0$, Eq. (6.22) reduces to $q = -(1/8)\partial p/\partial z$, which is the Hagen–Poiseuille law in dimensionless form [31].

In previous studies of steady incompressible flow and FSI in tubes [160], the flow rate q was specified. Then, by conservation of mass $q = const$ throughout the tube and, therefore, Eq. (6.22) is simply an ordinary differential equation (ODE) in $p(z)$. In this paper, however, since we deal with unsteady compressible flow, q from Eq. (6.22) is *not* constant, i.e., $q = q(z, t)$.

To determine the governing equation for q, we integrate the continuity Eq. (6.3) across the radial extent of the tube. Upon using the boundary conditions from Eqs. (6.18) and (6.19), we obtain

$$\frac{\partial}{\partial t}\left[\frac{1}{2}\rho(1 + \beta u_r)^2\right] + \frac{\partial(\rho q)}{\partial z} = 0. \qquad (6.23)$$

Observe that the unsteady term in Eq. (6.23) can be written out as

$$\frac{\partial}{\partial t}\left[\frac{1}{2}\rho(1 + \beta u_r)^2\right] =$$

$$\frac{1}{2}\underbrace{\left(1 + \frac{\bar{u}_{\bar{r}}}{a}\right)^2}_{O(1)}\underbrace{\frac{\partial}{\partial \bar{t}}\left(\frac{\bar{p} - p_0}{\mathcal{P}_c}\right)}_{O(1)}(\alpha\mathcal{T}_f) + \underbrace{\left(1 + \frac{\bar{p} - p_0}{\mathcal{B}_T}\right)}_{O(1)}\underbrace{\left(1 + \frac{\bar{u}_{\bar{r}}}{a}\right)}_{O(1)}\underbrace{\frac{\partial}{\partial \bar{t}}\left(\frac{\bar{u}_{\bar{r}}}{\mathcal{U}_c}\right)}_{O(1)}(\beta\mathcal{T}_f). \quad (6.24)$$

From the first term on the right-hand side of Eq. (6.24), we deduce that to retain the transient response of the pressure changes in the balanced continuity equation (6.23), we must

choose time scale of compressibility as $\mathcal{T}_\alpha \sim \alpha \mathcal{T}_f = \alpha \ell / \mathcal{V}_z = O(1)$. Likewise, from the second term on the right-hand side of Eq. (6.24), we deduce that $\mathcal{T}_\beta \sim \beta \mathcal{T}_f = \beta \ell / \mathcal{V}_z = O(1)$ is the time scale of FSI (transient deformation response). The latter is same time scale deduced in prior work on microchannels [211] and microtubes [63].

The fact that we have chosen to neglect the local acceleration of the fluid, but incorporated the transient effects of compressibility and FSI, leads us to the following requirement on the dimensionless parameters:

$$\epsilon Re \ll \beta \ll 1, \qquad \epsilon Re \ll \alpha \ll 1. \tag{6.25}$$

These conditions must be satisfied for our quasi-steady lubrication theory. Observe that Eq. (6.25) does not yield an ordering between the small parameters α and β. Thus, given the lack of *a priori* scale separation, all quadratic terms in the perturbation expansions that follow are neglected.

Equations (6.22) and (6.23) contain three unknowns, namely u_r, p, q. We need another equation to uniquely determine these quantities. To that end, we turn our attention to the structural mechanics problem.

6.1.2 Structural mechanics

For this chapter, our goal is to formulate a theory of transient FSIs due to compressible flow being conveyed in a viscoelastic tube. Having delineated the fluid mechanical aspects of the FSI problem in the previous sections, we shift our focus to the structural mechanical domain. To this end, we begin by first extending Donnell's theory of thin [172], linearly elastic shells [164, 173] to include the viscoelastic response of the material.

Donnell's shell theory for a linearly elastic solid

Linearly elastic Donnell shell

In what follows, the notation is the same as that described in the schematic of the microtube in Fig. 6.1. Under the assumptions of an axisymmetric load with negligible

axial displacement [212], the normal stress resultant in the circumferential direction and the bending moment (see, e.g., [164, 173]) are

$$\bar{N}_{\theta\theta} = h\hat{E}\frac{\bar{u}_{\bar{r}}}{a}, \tag{6.26a}$$

$$\bar{M}_{\bar{z}\bar{z}} = -\frac{h^3}{12}\hat{E}\frac{\partial^2 \bar{u}_{\bar{r}}}{\partial \bar{z}^2}, \tag{6.26b}$$

respectively. Here, $\hat{E} = E/(1-\nu^2)$ is the plane strain Young's modulus, and ν is the Poisson ratio, both at steady state. Meanwhile, the equation of equilibrium in the radial direction (see, e.g., [164, 173]) is

$$\frac{\partial^2 \bar{M}_{\bar{z}\bar{z}}}{\partial \bar{z}^2} - \frac{\bar{N}_{\theta\theta}}{a} + \bar{p} = \rho_s h \frac{\partial^2 \bar{u}_{\bar{r}}}{\partial \bar{t}^2}, \tag{6.27}$$

where $\bar{p}$ is the radial load on the structure due to the fluid flow within, keeping in mind that $\bar{p} = \bar{p}(\bar{z}, \bar{t})$, and ρ_s is the constant density of the solid material.

Linearly viscoelastic Donnell shell

The correspondence between the constitutive equations of linear elasticity and the KV model of viscoelasticity [213] allows us to analogously write the versions of the constitutive relations (6.26), for a viscoelastic Donnell shell, as (see, e.g., [214, 215]):

$$\bar{N}_{\theta\theta} = \left(\frac{h}{a}\right)\hat{E}\bar{u}_{\bar{r}} + \left(\frac{h}{a}\right)C_v\frac{\partial \bar{u}_{\bar{r}}}{\partial \bar{t}}, \tag{6.28a}$$

$$\bar{M}_{\bar{z}\bar{z}} = -\frac{h^3}{12}\hat{E}\frac{\partial^2 \bar{u}_{\bar{r}}}{\partial \bar{z}^2} - \frac{h^3}{12}C_v\frac{\partial^3 \bar{u}_{\bar{r}}}{\partial \bar{t}\partial \bar{z}^2}. \tag{6.28b}$$

In short, the corresponding linearly viscoelastic Donnell shell's constitutive equations are obtained by applying the relaxation operator $1 + (C_v/\hat{E})\partial/\partial \bar{t}$ to the constitutive equations (6.26). Here, C_v is a viscoelastic modulus analogous to $\hat{E}$.

Substituting Eqs. (6.28) into the equilibrium equation (6.27), yields the following transient PDE for the radial deformation of a thin cylindrical tube made from a linearly viscoelastic material (see also [216]):

$$\frac{h^3}{12}\hat{E}\frac{\partial^4 \bar{u}_{\bar{r}}}{\partial \bar{z}^4} + \frac{h^3}{12}C_v\frac{\partial^5 \bar{u}_{\bar{r}}}{\partial \bar{t}\partial \bar{z}^4} + \frac{h}{a^2}\hat{E}\bar{u}_{\bar{r}} + \frac{h}{a^2}C_v\frac{\partial \bar{u}_{\bar{r}}}{\partial \bar{t}} + \rho_s h\frac{\partial^2 \bar{u}_{\bar{r}}}{\partial \bar{t}^2} = \bar{p}. \tag{6.29}$$

Next, we make the governing equation (6.29) dimensionless by introducing the dimensionless variables from Eq. (4.2):

$$\underbrace{\frac{\mathcal{E}^4}{12}\frac{\partial^4 u_r}{dz^4}}_{\text{bending}} + \underbrace{\frac{\mathcal{E}^4}{12De}\frac{\partial^5 u_r}{\partial z^4 \partial t}}_{\text{damping}} + \underbrace{u_r}_{\text{stretching}} + \underbrace{\frac{1}{De}\frac{\partial u_r}{\partial t}}_{\text{damping}} + \underbrace{St\frac{\partial^2 u_r}{\partial t^2}}_{\text{inertia}} = \underbrace{\frac{\mathcal{P}_c a^2}{\hat{E} h \mathcal{U}_c}p}_{\text{loading}}, \qquad (6.30)$$

where $\mathcal{U}_c$ is the characteristic deformation scale to be determined. There are three dimensionless numbers that determine the evolution of the deformation profile: $\mathcal{E}$, De, and St. First, $\mathcal{E} = \sqrt{ha/\ell^2}$ is a dimensionless number that determines the width of the bending boundary layers in the tube near its clamped edges at $z = 0, 1$. For example, $\mathcal{E} \ll 1$ means that most of the tube is in a stretching state, while $\mathcal{E} \gg 1$ corresponds to the case of a tube in a mostly bending-dominated state [173, Ch. 5]. Second, the Deborah number $De = \hat{E}\mathcal{T}_f/C_v$ [217] quantifies the viscoelastic response of the tube. For example, for $De \gg 1$, the tube behaves like an elastic solid, while for $De \ll 1$ the viscous/damping response of the tube dominates. We expect that $De > 1$ is sufficiently large to ensure that the tube structure behaves like an elastic solid (with weak damping), rather than a (non-Newtonian) liquid (with strong elasticity). Third, the Strouhal number $St = \rho_s a^2/(\mathcal{T}_f^2 \hat{E})$ quantifies the inertial response of the tube; for $St \ll 1$, the inertial response of the tube is negligible.

The unknown scale of elastic deformation $\mathcal{U}_c$ is now chosen to make the coefficient of the right-hand side of Eq. (6.30) equal to unity: $\mathcal{U}_c = \mathcal{P}_c a^2/(\hat{E} h)$, which is as in previous work on the steady problem [160], except here we have incorporated the factor $(1 - \nu^2)$ into $\hat{E}$ for convenience. Next, we neglect bending (i.e., $\mathcal{E}^4 \ll 1 \Rightarrow \mathcal{E}^4/De \ll 1$), which is justified by the prior assumptions of slenderness and thinness [171, 173].

Then, the final form of the governing equation for the radial deformation of the thin viscoelastic tube under hydrodynamic loading is

$$u_r + \frac{1}{De}\frac{\partial u_r}{\partial t} + St\frac{\partial^2 u_r}{\partial t^2} = p. \qquad (6.31)$$

Importantly, observe that the Eq. (6.31) has a proper linearly elastic balance in the limit $De \to \infty$. We also deduce from Eq. (6.31) that the tube's damping time scale is $\mathcal{T}_{\text{damping}} \sim \mathcal{T}_f/De$, while the tube's inertial time scale is $\mathcal{T}_{\text{inertial}} \sim \sqrt{St}\mathcal{T}_f$.

6.1.3   Summary of the model's governing equations

The fluid mechanics problem is governed by Eqs. (6.22) and (6.23), and the structural mechanics problem is governed by Eq. (6.31). These are supplemented by the equation of state, Eq. (6.8). This set of four coupled partial differential and algebraic equations governs the evolution of fluid's density $\rho(z, t)$, flow rate $q(z, t)$, hydrodynamic pressure $p(z, t)$, and the radial deformation $u_r(z, t)$ of the tube. The model's dimensionless parameters are summarized in table 6.1, along with their relative orders of magnitude, wherever applicable.

The next step in our analysis is to solve the governing equations and analyze the dynamics of the transient FSI problem of compressible flow in a viscoelastic tube.

6.2   Exact and perturbative solutions to the coupled problem

6.2.1   Steady response

First, consider the steady-state problem, wherein the linearly viscoelastic tube model reduces to a linearly elastic tube model. Setting $\partial(\,\cdot\,)/\partial t = 0$ in Eq. (6.23), we obtain that the mass flow rate in any tube cross-section is the same constant:

$$\frac{\partial(\rho q)}{\partial z} = 0 \quad \Rightarrow \quad \rho q = \dot{m}_0 = const. \tag{6.32}$$

Note that unlike the case of systems with imposed mass flow rates, here $\dot{m}_0$ is an *unknown* constant, whose value is to be determined from the imposed boundary conditions for pressure.

The structural mechanics equation (6.31) at steady state is simply a linear deformation–pressure relation: $u_r(z) = p(z)$. Substituting this relation, q from Eq. (6.22) and ρ from Eq. (6.8) into Eq. (6.32b) leads to an ODE in $p(z)$:

$$\frac{1 + \alpha p(z)}{16 p(z)} \left\{ p[1 + \beta p(z)]^4 + 4\sigma K n_0 [1 + \beta p(z)]^3 \right\} \left(-\frac{\mathrm{d}p}{\mathrm{d}z} \right) = \dot{m}_0. \tag{6.33}$$

Table 6.1.

Dimensionless parameters that govern the FSI problem, their mathematical definitions, and their relative orders of magnitude.

Parameter	ϵ	ϵRe	α	β	$\mathcal{E}$	De	St
Definition	a/ℓ	$\rho_0 \mathcal{V}_z a^2/(\mu\ell)$	$\mathcal{P}_c/\mathcal{B}_T$	$\mathcal{U}_c/a = \mathcal{P}_c a/(\hat{E}h)$	$\sqrt{ha/\ell^2}$	$\hat{E}\mathcal{T}_f/C_v$	$\rho_s a^2/(\mathcal{T}_f^2 \hat{E})$
Magnitude	$\ll 1$	$\ll 1$	$\epsilon Re \ll \alpha \ll 1$	$\epsilon Re \ll \beta \ll 1$	$\mathcal{E}^4 \ll 1$	> 1	$= \mathcal{O}(1)$

This ODE can be solved to yield an implicit solution for the pressure profile:

$$5\alpha\beta^4 \left[1 - p(z)^6\right] + 6\beta^3 \left(\beta + 4\alpha\right) \left[1 - p(z)^5\right] + 15\beta^2 \left[2\beta \left(\alpha\sigma Kn_0 + 1\right) + 3\alpha\right] \left[1 - p(z)^4\right]$$

$$+ 20\beta \left[\beta \left(2 \left(\beta + 3\alpha\right) \sigma Kn_0 + 3\right) + 2\alpha\right] \left[1 - p(z)^3\right]$$

$$+ 15 \left[4\beta \left(3 \left(\beta + \alpha\right) \sigma Kn_0 + 1\right) + \alpha\right] \left[1 - p(z)^2\right]$$

$$+ 30 \left[4 \left(3\beta + \alpha\right) \sigma Kn_0 + 1\right] \left[1 - p(z)\right] - 120\sigma Kn_0 \ln \left|p(z)\right| = 480\dot{m}_0 z, \quad (6.34)$$

where we have imposed the inlet boundary condition $p(0) = 1$. Equation (6.34) can be inverted to yield the pressure distribution $p(z)$ in a linearly elastic tube conveying steady, compressible flow of a Newtonian fluid subject to rarefaction.

Note that because of the slip boundary condition, Eq. (6.34) cannot satisfy zero gauge pressure at $z = 1$. To determine the unknown constant $\dot{m}_0$, we can impose a non-zero outlet pressure

$$p(1) = p_{\text{out,slip}} \in (0, 1). \quad (6.35)$$

Consequently, for this problem, p_0 and ρ_0 are not the pressure and the density at the outlet, but at some other arbitrary location. Then, $\dot{m}_0$ is found from Eq. (6.34) in terms of $p_{\text{out,slip}}$.

For the special case of no rarefaction ($Kn_0 \equiv 0$), Eq. (6.34) reduces to:

$$[1 + \beta]^5 \left\{[6 + 5\alpha]\beta - \alpha\right\} - [1 + \beta p(z)]^5 \left\{[6 + 5\alpha p(z)]\beta - \alpha\right\} = 480\beta^2 \dot{m}_0 z \quad (6.36)$$

This equation describes the pressure variation due to FSI between a compressible flow and a linearly elastic tube. In this case, $\dot{m}_0$ is found by imposing the usual boundary condition at the outlet: $p(1) = 0$.

6.2.2 Impulsively pressurization of the inlet

Next, we solve the transient problem driven by an impulsive inlet pressure boundary condition. To solve this problems, we neglect rarefaction ($Kn_0 \rightarrow 0$). To this end, first

Eqs. (6.22) and (6.23) are written in terms of the deformed radius $R(z,t) = 1 + \beta u_r(z,t)$, taking $Kn_0 \equiv 0$, to yield:

$$q = -\frac{R^4}{8}\frac{\partial p}{\partial z}, \tag{6.37a}$$

$$\frac{\partial}{\partial t}\left(\frac{\rho R^2}{2}\right) + \frac{\partial(\rho q)}{\partial z} = 0. \tag{6.37b}$$

Substitution of Eq. (6.37a) into Eq. (6.37b) eliminates q and yields:

$$\rho R\frac{\partial R}{\partial t} + \frac{\partial \rho}{\partial t}\left(\frac{R^2}{2}\right) - \frac{\partial^2 p}{\partial z^2}\frac{\rho R^4}{8} - \frac{R^4}{8}\frac{\partial \rho}{\partial z}\frac{\partial p}{\partial z} - \frac{4R^3}{8}\frac{\partial R}{\partial z}\frac{\partial p}{\partial z}\rho = 0. \tag{6.38}$$

Next, a perturbation expansion is introduced in the compressibility parameter $\alpha \ll 1$:

$$p = p^0 + \alpha p^1 + \cdots, \tag{6.39a}$$

$$u_r = u_r^0 + \alpha u_r^1 + \cdots, \tag{6.39b}$$

$$R = R^0 + \alpha R^1 + \cdots, \tag{6.39c}$$

$$\rho = \rho^0 + \alpha \rho^1 + \cdots \tag{6.39d}$$

$$= 1 + \alpha\left(p^0 + \alpha p^1 \cdots\right). \tag{6.39e}$$

Substituting this perturbation expansion into Eq. (6.38) yields Eq. (6.40) as given below.

$$\left(1 + \alpha p^0\right)\left(R^0 + \alpha R^1\right)\frac{\partial\left(R^0 + \alpha R^1\right)}{\partial t} + \frac{\partial\left(1 + \alpha p^0\right)}{\partial t}\left[\frac{\left(R^0 + \alpha R^1\right)^2}{2}\right]$$

$$- \frac{\partial^2\left(p^0 + \alpha p^1\right)}{\partial z^2}\frac{\left(1 + \alpha p^0\right)\left(R^0 + \alpha R^1\right)^4}{8} - \frac{\left(R^0 + \alpha R^1\right)^4}{8}\frac{\partial\left(1 + \alpha p^0\right)}{\partial z}\frac{\partial\left(p^0 + \alpha p^1\right)}{\partial z}$$

$$- \frac{4\left(R^0 + \alpha R^1\right)^3}{8}\frac{\partial\left[R^0 + \alpha R^1\right]}{\partial z}\frac{\partial\left(p^0 + \alpha p^1\right)}{\partial z}\left(1 + \alpha p^0\right) = 0. \tag{6.40}$$

At the leading order in α, from Eq. (6.40), we have,

$$R^0\frac{\partial R^0}{\partial t} - \frac{\left(R^0\right)^4}{8}\frac{\partial^2 p^0}{\partial z^2} - \frac{1}{2}\left(R^0\right)^3\frac{\partial p^0}{\partial z}\frac{\partial R^0}{\partial z} = 0. \tag{6.41}$$

On the other hand, at $O(\alpha)$, Eq. (6.40)gives us Eq. (6.42) as given below:

$$
\left(R^1 \frac{\partial R^0}{\partial t} + \frac{\partial R^1}{\partial t} R^0 + p^0 R^0 \frac{\partial R^0}{\partial t} \right) + \frac{\left(R^0 \right)^2}{2} \frac{\partial p^0}{\partial t}
$$

$$
- \frac{\left(R^0 \right)^4}{8} \left(4 \frac{R^1}{R^0} \frac{\partial^2 p^0}{\partial z^2} + p^0 \frac{\partial^2 p^0}{\partial z^2} + \frac{\partial^2 p^1}{\partial z^2} \right) - \frac{\left(R^0 \right)^4}{8} \left(\frac{\partial p^0}{\partial z} \right)^2
$$

$$
- \frac{1}{8} \left[12 \left(R^0 \right)^2 \frac{\partial p^0}{\partial z} R^1 \frac{\partial R^0}{\partial z} + 4 \left(R^0 \right)^3 \frac{\partial p^0}{\partial z} \frac{\partial R^1}{\partial z} \right.
$$

$$
\left. + 4 \left(R^0 \right)^3 \frac{\partial p^0}{\partial z} \frac{\partial R^0}{\partial z} p^0 + 4 \left(R^0 \right)^3 \frac{\partial p^1}{\partial z} \frac{\partial R^0}{\partial z} \right] = 0. \quad (6.42)
$$

(see Appendix). The structural mechanics Eq. (6.31) does not explicitly involve α, thus at every order of α^j $(j = 0, 1, \ldots)$ it keeps its form, providing us with

$$
u_r^j + \frac{1}{De} \frac{\partial u_r^j}{\partial t} + St \frac{\partial^2 u_r^j}{\partial t^2} = p^j(z). \quad (6.43)
$$

Leading-order solution

First, we solve the leading-order FSI problem, that is Eqs. (6.41) and (6.43). Since the problem is still nonlinear, we address the nonlinearity by introducing a (second) perturbation expansion in the small FSI parameter β:

$$
p^0 = p^{0,0} + \beta p^{0,1} + \cdots, \quad (6.44a)
$$

$$
u_r^0 = u_r^{0,0} + \beta u_r^{0,1} + \cdots, \quad (6.44b)
$$

$$
R^0 = R^{0,0} + \beta R^{0,1} + \cdots \quad (6.44c)
$$

$$
= 1 + \beta \left(u_r^{0,0} + \beta u_r^{0,1} + \cdots \right). \quad (6.44d)
$$

Here, the first superscript denotes the perturbation order with respect to α, while the second superscript, after the comma, denotes the perturbation order with respect to β. Substituting the perturbation expansion (6.44) into Eq. (6.41) yields:

$$\beta\frac{\partial R^{0,1}}{\partial t} + \beta^2 R^{0,1}\frac{\partial R^{0,1}}{\partial t} - \frac{1}{8}\left(\frac{\partial^2 p^{0,0}}{\partial z^2} + 4\beta R^{0,1}\frac{\partial^2 p^{0,0}}{\partial z^2} + \beta\frac{\partial^2 p^{0,1}}{\partial z^2}\right)$$

$$- 4\beta\frac{\partial p^{0,0}}{\partial z}\frac{\partial R^{0,1}}{\partial z} + O(\beta^2) = 0. \quad (6.45)$$

To the leading order in β, we simply have

$$\frac{\partial^2 p^{0,0}}{\partial z^2} = 0, \quad (6.46)$$

which, obviously, also holds for the pressure in an incompressible flow in a rigid tube ($\alpha = \beta = 0$). The tube is impulsively pressurized at the inlet, subject to zero gauge pressure at the outlet, thus the boundary conditions for Eq. (6.46) are

$$p^{0,0}\Big|_{z=0} = H(t), \qquad p^{0,0}\Big|_{z=1} = 0. \quad (6.47)$$

Thus, the leading-order (in both α and β) solution for an impulsively pressurized tube is simply

$$p^{0,0}(z, t) = H(t)(1 - z). \quad (6.48)$$

Next, substituting the perturbation expansion from Eq. (6.44) into the leading-order-in-α structural mechanical equation (6.43) ($j = 0$), and collecting the leading-order-in-β terms, yields

$$u_r^{0,0} + \frac{1}{De}\frac{\partial u_r^{0,0}}{\partial t} + St\frac{\partial^2 u_r^{0,0}}{\partial t^2} = p^{0,0}(z)$$

$$= H(t)(1 - z). \quad (6.49)$$

The initial conditions corresponding to starting from rest are:

$$u_r^{0,0}\big|_{t=0} = 0, \qquad \frac{\partial u_r^{0,0}}{\partial t}\bigg|_{t=0} = 0. \quad (6.50)$$

Equation (6.49) subject to the latter ICs has the following solution:

$$u_r^{0,0}(z, t) = \frac{1}{St}(1 - z)H(t)\Xi_0(t), \quad (6.51)$$

where

$$\Xi_0(t) = A + \left[-A\cos\left(\Omega t\right) + \left(\frac{B}{\Omega} + \frac{A}{t_c\Omega}\right)\sin\left(\Omega t\right)\right]e^{-t/t_c}, \tag{6.52a}$$

$$A = St, \tag{6.52b}$$

$$B = -\frac{1}{De}, \tag{6.52c}$$

$$\Omega = \sqrt{\frac{1}{St} - \frac{1}{4St^2 De^2}}. \tag{6.52d}$$

Here, for convenience, we have introduced $t_c = 2St\,De$ as a dimensionless time constant. Observe that for the above solution to allow oscillations, the term under the square root in the expression for the damped frequency Ω from Eq. (6.52d) must be positive; i.e., the "ratio of critical damping" $\zeta = 1/(2De\sqrt{St}) < 1$.[4]

To obtain the first-order-in-β correction to the pressure, namely $p^{0,1}(z,t)$, we use Eq. (6.45). Collecting all the terms of $O(\beta)$, and substituting the expressions for $\partial u_r^{0,0}/\partial z$, $\partial u_r^{0,0}/\partial t$ and $\partial p^{0,0}/\partial z$ calculated from Eqs. (6.51) and (6.48), we obtain:

$$\frac{1}{St}(1-z)\Xi_1(t) - \frac{1}{8}\frac{\partial^2 p^{0,1}}{\partial z^2} - \frac{1}{2St}H(t)\Xi_0(t) = 0, \qquad \Xi_1(t) = \frac{\partial(H(t)\Xi_0(t))}{\partial t}. \tag{6.53}$$

The solution of Eq. (6.53), subject to homogeneous boundary conditions, is

$$p^{0,1}(z,t) = \frac{8}{St}\Xi_1(t)F(z) - \frac{2}{St}H(t)\Xi_0(t)G(z), \tag{6.54}$$

where

$$F(z) = \frac{z^2}{2} - \frac{z^3}{6} - \frac{z}{3}, \qquad G(z) = z^2 - z. \tag{6.55}$$

---

[4] The overdamped case of $\zeta > 1$ is not of interest here, as we assumed $De > 1$ is sufficiently large so that the tube is sufficiently elastic, and the viscous damping is small.

First-order correction in α and β

Next, we solve the first-order equation (6.42). Again, we introduce a perturbation expansion in the FSI parameter β:

$$p^1 = p^{1,0} + \beta p^{1,1} + \cdots, \tag{6.56a}$$

$$u_r^1 = u_r^{1,0} + \beta u_r^{1,1} + \cdots, \tag{6.56b}$$

$$R^1 = R^{1,0} + \beta R^{1,1} + \cdots, \tag{6.56c}$$

$$= 0 + \beta \left(u_r^{1,0} + \beta u_r^{1,1} + \cdots \right). \tag{6.56d}$$

We substitute the perturbation expansion (6.56) into Eq. (6.42) to obtain

$$
\begin{aligned}
& \left(\beta R^{1,1} \right) \frac{\partial \left(1 + \beta R^{0,1} \right)}{\partial t} + \frac{\partial \left(\beta R^{1,1} \right)}{\partial t} \left(1 + \beta R^{0,1} \right) \\
& + \left(p^{0,0} + \beta p^{0,1} \right) \left(1 + \beta R^{0,1} \right) \frac{\partial \left(1 + \beta R^{0,1} \right)}{\partial t} + \frac{\left(1 + \beta R^{0,1} \right)^2}{2} \frac{\partial \left(p^{0,0} + \beta p^{0,1} \right)}{\partial t} \\
& - \frac{\left(1 + \beta R^{0,1} \right)^4}{8} \left[4 \frac{\left(\beta R^{1,1} \right)}{\left(1 + \beta R^{0,1} \right)} \frac{\partial^2 \left(p^{0,0} + \beta p^{0,1} \right)}{\partial z^2} + \left(p^{0,0} + \beta p^{0,1} \right) \frac{\partial^2 \left(p^{0,0} + \beta p^{0,1} \right)}{\partial z^2} \right. \\
& \left. + \frac{\partial^2 \left(p^{1,0} + \beta p^{1,1} \right)}{\partial z^2} \right] - \frac{\left(1 + \beta R^{0,1} \right)^4}{8} \left[\frac{\partial \left(p^{0,0} + \beta p^{0,1} \right)}{\partial z} \right]^2 \\
& - \frac{1}{8} \left[12 \left(1 + \beta R^{0,1} \right)^2 \frac{\partial \left(p^{0,0} + \beta p^{0,1} \right)}{\partial z} \left(\beta R^{1,1} \right) \frac{\partial \left(1 + \beta R^{0,1} \right)}{\partial z} \right. \\
& + 4 \left(1 + \beta R^{0,1} \right)^3 \frac{\partial \left(p^{0,0} + \beta p^{0,1} \right)}{\partial z} \frac{\partial \left(\beta R^{1,1} \right)}{\partial z} \\
& + 4 \left(1 + \beta R^{0,1} \right)^3 \frac{\partial \left(p^{0,0} + \beta p^{0,1} \right)}{\partial z} \frac{\partial \left(1 + \beta R^{0,1} \right)}{\partial z} \left(p^{0,0} + \beta p^{0,1} \right) \\
& \left. + 4 \left(1 + \beta R^{0,1} \right)^3 \frac{\partial \left(p^{1,0} + \beta p^{1,1} \right)}{\partial z} \frac{\partial \left(1 + \beta R^{0,1} \right)}{\partial z} \right] = 0. \quad (6.57)
\end{aligned}
$$

To the leading order in β, Eq. (6.57) reduces to:

$$\frac{1}{2} \frac{\partial p^{0,0}}{\partial t} - \frac{1}{8} \frac{\partial^2 p^{1,0}}{\partial z^2} - \frac{1}{8} \left(\frac{\partial p^{0,0}}{\partial z} \right)^2 = 0, \tag{6.58}$$

and its solution, subject to homogeneous boundary conditions for $p^{1,0}(z,t)$, is

$$p^{1,0}(z,t) = 4\delta(t)F(z) - \frac{1}{2}H(t)G(z). \tag{6.59}$$

Summary of the perturbation solution

In summary, the solution for deformed radius in a viscoelastic tube conveying transient compressible flow with suddenly imposed pressure at the inlet is

$$R(z,t) = 1 + \beta u_r^{0,0}(z,t) + O(\alpha\beta, \beta^2, \alpha^2), \tag{6.60}$$

$u_r^{0,0}$ is given by Eq. (6.51). As discussed in Sec. 6.1.1, $\alpha \ll 1$ and $\beta \ll 1$, therefore all quadratic perturbation terms are neglected. The pressure distribution within the tube is

$$p(z,t) = p^{0,0}(z,t) + \beta p^{0,1}(z,t) + \alpha p^{1,0}(z,t) + O(\alpha\beta, \beta^2, \alpha^2), \tag{6.61}$$

where $p^{0,0}$ is given by Eq. (6.48), $p^{0,1}$ is given by Eq. (6.54), and $p^{1,0}$ is given by Eq. (6.59).

6.2.3 Oscillatory pressure at the inlet

Next, we consider an oscillatory pressure suddenly imposed at the inlet. Again, we neglect rarefaction ($Kn_0 \to 0$). Now, the boundary condition at the inlet, in dimensional form, is

$$\bar{p}|_{\bar{z}=0} = \mathcal{P}_c H(t)\cos(\bar{\omega}\bar{t}), \qquad \bar{p}|_{\bar{z}=1} = 0. \tag{6.62}$$

The angular frequency $\bar{\omega}$ imposes a new time scale $\mathcal{T}_o = 1/\bar{\omega}$ on the flow. Although, in the nondimensionalization scheme in Sec. 6.1.1 we chose $\mathcal{T}_f = \ell/\mathcal{V}_z$, where $\mathcal{V}_z$ was set by $\mathcal{P}_c$ via Eq. (6.12), we could just as well set $\mathcal{T}_f = \mathcal{T}_o$ (while keeping $\mathcal{V}_z$ set by $\mathcal{P}_c$ via Eq. (6.12)). Then, the the dimensionless governing equations of the flow have the same form as those derived in Sec. 6.1.1, except ϵRe is replaced by Wo^2 [218], where Wo is the Womeresley number, conventionally defined as

$$Wo^2 = \frac{\rho_0 \bar{\omega} a^2}{\mu}. \tag{6.63}$$

Consonant with our lubrication assumption that $\epsilon Re \ll 1$, $Wo^2 \ll 1$ is required. Physically, this assumption means that we the time scale of viscous diffusion to be much smaller than the time scale of imposed oscillations, and the flow is quasi-static with respect to the forcing (see also [154, Ch. 4]).

Leading-order solution

Following the double perturbation approach as in Sec. 6.2.2, the governing equation for $p^{0,0}(z,t)$ is still given by Eq. (6.46). Using Eq. (6.2), the dimensionless boundary conditions are

$$p|_{z=0} = H(t)\cos(\omega t), \qquad p|_{z=1} = 0, \tag{6.64}$$

where $\omega = \mathcal{T}_f \bar{\omega}$ is the dimensionless frequency. Thus, $p^{0,0}$ must satisfy Eqs. (6.64) and higher perturbations satisfy homogeneous boundary conditions. Hence,

$$p^{0,0}(z,t) = H(t)\cos(\omega t)(1-z). \tag{6.65}$$

Similarly, from Eq. (6.49), the equation governing the leading-order (in α and β) radial deformation profile $u_r^{0,0}$ is

$$u_r^{0,0} + \frac{1}{De}\frac{\partial u_r^{0,0}}{\partial t} + St\frac{\partial^2 u_r^{0,0}}{\partial t^2} = p^{0,0}(z)$$
$$= H(t)\cos(\omega t)(1-z). \tag{6.66}$$

The solution of this equation, subject to homogeneous initial conditions (starting from rest), as in Eq. (6.50), is

$$u_r^{0,0}(z,t) = \frac{1}{St}H(t)\Psi_0(\omega,t)(1-z), \tag{6.67}$$

where

$$\Psi_0(\omega, t) = \hat{A}(\omega)\cos(\omega t) + \frac{\hat{B}(\omega)}{\omega}\sin(\omega t) \tag{6.68a}$$

$$+ \left\{ -\hat{A}(\omega)\cos(\Omega t) + \left[\frac{\hat{C}(\omega)}{\Omega} + \frac{\hat{A}(\omega)}{t_c\Omega} \right]\sin(\Omega t) \right\} e^{-t/t_c},$$

$$\hat{A}(\omega) = \frac{\left(1 - St\,\omega^2\right)De^2St}{\left(De - St\,\omega^2 De\right)^2 + \omega^2}, \tag{6.68b}$$

$$\hat{B}(\omega) = \frac{\omega^2 St\,De}{\left(De - St\,\omega^2 De\right)^2 + \omega^2}, \tag{6.68c}$$

$$\hat{C}(\omega) = -\frac{De}{\left(De - St\,De\,\omega^2\right)^2 + \omega^2}, \tag{6.68d}$$

and $t_c = 2St\,De$ as before.

First-order corrections in α and β

The governing equation for $p^{0,1}(z,t)$ is obtained as in Sec. 6.2.2 (recall derivation of Eq. (6.53)), and its solution, subject to homogeneous boundary conditions, is

$$p^{0,1}(z,t) = \frac{8}{St}F(z)\Psi_1(\omega, t) + \frac{2}{St}G(z)\Psi_0(\omega, t)H(t)\cos(\omega t),$$

$$\Psi_1(\omega, t) = \frac{\partial(H(t)\Psi_0(\omega, t))}{\partial t}. \tag{6.69}$$

Similarly, $p^{1,0}$ is still governed by Eq. (6.58), and its solution, given the leading-order solutions in Eqs. (6.65) and (6.67), is

$$p^{1,0}(z,t) = F(z)[4\delta(t)\cos(\omega t) - 4\omega\sin(\omega t)] - \frac{1}{2}G(z)\cos^2(\omega t). \tag{6.70}$$

Summary of the perturbation solution

In summary, the expression for the deformed radius of a viscoelastic tube conveying transient flow with oscillatory pressure imposed at the inlet is

$$R(z,t) = 1 + \beta u_r^{0,0}(z,t) + O(\alpha\beta, \beta^2, \alpha^2). \tag{6.71}$$

For our double perturbation expansion to be valid, $\alpha \ll 1$ and $\beta \ll 1$, therefore all quadratic perturbation terms are neglected. Here, $u_r^{0,0}$ is given by Eq. (6.67). The expression for the pressure pressure distribution within the tube is

$$p(z,t) = p^{0,0}(z,t) + \beta p^{0,1}(z,t) + \alpha p^{1,0}(z,t) + O(\alpha\beta, \beta^2, \alpha^2). \qquad (6.72)$$

Here, $p^{0,0}$ is given by Eq. (6.65) and $p^{0,1}$ is given by Eq. (6.69) and $p^{1,0}$ is given by Eq. (6.70).

6.3 Results and discussion

Having derived a mathematical theory of FSI in a viscoelastic tube (Sec. 6.1), as well as solutions to steady (Sec. 6.2.1) and unsteady problems (Sec. 6.2.2 and Sec. 6.2.3), in several distinguished limits, we use these results to discuss the physics of the FSI response in this section.

6.3.1 Steady response

In this subsection, we discuss the results pertaining to steady compressible flow (accounting for rarefaction) in a linearly elastic tube, based on the analysis in Sec. 6.2.1.

First we illustrate the effect of rarefaction (slip) in Fig. 6.2. As a direct consequence of the enhanced slip at the wall, the velocity increases with Kn_0 in Fig. 6.2(a). However, the increase in velocity is not the same across all radial locations, i.e., slip affects not only the velocity magnitude (momentum advection) but also the velocity gradients (momentum diffusion). This observation is clearly related to the nonlinear nature of the slip law in Eq. (6.18). Likewise, the pressure profiles in Fig. 6.2(b) are also clearly not linear.

Next, we explore the effect of FSI on the flow field through the dimensionless group β. Higher values of β correspond to a wider tube and consequently higher throughput (flow rate q), which results in an enhanced average axial velocity (consequently, larger centerline velocity of the flow profile), as shown in Fig. 6.3(a). Thus, the fluid exerts more pressure on the tube wall, on average, as supported by the example plot in Fig. 6.3(b).

Finally, the effect of the compressibility parameter α on the flow field is shown in Fig. 6.4. As explained earlier, the compressibility parameter α quantifies the "sensitivity" of fluid's density to the applied pressure. A larger value of α means a denser fluid. Therefore, for the same pressure difference, the flow rate (and the velocity profile) reduces with increase in α, as shown in Fig. 6.4(a). By similar arguments, since a larger pressure is required to pump a denser fluid, the pressure profile increases with α in Fig. 6.4(b).

We have shown that, compared to incompressible flow in a rigid tube, both FSI and compressibility alter the velocity field. In capillary viscometers, the classical Hagen–Poiseuille law is employed for viscosity estimation of gases. Neglecting compressibility may lead to incorrect estimation of the viscosity in such devices [77]. Similarly, in microscale rheometry, a conduit constituted of a soft material like PDMS may "pollute" the viscosity estimation, thus necessitating the use of the steady FSI theory developed in Sec. 6.2.1.

6.3.2   Impulsive pressurization of the inlet

Deformation and pressure response

For the case of a viscoelastic tube impulsively pressurized at the inlet, the deformed radius is given by Eq. (6.60) and the pressure profile is given by Eq. (6.61), along with the pertinent supporting equations. From Eqs. (6.60) and (6.61), we deduce that the solutions for $R(z, t)$ and $p(z, t)$ have a decaying transient on top of a steady state. The steady state of the deformed radius is given by

$$\lim_{t \to \infty} R(z, t) = 1 + \beta(1 - z) + O(\alpha\beta, \alpha^2, \beta^2). \tag{6.73}$$

The pressure profile at the steady state is given by

$$\lim_{t \to \infty} p(z, t) = (1 - z)\left(1 + 2\beta z + \frac{\alpha}{2}z\right) + O(\alpha\beta, \alpha^2, \beta^2). \tag{6.74}$$

The time evolution of R and p is shown in panels (a) and (b), respectively, of Figs. 6.5 and 6.6. Obviously, the steady states are independent of De and St. The nonzero constant
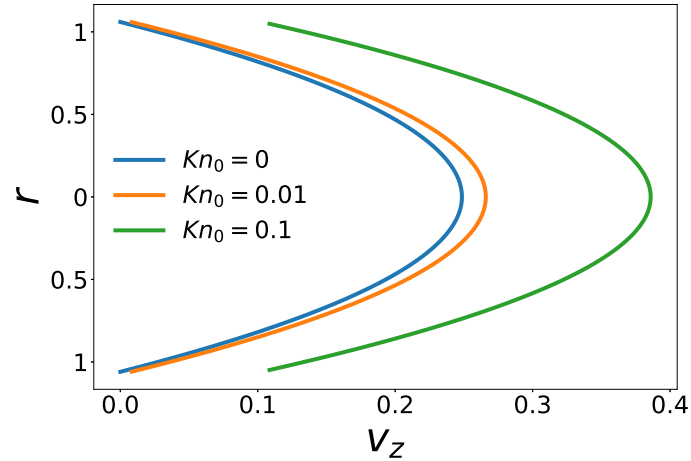
(a) Axial velocity profile, different Kn_0
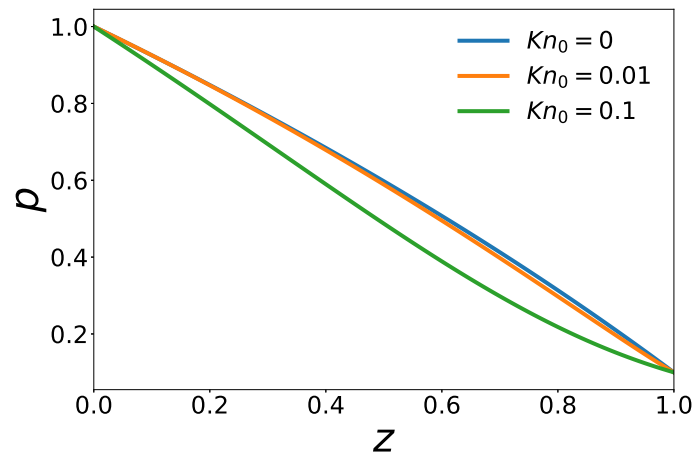
(b) Axial pressure profile, different Kn_0

Fig. 6.2. Steady-state problem: Kn_0 dependence of (a) the axial velocity profile $v_z(z)$ at $z = 0.5$, and (b) the pressure distribution $p(z)$ obtained by inverting Eq. (6.34). In both panels: $\sigma = 1$, $\alpha = p_{\text{out,slip}} = \beta = 0.1$.

deformation at steady state, after a suddenly applied pressure load, is the result of the bounded *creep* response of the chosen KV model [57, Ch. 2]. That is, the steady state is characterized only by the elasticity (not viscoelasticity) of the system, and the ratio of
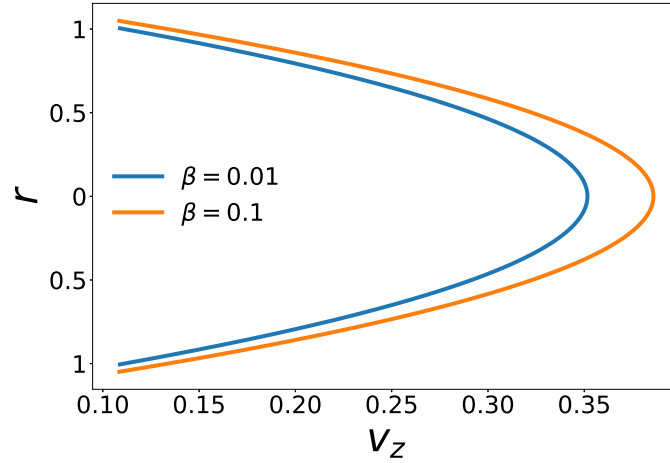
(a) Axial velocity profile, different β
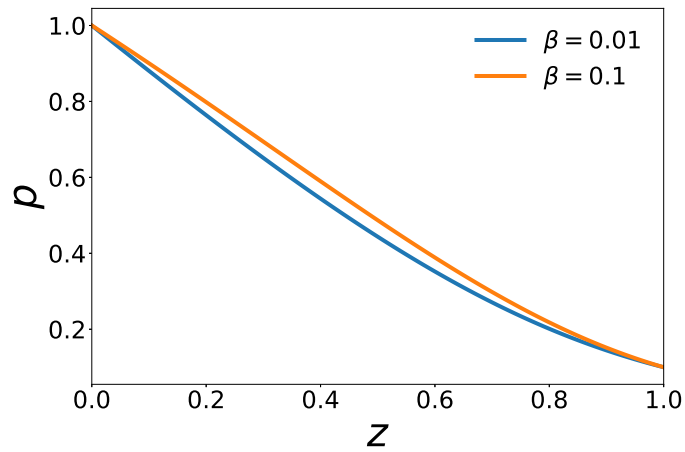
(b) Axial pressure profile, different β

Fig. 6.3. Steady-state problem: β dependence of (a) the axial velocity profile $v_z(r, z)$ at $z = 0.5$, and (b) the pressure distribution $p(z)$, obtained by inverting Eq. (6.34). In both panels: $\sigma = 1$, $\alpha = p_{\text{out,slip}} = 0.1$, and $Kn_0 = 0.1$.

applied load to the elastic constant determines the local deformation at the steady state, which in this case is found from Eq. (6.49) to be = 1. In other words,

$$\lim_{t \to \infty} u_r^{0,0}(z, t) = \lim_{t \to \infty} p^{0,0}(z, t) = 1 - z. \tag{6.75}$$
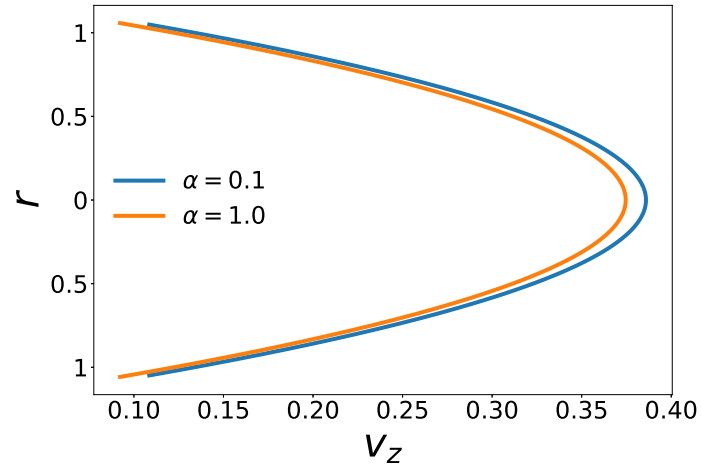
(a) Axial velocity profile, different α
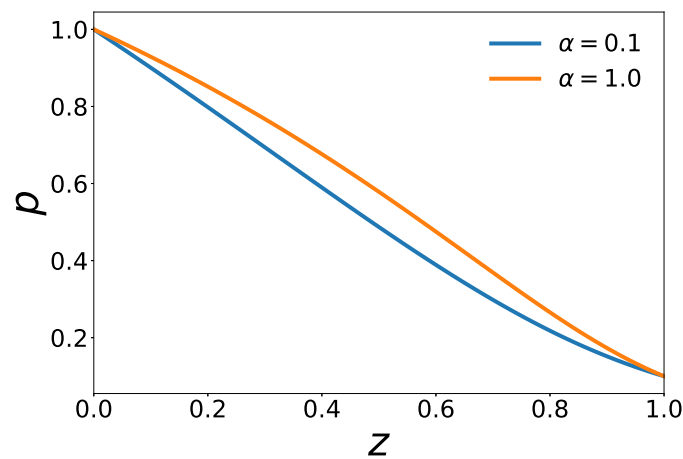
(b) Axial pressure profile, different α

Fig. 6.4. Steady-state problem: α dependence of (a) the axial velocity profile $v_z(r, z)$ at $z = 0.5$, and (b) the pressure distribution $p(z)$ obtained by inverting Eq. (6.34). In both panels: $\sigma = 1$, $\beta = p_{\text{out,slip}} = 0.1$, and $Kn_0 = 0.1$.

Once the transients die out, the inertial and viscoelastic effects are gone, and, naturally, Eq. (6.75) agrees with the steady-state result for a linearly elastic tube (without inertia) [160].

Next, we focus on the relationship between the transient characteristics of the system and St and De. We recall that the St quantifies the inertial response of the tube, while De

quantifies the damping (dissipation) of the viscoelastic structure. Therefore, an increase in either St or De would prolong the transient response of the tube, by enhancing the capacity of the tube to store energy, as opposed to its capacity to dissipate energy. Indeed, the transient part of $u_r^{0,0}$ from Eq. (6.51) is

$$\mathfrak{U}_r(z,t) = e^{-t/t_c} \frac{1}{St} \left[-A \cos{(\Omega t)} + \left(\frac{B}{\Omega} + \frac{A}{t_c \Omega} \right) \sin{(\Omega t)} \right] (1-z) \qquad (t>0), \qquad (6.76)$$

where recall that $t_c = 2St\,De$ is a dimensionless time constant, and Ω is the damped frequency of the system, given by Eq. (6.52d). Now, the straightforward observation about the effect of St and De on the transient is obvious and also corroborated by Fig. 6.5.

We observe from the plots in Fig. 6.5 that both St and De also enhance the amplitude of the oscillations. This is again attributed to the enhanced energy storing capacity of the tube at higher values of St and De. To quantify this effect, we express the damped frequency as

$$\Omega = \omega_o \sqrt{1 - \zeta^2}, \qquad (6.77)$$

where $\omega_o = \sqrt{1/St}$ is the "natural" frequency of the system (without any damping) and $\zeta = 1/(2De\sqrt{St})$ is the critical damping ratio of the system as above, which controls the ratio of successive peaks at a location z in $\mathfrak{U}_r(z,t)$. A fluid particle reaches its consecutive maximum (or minimum) location after a time period $T = 2\pi/\Omega$. So, we calculate the ratio of the successive peaks in the transient response at a given location and separated by one period $T = 2\pi/\Omega$ to be

$$\frac{\mathfrak{U}_r(z, t+T)}{\mathfrak{U}_r(z,t)} = \exp\left(-\frac{2\pi\zeta}{\sqrt{1-\zeta^2}} \right). \qquad (6.78)$$

From Eq. (6.78), it follows that both De and St influence the amplitude of oscillations, through ζ.

It is also instructive to consider the transient response of the pressure field, which is found from Eq. (6.54) to be

$$\mathfrak{P}(z,t) = \beta e^{-t/t_c} \frac{8}{St} \left[\left(B + \frac{2A}{t_c} \right) \cos{(\Omega t)} + \left(A\Omega - \frac{A}{t_c^2 \Omega} - \frac{B}{t_c \Omega} \right) \sin{(\Omega t)} \right] F(z)$$

$$- \beta e^{-t/t_c} \frac{2}{St} \left[-A \cos{(\Omega t)} + \left(\frac{B}{\Omega} + \frac{A}{t_c \Omega} \right) \sin{(\Omega t)} \right] G(z) \qquad (t>0). \quad (6.79)$$
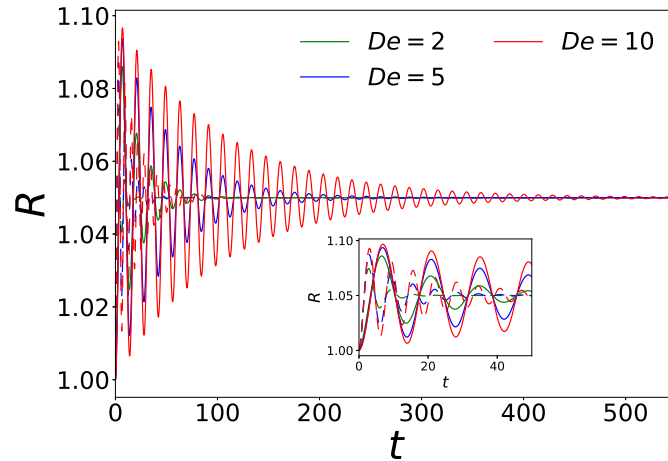
(a) Deformed tube radius at $z = 0.5$
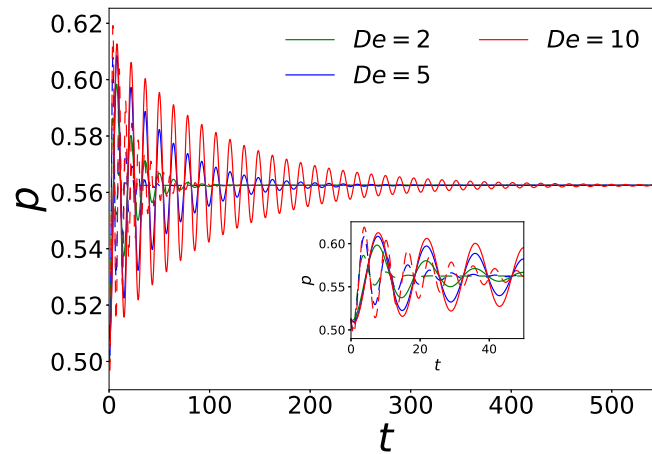
(b) Pressure at $z = 0.5$

Fig. 6.5. Evolution of the deformed tube radius $R(z = 0.5, t)$ and pressure $p(z = 0.5, t)$ at the midpoint of the tube, for different values of De and St in the case of an impulsively pressurized tube, obtained from Eqs. (6.60)–(6.61). The solid curves correspond to $St = 5$, while the dashed curves correspond to $St = 1$.

First, note that $\mathfrak{P}(z, t) = O(\beta)$, thus this transient is solely due to FSI, and compressibility has no effect on the transient pressure response. Stokes flow (in a rigid conduit) is inertia-less and reacts instantaneously to any unsteadiness imposed by its boundaries [123, Ch. 21]. However, as Eq. (6.79) shows, FSI introduces a delay in the response of the fluid by perpet-
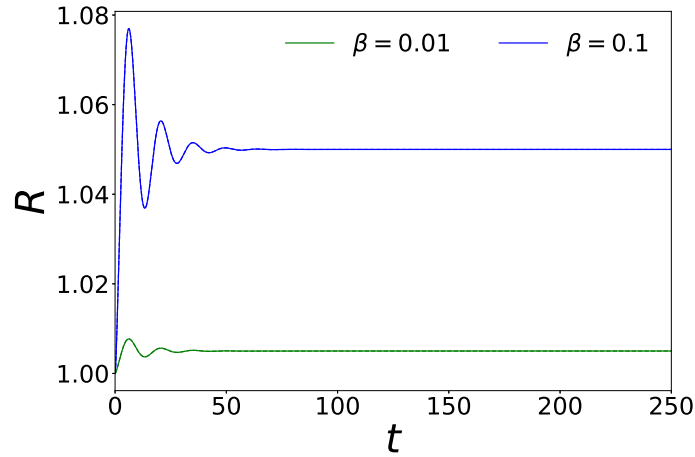
(a) Deformed radius at $z = 0.5$
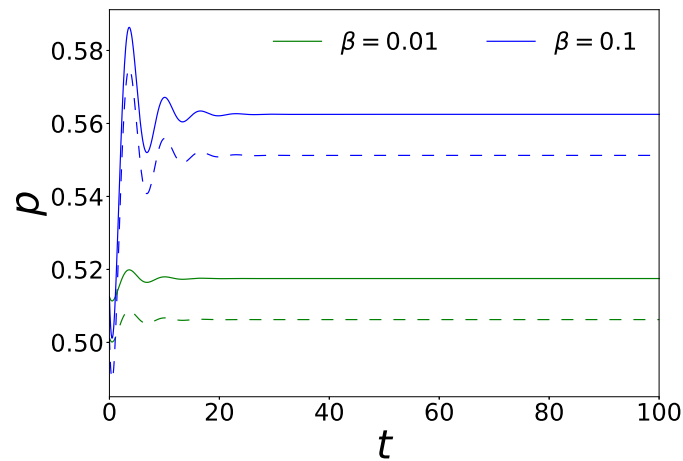
(b) Pressure at $z = 0.5$

Fig. 6.6. Evolution of the deformed radius and pressure at $z = 0.5$ for different values of β and α, for the case of impulsively pressurized tube, as obtained from Eqs. (6.60)–(6.61). The solid curves correspond to $\alpha = 0.1$, while the dashed curves correspond to $\alpha = 0.01$. In both panels: $De = 2$ and $St = 1$.

uating exponentially decaying transients in the flow. Figure 6.6 highlights the FSI-induced transients, showing that the time taken by the system (both the deformed radius and the pressure) to equilibrate increases with β. Of course, this equilibration time is independent of α (compare the solid and dashed curves).

In summary, there are different transient phenomena occurring in our FSI problem, due to changes in density (with a time scale $\sim \alpha \mathcal{T}_f$), deformation of the wall (with a time scale $\sim \beta \mathcal{T}_f$), inertia of the solid (with a time scale $\sim \sqrt{St}\mathcal{T}_f$), and the damping of the solid (with a time scale $\sim \mathcal{T}_f/De$). The problem we are solving, in the limit of weak compressibility and weak FSI, puts a limit on the magnitudes of α and β, both of which must be small ($\ll 1$). However, no such constraint exists on St and on De, which are allowed to be moderate, even large. Therefore, St and De, being associated with the largest time scale in the system, set the time constant of the (whole) FSI system.

Flow rate enhancement

In flow-rate-controlled FSI problems [160, 211], a reduction in the deformation of the tube (channel) leads to an increase in the pressure, which is attributed to the enhanced resistance to flow on account of the reduction in flow area. On the other hand, in pressure-controlled situations, such as those studied here and also in [211], an increase in pressure is actually accompanied by an increase in the deformation. This observation leads to the question: how is the flow rate across the tube influenced by FSI and compressibility in pressure-controlled FSI systems? The expression for flow rate, assuming no rarefaction (i.e., enforcing no slip, $Kn_0 \to 0$), is found from Eq. (6.22):

$$q(z,t) = -\frac{1}{8}\frac{\partial p}{\partial z}\left[1 + 4\beta u_r(z,t)\right] + O(\beta^2). \tag{6.80}$$

For post-transient steady flow in an impulsively pressurized tube, we substitute the expressions from Eqs. (6.73) and (6.74) into Eq. (6.80) to obtain:

$$q(z) = \underbrace{-\frac{1}{8}\frac{\partial p^{0,0}}{\partial z}}_{q^{0,0}} + \frac{\beta}{4}G'(z) + \frac{\alpha}{16}G'(z) - \frac{\beta}{2}(1-z)\frac{\partial p^{0,0}}{\partial z} + O(\alpha\beta, \alpha^2, \beta^2). \tag{6.81}$$

Here, $q^{0,0}$ denotes the flow rate in absence of FSI and compressibility. Therefore the "flow rate enhancement" due to FSI and compressibility is given by

$$\begin{aligned} q^*(z) = q(z) - q^{0,0}(z) &= \frac{\beta}{4}G'(z) + \frac{\alpha}{16}G'(z) - \frac{\beta}{2}(1-z)\frac{\partial p^{0,0}}{\partial z} \\ &= \frac{\beta}{4} + \frac{\alpha}{16}(2z-1). \end{aligned} \tag{6.82}$$
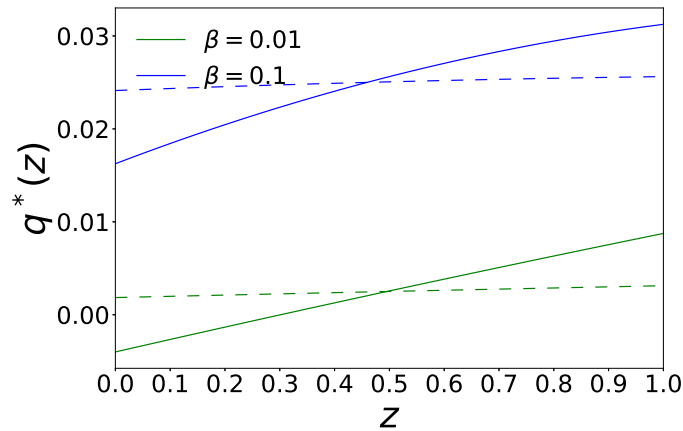
Fig. 6.7. The flow-wise profile of profile $q^*(z)$ for enhancement in the flow rate for the impulsively pressurized tube, from Eq. (6.82), for different values of β and α. The solid curves are for $\alpha = 0.1$, while the dashed curves are for $\alpha = 0.01$.

Note that even though the flow is steady, both q and q^* still vary along the axial z-direction due to the compressibility of the flow; $q^*(z)$ is shown in Fig. 6.7(a). For weak compressibility ($\alpha \ll 1$), the variation of q^* across the tube is quite low (compare the dashed curves with the solid curves). Note that $q^*(0) = \beta/4 - \alpha/16$ so that $q^*(0) < 0$ for $\beta < \alpha/4$. Meanwhile $q^*(1) = \beta/4 + \alpha/16 > 0$ for all α and β. The strictly increasing nature of q^* with z follow from the fact that the pressure gradient in the tube gives rise to a density gradient, and therefore the density decreases along the tube. By conservation of mass, higher density at the inlet means lower volume flow rate there, and the conversely, and vice versa at the outlet, as shown in Fig. 6.7. Finally, the enhanced mass flow rate at the outlet is simply $\dot{m}^*(1) \equiv (\rho q^*)|_{z=1} = \beta/4 + \alpha/16$ since $\rho(1) = 1$ in our nondimensionalization. In the post-transient FSI regime, the mass flow rate is constant, independent of z, and equal to $\dot{m}^*(1)$ throughout the tube.

6.3.3 Oscillating pressure at the inlet

Next, we analyze the FSI due to an oscillating pressure imposed at the tube's inlet. For this case, the solution for the deformed radius $R(z, t)$ is given by Eq. (6.71), while the pressure profile $p(z, t)$ is given by Eq. (6.72).

Deformation response

As before, $R(z, t)$ consists of an exponentially decaying transient and a post-transient (i.e., quasi-steady) component. The exponentially decaying transient has the same time constant t_c as the impulsively pressurized tube (Sec. 6.3.2), and the same oscillation frequency Ω given in Eq. (6.77). Therefore, in this section, we concern ourselves only with the post-transient response of the system, which has the same frequency ω as the forcing frequency.

After the transients die out, the post-transient deformed radius is given by

$$\mathscr{R}(z, t) = 1 + \beta \mathscr{U}_r^{0,0}(z, t) + O(\alpha\beta, \alpha^2, \beta^2), \tag{6.83}$$

where

$$\mathscr{U}_r^{0,0}(z, t) = \frac{1}{St} \left[\hat{A}(\omega) \cos(\omega t) + \frac{\hat{B}(\omega)}{\omega} \sin(\omega t) \right] (1 - z). \tag{6.84}$$

On inserting the relevant expressions for $\hat{A}$ and $\hat{B}$ from Eqs. (6.68b), (6.68c) into the Eqs. (6.83),(6.84) and simplifying, the post-transient deformed radius is obtained as:

$$\mathscr{R}(z, t) = 1 + \beta \frac{De\,(1 - z)}{\sqrt{\left(1 - St\,\omega^2\right)^2 De^2 + \omega^2}} \sin\left(\omega t + \phi\right), \qquad \phi = \tan^{-1}\left(\frac{\hat{A}(\omega)\omega}{\hat{B}(\omega)}\right). \tag{6.85}$$

From Eq. (6.85), we observe that the tube radius maintains a phase difference with respect to pressure imposed at the inlet. Due to the axial variation of the pressure, the tube radius exhibits a maximum at the inlet, $z = 0$, and a minimum at the outlet, $z = 1$. Combined with the oscillatory forcing, the tube wall sustains a standing wave; the inlet $z = 0$ is antinode, whilst the outlet $z = 1$ is a node, as shown in Fig. 6.8(a).

In the formulation of our FSI theory, we neglected bending and the boundary layers required to enforce the clamped boundary conditions; thus, the latter cannot be satisfied by our theory. Thus, unlike the more common case of vibrating strings and musical instruments, the standing waves on the tube are not generated by the reflection of waves at the clamped ends. The standing wave pattern is the direct consequence of FSI. Specifically, the leading-order hydrodynamic pressure is itself in the form of a standing wave, as shown Eq. (6.65). The pressure standing wave then induces a deformation standing wave on the tube, at the same frequency but with a small phase difference (see Fig. 6.8(b)).

To that end, it is possible, indeed desirable, to interpret Eq. (6.85) in terms of the natural frequency of the system $\omega_o = 1/\sqrt{St}$ and its critical damping ratio $\zeta = 1/(2De\sqrt{St})$:

$$\mathscr{R}(z,t) = 1 + \beta \widehat{\mathscr{U}_r}^{0,0}(z,\omega) \sin(\omega t + \phi), \tag{6.86a}$$

where

$$\phi = \sin^{-1}\left\{ \frac{1 - (\omega/\omega_o)^2}{\sqrt{\left[1 - (\omega/\omega_o)^2\right]^2 + 4\zeta^2 (\omega/\omega_o)^2}} \right\}. \tag{6.86b}$$

and

$$\widehat{\mathscr{U}_r}^{0,0}(z,\omega) = \frac{(1 - z)}{\sqrt{\left[1 - (\omega/\omega_o)^2\right]^2 + 4\zeta^2 (\omega/\omega_o)^2}} \tag{6.86c}$$

is the (positive) spatially varying amplitude of the tube deformation.

Observe that the amplitude of the response reaches a maximum value at the "resonant frequency"

$$\omega = \omega_{\text{res}} = \omega_o \sqrt{1 - 2\zeta^2}. \tag{6.87}$$

Therefore, the viscoelastic tube conveying oscillatory flow may be construed as a *band-pass filter*, which allows signals close to ω_{res} to pass through, but attenuates signals with frequencies away from it, as shown in in Fig. 6.9.
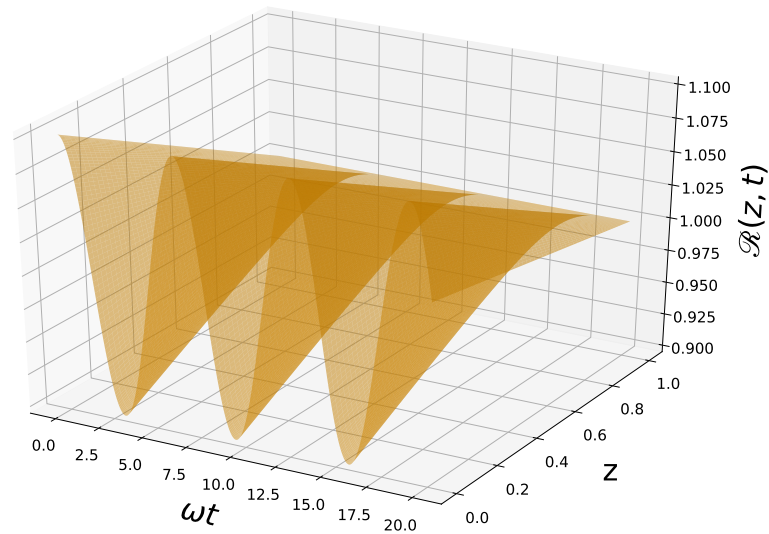
(a) Standing wave
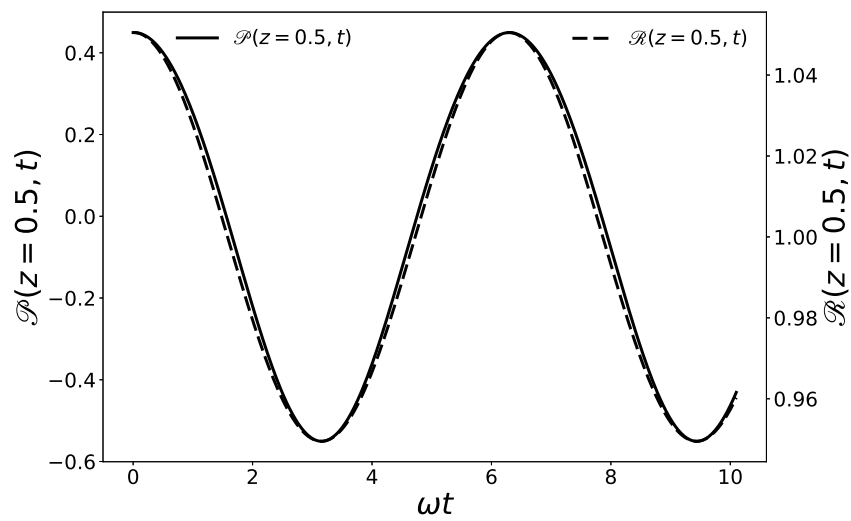
(b) Phase difference between $\mathscr{P}$ and $\mathscr{R}$

Fig. 6.8. Standing waves due to FSI in a viscoelastic tube with oscillatory pressure imposed at the inlet. (a) $\mathscr{R}(z, t)$ from Eq. (6.85) (b) $\mathscr{R}(z, t)$ and $\mathscr{P}(z, t)$ from Eq. (6.88) at $z = 0.5$, showing the phase difference ϕ between the two waves. Both plots are for $De = 10$, $St = 1$, $\alpha = 0.1$, and $\beta = 0.1$.
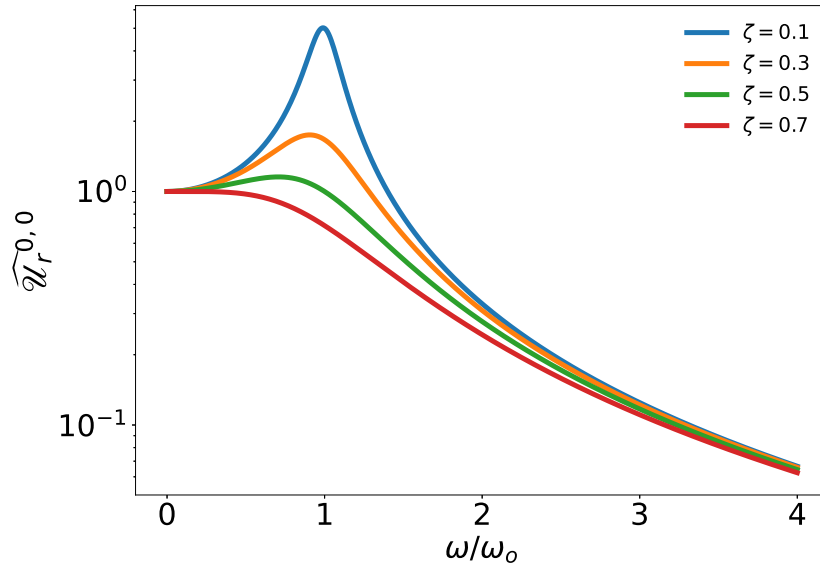
Fig. 6.9. Frequency response of the post-transient deformed tube for different values of $\zeta = 1/(2De\sqrt{St})$, plotted from Eq. (6.86c). Resonance occurs when the forcing frequency equals the resonant frequency of the system, given by Eq. (6.87).

Pressure response

Now, we move on to the fluid mechanical aspect of the problem. Similar to the case for impulsively pressurized inlet (Sec. 6.3.2), the pressure profile for imposed oscillatory inlet pressure exhibits exponentially decaying transients of $O(\beta)$. Using the results from Sec. 6.2.3, we find that, once the transients die out, the post-transient pressure profile is

$$\mathscr{P}(z,t) = \left[(1-z) + \beta\frac{8}{St}F(z)\hat{B}(\omega)\right]\cos(\omega t) - \left(4\alpha\omega + \beta\frac{8\hat{A}(\omega)\omega}{St}\right)F(z)\sin(\omega t)$$

$$+ \left(\beta\frac{\hat{A}(\omega)}{St} - \frac{\alpha}{4}\right)G(z)\cos(2\omega t) + \beta\frac{\hat{B}(\omega)}{St\,\omega}G(z)\sin(2\omega t) + \left(\beta\frac{\hat{A}(\omega)}{St} - \frac{\alpha}{4}\right)G(z). \quad (6.88)$$

Note that this expression has higher harmonic of frequency 2ω, as well as time-independent terms, at $O(\alpha, \beta)$ due to mode couplings cased by FSI and compressibility.

Separating the different harmonics in Eq. (6.88), we define the first harmonic:

$$\mathscr{P}_{1H}(z,t) = (1-z)\cos(\omega t) - 4\alpha\omega F(z)\sin(\omega t)$$
$$+ \beta \frac{8\omega F(z)}{\sqrt{\left[1-(\omega/\omega_o)^2\right]^2 + 4\zeta^2(\omega/\omega_o)^2}}\cos(\omega t + \phi),$$
$$\phi = \tan^{-1}\left(\frac{\hat{A}(\omega)\omega}{\hat{B}(\omega)}\right). \tag{6.89}$$

Importantly, the term of $O(\beta)$ has a frequency-dependent amplitude with resonant frequency $\omega = \omega_o$, which is the natural frequency of the system. The second harmonic can be defined as:

$$\mathscr{P}_{2H}(z,t) = -\frac{\alpha}{4}G(z)\cos(2\omega t) + \beta \frac{G(z)}{\sqrt{\left[1-(\omega/\omega_o)^2\right]^2 + 4\zeta^2(\omega/\omega_o)^2}}\sin(2\omega t + \phi), \tag{6.90}$$

where ϕ is given in Eq. (6.89). Note that the envelope of the $O(\beta)$ term in Eq. (6.90) has the same frequency dependence as that of the deformed radius (recall Eq. (6.86a)) and, therefore, has the same resonant frequency ω_{res} given in Eq. (6.87).

It is also instructive to note that, while both $\mathscr{P}_{1H}$ and $\mathscr{P}_{2H}$ exhibit similar frequency response, the spatial variations of their envelopes are different. For $\mathscr{P}_{1H}$ it follows that, the spatial variation of the envelope is set by $F(z)$, while for $\mathscr{P}_{2H}$, the spatial variation of the envelope is given $G(z)$. From Eq. (6.55), since both $F(z)$ and $G(z)$ have the same zeros in $(0,1)$, the nodes of the two harmonics are also the same. On the other hand, the antinodes are different. They are at $z = (3 - \sqrt{3})/3$ for the first harmonic, and at $z = 1/2$ for the second harmonic.

Acoustic streaming

Next, we move onto the velocity field inside the tube, which, for the case with negligible rarefaction ($Kn_0 \to 0$), is found from Eq. (6.21) to be

$$v_z(r,z,t) = -\frac{1}{4}\frac{\partial p}{\partial z}\left[(1-r^2) + 2\beta u_r)\right] + O\left(\beta^2\right). \tag{6.91}$$

When we substitute the post-transient pressure profile from Eq. (6.88) into the latter, we obtain the post-transient axial velocity profile:

$$
\mathcal{V}_z(r, z, t) = \frac{(1 - r^2)}{4} \left\{ \alpha \frac{G'(z)}{4} + \beta \frac{\hat{A}(\omega)}{St} G'(z) \cos(\omega t) \left[1 - \beta \frac{8}{St} F'(z) \hat{B}(\omega) \right] \right.
$$

$$
+ \sin(\omega t) \left[4\alpha\omega F'(z) + \beta \frac{8\hat{A}(\omega)\omega}{St} F'(z) \right] + \cos(2\omega t) \left[\alpha \frac{G'(z)}{4} - \beta \frac{\hat{A}(\omega)}{St} G'(z) \right]
$$

$$
\left. - \beta \sin(2\omega t) \left[\frac{\hat{B}(\omega)}{St\,\omega} G'(z) \right] \right\} + \frac{\beta}{4} \frac{\left[\cos\phi \sin(2\omega t) + \sin\phi \cos(2\omega t) + \sin\phi \right]}{\sqrt{\left[1 - (\omega/\omega_o)^2 \right]^2 + 4\zeta^2 (\omega/\omega_o)^2}} (1 - z).
$$

$$(6.92)$$

Observe that the velocity profile in the fluid consists of higher harmonics as well as a time-independent (steady-state) response. The time-independent part will lead to a nonzero mean flow (after averaging over a period of forcing). This observation leads us to consider *acoustic streaming*, which is commonly observed in oscillatory flows [219]. In the context of flows in tubes, a secondary nonzero mean flow has been observed for tubes with slowly varying radius [220], and in curved tubes [221] (see also [50, Ch. 4]). Such flows can also be generated by preset periodic boundary motion (peristalsis) for MEMS applications [222]. On the other hand, for the problem considered herein, streaming (and the underlying oscillatory flow) is induced by the pressure boundary conditions via FSI.

In an ideal fluid undergoing oscillatory flow, a fluid particle oscillates about its position with a constant amplitude. Therefore, the average displacement of the fluid particle over a time period is zero. However, if a dissipative mechanism is introduced in the flow such that the restoring force acting on the fluid particle does not remain the same on both the sides of the mean position, then the mean position of the fluid particle undergoes a net (time averaged) displacement. Traditionally, the dissipative effects in the fluid have been introduced through viscous flow (e.g., Rayleigh streaming [223]) or by a non-conservative body force [219]. However, our results show that it is also possible to create a streaming flow through FSI. FSI couples the pressure gradient in the flow to the viscoelastic response of the tube, due to which the restoring force acting on the fluid particle varies, and a net displacement of the fluid particle occurs over a time period.

To this end, the time-averaged acoustic streaming velocity is calculated to be

$$\langle \mathcal{V}_z \rangle (r, z) = \frac{(1 - r^2)}{4} \left\{ \frac{\alpha}{4} - \beta \frac{1 - (\omega/\omega_o)^2}{\left[1 - (\omega/\omega_o)^2\right]^2 + 4\zeta^2 (\omega/\omega_o)^2} \right\} G'(z)$$
$$+ \frac{\beta}{4} \frac{1 - (\omega/\omega_o)^2}{\left[1 - (\omega/\omega_o)^2\right]^2 + 4\zeta^2 (\omega/\omega_o)^2} (1 - z), \quad (6.93)$$

where $\langle \cdot \rangle \equiv \frac{1}{T} \int_t^{t+T} (\cdot) \, dt$, and, as before, $T = 2\pi/\Omega$ is period of oscillation (see Eq. (6.52d)). In the absence of FSI, $\beta = 0$, and $\langle \mathcal{V}_z \rangle$ vanishes wherever $G'(z) = 0$, which are the pressure anti-nodes. Therefore, the pressure anti-nodes coincide with streaming velocity nodes, as is common in the acoustic streaming systems [224]. But due to FSI, the relative location of pressure and velocity nodes/antinodes in acoustic streaming changes. This trend is more clearly shown in Fig. 6.10. We note that for no FSI ($\beta = 0$), the velocity nodes are along the middle of the tubes ($z = 0$). However, for $\beta \neq 0$, the position of nodes shifts as well as the direction of the streaming velocity reverses.

Perhaps, the most striking feature of the streaming velocity profile due to FSI, is the nonzero apparent slip velocity at $r = 1$. As seen in Fig. 6.10, the velocity vectors have finite values at $r = 1$, for $\beta \neq 0$. This observation is also corroborated by Eq. (6.93). At a cursory level, this observation appears to be counter intuitive since we explicitly enforced a no-slip boundary condition at the wall. However, we can explain this observation as follows. The no-slip boundary condition is imposed at the deformed wall, i.e., at $r = R(z,t) = 1 + \beta u_r(z,t)$. But, since the time-averaged mean deformation is zero, $\langle u_r(z,t) \rangle = 0$ and $\langle R(z,t) \rangle = 1$, the apparent boundary for the streaming velocity profile is at $r = 1$, where the no-slip has not been imposed and the velocity is nonzero. Therefore, the streaming velocity appears to slip at its boundary, $r = 1$.
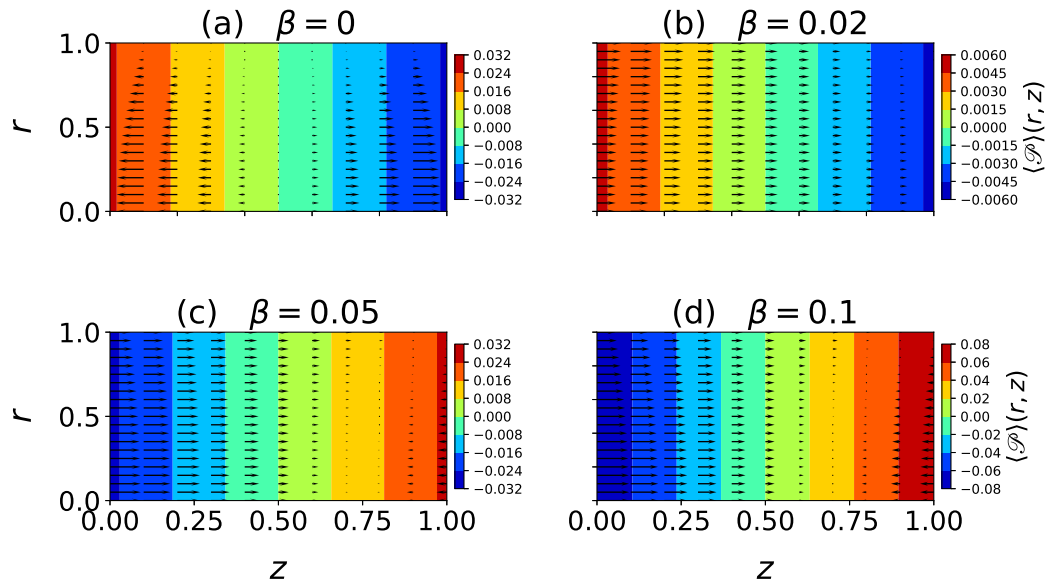
Fig. 6.10. Contour and vector plots for steady state acoustic streaming velocity profile $\langle \mathcal{V}_z \rangle (r, z)$ from Eq. (6.93), for different values of β with $\alpha = 0.1$ and $\omega / \omega_o = 0.1$.

The stationary (time–independent) part of the pressure field is given from Eq. (6.88) as:

$$\langle \mathscr{P} \rangle (z) = -\alpha \frac{G(z)}{4} + \beta \frac{\hat{A}(\omega)}{St} G(z) = \left\{ -\frac{\alpha}{4} + \beta \frac{1 - \left(\omega / \omega_o \right)^2}{\left[1 - \left(\omega / \omega_o \right)^2 \right]^2 + 4 \zeta^2 \left(\omega / \omega_o \right)^2} \right\} G(z).$$

(6.94)

The nonzero mean pressure in an oscillatory field leads to acoustic radiation forces [225]. These forces can then be harnessed in many practical devices for varied uses like cell manipulation, droplet levitation etc., which are studied under the umbrella of *acoustophoresis* [226].

Acoustic radiation forces are thus expected to arise from $\langle \mathscr{P} \rangle (z)$ in Eq. (6.94), which has a spatially varying envelope given by $G(z)$. Therefore, the points of maximum pressure
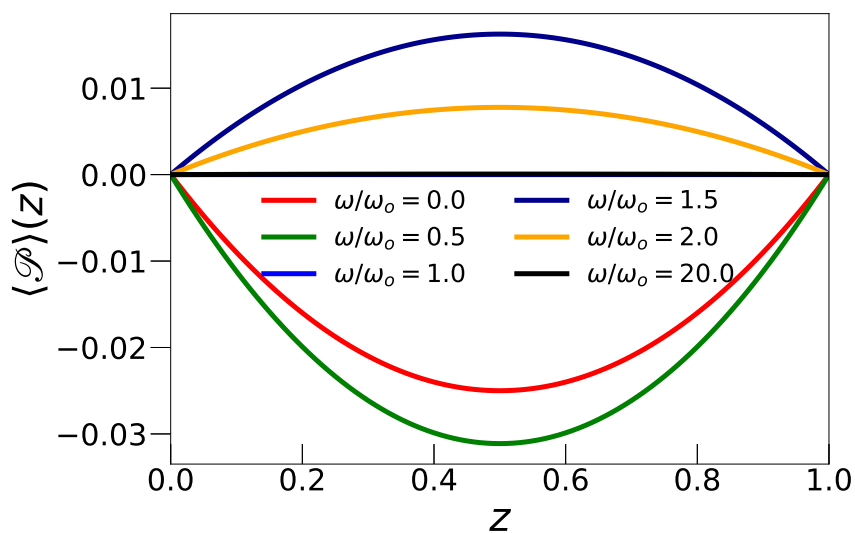
(a)
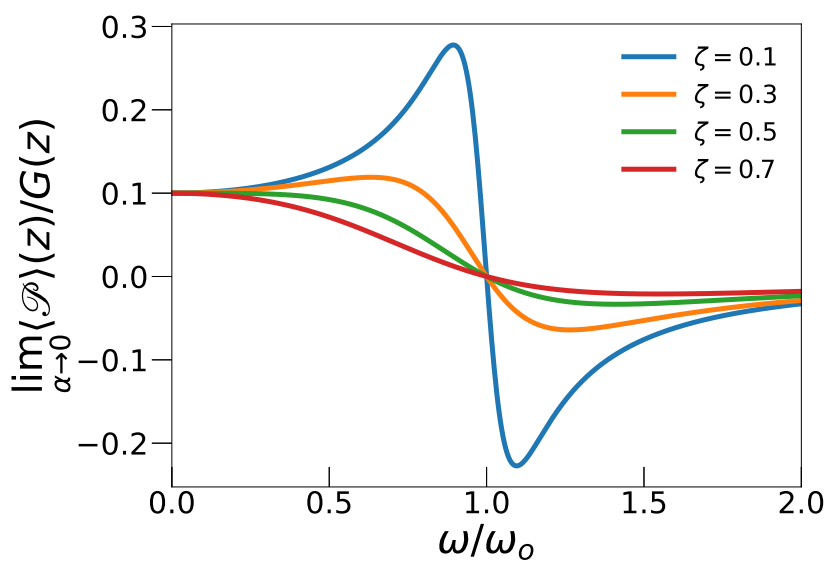
(b)

Fig. 6.11. (a) The period-averaged acoustic radiation pressure profile $\langle \mathscr{P} \rangle(z)$ from Eq. (6.94) for $\alpha = 0$ and $\beta = 0.1$. (b) Frequency response of $\langle \mathscr{P} \rangle(z)$ for negligible compressibility $\alpha \to 0$ and different values of ζ, where $\lim_{\alpha \to 0} \langle \mathscr{P} \rangle(z)/G(z)$ is evaluated from Eq. (6.95).

(i.e., the anti-nodes) are at z such that $G'(z) = 0$, i.e., at $z = 1/2$, while the points corresponding to zero pressure (i.e., the nodes), are at $z = 0, 1$. These facts are illustrated in Fig. 6.11(a). We also see from Eq. (6.94), that the $O(\beta)$ term in the expression for $\langle \mathscr{P} \rangle (z)$ has a frequency-dependent response:

$$\lim_{\alpha \to 0} \frac{\langle \mathscr{P} \rangle (z)}{G(z)} = \beta \frac{1 - (\omega/\omega_o)^2}{\left[1 - (\omega/\omega_o)^2 \right]^2 + 4\zeta^2 (\omega/\omega_o)^2}. \tag{6.95}$$

Equation (6.95) is plotted in Fig. 6.11(b), showing an increasing trend as $\omega \to \omega_o$. However, near $\omega = \omega_o$, the profile undergoes a sharp dip to zero and becomes negative, before tapering off back to zero for $\omega \gg \omega_o$. The maximum is reached at $\omega = \omega_o \sqrt{1 - 2\zeta}$. Clearly, the time-averaged pressure in a viscoelastic tube can be harnessed as a low-pass filter, where only the (pressure) signals with frequencies $\omega < \omega_o \sqrt{1 - 2\zeta}$ are allowed through, and signals with higher frequencies are attenuated.

The period-averaged post-transient flow rate enhancement, neglecting the terms of $O(\beta^2)$, is calculated (from Eqs. (6.80), (6.85) and (6.88)) as,

$$\langle q^* \rangle = -\frac{1}{8} \left\{ -\frac{\alpha}{4} + \beta \frac{\left[1 - (\omega/\omega_o)^2 \right]}{\left[1 - (\omega/\omega_o)^2 \right]^2 + 4\zeta^2 (\omega/\omega_o)^2} \right\} G'(z)$$

$$+ \frac{\beta}{4} \frac{(1 - z)}{\sqrt{\left[1 - (\omega/\omega_o)^2 \right]^2 + 4\zeta^2 (\omega/\omega_o)^2}} \sin \phi. \tag{6.96}$$

At the outlet ($z = 1$), the second term in Eq. (6.96) vanishes. Thus, for negligible compressibility ($\alpha \to 0$), the nonzero mean enhanced flow at the outlet has the same frequency response as the streaming pressure from Eq. (6.95). Consequently, the streaming-enhanced flow rate at the outlet also exhibits the low-pass feature, with the cut-off frequency $\omega_o \sqrt{1 - 2\zeta}$.

6.4 Conclusion

In this paper, we studied compressible viscous flow at low Re in a compliant viscoelastic tube. The assumptions pertaining to the scale and geometry of the system render the

flow inertialess, allowing us to invoke the lubrication approximation. The compressibility effects are introduced through an equation of state, which relates the density to the pressure through a compressibility parameter. Rarefaction effects can be accounted for at steady state through an apparent slip boundary condition. For the structural mechanics domain, we extended the classical (linearly elastic) Donnell shell theory to incorporate Kelvin–Voigt (KV) linear viscoelasticity. We neglected bending, and obtained a deformation equation, wherein the dimensionless Deborah number quantified the relative magnitude of structural elasticity and structural viscosity, while a Strouhal number quantified the strength of (unsteady) inertial effects in the tube.

The set of governing equations formulated were then solved within the framework of three illustrative sub-problems. The first of these problems involved steady-state compressible flow with rarefaction, wherein the viscoelastic structural model reduced to an elastic structural model. The other two problems were concerned with transient dynamics, wherein rarefaction (slip) had to be neglected to render the equations amenable to analytical solution. The first of these transient cases involved impulsive pressurization of the inlet, while the second case involved an oscillatory pressure at the inlet. While the steady-state problem reduces to a nonlinear separable ODE, the transient problems involve nonlinear PDEs, which require a double perturbation expansion in β and α to make analytical progress.

The interplay of different physical effects such as fluid–structure interaction (FSI), compressibility, rarefaction, viscoelasticity, and inlet conditions was analyzed. The main results of this paper are as follows. First, we find that, due to FSI, the Stokes flow takes a finite time to adjust to any changes emanating from the boundary motion. Second, the time constant pertaining to the exponentially-decaying transient response of the system is independent of the inlet boundary condition (impulsive or oscillatory pressure). Third, we show that, in the case of oscillatory pressure imposed at the tube's inlet, FSI leads to acoustic streaming in the flow. The acoustic streaming induces an enhancement in flow rate, which when averaged over a period of oscillation, displays a frequency response like that of a low pass filter with a cut-off frequency of $\omega_o \sqrt{1 - 2\zeta}$. In particular, oscillatory flow in viscoelastic tubes

leads to resonances at a particular value of the inlet pressure frequency, which maximize the deformation of the tube.

Our study neglected the convective acceleration of the fluid since we assumed that $\epsilon Re \ll 1$, which yielded a unidirectional flow field and a pressure field depending only on the flow-wise coordinate. However, the compressible flow inside both tubes and channels has been analyzed in literature without neglecting the convective acceleration, for arbitrary values of ϵRe, i.e. when the conduit is not necessarily slender [79–81]. Such an analysis accounts for both transverse velocity as well as the variation of the pressure field in the transverse direction. Perhaps, in the future, it may be of interest to extend their line of research to include FSI in a deformable conduit, and explore the interactions of a radially varying pressure field with a soft structure undergoing transient deformations, ultimately resulting in a more accurate version of our FSI theory.

7. SUMMARY AND OUTLOOK

This chapter summarizes the main accomplishments of this thesis and presents avenues for future work.

7.1   Thesis summary

In this thesis, we have analyzed, through theoretical calculations and computer simulations, the phenomena of fluid–structure interactions (FSIs) taking place due to an internal flow inside a soft conduit. Specifically, as the stated aim of this research, we found the flow rate–pressure drop relation for low Re flow in elastic tubes and channels. Because of fluid–structure interactions, the flow rate–pressure drop relation involves the material properties of the structure, and thus may be interpreted as an extension to deformable conduits of the classical Hagen–Poiseuille law.

The chapter-wise accomplishments of this thesis are:

- **Chapter 2:** We determined the flow rate–pressure drop relation for the flow of a power-law fluid in a rectangular microchannel with a deformable top wall. We obtain a nonlinear differential equation for pressure as a function of imposed steady flow rate, consisting of infinite expansions of hypergeometric functions. In doing so, we demonstrated that, under the lubrication approximation, the rheology of the fluid does not explicitly enter into the coupling with structural mechanics problem.

- **Chapter 3:** We extended and applied the low-Re theory of fluid–structure interactions in microchannels to develop a technique for *hydrodynamic* bulge testing. We demonstrated that this proposed experimental method allows the estimation of material properties (such as the Young's modulus), from the the flow rate–pressure drop relation, given only a pressure drop measurement (i.e., without measuring the de-

formation at all). A sensitivity analysis showed that the hydrodynamic bulge test is only slightly less accurate than the traditional hydrostatic bulge test, but it is less susceptible to noise in the measured quantity.

- **Chapter 4:** We formulated and analyzed the fluid–structure interaction problem for a thin linearly elastic tube conveying a power-law fluid. We found the expressions for the radial deformation of the tube, taking into account the bending boundary layers near its clamped ends. We also improved upon the classical theories by Laplace and Fung, and updated them to match with the computer simulations carried out in ANSYS.

- **Chapter 5:** We formulated and analyzed the fluid–structure interaction problem for hyperelastic tubes, extending some of the results of Chapter 4. Using the stretching dominant membrane theory to model the deformation of thin walled tube, we obtained a closed form relationship between the imposed flow rate and local deformation. Specifically, we showed that, due to strain hardening, the hyperelastic tube is overall "less compliant" during FSI than a linearly elastic tube.

- **Chapter 6:** We formulated and analyzed the transient fluid–structure interactions due to compressible internal fluid flow in a viscoelastic tube, taking into account the tube's inertia. A perturbation approach accounted for weak fluid–structure interaction and weak compressibility. We found that a low-frequency oscillatory pressure at the inlet leads to streaming in the flow. The ensuing enhancement in the flow rate, when averaged over a period of oscillation, has a frequency response similar to that of a low pass filter. Then, we demonstrated that oscillatory flow in viscoleastic tubes leads to resonances at a particular value of the inlet pressure frequency, which maximize the deformation of the tube.

7.2 Future work

In future work pertaining to rectangular microchannels, it is of interest to determine the first correction due to friction at the lateral side walls, i.e., to relax the assumption $\delta = h_0/w \ll 1$. In [37], the latter calculation was accomplished by using the known two-dimensional (2D) solution for flow of a Newtonian fluid in a rectangular channel. For the power-law fluid considered in Chapter 2, however, the rate of shear strain becomes a nonlinear function of the velocity gradient in 2D, thus an exact 2D flow solution is unavailable [227]. The latter fact makes the mathematical extension of [37, Appendix B] a challenging open problem.

Our theoretical discussions largely considered flows actuated by a pressure difference. On the other hands, in microfluidics, flows are frequently actuated electro-kinetically [21] or magneto-hydrodynamically. How these modes of flow actuation affect the FSI in a tube or channel may also be an area of research worth pursuing. In addition to actuation strategies, a theory of FSI in microchannels with *viscoelastic* top walls (extending the results on viscoelastic tubes from Chapter 6) could be developed to ultimately yield a hydrodynamic bulge test for the estimation of viscoelastic properties (loss and storage moduli, for example). Much like the hydrodynamic bulge test for estimation of linearly elastic properties proposed in Chapter 3.

Our FSI theory of microchannels is hinged on the assumptions of small strains, which allows us to linearize the differential equations in structural mechanical domain, and helps to solve the equations analytically. Venturing into the domain of large strains would be mathematically challenging, but also potentially rewarding. At larger strains, it is known that PDMS may exhibit a hyperelastic response [228]. Thus, in future work, it would be of interest to extend the proposed FSI theory of rectangular microchannels to capture this nonlinear material behavior. The proposed hydrodynamic bulge testing technique from Chapter 3 could also be extended to handle liquid blister tests [27], which are used to measure the strength of bonding (via the work of adhesion), if the fluid layer is made much thinner than the solid film. Beyond bulge tests, the FSI between a viscous fluid and a

pre-stressed plate-like elastic structure can be harnessed to create soft microfluidic actuators [118]. Similar multiphysics problems can also be motivated by biomedical and physiological applications, such as the reopening of strongly collapsed airways [117]. These problems are unsteady [211], thus one must obtain dynamic equations for the motion of the fluid front during expansion (or collapse) [29, 54, 64, 178]. Therefore, the present analysis could be extended/become the foundation of further research on these problem as well.

In future work pertaining to microtubes, the FSI theory developed herein can be extended to incorporate further physical effects that arise in microscale fluid mechanics. For example, the material composing the tube may not be only elastic but also porous (i.e., *poroelastic*) [229]. Moreover, the FSI of hyperelastic tubes analyzed in this chapter concerned with only the leading order terms, where the bending terms were neglected. It may be worthwhile to pursue a more nuanced approach wherein the bending of the tube at the clamped ends are also accounted for.

REFERENCES

REFERENCES

[1] T. M. Squires and S. R. Quake, "Microfluidics: Fluid physics at the nanoliter scale," *Rev. Mod. Phys.*, vol. 77, pp. 977–1026, 2005.

[2] J. R. Happel and H. Brenner, *Low Reynolds Number Hydrodynamics*, 2nd ed., ser. Mechanics of fluids and transport processes. The Hague: Martinus Nijhoff Publishers, 1983, vol. 1.

[3] H. Bruus, *Theoretical Microfluidics*, ser. Oxford Master Series in Condensed Matter Physics. Oxford, UK: Oxford University Press, 2008.

[4] Y. Xia and G. M. Whitesides, "Soft lithography," *Annu. Rev. Mater. Sci.*, vol. 28, pp. 153–184, 1998.

[5] P. J. Kitson, M. H. Rosnes, V. Sans, V. Dragone, and L. Cronin, "Configurable 3D-Printed millifluidic and microfluidic 'lab on a chip' reactionware devices," *Lab Chip*, vol. 12, pp. 3267–3271, 2012.

[6] W. Su, B. S. Cook, Y. Fang, and M. M. Tentzeris, "Fully inkjet-printed microfluidics: A solution to low-cost rapid three-dimensional microfluidics fabrication with numerous electrical and sensing applications," *Sci. Rep.*, vol. 6, p. 35111, 2016.

[7] N.-T. Nguyen and S. T. Wereley, *Fundamentals and Applications of Microfluidics*, 2nd ed., ser. Integrated Microsystems Series. Norwood, MA: Artech House, 2006.

[8] G. M. Whitesides, "The origins and the future of microfluidics," *Nature*, vol. 442, pp. 368–373, 7 2006.

[9] A. Weisberg, H. H. Bau, and J. N. Zemel, "Analysis of microchannels for integrated cooling," *Int. J. Heat Mass Transfer*, vol. 35, pp. 2465–2474, 1992.

[10] T. Dixit and I. Ghosh, "Review of micro- and mini-channel heat sinks and heat exchangers for single phase fluids," *Renew. Sust. Energ. Rev.*, vol. 41, pp. 1298–1311, 2015.

[11] P. Abgrall and A. M. Gué, "Lab-on-chip technologies: making a microfluidic network and coupling it into a complete microsystem—a review," *J. Micromech. Microeng.*, vol. 17, p. R15, 2007.

[12] M. Madou, J. Zoval, G. Jia, H. Kido, J. Kim, and N. Kim, "Lab on a CD," *Annu. Rev. Biomed. Eng.*, vol. 8, pp. 601–628, 2006.

[13] L. X. Kong, A. Perebikovsky, J. Moebius, L. Kulinsky, and M. Madou, "Lab-on-a-CD," *J. Lab. Automat.*, vol. 21, pp. 323–355, 2016.

[14] S. Nagrath, L. V. Sequist, S. Maheswaran, D. W. Bell, D. Irimia, L. Ulkus, M. R. Smith, E. L. Kwak, S. Digumarthy, A. Muzikansky, P. Ryan, U. J. Balis, R. G. Tompkins, D. A. Haber, and M. Toner, "Isolation of rare circulating tumour cells in cancer patients by microchip technology," *Nature*, vol. 450, pp. 1235–1239, 2007.

[15] J. Sun, M. D. Masterman-Smith, N. A. Graham, J. Jiao, J. Mottahedeh, D. R. Laks, M. Ohashi, J. DeJesus, K. I. Kamei, K. B. Lee, H. Wang, Z. F. Yu, Y. T. Lu, S. Hou, K. Li, M. Liu, N. Zhang, S. Wang, B. Angenieux, E. Panosyan, E. R. Samuels, J. Park, D. Williams, V. Konkankit, D. Nathanson, R. M. Van Dam, M. E. Phelps, H. Wu, L. M. Liau, P. S. Mischel, J. A. Lazareff, H. I. Kornblum, W. H. Yong, T. G. Graeber, and H. R. Tseng, "A microfluidic platform for systems pathology: Multiparameter single-cell signaling measurements of clinical brain tumor specimens," *Cancer Res.*, vol. 70, pp. 6128–6138, 2010.

[16] D. R. Reyes, D. Iossifidis, P.-A. Auroux, and A. Manz, "Micro total analysis systems. 1. Introduction, theory, and technology," *Anal. Chem.*, vol. 74, pp. 2623–2636, 6 2002.

[17] P.-A. Auroux, D. Iossifidis, D. R. Reyes, and A. Manz, "Micro total analysis systems. 2. Analytical standard operations and applications," *Anal. Chem.*, vol. 74, pp. 2637–2652, 6 2002.

[18] D. L. Hu and J. W. M. Bush, "Meniscus-climbing insects," *Nature*, vol. 437, pp. 733–736, 2005.

[19] H. A. Stone, A. D. Stroock, and A. Ajdari, "Engineering flows in small devices: Microfluidics toward a Lab-on-a-Chip," *Annu. Rev. Fluid Mech.*, vol. 36, pp. 381–411, 2004.

[20] J.-J. Shu, J. Bin Melvin Teo, and W. Kong Chan, "Fluid velocity slip and temperature jump at a solid surface," *Appl. Mech. Rev.*, vol. 69, p. 020801, 2017.

[21] J. R. Melcher and G. I. Taylor, "Electrohydrodynamics: A review of the role of interfacial shear stresses," *Annu. Rev. Fluid Mech.*, vol. 1, pp. 111–146, 1969.

[22] C. J. Pipe and G. H. McKinley, "Microfluidic rheometry," *Mech. Res. Commun.*, vol. 36, pp. 110–120, 2009.

[23] S. Girardo, R. Cingolani, and D. Pisignano, "Microfluidic rheology of non-Newtonian liquids," *Anal. Chem.*, vol. 79, pp. 5856–5861, 2007.

[24] C. Duprat and H. A. Stone, Eds., *Fluid–Structure Interactions in Low-Reynolds-Number Flows*. Cambridge, UK: The Royal Society of Chemistry, 2016.

[25] P. Karan, J. Chakraborty, and S. Chakraborty, "Small-scale flow with deformable boundaries," *J. Indian Inst. Sci.*, vol. 98, pp. 159–183, 2018.

[26] L. B. Sandberg, W. R. Gray, and C. Franzblau, Eds., *Elastin and Elastic Tissue*, ser. Advances in Experimental Medicine and Biology. New York: Plenum Press, 1977, vol. 79.

[27] J. Chopin, D. Vella, and A. Boudaoud, "The liquid blister test," *Proc. R. Soc. A*, vol. 464, pp. 2887–2906, 2008.

[28] A. Juel, D. Pihler-Puzović, and M. Heil, "Instabilities in blistering," *Annu. Rev. Fluid Mech.*, vol. 50, pp. 691–714, 2018.

[29] I. J. Hewitt, N. J. Balmforth, and J. R. De Bruyn, "Elastic-plated gravity currents," *Eur. J. Appl. Math.*, vol. 26, pp. 1–31, 2015.

[30] T. Gervais, J. El-Ali, A. Günther, and K. F. Jensen, "Flow-induced deformation of shallow microfluidic channels," *Lab Chip*, vol. 6, pp. 500–507, 2006.

[31] S. P. Sutera and R. Skalak, "The history of Poiseuille's Law," *Annu. Rev. Fluid Mech.*, vol. 25, pp. 1–19, 1993.

[32] B. S. Hardy, K. Uechi, J. Zhen, and H. Pirouz Kavehpour, "The deformation of flexible PDMS microchannels under a pressure driven flow," *Lab Chip*, vol. 9, pp. 935–938, 2009.

[33] E. Seker, D. C. Leslie, H. Haj-Hariri, J. P. Landers, M. Utz, and M. R. Begley, "Nonlinear pressure-flow relationships for passive microfluidic valves," *Lab Chip*, vol. 9, pp. 2691–2697, 2009.

[34] O. Ozsun, V. Yakhot, and K. L. Ekinci, "Non-invasive measurement of the pressure distribution in a deformable micro-channel," *J. Fluid Mech.*, vol. 734, p. R1, 2013.

[35] C. Kang, C. Roh, and R. A. Overfelt, "Pressure-driven deformation with soft poly-dimethylsiloxane (PDMS) by a regular syringe pump: challenge to the classical fluid dynamics by comparison of experimental and theoretical results," *RSC Adv.*, vol. 4, pp. 3102–3112, 2014.

[36] M. K. Raj, S. DasGupta, and S. Chakraborty, "Hydrodynamics in deformable microchannels," *Microfluid. Nanofluid.*, vol. 21, p. 70, 2017.

[37] I. C. Christov, V. Cognet, T. C. Shidhore, and H. A. Stone, "Flow rate–pressure drop relation for deformable shallow microfluidic channels," *J. Fluid Mech.*, vol. 814, pp. 267–286, 2018.

[38] T. C. Shidhore and I. C. Christov, "Static response of deformable microchannels: a comparative modelling study," *J. Phys.: Condens. Matter*, vol. 30, p. 054002, 2018.

[39] R. D. Mindlin, "Influence of rotatory inertia and shear on flexural motions of isotropic, elastic plates," *ASME J. Appl. Mech.*, vol. 18, pp. 31–38, 1951.

[40] X. Wang and I. C. Christov, "Theory of the flow-induced deformation of shallow compliant microchannels with thick walls," *Proc. R. Soc. A*, vol. 475, p. 20190513, 11 2019.

[41] B. Tavakol, G. Froehlicher, H. A. Stone, and D. P. Holmes, "Extended lubrication theory: Improved estimates of flow in channels with variable geometry," *Proc. R. Soc. A*, vol. 473, p. 20170234, 2017.

[42] A. Raj and A. K. Sen, "Flow-induced deformation of compliant microchannels and its effect on pressure–flow characteristics," *Microfluid. Nanofluid.*, vol. 20, p. 31, 2016.

[43] W. K. Schomburg, *Introduction to Microsystem Design.* Berlin/Heidelberg: Springer-Verlag, 2011.

[44] J. B. Grotberg, "Pulmonary flow and transport phenomena," *Annu. Rev. Fluid Mech.*, vol. 26, pp. 529–571, 1994.

[45] J. B. Grotberg and O. E. Jensen, "Biofluid mechanics in flexible tubes," *Annu. Rev. Fluid Mech.*, vol. 36, pp. 121–147, 2004.

[46] M. Heil and A. L. Hazel, "Fluid-structure interaction in internal physiological flows," *Annu. Rev. Fluid Mech.*, vol. 43, pp. 141–162, 2011.

[47] A. H. Shapiro, "Steady flow in collapsible tubes," *ASME J. Biomech. Eng.*, vol. 99, pp. 126–147, 1977.

[48] C. D. Bertram and T. J. Pedley, "A mathematical model of unsteady collapsible tube behaviour," *J. Biomech.*, vol. 15, pp. 39–50, 1982.

[49] R. J. Whittaker, M. Heil, O. E. Jensen, and S. L. Waters, "A rational derivation of a tube law from shell theory," *Q. J. Mech. Appl. Math.*, vol. 63, pp. 465–496, 2010.

[50] T. J. Pedley, *The Fluid Mechanics of Large Blood Vessels*. Cambridge: Cambridge University Press, 1980.

[51] N. Kizilova, M. Hamadiche, and M. Gad-el Hak, "Mathematical models of biofluid flows in compliant ducts," *Arch. Mech.*, vol. 64, pp. 65–94, 2012.

[52] F. Gay-Balmaz, D. Georgievskii, and V. Putkaradze, "Stability of helical tubes conveying fluid," *J. Fluids Struct.*, vol. 78, pp. 146–174, 2018.

[53] S. Čanic and A. Mikelić, "Effective equations modeling the flow of a viscous incompressible Ffuid through a long elastic tube arising in the study of blood flow through small arteries," *SIAM J. Appl. Dyn. Syst.*, vol. 2, pp. 431–463, 2003.

[54] F. Meng, J. Huang, and M. D. Thouless, "The collapse and expansion of liquid-filled elastic channels and cracks," *ASME J. Appl. Mech.*, vol. 82, p. 101009, 2015.

[55] S. Chakraborty, "Dynamics of capillary flow of blood into a microfluidic channel," *Lab Chip*, vol. 5, pp. 421–430, 2005.

[56] L. J. Lee, "BioMEMS," in *Encyclopedia of Chemical Processing*, S. Lee, Ed. New York: Taylor & Francis, 2006, vol. 1, pp. 161–169.

[57] Y. C. Fung, *Biomechanics: Mechanical Properties of Living Tissues*. New York, NY: Springer-Verlag, 1993.

[58] E. Boyko, M. Bercovici, and A. D. Gat, "Viscous-elastic dynamics of power-law fluids within an elastic cylinder," *Phys. Rev. Fluids*, vol. 2, p. 073301, 2017.

[59] K. Raj M, J. Chakraborty, S. DasGupta, and S. Chakraborty, "Flow-induced deformation in a microchannel with a non-Newtonian fluid," *Biomicrofluidics*, vol. 12, p. 034116, 5 2018.

[60] V. Anand, J. David JR, and I. C. Christov, "Non-Newtonian fluid–structure interactions: Static response of a microchannel due to internal flow of a power-law fluid," *J. Non-Newtonian Fluid Mech.*, vol. 264, pp. 62–72, 2019.

[61] J. Paek, I. Cho, and J. Kim, "Microrobotic tentacles with spiral bending capability based on shape-engineered elastomeric microtubes," *Sci. Rep.*, vol. 5, p. 10768, 2015.

[62] F. Wu, S. Chen, B. Chen, M. Wang, L. Min, J. Alvarenga, J. Ju, A. Khademhosseini, Y. Yao, Y. S. Zhang, J. Aizenberg, and X. Hou, "Bioinspired universal flexible elastomer-based microchannels," *Small*, vol. 14, p. 1702170, 2018.

[63] S. B. Elbaz and A. D. Gat, "Dynamics of viscous liquid within a closed elastic cylinder subject to external forces with application to soft robotics," *J. Fluid Mech.*, vol. 758, pp. 221–237, 2014.

[64] ——, "Axial creeping flow in the gap between a rigid cylinder and a concentric elastic tube," *J. Fluid Mech.*, vol. 806, pp. 580–602, 2016.

[65] V. V. Vedeneev and A. B. Poroshina, "Stability of an elastic tube conveying a non-Newtonian fluid and having a locally weakened section," *Proc. Steklov Inst. Math.*, vol. 300, pp. 34–55, 2018.

[66] D. S. Chang, "Compressible Flows for Fluidic Control in Microdevices," Ph.D. dissertation, University of Michigan, 2010. [Online]. Available: http://hdl.handle.net/2027.42/75919%0A

[67] C.-M. Ho and Y.-C. Tai, "REVIEW: MEMS and Its Applications for Flow Control," *ASME J. Fluids Eng.*, vol. 118, pp. 437–447, 1996.

[68] ——, "Micro-electro-mechanical-systems (MEMS) and fluid flows," *Annu. Rev. Fluid Mech.*, vol. 30, pp. 579–612, 1 1998.

[69] J. Liu, Y.-C. Tai, and C.-M. Ho, "MEMS for pressure distribution studies of gaseous flows in microchannels," in *Proceedings IEEE Micro Electro Mechanical Systems*. IEEE, 1995, pp. 209–215.

[70] Y. Zohar, S. Y. K. Lee, W. Y. Lee, L. Jiang, and P. Tong, "Subsonic gas flow in a straight and uniform microchannel," *J. Fluid Mech.*, vol. 472, pp. 125–151, 2002.

[71] W. Y. Lee, M. Wong, and Y. Zohar, "Microchannels in series connected via a contraction/expansion section," *J. Fluid Mech.*, vol. 459, pp. 187–206, 2002.

[72] S. Y. K. Lee, M. Wong, and Y. Zohar, "Gas flow in microchannels with bends," *J. Micromech. Microeng.*, vol. 11, pp. 635–644, 2001.

[73] E. B. Arkilic, M. A. Schmidt, and K. S. Breuer, "Gaseous slip flow in long microchannels," *J. Microelectromechan. Syst.*, vol. 6, pp. 167–178, 1997.

[74] Q. Fan and H. Xue, "Compressible effects in microchannel flows [MEMS]," in *Proceedings of 2nd Electronics Packaging Technology Conference*. Singapore: IEEE, 1998, pp. 224–228.

[75] S. Wu, J. Mai, Y. Zohar, Y. Tai, and C. Ho, "A suspended microchannel with integrated temperature sensors for high-pressure flow studies," in *Proc. 11th IEEE Workshop on Micro Electro Mechanical Systems, MEMS'98,*, 1998, pp. 87–92.

[76] R. K. Prud'Homme, T. W. Chapman, and J. R. Bowen, "Laminar compressible flow in a tube," *Appl. Sci. Res.*, vol. 43, pp. 67–74, 1986.

[77] H. R. van den Berg, C. A. ten Seldam, and P. S. van der Gulik, "Working equation for a capillary viscometer with non-steady compressible flow," *Physica A*, vol. 167, pp. 457–480, 1990.

[78] ——, "Compressible laminar flow in a capillary," *J. Fluid Mech.*, vol. 246, pp. 1–20, 1993.

[79] D. C. Venerus, "Laminar capillary flow of compressible viscous fluids," *J. Fluid Mech.*, vol. 555, pp. 59–80, 2006.

[80] D. C. Venerus and D. J. Bugajsky, "Compressible laminar flow in a channel," *Phys. Fluids*, vol. 22, pp. 1–11, 2010.

[81] E. G. Taliadorou, M. Neophytou, and G. C. Georgiou, "Perturbation solutions of Poiseuille flows of weakly compressible Newtonian liquids," *J. Non-Newtonian Fluid Mech.*, vol. 163, pp. 25–34, 2009.

[82] L. W. Schwartz, "A perturbation solution for compressible viscous channel flows," *J. Eng. Math.*, vol. 21, pp. 69–86, 1987.

[83] A. Mehboudi and J. Yeom, "A one-dimensional model for compressible fluid flows through deformable microchannels," *Phys. Fluids*, vol. 30, p. 092003, 2018.

[84] S. B. Elbaz, H. Jacob, and A. D. Gat, "Transient gas flow in elastic microchannels," *J. Fluid Mech.*, vol. 846, pp. 460–481, 2018.

[85] M. Zhang, K. Feng, K. Zhang, Z. Zhao, and Y. Cao, "Transient characteristics of a straight tube actuated by viscous compressible flow with consideration of large axisymmetric deformation," *Acta Mech.*, vol. 230, pp. 105–120, 2019.

[86] J. C. McDonald and G. M. Whitesides, "Poly(dimethylsiloxane) as a material for fabricating microfluidic devices," *Acc. Chem. Res.*, vol. 35, pp. 491–499, 2002.

[87] Y. C. Fung, *Biomechanics: Circulation*, 2nd ed.   New York, NY: Springer-Verlag, 1997.

[88] B. K. Wunderlich, U. A. Kleßinger, and A. R. Bausch, "Diffusive spreading of time-dependent pressures in elastic microfluidic devices," *Lab Chip*, vol. 10, pp. 1025–1029, 2010.

[89] M. Kiran Raj, S. Dasgupta, and S. Chakraborty, "Biomimetic pulsatile flows through flexible microfluidic conduits," *Biomicrofluidics*, vol. 13, p. 014103, 2019.

[90] C. M. Ionescu, "Modeling the respiratory tree by means of mechanical analogy," in *The Human Respiratory System: An Analysis of the Interplay between Anatomy, Structure, Breathing and Fractal Dynamics*, ser. Series in BioEngineering.   London: Springer-Verlag, 2013, ch. 6, pp. 77–98.

[91] D. Mitsotakis, D. Dutykh, Q. Li, and E. Peach, "On some model equations for pulsatile flow in viscoelastic vessels," *Wave Motion*, vol. 90, pp. 139–151, 2019.

[92] K. Shimoga and A. Goldenberg, "Soft Robotic Fingertips: Part I: A Comparison of Construction Materials," *Int. J. Robot. Res.*, vol. 15, pp. 320–334, 1996.

[93] ——, "Soft robotic fingertips: Part II: Modeling and impedance regulation," *Int. J. Robot. Res.*, vol. 15, pp. 335–350, 8 1996.

[94] S. Coyle, C. Majidi, P. LeDuc, and K. J. Hsia, "Bio-inspired soft robotics: Material selection, actuation, and design," *Extreme Mech. Lett.*, vol. 22, pp. 51–59, 7 2018.

[95] S. Kim, C. Laschi, and B. Trimmer, "Soft robotics: A bioinspired evolution in robotics," *Trends Biotech.*, vol. 31, pp. 287–294, 2013.

[96] K. Ando, T. Sanada, K. Inaba, J. S. Damazo, J. E. Shepherd, T. Colonius, and C. E. Brennen, "Shock propagation through a bubbly liquid in a deformable tube," *J. Fluid Mech.*, vol. 671, pp. 339–363, 2011.

[97] L. Suo and E. B. Wylie, "Complex wavespeed and hydraulic transients in viscoelastic pipes," *ASME J. Fluids Eng.*, vol. 112, pp. 496–500, 1990.

[98] D. C. Wiggert and A. S. Tijsseling, "Fluid transients and fluid-structure interaction in flexible liquid-filled piping," *App. Mech. Rev.*, vol. 54, pp. 455–481, 9 2001.

[99] D. C. Leslie, C. J. Easley, E. Seker, J. M. Karlinsey, M. Utz, M. R. Begley, and J. P. Landers, "Frequency-specific flow control in microfluidic circuits with passive elastomeric features," *Nat. Phys.*, vol. 5, pp. 231–235, 2009.

[100] D. P. Holmes, B. Tavakol, G. Froehlicher, and H. A. Stone, "Control and manipulation of microfluidic flow via elastic deformations," *Soft Matter*, vol. 9, pp. 7049–7053, 5 2013.

[101] M. Gomez, D. E. Moulton, and D. Vella, "Passive control of viscous flow via elastic snap-through," *Phys. Rev. Lett.*, vol. 119, p. 144502, 2017.

[102] C. De Loubens, A. Magnin, M. Doyennette, I. C. Tréléa, and I. Souchon, "A biomechanical model of swallowing for understanding the influence of saliva and food bolus viscosity on flavor release," *J. Theor. Biol.*, vol. 280, pp. 180–188, 2011.

[103] P. Goswami, J. Chakraborty, A. Bandopadhyay, and S. Chakraborty, "Electrokinetically modulated peristaltic transport of power-law fluids," *Microvascular Research*, vol. 103, pp. 41–54, 2016.

[104] A. H. Shapiro, M. Y. Jaffrin, and S. L. Weinberg, "Peristaltic pumping with long wavelengths at low Reynolds number," *J. Fluid Mech.*, vol. 37, pp. 799–825, 1969.

[105] A. Bandopadhyay, D. Tripathi, and S. Chakraborty, "Electroosmosis-modulated peristaltic transport in microfluidic channels," *Phys. Fluids*, vol. 28, p. 052002, 2016.

[106] M. K. Small and W. D. Nix, "Analysis of the accuracy of the bulge test in determining the mechanical properties of thin films," *J. Mat. Res.*, vol. 7, pp. 1553–1563, 1992.

[107] W. P. Jackson, "Characterization of Soft Polymers and Gels using the Pressure-Bulge Technique," Ph.D. dissertation, California Institute of Technology, 2008. [Online]. Available: https://thesis.library.caltech.edu/2322/

[108] J.-H. Huang, K. Haffey, A. Arefin, L. E. Akhadov, J. F. Harris, R. Iyer, and P. Nath, "A microfluidic method to measure bulging heights for bulge testing of polydimethylsiloxane (PDMS) and polyurethane (PU) elastomeric membranes," *RSC Adv.*, vol. 8, pp. 21 133–21 138, 2018.

[109] W. Zhou, J. Yang, G. Sun, X. Liu, F. Yang, and J. Li, "Fracture properties of silicon carbide thin films by bulge test of long rectangular membrane," *J. Microelectromechan. Syst.*, vol. 17, pp. 453–461, 2008.

[110] W. Zhou, J. Yang, Y. Li, A. Ji, F. Yang, and Y. Yu, "Bulge testing and fracture properties of plasma-enhanced chemical vapor deposited silicon nitride thin films," *Thin Solid Films*, vol. 517, pp. 1989–1994, 2009.

[111] J. Yang and O. Paul, "Fracture properties of LPCVD silicon nitride thin films from the load-deflection of long membranes," *Sensors Actuators A: Physical*, vol. 97-98, pp. 520–526, 2002.

[112] J. Neggers, J. P. M. Hoefnagels, and M. G. D. Geers, "On the validity regime of the bulge equations," *J. Mat. Res.*, vol. 27, pp. 1245–1250, 2012.

[113] J. J. Vlassak and W. D. Nix, "A new bulge test technique for the determination of Young's modulus and Poisson's ratio of thin films," *J. Mat. Res.*, vol. 7, pp. 3242–3249, 12 1992.

[114] S. Shafqat, O. van der Sluis, M. Geers, and J. Hoefnagels, "A bulge test based methodology for characterizing ultra-thin buckled membranes," *Thin Solid Films*, vol. 660, pp. 88–100, 2018.

[115] L. Yang, S.-G. Long, Z.-S. Ma, and Z.-H. Wang, "Accuracy analysis of plane-strain bulge test for determining mechanical properties of thin films," *Trans. Nonferrous Metals Soc. China*, vol. 24, pp. 3265–3273, 10 2014.

[116] V. Ziebart, O. Paul, U. Münch, J. Schwizer, and H. Baltes, "Mechanical properties of thin films from the load deflection of long clamped plates," *J. Microelectromechan. Syst.*, vol. 7, pp. 320–327, 1998.

[117] L. Ducloué, A. L. Hazel, A. B. Thompson, and A. Juel, "Reopening modes of a collapsed elasto-rigid channel," *J. Fluid Mech.*, vol. 819, pp. 121–146, 2017.

[118] E. Boyko, R. Eshel, K. Gommed, A. D. Gat, and M. Bercovici, "Elastohydrodynamics of a pre-stretched finite elastic sheet lubricated by a thin viscous film with application to microfluidic soft actuators," *J. Fluid Mech.*, vol. 862, pp. 732–752, 2019.

[119] F. L. Moody, "Friction Factors for Pipe Flow," *Trans. ASME*, vol. 66, pp. 671–684, 1944.

[120] P. J. Pritchard, *Fox & McDonald's Introduction to Fluid Mechanics*, 8th ed. Hoboken, NJ: John Wiley & Sons, 2011.

[121] X. Yang, N. T. Weldetsadik, Z. Hayat, T. Fu, S. Jiang, C. Zhu, and Y. Ma, "Pressure drop of single phase flow in microchannels and its application in characterizing the apparent rheological property of fluids," *Microfluid. Nanofluid.*, vol. 23, p. 75, 2019.

[122] S. Gupta, W. S. Wang, and S. A. Vanapalli, "Microfluidic viscometers for shear rheology of complex fluids and biofluids," *Biomicrofluidics*, vol. 10, p. 043402, 2016.

[123] R. L. Panton, *Incompressible Flow*, 4th ed. Hoboken, NJ: John Wiley & Sons, 2013.

[124] S. H. Davis, "The importance of being thin," *J. Eng. Math.*, vol. 105, pp. 3–30, 2017.

[125] S. K. Wilson, B. R. Duffy, and R. Hunt, "A slender rivulet of a power-law fluid driven by either gravity or a constant shear stress at the free surface," *Quart. J. Mech. Appl. Math.*, vol. 55, pp. 385–408, 8 2002.

[126] F. H. H. Al Mukahal, S. K. Wilson, and B. R. Duffy, "A rivulet of a power-law fluid with constant width draining down a slowly varying substrate," *J. Non-Newtonian Fluid Mech.*, vol. 224, pp. 30–39, 10 2015.

[127] S. Chien, S. Usami, H. M. Taylor, J. L. Lundberg, and M. I. Gregersen, "Effects of hematocrit and plasma proteins on human blood rheology at low shear rates," *J. Appl. Physiol.*, vol. 21, pp. 81–87, 1966.

[128] R. B. Bird, "Useful non-Newtonian models," *Annu. Rev. Fluid Mech.*, vol. 8, pp. 13–34, 1976.

[129] R. B. Bird, R. C. Armstrong, and O. Hassager, *Dynamics of Polymeric Liquids*, 2nd ed.   New York: John Wiley, 1987, vol. 1.

[130] N. W. Bartlett and R. J. Wood, "Comparative analysis of fabrication methods for achieving rounded microchannels in PDMS," *J. Micromech. Microeng.*, vol. 26, p. 115013, 2016.

[131] A. E. H. Love, "The small free vibrations and deformation of a thin elastic shell," *Phil. Trans. R. Soc. Lond. A*, vol. 179, pp. 491–546, 1888.

[132] S. Timoshenko and S. Woinowsky-Krieger, *Theory of Plates and Shells*, 2nd ed. New York: McGraw-Hill, 1959.

[133] E. Reissner, "The effect of transverse shear deformation on the bending of elastic plates," *ASME J. Appl. Mech.*, vol. 12, pp. A68–A77, 1945.

[134] G. R. Cowper, "The shear coefficient in Timoshenko's beam theory," *ASME J. Appl. Mech.*, vol. 33, pp. 335–340, 1966.

[135] J. R. Hutchinson, "Shear coefficients for Timoshenko beam theory," *ASME J. Appl. Mech.*, vol. 68, pp. 87–92, 2001.

[136] S. Zhang, "On the accuracy of Reissner–Mindlin plate model for stress boundary conditions," *ESAIM: M2AN*, vol. 40, pp. 269–294, 2006.

[137] O. C. Zienkiewicz, R. L. Taylor, and J. Z. Zhu, *The Finite Element Method: Its Basis and Fundamentals*, 7th ed.   Oxford: Butterworth-Heinemann, 2013.

[138] E. W. Weisstein, "Binomial Coefficient," MathWorld–A Wolfram Web Resource, 2018. [Online]. Available: http://mathworld.wolfram.com/BinomialCoefficient.html

[139] ——, "Regularized Hypergeometric Function," MathWorld–A Wolfram Web Resource, 2018. [Online]. Available: http://mathworld.wolfram.com/RegularizedHypergeometricFunction.html

[140] P. Virtanen, R. Gommers, T. E. Oliphant, M. Haberland, T. Reddy, D. Cournapeau, E. Burovski, P. Peterson, W. Weckesser, J. Bright, S. J. van der Walt, M. Brett, J. Wilson, K. J. Millman, N. Mayorov, A. R. J. Nelson, E. Jones, R. Kern, E. Larson, C. J. Carey, I. Polat, Y. Feng, E. W. Moore, J. VanderPlas, D. Laxalde, J. Perktold, R. Cimrman, I. Henriksen, E. A. Quintero, C. R. Harris, A. M. Archibald, A. H. Ribeiro, F. Pedregosa, and P. van Mulbregt, "SciPy 1.0: fundamental algorithms for scientific computing in Python," *Nature Methods*, vol. 17, pp. 261–272, 2020.

[141] ANSYS Inc., "ANSYS® Academic Research Mechanical, Release 19.0 Help System, Coupled Field Analysis Guide, ANSYS, Inc." Tech. Rep., 2018.

[142] D. Chakraborty, J. R. Prakash, J. Friend, and L. Yeo, "Fluid-structure interaction in deformable microchannels," *Phys. Fluids*, vol. 24, p. 102002, 2012.

[143] M. A. Hussain, S. Kar, and R. R. Puniyani, "Relationship between power law coefficients and major blood constituents affecting the whole blood viscosity," *J. Biosci.*, vol. 24, pp. 329–337, 1999.

[144] J. D. Cutnell and K. Johnson, *Physics*, 4th ed.   Wiley, 1998.

[145] V. Anand, S. C. Muchandimath, and I. C. Christov, "Hydrodynamic Bulge Testing: Materials Characterization Without Measuring Deformation," *ASME J. Appl. Mech.*, vol. 87, p. 051012, 2020.

[146] N. Challamel and I. Elishakoff, "A brief history of first-order shear-deformable beam and plate models," *Mech. Res. Commun.*, vol. 102, p. 103389, 2019.

[147] J. N. Reddy, *Theory and Analysis of Elastic Plates and Shells*, 2nd ed.   Boca Raton, FL: CRC Press, an imprint of Taylor & Francis Group, 2007.

[148] P. Howell, G. Kozyreff, and J. Ockendon, *Applied Solid Mechanics*.   Cambridge, UK: Cambridge University Press, 2009.

[149] J. Blaauwendraad, *Plates and FEM: Surprises and Pitfalls*, ser. Solid Mechanics and Its Applications.   Dordrecht: Springer, 2010, vol. 171.

[150] S. P. Timoshenko, "On the correction for shear of the differential equation for transverse vibrations of prismatic bars," *Phil. Mag., Ser. 6*, vol. 41, no. 245, pp. 744–746, 1921.

[151] F. Gruttmann and W. Wagner, "Shear correction factors in Timoshenko's beam theory for arbitrary shaped cross-sections," *Comput. Mech.*, vol. 27, pp. 199–207, 2001.

[152] J. N. Reddy, *An Introduction to Nonlinear Finite Element Analysis*.   Oxford, UK: Oxford University Press, 2004.

[153] A. E. H. Love, *A treatise on mathematical theory of elasticity*, 4th ed.   New York: Dover Publications, 1944.

[154] L. G. Leal, *Advanced Transport Phenomena: Fluid Mechanics and Convective Transport Processes*, ser. Cambridge Series in Chemical Engineering.   New York, NY: Cambridge University Press, 2007, vol. 7.

[155] ANSYS Inc., "ANSYS® Academic Research Mechanical, Release 19R2 Help System, Coupled Field Analysis Guide, ANSYS, Inc." Tech. Rep., 2019.

[156] O. Paul and H. Baltes, "Mechanical behavior and sound generation efficiency of pre-stressed, elastically clamped and thermomechanically driven thin film sandwiches," *J. Micromech. Microeng.*, vol. 9, pp. 19–29, 1999.

[157] S. C. Chapra and R. P. Canale, *Numerical Methods for Engineers*, 7th ed.   New York, NY: McGraw-Hill Education, 2015.

[158] A. Mehboudi and J. Yeom, "Experimental and theoretical investigation of a low-Reynolds-number flow through deformable shallow microchannels with ultra-low height-to-width aspect ratios," *Microfluid. Nanofluid.*, vol. 23, p. 66, 2019.

[159] J. Mandel, *The Statistical Analysis of Experimental Data*.   Mineola, NY: Dover Publications, 1984.

[160] V. Anand and I. C. Christov, "Revisiting steady viscous flow of a generalized Newtonian fluid through a slender elastic tube using shell theory," *preprint*, no. arXiv:1810.05155, 2018.

[161] K. Perktold, G. Karner, A. Leuprecht, and M. Hofer, "Influence of non-Newtonian flow behavior on local hemodynamics," *Z. Angew. Math. Mech. (ZAMM)*, vol. 79, no. S1, pp. 187–190, 1999.

[162] N. J. Balmforth, I. A. Frigaard, and G. Ovarlez, "Yielding to stress: Recent developments in viscoplastic fluid mechanics," *Annu. Rev. Fluid Mech.*, vol. 46, pp. 121–146, 2014.

[163] M. M. Denn, *Process Fluid Mechanics*.   Edgewood Cliffs, NJ: Prentice-Hall, 1980.

[164] H. Kraus, *Thin Elastic Shells*.   New York, NY: John Wiley & Sons, 1967.

[165] W. Flügge, *Stresses in Shells*.   Berlin/Heidelberg: Springer, 1960.

[166] C. Vlachopoulos, M. O'Rourke, and W. W. Nichols, *McDonald's Blood Flow in Arteries: Theoretical, Experimental and Clinical Principles*.   Boca Raton, FL: CRC Press, 2011.

[167] F. Nobile and A. Veneziani, "Fluid structure interaction in blood flow problems," *Z. Angew. Math. Mech. (ZAMM)*, vol. 79, no. S1, pp. 255–258, 1999.

[168] A. Quarteroni, M. Tuveri, and A. Veneziani, "Computational vascular fluid dynamics: problems, models and methods," *Comput. Visual. Sci.*, vol. 2, pp. 163–197, 2000.

[169] L. Formaggia, J. F. Gerbeau, F. Nobile, and A. Quarteroni, "On the coupling of 3D and 1D Navier-Stokes equations for flow problems in compliant vessels," *Comput. Meth. Appl. Mech. Engng*, vol. 191, pp. 561–582, 2001.

[170] S. Čanić, D. Lamponi, A. Mikelić, and J. Tambača, "Self-consistent effective equations modeling blood flow in medium-to-large compliant arteries," *Multiscale Model. Simul.*, vol. 3, pp. 559–596, 2005.

[171] S. Čanić, G. Guidoboni, and A. Mikelić, "Fluid-structure interaction in a pre-stressed tube with thick elastic walls I: the stationary Stokes problem," *Netw. Heterog. Media*, vol. 2, pp. 397–423, 2007.

[172] L. H. Donnell, "Stability of thin-walled tubes under torsion," NACA-TR-479, Tech. Rep., 1933. [Online]. Available: https://ntrs.nasa.gov/search.jsp?R=19930091553

[173] C. L. Dym, *Introduction to the Theory of Shells*. New York, NY: Hemisphere Publishing Corporation, 1990.

[174] E. Winkler, *Die Lehre von der Elastizität und Festigkeit mit besonderer Rücksicht auf ihre Anwendung in der Technik*. Prag: Verlag von H. Dominicus, 1867. [Online]. Available: https://www.google.com/books/edition/_/25E5AAAAcAAJ

[175] M. Hetényi, *Beams On Elastic Foundation: Theory with Applications in The Fields of Civil and Mechanical Engineering*. Ann Arbor, MI: The University of Michigan Press, 1946.

[176] D. A. Dillard, B. Mukherjee, P. Karnal, R. C. Batra, and J. Frechette, "A review of Winkler's foundation and its profound influence on adhesion and soft matter applications," *Soft Matter*, vol. 14, pp. 3669–3683, 2018.

[177] A. P. Bunger and A. R. Cruden, "Modeling the growth of laccoliths and large mafic sills: Role of magma body forces," *J. Geophys. Res. Solid Earth*, vol. 116, p. B02203, 2011.

[178] T. V. Ball and J. A. Neufeld, "Static and dynamic fluid-driven fracturing of adhered elastica," *Phys. Rev. Fluids*, vol. 3, p. 074101, 2018.

[179] S. I. Rubinow and J. B. Keller, "Flow of a viscous fluid through an elastic tube with applications to blood flow," *J. Theor. Biol.*, vol. 34, pp. 299–313, 1972.

[180] H. B. Keller, *Numerical Solution of Two Point Boundary Value Problems*, ser. CBMS-NSF Regional Conference Series in Applied Mathematics. Philadelphia, PA: SIAM, 1976, vol. 24.

[181] M. H. Holmes, *Introduction to Perturbation Methods*, ser. Texts in Applied Mathematics. New York, NY: Springer Science+Business Media, 2013, vol. 20.

[182] J. C. Neu, *Singular Perturbation in the Physical Sciences*, ser. Graduate Studies in Mathematics. Providence, RI: American Mathematical Society, 2015, vol. 167.

[183] M. Heil and T. J. Pedley, "Large axisymmetric deformation of a cylindrical shell conveying a viscous flow," *J. Fluids Struct.*, vol. 9, pp. 237–256, 1995.

[184] T. Matsumoto, S. Sugita, and T. Yaguchi, "Biomechanics of blood vessels: Structure, mechanics, and adaptation," in *Advances in Metallic Biomaterials*, ser. Springer Series in Biomaterials Science and Engineering. Berlin/Heidelberg: Springer-Verlag, 2015, vol. 3, ch. 4, pp. 71–98.

[185] A. P. Ebrahimi, "Mechanical properties of normal and diseased cerebrovascular system," *J. Vasc. Interv. Neurol.*, vol. 2, pp. 155–162, 2009.

[186] C. Kleinstreuer, *Biofluid Dynamics: Principles and Selected Applications*. Boca Raton, FL: CRC Press, an imprint of Taylor & Francis Group, 2006.

[187] C. D. Bertram and J. Tscherry, "The onset of flow-rate limitation and flow-induced oscillations in collapsible tubes," *J. Fluids Struct.*, vol. 22, pp. 1029–1045, 2006.

[188] Y. Bazilevs, K. Takizawa, and T. E. Tezduyar, *Computational Fluid-Structure Interaction Methods and Applications*. Chichester, UK: John Wiley & Sons Inc., 2013.

[189] G. Bugliarello and J. Sevilla, "Velocity distribution and other characteristics of steady and pulsatile blood flow in fine glass tubes," *Biorheology*, vol. 7, pp. 85–107, 1970.

[190] S. Čanić, C. J. Hartley, D. Rosenstrauch, J. Tambača, G. Guidoboni, and A. Mikelić, "Blood flow in compliant arteries: An effective viscoelastic reduced model, numerics, and experimental validation," *Ann. Biomed. Eng.*, vol. 34, pp. 575–592, 2006.

[191] P. S. Ayyaswamy, "Introduction to Biofluid Mechanics," in *Fluid Mechanics*, 6th ed., P. K. Kundu, I. M. Cohen, and D. R. Dowling, Eds. San Diego, CA: Academic Press, an imprint of Elsevier Inc., 2016, ch. 16, pp. e1–e73.

[192] F. Costanzo and J. G. Brasseur, "The invalidity of the Laplace law for biological vessels and of estimating elastic modulus from total stress vs. strain: A new practical method," *Math. Med. Biol.*, vol. 32, pp. 1–37, 2015.

[193] V. Anand and I. C. Christov, "On the Deformation of a Hyperelastic Tube Due to Steady Viscous Flow Within," in *Dynamical Processes in Generalized Continua and Structures*, ser. Springer Series on Advanced Structured Materials, H. Altenbach, A. Belyaev, V. A. Eremeyev, A. Krivtsov, and A. V. Porubov, Eds. Cham, Switzerland: Springer Nature, 2019, vol. 103, ch. 2, pp. 17–35.

[194] N. J. Wagner and J. F. Brady, "Shear thickening in colloidal dispersions," *Phys. Today*, vol. 62, no. 10, pp. 27–32, 10 2009.

[195] J. Bonet and R. J. Wood, *Nonlinear Continuum Mechanics for Finite Element Analysis*, 2nd ed. New York, NY: Cambridge University Press, 2008.

[196] Y. Başar and D. Weichert, *Nonlinear Continuum Mechanics of Solids*. Berlin/Heidelberg: Springer-Verlag, 2000.

[197] A. I. Lurie, *Theory of Elasticity*, ser. Foundations of Engineering Mechanics. Berlin/Heidelberg: Springer-Verlag, 2005.

[198] R. W. Ogden, "Large deformation isotropic elasticity – On the correlation of theory and experiment for incompressible rubberlike solids," *Proc. R. Soc. Lond. A*, vol. 326, pp. 565–584, 2 1972.

[199] I. S. Liu, "A note on the Mooney–Rivlin material model," *Continuum Mech. Thermodyn.*, vol. 24, no. 4-6, pp. 583–590, 2012.

[200] H. Moon and C. Truesdell, "Interpretation of adscititious inequalities through the effects pure shear stress produces upon an isotropie elastic solid," *Arch. Rational Mech. Anal.*, vol. 55, pp. 1–17, 1974.

[201] L. A. Mihai and A. Goriely, "Positive or negative Poynting effect? the role of adscititious inequalities in hyperelastic materials," *Proc. R. Soc. A*, vol. 467, pp. 3633–3646, 2011.

[202] N. I. Muskhelishvili, *Some Basic Problems of the Mathematical Theory of Elasticity: Fundamental Equations, Plane Theory of Elasticity, Torsion and Bending*, 2nd ed. Dordrecht: Springer Science+Business Media, 1977.

[203] M. Vable, *Mechanics of Materials*, 2nd ed. Expanding Educational Horizons, LLC, 2009. [Online]. Available: http://madhuvable.org

[204] A. Lazopoulos and S. Tsangaris, "Flow of incompressible viscous fluid through a tube with non-linear elastic membrane insertion: Applications," *Eng. Appl. Comput. Fluid Mech.*, vol. 2, pp. 222–233, 2008.

[205] ——, "Fluid flow of incompressible viscous fluid through a non-linear elastic tube," *Arch. Appl. Mech.*, vol. 78, pp. 895–907, 2008.

[206] V. Anand and I. C. Christov, "Transient compressible flow in a compliant viscoelastic tube," *preprint*, no. arXiv:2007.03077, 2020.

[207] P. K. Kundu, I. M. Cohen, and D. R. Dowling, *Fluid Mechanics*, 6th ed. San Diego, CA: Academic Press, an imprint of Elsevier, 2016.

[208] P. A. Chambre and S. A. Schaaf, *Flow of Rarefied Gases*, ser. Princeton Aeronautical Paperbacks. Princeton, NJ: Princeton University Press, 1961, vol. 8.

[209] E. Lauga, M. Brenner, and H. Stone, "Microfluidics: The No-Slip Boundary Condition," in *Springer Handbook of Experimental Fluid Mechanics*, C. Tropea, A. L. Yarin, and J. F. Foss, Eds. Berlin/Heidelberg: Springer-Verlag, 2007, ch. 19, pp. 1219–1240.

[210] M. Hattori, S. Kosuge, and K. Aoki, "Slip boundary conditions for the compressible Navier-Stokes equations for a polyatomic gas," *Phys. Rev. Fluids*, vol. 3, p. 063401, 2018.

[211] A. Martínez-Calvo, A. Sevilla, G. G. Peng, and H. A. Stone, "Start-up flow in shallow deformable microchannels," *J. Fluid Mech.*, vol. 885, p. A25, 2020.

[212] S. Čanić, J. Tambača, G. Guidoboni, A. Mikelić, C. J. Hartley, and D. Rosenstrauch, "Modeling viscoelastic behavior of arterial walls and their interaction with pulsatile blood flow," *SIAM J. Appl. Math.*, vol. 67, pp. 164–193, 2006.

[213] W. Flügge, *Viscoelasticity*, 2nd ed. Berlin/Heidelberg: Springer-Verlag, 1975.

[214] H. T. Banks, R. C. Smith, and Y. Wang, "The modeling of piezoceramic patch interactions with shells, plates, and beams," *Quart. Appl. Math.*, vol. 53, pp. 353–381, 1995.

[215] H. T. Banks, R. C. H. del Rosario, and R. C. Smith, "Reduced-order model feedback control design: numerical implementation in a thin shell model," *IEEE Trans. Automat. Contr.*, vol. 45, pp. 1312–1324, 2000.

[216] Z. J. G. N. del Prado, M. Amabili, and P. B. Gonçalves, "Non linear vibrations of imperfect fluid-filled viscoelastic cylindrical shells," *Procedia Engineering*, vol. 199, pp. 570–576, 2017.

[217] M. Reiner, "The Deborah Number," *Physics Today*, vol. 17, no. 1, p. 62, 1964.

[218] G. Taylor and P. G. Saffman, "Effects of compressibility at low Reynolds number," *J. Aeronaut. Sci.*, vol. 24, pp. 553–562, 1957.

[219] N. Riley, "Steady treaming," *Annu. Rev. Fluid Mech.*, vol. 33, pp. 43–65, 2001.

[220] P. Hall, "Unsteady viscous flow in a pipe of slowly varying cross-section," *J. Fluid Mech.*, vol. 64, pp. 209–226, 6 1974.

[221] W. H. Lyne, "Unsteady viscous flow in a curved pipe," *J. Fluid Mech.*, vol. 45, pp. 13–31, 1971.

[222] K. P. Selverov and H. A. Stone, "Peristaltically driven channel flows with applications toward micromixing," *Phys. Fluids*, vol. 13, pp. 1837–1859, 2001.

[223] J. W. Strutt, "I. On the circulation of air observed in Kundt's tubes, and on some allied acoustical problems," *Phil. Trans. R. Soc. Lond. A*, vol. 175, pp. 1–21, 1884.

[224] S. S. Sadhal, "Acoustofluidics 13: Analysis of acoustic streaming by perturbation methods," *Lab Chip*, vol. 12, pp. 2292–2300, 2012.

[225] M. J. Lighthill, *Waves in Fluids*. Cambridge, UK: Cambridge University Press, 2001.

[226] A. Lenshof and T. Laurell, "Acoustophoresis," in *Encyclopedia of Nanotechnology*, B. Bhushan, Ed. Dordrecht: Springer Science+Business Media, 2015, pp. 1–6.

[227] S. Middleman, "Flow of power law fluids in rectangular ducts," *Trans. Soc. Rheol.*, vol. 9, pp. 83–93, 1965.

[228] T. K. Kim, J. K. Kim, and O. C. Jeong, "Measurement of nonlinear mechanical properties of PDMS elastomer," *Microelectron. Eng.*, vol. 88, pp. 1982–1985, 2011.

[229] L. C. Auton and C. W. MacMinn, "From arteries to boreholes: steady-state response of a poroelastic cylinder to fluid injection," *Proc. R. Soc. A*, vol. 473, p. 20160753, 2017.

VITA

VITA

Vishal Anand

Education

- Ph.D. in Mechanical Engineering (Aug. 2016 – Aug. 2020), Purdue University, West Lafayette, IN.

- M.Tech in Thermal, Fluid and Environmental Engineering + B.Tech in Mechanical Engineering, Dual Degree Program (July 2004 – June 2010), Department of Mechanical Engineering, Indian Institute of Technology Kharagpur West Bengal, India.

Work Experience

- Airframe Engineer, AIRBUS INDIA, Bengaluru, India (Dec. 2015 – Aug. 2016).

- Team Leader, CYIENT India Limited, Hyderabad, India (May 2011 – Dec. 2015).

Publications resulting from this dissertation

- **Vishal Anand** and Ivan C. Christov, *Transient compressible flow in a compliant viscoelastic tube.* Submitted (2020). Preprint: arXiv:2007.03077.

- **Vishal Anand** and Ivan C. Christov, *Revisiting steady viscous flow of a generalized Newtonian fluid through a slender elastic tube using shell theory.* Under review (2019). Preprint: arXiv:1810.05155.

- **Vishal Anand**, Sanjan C. Muchandimath, and Ivan C. Christov, *Hydrodynamic Bulge Testing of Pre-Stressed Thick Elastic Plates*. ASME Journal of Applied Mechanics. 87(5): 051012. DOI:10.1115/1.4046297

- **Vishal Anand** and Ivan C. Christov, *On the Deformation of a Hyperelastic Tube Due to Steady Viscous Flow Within*. In: Altenbach H., Belyaev A., Eremeyev V., Krivtsov

A., Porubov A. (eds) Dynamical Processes in Generalized Continua and Structures. Advanced Structured Materials, vol 103. Springer, Cham. DOI:978-3-030-11665-1

- **Vishal Anand**, Joshua David JR, and Ivan C. Christov, *Non-Newtonian fluid–structure interactions: Static response of a microchannel due to internal flow of a power-law fluid*. Journal of Non-Newtonian Fluid Mechanics, Volume 264, Pages 62-72. DOI:10.1016/j.jnnfm.2018.12.008